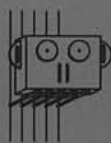


Proceedings

1996 National Sensor Conference

March 20 - 21, 1996

Delft, The Netherlands.



TU Delft

An initiative of the Platform "Sensor Technology"



649159

Proceedings

1996 National Sensor Conference

March 20 - 21, 1996

Delft, The Netherlands.

Bibliotheek TU Delft



C 0003813875



TU Delft

An initiative of the Platform "Sensor Technology"

2414
569
1



Proceedings

1996 National Sensor Conference

March 20 - 21, 1996

Delft, The Netherlands

Conference Secretariat

Delft University of Technology
attn. R.F. Wolffenbuttel,
Department of Electrical Engineering,
Laboratory for Electronic Instrumentation,
Mekelweg 4, NL-2628 CD, Delft,
The Netherlands.

Published by

Delft University Press,
Stevinweg 1, NL-2628 CN, Delft,
The Netherlands.
Phone: +31 152783254

Proceedings 1996 National Sensor Conference
ISBN 90-407-1321-9 / CIP
NUGI 832

Subject headings

Sensors, Actuators, Microsystems.

© Copyright

Copyright 1996 by R.F. Wolffenbuttel
Department of Electrical Engineering,
Laboratory for Electronic Instrumentation,
Delft University of Technology, The Netherlands.

All rights reserved. No part of this proceedings may be reproduced, stored in a retrieval system, or transmitted, in any form or by any means, electronic, mechanical, photocopying, recording, or otherwise, without the prior permission of the publisher.

The publisher assumes no responsibility for the contents of the papers comprising this proceedings. No responsibility is assumed for any injury and/or damage to persons or property as a matter of products liability, negligence or otherwise, or from any use or operation of any methods, products, instructions, or ideas contained in the material herein. Neither does the publisher assume any responsibility for the eventual infringement on intellectual properties.

Printed in The Netherlands.

PREFACE

Sensors have been promising devices for a long period of time. Sensors in general, because these are essential elements in measurement systems and silicon sensors in particular, because of the potential to be merged with integrated circuits in silicon. In the footsteps of sensor research also the actuators have become of importance due to the fact that an information processing system is usually composed of both a measurement and control unit. Downscaling of the dimensions of the entire system has prompted research on microsystems. However, all these devices and especially the silicon sensor, have a problem in making the promise come true. Much scientific work has been done and the field has been gradually recognized as mature, which is reflected by the number and quality of international conferences devoted to these devices. However, if the sensor is really such a strategic component with a lot of room for improvement in terms of performance-to-price ratio when compared e.g. to integrated circuits, it should also have given rise to a considerable industrial infrastructure.

The reasons for the limited transfer of the impressive results of (basic) research into industrial activity is due to many factors of which some are intrinsic to the device, such as low volume production, application specific package and a component cost that is in a far lesser extent set by wafer processing compared to integrated circuits, but also by a number of factors that can be influenced, such as the flow of information between research and industry and the bridging of the (long) time interval between concept and product. This mismatch and the widely recognized strategic importance of sensors, actuators and microsystems has prompted initiatives at the National and European level to support the bidirectional flow of information between research (universities, institutes and industrial laboratories) and industry, as well as to provide financial support to bridge the time gap between the academic feasibility study and the prototype (the basic research and subsequent pre-competitive phase). These initiatives are expected to give a strong increase in the number of successful commercial applications.

In the Netherlands the Platform "Sensor Technology" has been established to take initiatives that are aiming on stimulating industry in using scientific results. One method to improve the flow of information is by organizing conferences and the 1996 National Sensor Conference is the second in a series of biennial events organized for this reason under the auspices of the Platform and the Cross Coordinating Committee "Sensor Technology" as part of the STW/NWO joint priority programme "Sensor Technology". Therefore, the purpose of this Sensor Conference is both to provide an opportunity for the presentation of recent results in all relevant aspects of research on sensors, actuators and microsystems as well as to serve as a meeting point between researchers from universities, institutes and industry and managers and systems designers involved in promising application areas of sensors, actuators and microsystems.

This book contains 5 invited papers and 44 contributed papers covering most aspects of the field. This event has only been possible as a result of the efforts of the programme committee, the local organizing committee, STW, many members of the Laboratory for Electronic Instrumentation of the Delft University of Technology and the authors, which are highly appreciated.

R.F. Wolffenbuttel
Chairman

Programme Committee

R.F. Wolffenbuttel; Chairman (Delft University of Technology)
P.J. French (Delft University of Technology)
P.P.L. Regtien (Twente University)
P.V. Lambeck (Twente University)
A.W. van Herwaarden (XI, on behalf of SME)
M. de Samber (Philips)

Manuscript preparation

M.R. Wolffenbuttel

CONTENTS

Automotive exhaust gas constituents sensors (invited paper) <i>J. Visser, M. Zanini, A. Kovalchuk, R. Soltis and E. Logothetis</i>	1
Glucose sensor based on microdialysis <i>A. Schoonen and K. Wientjes</i>	13
Measurement of the dynamic surface tension in liquids by means of gas bubbles generated at single nucleation site electrodes <i>A. Volanschi, W. Olthuis and P. Bergveld</i>	17
Electrochemical microvalve <i>C. Neagu, J. Gardeniers, M. Elwenspoek and J. Fluitman</i>	21
Microsystems activities at CSEM (invited paper) <i>T. Smith, H. van der Vlekkert and F. Rudolf</i>	25
Design, fabrication and characterisation of a planar microcoil inductor for power supply in and data exchange with implantable microsystems <i>A. Smith, C. Neagu, J. Gardeniers, M. Elwenspoek and J. Fluitman</i>	35
Range camera at 12-bit resolution and video speed <i>M. de Bakker, P. Verbeek and G. Steenvoorden</i>	39
Light-to-frequency converter with a digital output <i>G. de Graaf and R. Wolffenbuttel</i>	45
First results on a new type of photon counting Avalanche photodiode <i>W. Kindt, N. Shahrjerdy and H. van Zeijl</i>	51
Exploiting a coulometrically obtained acid-base titration curve for automated acid concentration determination <i>J. Hendrikse, F. Pierdominici, W. Olthuis and P. Bergveld</i>	55
Bragg reflector used as integrated chemo-optical sensor <i>G. Veldhuis, J. Berends, R. Heideman and P. Lambeck</i>	59
Acid-base titration with an ISFET microsensors as a tool for protein detection <i>J. Kruijs, J. Eijkel and P. Bergveld</i>	63
Detection of staphylococcal enterotoxin B employing a piezoelectric crystal immunosensor <i>J. Hartevelde, M. Nieuwenhuizen and E. Wils</i>	67

The integrated Mach-Zehnder interferometer sensor for the detection of biological molecules <i>E.Schipper, A.Brugman, C.Dominguez, L.Lechuga, R.Kooyman and J.Greve</i>	71
Development of on-line immunosensors for cortisol and other metabolites <i>W.Kapteijn, J.Zwaagstra, K.Venema, M.Ruiters and J.Korf</i>	75
Durable anion-selective sensors based on polysiloxane membranes <i>M.Antonisse, R.Lugtenberg, J.Engbersen and D.Reinhoudt</i>	79
Durable chemical sensors for heavy metal ions based on FET's <i>R.Lugtenberg, R.Egberink, J.Engbersen and D.Reinhoudt</i>	83
Development of a low-cost ventilation rate sensor combined with an ammonia sensor for ammonia emission measurement and control <i>D.BERCKMANS, E.Vranken, J.Ni, J.Roggen and G.Huybrechts</i>	87
Silicon fusion bonding with chemical mechanical polishing <i>C.Gui, H.Albers, J.Gardeniers, M.Elwenspoek and P.Lambeek</i>	93
A high-T_c superconductor bolometer on a Si_3N_4/Si membrane <i>S.Sánchez, M. de Nivelle, W.Michalke, E.Steinbeiss, M.Burnus, T.Heidenblut, B.Schwierzi, R. de Vries, P. de Korte and M. Elwenspoek</i>	99
Silicon drift detectors for the detection of X- and γ-rays <i>H.Valk, E.Hijzen, J.Huizenga, C. van Eijk, R.Hollander, L.Nanver, P.Sarro, A. van den Boogaard and J.Slabbekoorn</i>	103
Active interference filters using silicon-compatible materials <i>D.Poenar, P.French and R.Wolffenbuttel</i>	109
A humidity sensitive capacitor based on a porous silicon dielectric <i>G. O'Halloran, M.Kuhl, P.Trimp and P.French</i>	113
On-chip micromachined corrector of a focal distance <i>G.Vdovin and S.Middelhoek</i>	117
Flexible package for a tactile sensor array <i>Z.Chu</i>	121
A smart voltage processor for thermocouples <i>S.Khadouri, G.Meijer, and F. van der Goes</i>	125
Microsystem technology: Status and infrastructure <i>J.Elders and V.Spiering</i>	131

Model-based parameter estimation from eddy-current images and application in a multi-sensor waste separation system <i>N.Gorte-Kroupnova, Z.Houkes and P.Regtien</i>	135
New methods for non-destructive sterility testing of aseptically packed food products <i>S.Nihtianov, G.Meijer, H.Kerkvliet and E.Demeijer</i>	139
A μsensor array in a fluidic system for space applications <i>V.Spiering, P.Bergveld, M.Elwenspoek and A. van den Berg</i>	143
A low-cost universal measurement system for resistive (bridge) and capacitive sensors <i>G.Wang, F. van der Goes, G.Meijer and H.Kerkvliet</i>	147
A low-cost high-performance capacitive absolute angular encoder <i>X.Li and G.Meijer</i>	151
Sensor interface environment <i>F.Riedijk, M.Balijon, E. van Kampen, M. de Groot and J.Huijsing</i>	155
Optical and acoustic sensor systems for autonomous mobile robots <i>P.Trimp, G.Buis and P.French</i>	159
Simulation and development of a 1-bar capacitive differential pressure sensor <i>M.Pedersen, M.Meijerink, W.Olthuis and P.Bergveld</i>	163
Development of a high-temperature resistance thermometer using noise thermometry <i>M. de Groot, J.DUBBELDAM, H.BRIXY, F.EDLER, G.Dhupia and M.Chattle</i>	167
Superconductive tunnel junctions for X-ray spectroscopy <i>M. van den Berg, M.Bruijn, J.Gomez, F.Kiewiet, H. van Lieshout, O.Luiten, N.Snijders and P. de Korte</i>	173
Micromechanics at MIC (invited paper) <i>S.Bouwstra</i>	177
Thick polysilicon microstructures by combination of epitaxial and poly growth in a single deposition step <i>P.Gennissen, M.Bartek, P.French and P.Sarro</i>	189
Problems of sacrificial etching in a combined surface micromachining and electronic process <i>J.Goosen, B. van Drieënhuizen, P.French and R.Wolffenbuttel</i>	193

Calibration of a poly-silicon piezo-resistor array for package stress measurements <i>A.Bossche and J.Mollinger</i>	197
Advances in biosensors (invited paper) <i>D.Cullen and A.Turner</i>	201
Self-assembled monolayers of receptor adsorbates on a gold surface <i>M.Beulen, B.-H.Huisman, E.Thoden van Velzen, F. van Veggel and D.Reinhoudt</i> . .	207
Sensors for agricultural production in the 21st century <i>F.Kampers, J.Bakker, G.Bot, H.Breteler, C.Eerkens and O. de Kuijer</i>	211
A symmetrical triaxial capacitive accelerometer for biomedical purposes <i>J.Lötters, W.Olthuis, P.Veltink and P.Bergveld</i>	217
A waveguide material for integrated optical sensors: silicon oxynitride (invited paper) <i>H.Albers, L.Hilderink, J.Berends, K.Wörhoff, N. van Hulst and P.Lambeck</i>	221
Electro-optical phase modulation in zincoxide (ZnO) <i>R.Heideman, R.Lammers and P.Lambeck</i>	231
High-voltage probe <i>A.Fransen, G.Lubking and M.Vellekoop</i>	235
Luminescence quenching for chemo-optical sensing <i>G.Hesselink, P.Lambeck, Th.Popma, H. v.d. Bovenkamp and J.Engbersen</i>	239

AUTOMOTIVE EXHAUST GAS CONSTITUENTS SENSORS

J. H. Visser, M. Zanini, A. Kovalchuk, R. E. Soltis, E. M. Logothetis

Ford Motor Company, Research Laboratory MD3028,
P.O. Box 2053, Dearborn MI 48121-2053, USA
E-mail: jvisser@ford.com, Ph.: (313) 845-0101, Fx.: (313) 322-7044

ABSTRACT

Oxygen sensors play a crucial role in obtaining low exhaust gas emissions in gasoline-powered vehicles. More stringent emissions control legislation and the new requirement of having on-board diagnostic systems (OBD) to monitor the performance of a number of emissions-related vehicle components and systems for 100,000 miles or 10 years, necessitate research on Exhaust Gas Constituent (EGC) sensors, i.e. sensors for measuring hydrocarbons, carbon monoxide, and oxides of nitrogen. First, this paper briefly reviews the emissions standards, test procedures and OBD requirements, and then explains the present engine control system and the functioning and role of the ZrO_2 oxygen sensor. The remainder of the paper discusses some EGC sensor technologies under investigation at the Ford Research Laboratory, e.g., oxygen pumping devices and catalytic (micro)calorimetric sensors.

INTRODUCTION

Since the mid-1960s, when emissions standards for motor vehicles were introduced (first in California and then throughout the USA), a worldwide effort has been underway to reduce the exhaust emissions from automotive internal combustion engines, as well as the evaporative emissions from the fuel system. The undesirable emissions fall into four categories: hydrocarbons HC (including oxygenated HC, such as aldehydes and ketones), carbon monoxide CO, oxides of nitrogen NO_x , and particulates (mainly from diesel engines). In addition, carbon dioxide ("greenhouse gas") emissions have come under scrutiny as well. The emissions standards have become increasingly stringent since their first introduction to the point that gasoline-powered vehicles sold in the US market between 1983 and 1992 had their hydrocarbons and carbon monoxide exhaust emissions reduced by 96% and

their oxides of nitrogen exhaust emissions by 76%, compared to the uncontrolled levels. These reductions are made possible through the application of several advanced technologies including electronic fuel injection systems, on-board computers, catalytic converters, exhaust gas recirculation, and feedback control systems (based on the oxygen sensor) for metering air and fuel mixture [1]. Further reductions in emissions, to be phased-in over a number of years, have been legislated in the USA (1990 Clean Air Act Amendment), European Union ("Stage III" emissions regulations), and other parts of the world. For example, the levels of hydrocarbons in California (which imposes very strict standards because of unique air quality problems in some of its metropolitan areas) must be reduced by a factor of 10 compared with 1992 levels, and carbon monoxide and oxides of nitrogen must be reduced at least in half. In addition, emissions requirements have been extended from 50,000 to 100,000 miles (or 10 years, whichever comes first).

The emissions standards in the USA are expressed in grams/mile as measured over the Federal Test Procedure (FTP). The FTP is a drive cycle that simulates an average trip in a city area and includes cold start, several accelerations and decelerations, idling and cruises. It is carried out on a chassis-dynamometer under well-controlled, standardized conditions. The FTP is shown in Fig. 1 and consists of three (driving) parts: the cold phase (0-505 s), the stabilized phase (505-1372 s), a 10 minute break with the engine off, and the hot phase (1972-2477 s, a repeat of the 505 s cold phase with a warmed-up engine). Other countries have either adapted this US test cycle or devised their own. As exhaust gas emissions have come down considerably over the years, the relative contribution of the "cold start" (approximately the first minute) has increased. In this portion of the test, the catalyst is not yet functional, because it has not heated up to its ideal operating temperature of approximately 400-800 °C. The exhaust gases produced during the FTP test are collected in three bags using the so-called constant-volume sampling method [2]. In this procedure the exhaust gas is greatly diluted with air to prevent condensation of water vapor (and water-soluble emissions) and inhibit reactions between emissions. Subsequent analysis is carried out to determine the total emissions mass in each three bags and a weighted average emissions mass (over the entire test) in grams/mile is obtained.

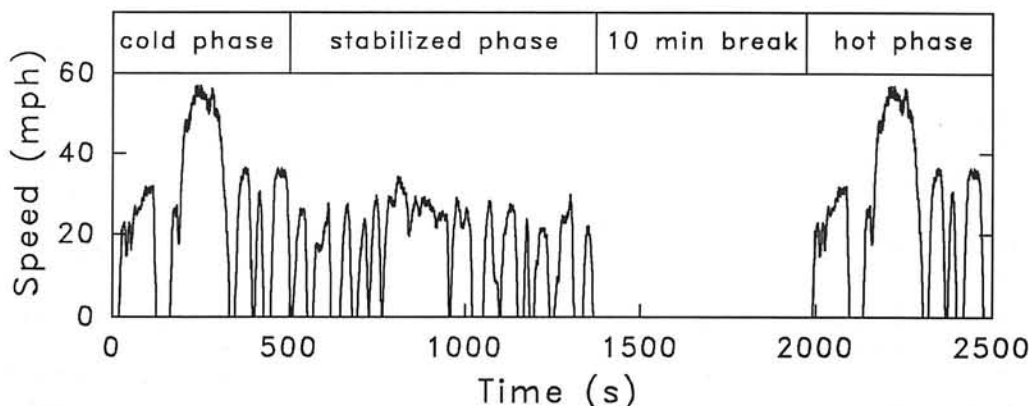


Figure 1: Speed (mph) during the Federal Test Procedure (FTP) drive cycle.

It is also possible to selectively obtain second-by-second volume concentrations of (total) hydrocarbons (by using a flame ionization detector), carbon monoxide (by using an infrared detector), and oxides of nitrogen (by using a detector based on chemiluminescence).

In addition to the lowering of emissions levels worldwide, the US regulations also require on-board diagnostic systems (OBD) to monitor the performance of a number of emissions-related vehicle components and systems. One of the challenging tasks is to determine the degradation in catalyst hydrocarbon conversion efficiency as the vehicle and its components age. Accurate measurements have to be made on the vehicle under real-world driving conditions and converted to an equivalent FTP emissions mass. Some other OBD tasks include detection of engine misfires, and determination of oxygen sensor, exhaust gas recirculation, and evaporative fuel recovery system performance.

THE ENGINE CONTROL SYSTEM AND THE OXYGEN SENSOR

Engine design and operation, and exhaust gas after-treatment with a three-way-catalyst are the main methods today used to achieve low emissions in gasoline-powered vehicles. To obtain a maximum efficiency of the three-way-catalyst for oxidizing hydrocarbons and carbon monoxide to carbon dioxide and water on one hand and reducing oxides of nitrogen to nitrogen and oxygen on the other hand, the engine must run at or close to the stoichiometric air/fuel mixture, as is shown in Fig. 2. Electronic fuel injection to precisely supply the amount of fuel is necessary, but not sufficient. Also needed is an oxygen sensor in or close to the exhaust manifold to detect the stoichiometric point. This and other information (i.e. engine speed, load, and coolant temperature, etc.) is feedback to the microprocessor-based engine control system to fine-tune the air/fuel ratio and modify other engine inputs (i.e. exhaust gas recirculation, ignition timing, etc.) in order to optimize the catalyst conversion efficiency, the fuel economy, and the vehicle driveability.

The oxygen sensor predominantly used today is a thimble-shaped yttria-stabilized zirconia solid-state electrochemical Nernst cell, as shown in Fig. 3. The inner surface is exposed to air and acts as the reference, and the outer is in contact with the exhaust gas. Both surfaces have porous platinum electrodes. In most cases, the sensor has a heater in the center of the thimble to enhance the equilibration of the exhaust gas on the outer platinum electrode. With a metal shroud for protection (with openings to allow for gas circulation) the sensor is approximately the size of a spark plug. At elevated temperature (when ZrO_2 becomes a good ionic conductor) the sensor generates an emf given by the Nernst equation:

$$\text{emf} = V_s = (kT/4e) \ln (P_1/P_2) \quad (1)$$

where k is the Boltzmann constant, e the electron charge, T the absolute temperature, and P_i the equilibrium oxygen partial pressures at the electrodes. Because the equilibrium oxygen partial pressure in the exhaust gas changes by many orders of magnitude around the stoichiometric air/fuel ratio (Fig. 4), the emf of a ZrO_2 oxygen sensor shows a large step change around stoichiometry.

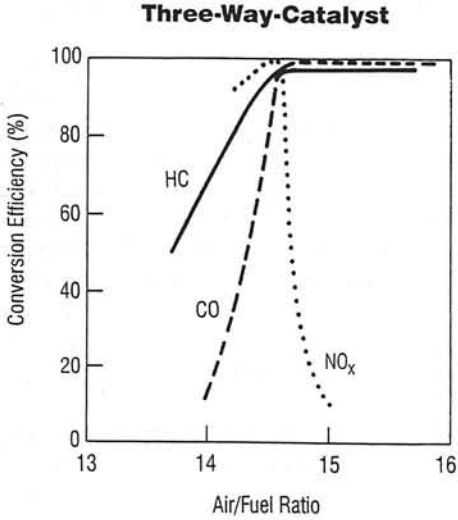


Figure 2: Three-way-catalyst conversion efficiency (%) for hydrocarbons (HC), carbon monoxide (CO), and oxides of nitrogen (NO_x) as a function of air mass to fuel mass ratio. Stoichiometry is at approximately 14.7.

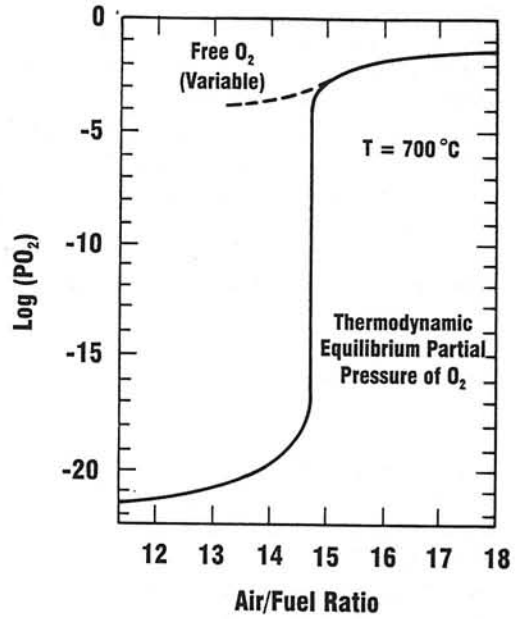


Figure 4: Oxygen partial pressure in the exhaust gas as a function of air mass to fuel mass ratio. Stoichiometry is at approximately 14.7.

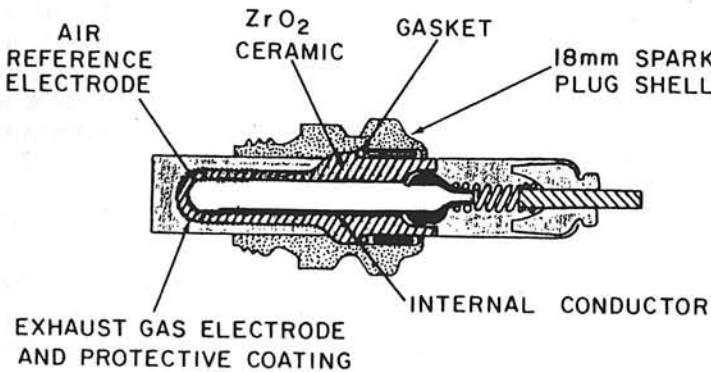


Figure 3: Schematic view of a ZrO_2 oxygen sensor.

EXHAUST GAS CONSTITUENTS SENSORS

It would be very desirable to know more about the composition of the exhaust gas and use that information to further optimize engine control and OBD strategies. Currently, gas sensors for hydrocarbons, carbon monoxide, and oxides of nitrogen suitable for automotive exhaust gas applications do not exist. The detectors mentioned earlier to measure hydrocarbons, carbon monoxide, and oxides of nitrogen are expensive bench-type analytical instruments that need frequent calibration and sophisticated gas sampling. The challenge is thus to devise gas sensors that are low-cost, durable and stable (no need for recalibration), sensitive and selective, fast, able to withstand high temperatures, soot/particulates, water/water vapor, and capable of operating in conditions of variable temperature, flow, and gas composition. For a hydrocarbons sensor the additional challenge is to be able to measure the mix of over 200 hydrocarbon species that are present in the automotive exhaust. NO_x sensors should be able to measure NO in the exhaust, because most of the NO_2 is formed in the ambient air. Two areas of exhaust gas sensing technology under investigation will be described below.

COMBUSTIBLE GAS SENSORS BASED ON OXYGEN PUMPING

Because the ZrO_2 -based oxygen sensor has proven to be a reliable automotive sensor, the question arises whether this or related sensor configurations can be used to measure combustible gases, in particular hydrocarbons. Our research shows that sensors based on the oxygen-pumping principle can (to some extent even selectively) be used for measuring combustible gases [3]. When an external voltage is applied across a ZrO_2 cell, oxygen is transferred (pumped) from the gas phase adjacent to the platinum electrode connected to the negative side of the external voltage supply to the gas phase adjacent to the platinum electrode connected to the positive side by means of the electric current passing through the cell by oxygen ion conduction. The rate at which oxygen is pumped by the electric current I_p is equal to $I_p/4e$. This is the principle of oxygen pumping with ZrO_2 electrochemical cells, which has been used in the past to develop sensitive oxygen sensors [4].

Figure 5 shows a schematic of a combustibles sensor, consisting of two ZrO_2 electrochemical cells arranged in a structure that defines a restricted volume v that communicates with the ambient gas through an aperture a . One of the cells is used to pump oxygen into or out of the restricted volume v . As a result the oxygen concentration inside v changes and an emf develops across the sensing cell. Under steady-state conditions the rate at which O_2 is pumped out or into volume v by the pumping current I_p is equal to the diffusional flux of O_2 (in molecules per second) into or out of volume v :

$$I_p/4e = A(D_{\text{O}_2}/kT)(P_2 - P_1) \quad (2)$$

D_{O_2} is the diffusion coefficient of oxygen, P_i are the equilibrium oxygen partial pressures at the sensing cell electrodes, and A is a constant that depends on the geometrical characteristics of the aperture a . Combining equations (1) and (2) results in:

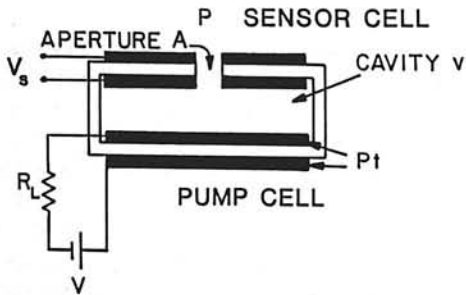


Figure 5: A double- ZrO_2 -cell device consisting of a pumping cell and a Nernst sensing cell.

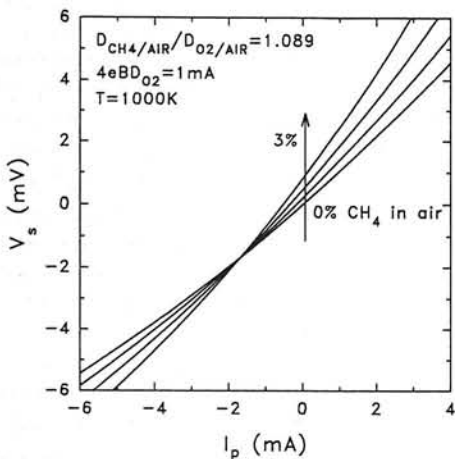


Figure 6: The calculated sensing cell emf V_s as a function of the pumping current I_p for various concentrations of methane in air at $T=1000\text{K}$.

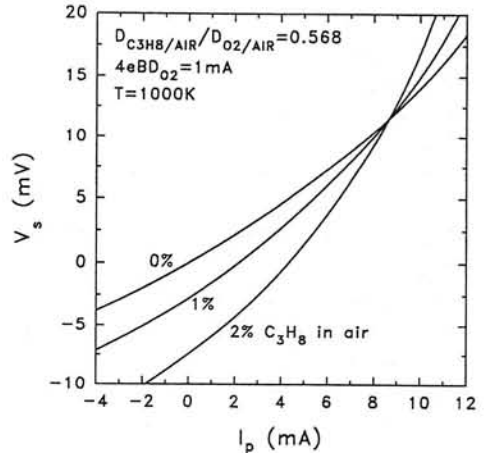


Figure 7: The calculated sensing cell emf V_s as a function of the pumping current I_p for various concentrations of propane in air at $T=1000\text{K}$.

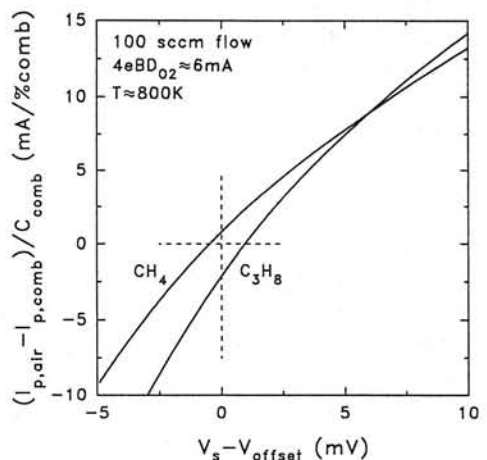


Figure 8: The measured sensitivity of the combustibles gas sensor as a function of the sensing cell emf $V_s - V_{\text{offset}}$ for methane in air and propane in air.

$$I_p = 4eA(D_{O_2}/kT)[1 - \exp(-4eV_s/kT)]P_2 \quad (3)$$

At constant V_s and T , the pumping current I_p is proportional to the oxygen partial pressure P_2 . A feedback circuit can be used to adjust the pumping current to keep V_s constant. In the presence of a combustible gas with concentration C_{comb} and (binary) diffusivity D_{comb} equation (3) becomes [3]:

$$I_p = 4eBD_{O_2}[\{1 - \exp(-4eV_s/kT)\}C_{O_2} - nC_{comb}\{D_{comb}/D_{O_2} - \exp(-4eV_s/kT)\}] \quad (4)$$

where B is a constant determined by the geometrical characteristics of aperture a and n is the number of oxygen molecules required to oxidize one molecule of the combustible gas. A measure for the sensitivity of the sensor is the change in pumping current (at constant V_s and T) with respect to the pumping current when no combustible is present, i.e. $I_{p,air} - I_{p,comb}$. Examination of equation (4) for the pumping current reveals that for every combustible with (binary) diffusion coefficient D_{comb} there is a value of V_s/T for which $D_{comb}/D_{O_2} - \exp(-4eV_s/kT)$ equals zero, i.e. the sensor is insensitive to the combustible for that particular value of V_s/T . Figures 6 and 7 show calculated results at constant temperature for methane in air and propane in air, respectively. Around $V_s = 12$ mV the sensor does not respond to propane, i.e. for any concentration of propane, the required pumping current to obtain $V_s = 12$ mV is identical to the current required for air. At $V_s = 12$ mV the sensor does respond to methane. On the other hand, the sensor becomes selective to propane in a propane/methane/air mixture if V_s is chosen to be equal to -2 mV. Figure 8 shows the measured sensitivity of the sensor for methane in air and propane in air. A qualitative agreement between the experimental results and the combustibles sensor model is obtained; the quantitative discrepancies are believed to originate from diffusion effects at the electrodes of the sensing cell (neglected in the model) and incomplete thermodynamic equilibrium (as assumed in the model) at the electrodes and inside volume v , and might be eliminated by optimizing the design of the sensor structure. In summary, differences in a physical property of the combustible gases (i.e. their diffusivity) can be used to obtain chemical selectivity in gas sensors based on oxygen pumping.

The results of our research show that concentrations below the lower explosive limit can easily be measured, but these combustible gas sensors do not have the sensitivity to accurately measure combustible gas concentrations substantially below 1%. However, the principle of oxygen pumping could still be applied to provide oxygen or a constant oxygen concentration environment to other types of sensors [5]. For example, metal-oxide semiconducting materials are very sensitive and could potentially be used as gas sensing materials. However, the resistance changes in these materials are not only dependent on the concentration of the combustible gas, but also on variations in oxygen concentration (as present in the automotive exhaust), which could be eliminated or reduced by using the oxygen pumping principle.

CATALYTIC (MICRO)CALORIMETRIC GAS SENSORS

Catalytic calorimetric gas sensors typically operate in the 300-550 °C temperature range, making

them in principle applicable for automotive applications. Although generally of lower sensitivity than semiconducting-type gas sensors, catalytic calorimetric sensors appear to be considerably more stable, faster responding, and less susceptible to varying amounts of water vapor and to varying amounts of oxygen (provided enough oxygen is present). Catalytic calorimetric gas sensors measure the rise in temperature of a (low thermal conductivity) substrate caused by the oxidation of combustible gases on a catalytic layer deposited on the substrate [6,7]. The temperature rise can be measured with a resistance thermometer, e.g. Pt; thermistors or thermocouples/thermopiles could also be used. To improve the detection limit of the sensor the temperature rise is usually measured differentially by adding a second element (e.g., a Pt resistor) with thermal characteristics identical to those of the sensing element, but without a catalytic layer. The resistances of the two elements are:

$$R_{\text{catalytic}} = R_0(1 + \alpha T + \alpha \Delta T_{\text{comb}}) \quad (5)$$

$$R_{\text{ref}} = R_0(1 + \alpha T) \quad (6)$$

with R_0 the resistance at 0°C , α the temperature coefficient of resistance, T the temperature of operation in $^\circ\text{C}$, and ΔT_{comb} the rise in temperature caused by the oxidation of combustible gases on the catalytic layer. ΔT_{comb} is given by:

$$\Delta T_{\text{comb}} = (R_{\text{catalytic}} - R_{\text{ref}}) / \alpha R_0 = \Delta R / \alpha R_0 \quad (7)$$

Existing calorimetric sensors, based on different fabrication technologies, have been characterized, and found not to be compatible with the automotive exhaust gas environment. Most of our research has been concentrated on silicon micromachined calorimetric sensors. One of our silicon implementations is shown in a perspective view and a cross-sectional diagram in Fig. 9 [8]: two thin-film resistors are fabricated on two micromachined membranes of low thermal conductivity, and one is covered by a catalytic layer. No heater was incorporated in this particular design and the devices were heated externally. Other approaches to obtain micro-hotplates for gas sensor applications have been published by other research groups [9-18]. Reducing the size of a calorimetric sensor by using silicon micromachining as the method of fabrication results in a faster response time by reducing the thermal mass (a 20 ms thermal response time was measured) and a potentially lower detection limit by better temperature compensation between reference and catalytic element while still minimizing cross-talk between the two elements (an approximately 5 ppm C_1 detection limit under laboratory conditions was measured). Other reasons to study silicon micromachined gas sensors are lower power consumption for operation, a potentially lower manufacturing cost, and the possibility to easily manufacture sensor arrays. Resistive heating elements can also be embedded in these differential structures to control the catalyst temperature.

Extensive thermal modeling was carried out. It was found and confirmed by experimental measurements that most of the heat on the membrane is lost through the surrounding gas. A substantial part of that heat travels only a short distance through the gas to the silicon bulk substrate. This latter contribution necessitated computational fluid dynamical calculations in order to obtain the correct results. Numerical and experimental results in air, vacuum, and helium are shown in Fig. 10,

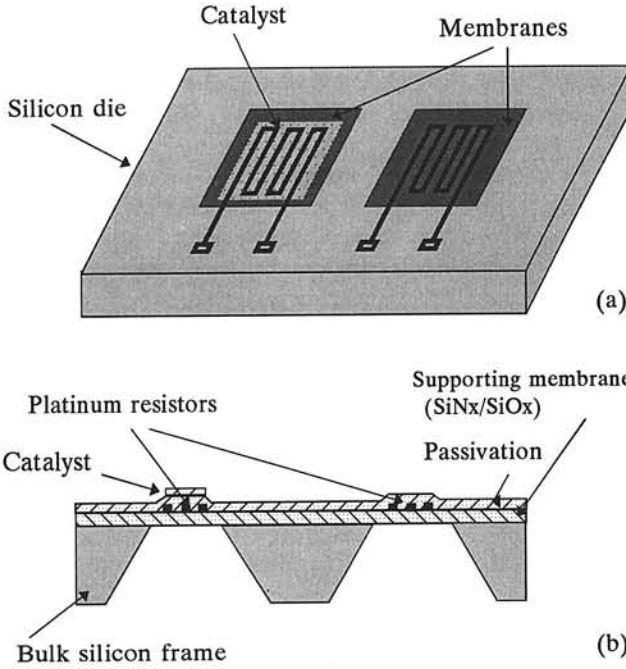


Figure 9: A perspective view (a) and a schematic cross-sectional diagram (b) of a silicon micromachined catalytic calorimetric gas sensor.

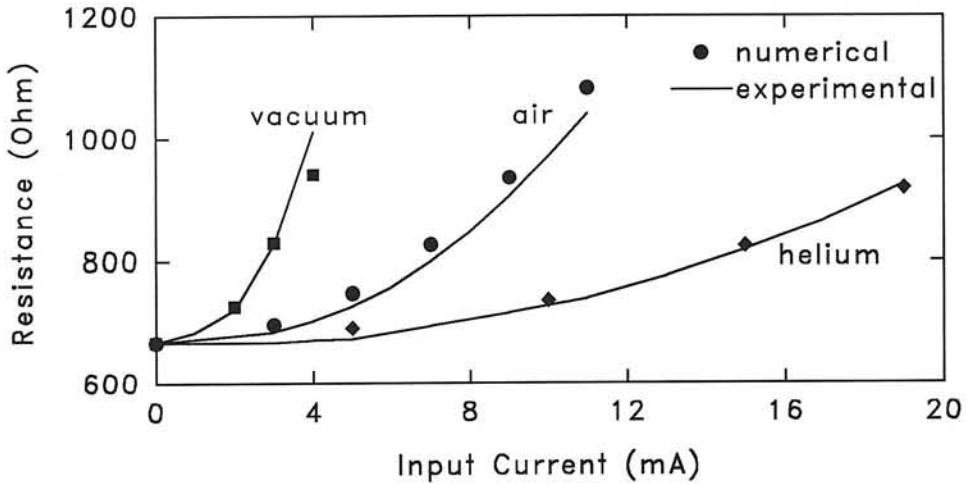


Figure 10: Resistance of the platinum resistance thermometer as a function of the input current for air, helium and vacuum. Numerical results (dotted) obtained from the thermal modeling are in good agreement with the experimental results (lines).

where the average rise in temperature on the membrane (as measured by the change in resistance) is shown as a function of input current. To get a good agreement between experiment and theory, it was important to use experimentally determined thermal conductivities for the various layers, because use of the monocrystalline, bulk values resulted in large errors [19].

Figure 11 shows the outputs ΔT_{comb} and ΔR as a function of the concentration for a number of combustible gases for the device shown in Fig. 9 using a high surface area noble metal catalyst. The sensor was mounted in a quartz tube, externally heated by a temperature-controlled furnace surrounding the tube (to approximately 360 °C), and subjected to a gas flow parallel to the plane of the sensor with a flow velocity of about 1 cm/s. The gas mixture contained 10% O₂ (by volume). Figure 12 shows the sensitivities ($\Delta T_{\text{comb}}/1000$ ppm of combustible gas, and $\Delta R/1000$ ppm of combustible gas) of a commercial calorimetric sensor (used for boiler control [20]) as a function of the number of carbon atoms for a number of combustible gases at 400 °C in 20 cm/s flow and in 5% O₂/N₂ mixtures for two different catalysts. In this experiment, the calorimetric sensor was mounted in a temperature-controlled aluminum block to obtain a uniform temperature. The dashed lines are a best fit through the data obtained for the paraffins/alkanes methane, ethane, propane, and n-butane. The sensor sensitivity for these paraffins is different for the two catalysts tested. The difference in sensitivity between sensors with the two different catalysts for the other combustible gases (e.g. olefins/alkenes, hydrogen, and carbon monoxide) is much smaller.

When the rate of oxidation of combustible gas molecules on the catalyst of the calorimetric sensor is much larger than the rate of arrival of the molecules, the device operation is mass-transfer limited. When the opposite is true, the operation is limited by the chemical-reaction rate. It is possible that neither the mass-transfer rate nor the chemical-reaction rate completely dominates. Mass-transfer limited operation is preferable, because a modest deterioration in the catalyst activity would not result in a change in the sensor response. We believe that for hydrogen, carbon monoxide and the olefins tested (ethylene and propylene) the sensor operation is mass-transfer limited for all catalysts we have tested. On the other hand, the oxidation of the paraffins tested seems to be limited by the reaction rate on the catalyst, resulting in different sensor outputs for different catalytic layers [21]. Studies of catalytic layers under well-controlled conditions are underway to further elucidate this issue.

In many applications the gas contains a mixture of combustible gases, e.g., different hydrocarbons, carbon monoxide, and hydrogen. In general, gas sensors have different sensitivities to the different combustible gases. Good selectivity for individual species is, at present, impossible to obtain. Even if selectivity were adequate, the additional problem of an insufficient detection limit exists, because individual gas species are present, in many cases, in very low concentrations. The problem is then how to interpret the output of a gas sensor which responds to several combustible gases. Preliminary results obtained on engine-dynamometers indicated some degree of correlation between the catalytic calorimetric sensor output and the concentration of hydrocarbons as measured by a flame ionization detector. More studies are in progress.

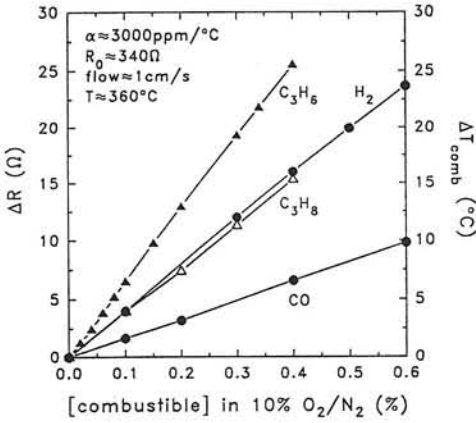


Figure 11: Measured ΔR and calculated ΔT_{comb} for the silicon microcalorimeter of Fig. 9 for different combustible gases.

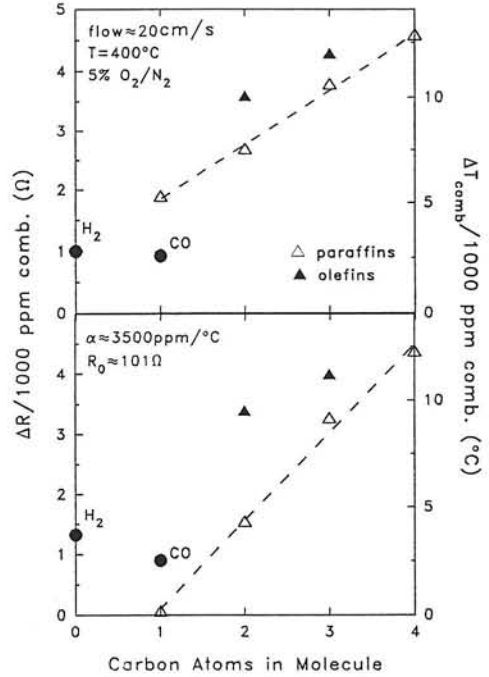


Figure 12: Sensitivity of a commercial calorimetric sensor to a number of combustible gases. Sensors with two different catalysts are measured under identical conditions.

CONCLUSIONS

Since the 1960s, significant progress has been made in reducing automotive emissions, but stricter legislation and on-board diagnostic system (OBD) requirements dictate further improvements in emissions control systems. In the future, these systems may include gas sensors that measure exhaust gas constituents such as hydrocarbons, carbon monoxide or oxides of nitrogen. Work on a variety of sensing technologies is continuing to develop on-vehicle EGC sensors for this purpose.

REFERENCES

- [1] J. T. Woestman and E. M. Logothetis, "Controlling automotive emissions," *The Industrial Physicist*, vol. 1, Dec. 1995, pp. 20-24.

- [2] Robert Bosch GmbH, *Automotive Handbook* 3rd Edition, SAE Society of Automotive Engineers, Warrendale, PA, USA, 1993, pp. 478-489.
- [3] J. H. Visser, L. Rimai, R. E. Soltis, E. M. Logothetis, "Selective combustibles sensors based on oxygen pumping," *Digest of Technical Papers 7th International Conference on Solid-State Sensors and Actuators (Transducers'93)*, 1993, pp. 346-349.
- [4] E. M. Logothetis, "Air-to-fuel sensors based on oxygen pumping," *Ceramic Engineering and Science Proc.*, vol. 8, The American Ceramic Society, 1987, p. 1058.
- [5] J. H. Visser, R. E. Soltis, L. Rimai, E. M. Logothetis, "Sensors for measuring combustibles in the absence of oxygen," *Sensors and Actuators B9*, 1992, pp. 233-239.
- [6] E. Jones, "The pellistor catalytic gas detector," in P. T. Moseley and B. C. Tofield (Eds.), *Solid State Gas Sensors*, A. Hilger, Bristol, United Kingdom, 1987, pp. 17-50.
- [7] W. Hemminger and G. Höhne, *Calorimetry - Fundamentals and Practice*, Verlag Chemie GmbH, Weinheim, Federal Republic of Germany, 1984.
- [8] M. Zanini, J. H. Visser, L. Rimai, R. E. Soltis, A. Kovalchuk, D. W. Hoffman, E. M. Logothetis, U. Bonne, L. Brewer, O. W. Bynum, M. A. Richard, "Fabrication and properties of a Si-based high-sensitivity microcalorimetric gas sensor," *Sensors and Actuators A48*, 1995, pp. 187-192.
- [9] P. Krebs and A. Grisel, "A low power integrated catalytic gas sensor," *Sensors and Actuators B13-14*, 1993, pp. 155-158.
- [10] M. Gall, "The Si planar pellistor: a low-power pellistor sensor in Si thin-film technology," *Sensors and Actuators B4*, 1991, pp. 533-538.
- [11] R. Aigner, M. Dietl, R. Katterloher, V. Klee, "Si-planar-pellistor: designs for temperature modulated operation," *Digest of Technical Papers 8th International Conference on Solid-State Sensors and Actuators (Transducers'95/EurosensorsIX)*, 1995, pp. 839-842
- [12] C. L. Johnson, J. W. Schwank, K. D. Wise, "Integrated ultra-thin-film gas sensors," *Sensors and Actuators B20*, 1994, pp. 55-62.
- [13] J. S. Suehle, R. E. Cavicchi, M. Gaitan, S. Semancik, "Tin oxide gas sensor fabricated using CMOS micro-hotplates and *in-situ* processing," *IEEE Electron Device Letters*, vol. 14, 1993, pp. 118-120.
- [14] R. E. Cavicchi, J. S. Suehle, K. G. Kreider, M. Gaitan, P. Chaparala, "Optimized temperature pulse sequences for the enhancement of chemically-specific response patterns from micro-hotplate gas sensors," *Digest of Technical Papers 8th International Conference on Solid-State Sensors and Actuators (Transducers'95/EurosensorsIX)*, 1995, pp. 823-826.
- [15] M. Kimura, J. Manaka, S. Satoh, S. Takano, N. Igarashi, K. Nagai, "Application of the air-bridge microheater to gas detection," *Technical Digest 5th International Meeting on Chemical Sensors*, 1994, pp. 1164-1167.
- [16] D. L. Polla, R. M. White, R. S. Muller, "Integrated chemical-reaction sensor," *Digest of Technical Papers 1985 International Conference on Solid-State Sensors and Actuators (Transducers'85)*, 1985, pp. 33-36.
- [17] C. Vauchier, D. Charlot, G. Delapierre, A. Accorsi, "Thin-film gas catalytic microsensor," *Sensors and Actuators B5*, 1991, pp. 33-36.
- [18] A. W. van Herwaarden, P. M. Sarro, J. W. Gardner, P. Bataillard, "Liquid and gas micro-calorimeters for (bio)chemical measurements," *Sensors and Actuators A43*, 1994, pp. 24-30.
- [19] C. H. Mastrangelo, *Thermal Applications of Microbridges*, Ph.D. Dissertation, University of California at Berkeley, 1991.
- [20] R. Dalla Betta and W. O. Bynum, "A new combustion control sensor," *Sensors*, vol. 6, 1989, p. 27.
- [21] J. H. Visser, M. Zanini, L. Rimai, R. E. Soltis, A. Kovalchuk, D. W. Hoffman, E. M. Logothetis, U. Bonne, L. T. Brewer, O. W. Bynum, M. A. Richard, "Catalytic calorimetric gas sensors," *Technical Digest 5th International Meeting on Chemical Sensors*, 1994, pp. 468-471.

Glucose sensor based on microdialysis

A.J.M. Schoonen and K.J.C. Wientjes

Farmaceutische Technologie RUG

Anthonius Deusinglaan 1, 9613 AV Groningen.

ABSTRACT

A glucose sensor is developed based on microdialysis. This sensor system has been tested *in vivo* on healthy volunteers and diabetic patients by implanting a hollow fibre probe in the abdominal subcutaneous tissue. Reliable results were obtained for several days up to a week. At this moment a new miniaturised system is tested for use in humans. Pump, electrode, flow system, electronics and battery are mounted in a box, sized: 12.4 x 7.9 x 2.0 cm.

In the literature there is an ongoing discussion about the glucose concentration measured in the interstitial subcutaneous fluid. Often lower values than blood glucose are reported. Also glucose sensors working properly *in vitro* show a considerable drift *in vivo* due to a loss of sensitivity. Using the microdialysis technique it could be shown that not the biocompatibility of membranes in contact with tissue causes these problems. Implantation itself is damaging capillaries, resulting in a severe limitation of blood supply around the probe during the first few days. Sensors designed without a barrier between selector and detector will show signal drift *in vivo*, due to fouling of the detector by substances diffusing from the body into the detector.

I - INTRODUCTION

The first step in designing a biosensor is the choice of a method of analysis for the substance of interest. For glucose sensors several methods are tried: Optical methods (Near Infra Red; optical rotation) and electrochemical methods (direct oxidation of glucose on a platinum black electrode; enzymatic oxidation followed by amperometric detection of oxygen or hydrogenperoxide with or without mediators for electron transport). In principle optical methods (NIR) could be used for non-invasive measurement of glucose through the skin. As yet the NIR-method is far from reliable and basic research is needed before the glucose signal

Proceedings 1996 National Sensor Conference, Delft, The Netherlands, March 20-21, 1996.

can be sufficiently separated from the fluctuating noise generated by the complex structure of skin and tissue during normal daily life.

Most investigators have chosen the subcutaneous adipose tissue for implanting their sensor. The blood compartment should be ideal for measuring blood glucose, but complications as thrombophlebitis prevent routinely use of this compartment. Moreover a sensor should be implanted by the diabetic patient himself.

Implantation of an artificial pancreas consisting of an insulin pump and a glucose sensor is not yet possible. This may be contemplated only when the glucose sensor produces a stable signal for at least half a year. So for the near future subcutaneous adipose tissue is the preferred site to test the performance of glucose sensors. Ideally the sensor should be applied with a small catheter. Therefore the glucose sensor should have a diameter as small as possible. A sensor based on a peroxide electrode, a layer of immobilised glucoseoxidase as a selector and dipped in some coating solution for the outer membrane can be very small indeed (1). A microdialysis probe also satisfies this condition, but it has the advantage that the measuring cell, placed outside the body, need not be so very small and is accessible for study and maintenance during the in vivo experiments.

2 - SELECTOR & DETECTOR

Crucial in the concept of a biosensor is the on-line processing of selection and detection of the analyte resulting in an electrical signal as output. The main problem of a hydrogen peroxide electrode is the violation of this definition. Hydrogen peroxide is a solute and the molecule is very small, so it is almost impossible to separate this molecule by filtration. This means no barrier can be mounted between the selector and the detector, so hydrogen peroxide diffuses into the electrode space together with all types of small molecules from the body. The enzyme selector produces a specific signal that is proportional with the glucose concentration, but it does not separate this signal from the background noise. As the electrode is not specific for hydrogen peroxide, fouling of the electrode space and loss of sensitivity occurs. Selection implies separation of the analyte from the noise. Oxygen is a gas and can be separated by a hydrophobic membrane that acts as a fluid/fluid barrier. Only gas molecules pass a Teflon membrane so no solutes from the body can enter the electrode space. Therefore glucose sensors based on oxygen detection with a fluid/fluid barrier do not show a loss of sensitivity in vivo as compared to hydrogen peroxide detectors.

For glucose sensors tested in vivo almost exclusively the enzyme glucoseoxidase (GOD) has been used as a selector. This enzyme is relatively robust with a shelflife of about 2.5 months at 37⁰ C. However the glucose oxidation catalysed by GOD is producing hydrogenperoxide, a highly reactive substance to the enzyme itself. In nature the enzyme is working in close collaboration with the enzyme catalase that reduces peroxide to water. So adding catalase will reduce the denaturation of glucoseoxidase by peroxide, but this is not possible when hydrogenperoxide is the analyte.

Another measure to reduce drift caused by degradation of glucoseoxidase is to apply a substantial excess of the enzyme. Below a certain enzyme concentration the amount of enzyme will become the rate limiting step in the reaction. As long as this critical concentration is not reached, no drift of the sensor signal will be noted.

For immobilised enzyme layers this approach may complicate the measurement as the position of the reaction site in the layer may vary in time. For instance the produced hydrogenperoxide diffuses into the electrode space, but mostly (80%) through the outer membrane into the body. In time when the reaction site is moving due to degradation of enzyme molecules close to the outer membrane, the proportionality between peroxide diffusing into the electrode and into the body may change.

In this respect introducing a microdialysis probe as a bridge between the body and the reaction site offers two advantages. First of all no reagents can enter the body, preventing inflammation and immunogenic reactions. Second there is more freedom in designing enzyme reactors and detectors to secure a stable operation of the measuring device.

3 - MICRODIALYSIS FIBRES AS OUTER MEMBRANES

The microdialysis technique is well suited to study the permeability of membranes and the behaviour of the surrounding tissue after implantation. The outer membranes of measuring instruments are the interface between the biological organism and the technological device. Their proper performance in tissue is vital for devices aiming retrieval of information from the organism. Therefore glucose flow from the body into microdialysis probes is studied for three weeks in healthy volunteers.

Preliminary results show a substantial increase of glucose uptake by the fibres during the first week, after which a more or less constant recovery is measured. So biocompatibility problems resulting in a decreased sensitivity do not occur during this time period. The first hour after implantation recovery of glucose decreases from a high value (about 100%) to values of about 50%. It is hypothesised that the catheter used for implantation of the probe damages capillaries resulting in a flow of blood into the interstitial space. Than capillaries are closed and blood and interstitium are separated again. During this period recovery is falling, because the closed up capillaries are dead ends in the blood circulation. Around the probe adipose cells are relatively shut off from the nutritive blood flow. If a probe is perfused with glucose, uptake of glucose from the fibre is significantly increased, whereas glucose flow into a fibre perfused with saline is significantly reduced.

In the first week after implantation blood supply of the adipose cells around the probe is restored and the recovery of glucose by the probe increases to 100% again.

These results clearly imply that the ultimate goal should be total implantation of a sensor, if an invasive technique is used. Leaving a sensor or a microdialysis probe for only a week in the subcutaneous tissue, is not a sound approach when repair processes take a week to complete.

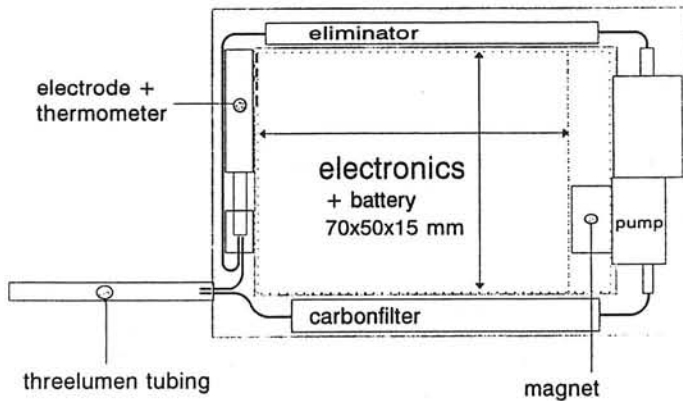
4 - PROSPECTS

Microdialysis may be fruitfully used to study in vivo monitoring, but could microdialysis also play a role in designing a totally implantable sensor?

Main disadvantage of the microdialysis technique is the need of a pump, a battery and a reservoir with perfusion fluid and a waste bag.

As a first step on the road to total implantation we designed a closed loop dialysis system, eliminating the reservoir and waste bag. After measurement by the oxygen electrode, the remaining glucose is eliminated, the used oxygen is replenished and possible traces of enzyme from the reactor are adsorbed on a coal filter (fig. 1).

Needless to say it will take quite a long time before total implantation may be achieved. Further miniaturisation of the microdialysis system is very well possible, but the more general problems of long term electrode and enzyme stability are yet to be solved or circumvented



Flowsystem, electrode and pump mounted on cover
Electronics and magnet mounted on bottom

Fig. 1: Glucose sensor with closed loop dialysis system.

MEASUREMENT OF THE DYNAMIC SURFACE TENSION IN LIQUIDS BY MEANS OF GAS BUBBLES GENERATED AT SINGLE NUCLEATION SITE ELECTRODES

A. Volanschi, W. Olthuis, P. Bergveld

MESA Research Institute, University of Twente
P.O.Box 217, 7500 AE Enschede, The Netherlands
phone:+31-53-4892722, fax: +31-53-4892287
email: a.volanschi@el.utwente.nl

Abstract: In-situ generation of gas bubbles by electrolysis is reported in this paper for the measurement of dynamic surface tension of aqueous solutions. Special microelectrodes having only one single nucleation site (SNS) were designed for this purpose. Two kinds of electrodes were fabricated, micro cavity electrodes (MCE) and gas phase nucleation core (GPNC) electrodes. The frequency of the electrogenerated bubbles is monotonously dependent on the dynamic surface tension showing the suitability of the proposed method.

1. INTRODUCTION

The measurement of the surface tension in liquids is important for various applications like, for instance, those employing surface active materials for wetting and washing. The surface tension is defined as half of the free energy due to cohesion of the material in vacuum per unit area. Distinction should be made between the static surface tension which characterises the equilibrium situations and the dynamic surface tension, which characterises the situations far from equilibrium. Wetting and cleaning processes are usually far from equilibrium and this is why the dynamic surface tension is the parameter that should be monitored.

To measure the dynamic surface tension, a surface or interface with changing area is needed. At this surface a dynamic process of coverage with surface active molecules takes place. A possibility to create a changing surface is to grow gas bubbles in the liquid giving rise to a controlled dynamic surface. A reproducible way to generate gas bubbles with a well defined size in a liquid is by blowing gas through a tube directly into the bulk of the liquid. The method is called *sparging* and the theory is quite well understood [1]. This method is widely used for dynamic surface tension measurements [2, 3]. The disadvantage is that a pump with a constant gas flow is needed resulting in quite a big set-up.

Electrolysis at metal electrodes is used in this paper as an alternative method of gas bubble generation. The challenge was to generate monosized bubbles in a controlled way and only on one specified site, such that the method is analogue to sparging. Single Nucleation Site (SNS) electrodes were made to generate bubbles on a specified site and with a reproducible size. Understanding of the nature of the nucleation processes resulted in two SNS

electrode designs, micro cavity electrodes (MCEs) [4] and gas phase nucleation core (GPNC) electrodes. The evolution of the gas bubbles on the SNS electrodes induces fluctuations of the electrode overpotential and of the impedance. The bubbles generated at SNS electrodes by constant current electrolysis were used for the measurement of the dynamic surface tension in aqueous solutions. The constant electrolysis current corresponds to a constant gas production (in analogy to the already mentioned sparging method). It is shown that the frequency of the electrogenerated bubbles is monotonously dependent on the dynamic surface tension.

2. EXPERIMENTAL

For practical reasons concerning mainly the reproducibility of the fabrication process, the SNS electrodes were made in silicon technology. Silicon wafers with a $\langle 100 \rangle$ crystal orientation were used. The SNS electrodes are schematically drawn in fig. 1. Surface shaping in the form of a reversed pyramid is used for the MCEs (fig. 1 left) to get a higher dissolved gas concentration on the bottom of the cavity than in the bulk of the aqueous solution. In other words, dissolved gas is concentrated on the bottom of the cavity until heterogeneous nucleation takes place. The result is a single bubble nucleation site. The cavities of the MCEs were anisotropically etched through a SiO_2 mask. By choosing the size of this mask ($40 \times 40 \mu\text{m}$), the dimensions of the reversed pyramid were completely specified.

A gas phase nucleus (Harvey nucleus) is created in the isotropically etched cavity under the working electrode (WE) of a GPNC electrode (fig. 1 right). This is achieved by electrolysis between the bulk electrode (BE) and a remote counter electrode. The single nucleation site is obtained in this case because the gas generated at the working electrode is diffusing to the already existing gas phase nucleus rather than nucleating a new bubble. The GPNC electrodes were made by isotropical etching through a SiO_2 mask. The mouth of the cavity was a circle with a diameter of $10 \mu\text{m}$. The cavity depth was controlled by changing the etching time.

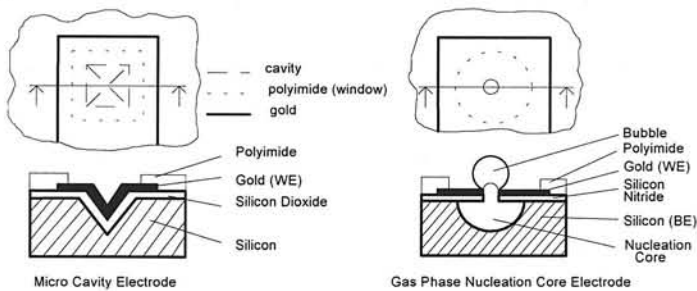


Fig. 1: Top and cross-sectional views of the SNS electrodes: (left) Micro Cavity Electrode (MCE), (right) Gas Phase Nucleation Core (GPNC) electrode.

After the etching step, the fabrication process of both SNS electrodes followed the same steps. This process was described in [4]. Here only the layout differences between the two electrodes are mentioned. The active area of the SNS electrodes is determined by the SiO_2 , Si_3N_4 , polyimide window. For the MCEs, the active area was a square of $60 \times 60 \mu\text{m}^2$ whereas for the GPNC electrodes the active area was a circle with the diameter of $35 \mu\text{m}$. The circuitry used for the bubble monitoring is given in fig. 2 and was also described in paper [4]. The current source (I2) was added to the scheme to drive the bulk electrode (BE) of the GPNC electrode.

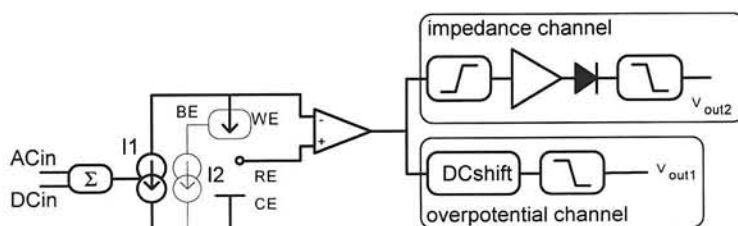


Fig. 2: Measurement set-up. WE is the working electrode, CE is the counter electrode, RE is the reference electrode, BE is the bulk electrode. I1 and I2 are the voltage controlled current sources used to drive the WE and the BE, respectively. ACin and DCin are the control voltages applied to the current source by means of the summing amplifier Σ . v_{out1} corresponds to the measured overpotential and v_{out2} corresponds to the measured impedance fluctuations.

The experiments were done in 10 mM solutions of sodium acetate (NaAc) or sodium sulphate (NaSO₄). The surface tension was changed by adding various concentrations of nonionic surfactant (Synperonic NP9 and Novel EO 4.5, courtesy of Unilever).

3. RESULTS AND DISCUSSION

The principle difference between the nucleation mechanisms used by the SNS electrodes, can be illustrated by an experiment in a liquid which was uniformly saturated with dissolved CO₂. If no current is passed through the working electrodes, bubbles should only grow on the GPNC electrode in the presence of the gas phase (Harvey) nucleus. It was observed that bubbles grew indeed on the GPNC electrode, only after the gas phase nucleus was generated by applying a short current pulse with I2 (fig. 2). No bubble was observed on the MCE. It means that the dissolved gas diffuses to the gas phase nucleus rather than nucleating a new bubble. The observed phenomena point out the difference between the heterogeneous nucleation and the nucleation in Harvey nuclei.

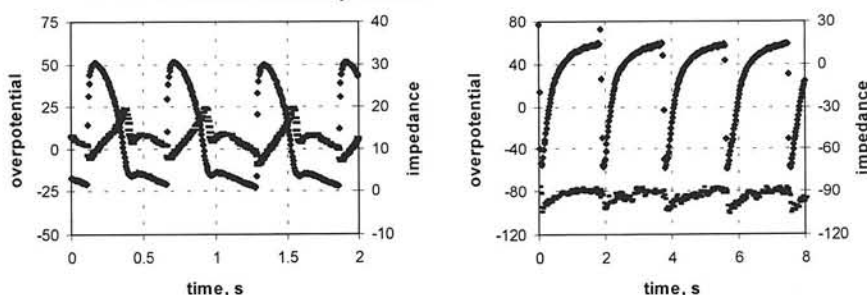


Fig. 3: Recordings of the overpotential and impedance fluctuations on the SNS electrodes: (left) MCE electrodes and (right) GPNC electrodes. \blacklozenge overpotential, left axis, $-$ impedance, right axis. The units of the overpotential and impedance are arbitrary.

In fig. 3, typical wave forms are presented of the overpotential and impedance fluctuations at the SNS electrodes. The bubble frequency can be estimated from the recording of either the overpotential or the impedance. It can be seen that the form of the fluctuations is different for the two SNS electrodes. This difference can be explained by the differences between the nucleation mechanisms and the surface shapes. The different surface shape leads to different

concentration profiles of dissolved gas during the bubble evolution process. Moreover, there is a time interval for the MCEs, when no bubble is present on the electrode. This time is used to reach again the critical concentration that is needed for the nucleation of a new bubble. No such time can be seen in the case of the GPNC electrodes.

The results of the measurements of the bubble frequency dependence on the surfactant concentration are given in fig. 4, left for the MCEs and right for the GPNC electrodes. The surfactant concentration is proportional to the dynamic surface tension of the liquid. A monotonous dependence of the bubble frequency on the surfactant concentration can be seen which means that the SNS electrodes are suited for the monitoring of the dynamic surface tension.

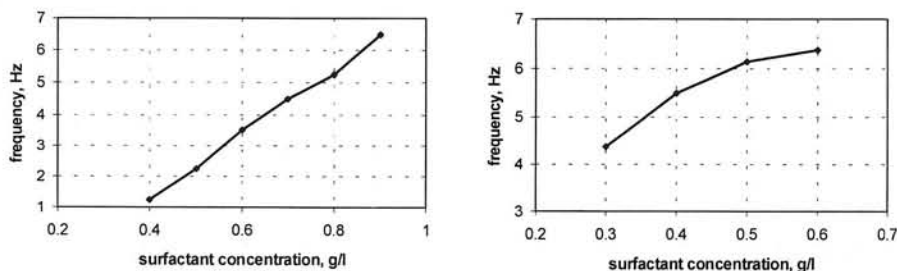


Fig. 4: Measured dependency of the bubble frequency on the surfactant concentration (dynamic surface tension). (left) measurements with MCEs in 10 mM Na₂SO₄ and with various concentrations of nonionic surfactant (Synperonic NP9) (right) measurements with GPNC electrodes in 10 mM NaAc with various concentrations of nonionic surfactant (Novel EO 4.5).

4. CONCLUSIONS

It is shown in this paper that the in-situ generation of gas bubbles by electrolysis is suitable for the measurement of dynamic surface tension of aqueous solutions. The differences between the working principles of the two SNS electrodes are pointed out. Both electrodes can be used for the monitoring of the dynamic surface tension because the frequency of the bubbles is monotonously dependent on the surfactant concentration. The SNS electrodes work as actuators because they can generate ("actuate") bubbles with a controlled size on a specified place as well as sensors because they can detect ("sense") the presence and the size of the electrogenerated bubbles.

5. ACKNOWLEDGEMENTS

The work presented in this paper is financially supported by Unilever.

6. REFERENCES

- 1 S.D. Lubetkin, Controlled particle, droplet and bubble formation, ed. D.J. Wedlock, Butherworth & Heinemann, ISBN 0 75061494 3, (1994) 159-190.
- 2 K.J. Mysels, Colloids and surfaces, 43 (1990) 241-262.
- 3 T. Mueller Kirschbaum, E. Smulders, W. Hofer, Patent WO 92/18680 (1992).
- 4 A. Volanschi, W. Olthuis, P. Bergveld, Proceedings of Transducers 95 Conference, Stockholm (1995) paper 91 PB-4.

Electrochemical Microvalve

C.R. Neagu, J.G.E. Gardeniers, M. Elwenspoek and J.H.J. Fluitman

*MESA Research Institute, University of Twente,
P.O. Box 217, 7500 AE Enschede, the Netherlands
tel: xx31 53 489 2805, fax: xx31 53 435 9047
email: c.neagu@el.utwente.nl*

ABSTRACT

A novel electrochemical microactuator has been developed as active valve, which may be used in microliquid systems or biomedical applications. The microactuator with a size of $5 \times 5 \times 1 \text{ mm}^3$ was made with the use of silicon micromachining and thin film techniques. This paper discusses the principle, fabrication and characterisation of the actuator.

1. INTRODUCTION

Micromechanics is a broad area, with a wide range of applications in many fields, e.g. in microliquid handling systems [1]. Basic components like pumps and valves, activated by different principles such as electrostatic, piezoelectric or thermopneumatic [2], have already been realised. The reported active valves differ in supply voltage, power consumption and dimensions (Table 1). An extensive comparison of active valves can be found in refs. [3, 4].

Actuation principle	Pressure [10^5 Pa]	Stroke [μm]	Voltage [V]	Power consumption [mW]
Electrostatic	< 0.5	< 10	100 - 200	< 1
Thermopneumatic	$1 < P < 100$	$30 < d < 100$	5 - 20	2000 - 5000
Electromagnetic	< 0.5	> 100	20 - 50	50 - 300
Piezoelectric	< 1	$10 < d < 50$	100 - 200	< 5

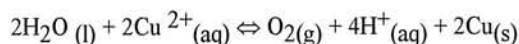
Table 1: Different types of micro-valves

Depending on the application, some principles may be preferable. For example, for large strokes, coil valves, shape memory alloys and thermally excited valves can be used; large forces can be obtained with electrostatic devices; for high speed operation, thermally operated valves are too slow, so that in that case piezovalves are preferred. Most of these types of actuation need either high voltages (electrostatic, piezoelectric) or have quite high power consumption with low efficiency (heat dissipation in case of thermal actuation), which limits the applications. To obtain a low energy consumption and to have the possibility of discontinuous supply of power, we chose for electrochemical actuation, which is based on the

electrolysis of an aqueous electrolyte solution [5, 6]. The reversible chemical reactions, which are driven by an external current source, lead to gas evolution or gas reduction, depending on the direction of the current. In a closed system the pressure rise or drop resulting, from this gas generation or reduction, can be used to change the deflection of a membrane, which again can be used to close or open a liquid channel. If such an electrolytic cell is operated under open-circuit conditions, the pressure and thus the deflection state of the membrane will (in an ideal situation) be maintained. This means that no energy is required to maintain the state of the valve. The electrochemical micro-valve is attractive for use in microfluidics or medical applications, since relatively large pressures (up to tens of bar) can be reached in the electrochemical actuator with only low energy consumption (in the range of μW). In this paper, the design, fabrication and characterisation of a micromachined electrochemical actuator are described.

2. PRINCIPLE

A solution of copper sulphate and platinum (Pt) and copper (Cu) electrodes were chosen to have reversible reactions. The Pt electrode acts as a catalyst for the formation of oxygen gas. The overall cell reaction for O_2 production is:



A serious problem with the chosen electrolyte-electrode combination is the following: Under open circuit conditions, the oxygen pressure built up in a previous electrolysis step should in principle remain constant. However, this "steady-state" can be disturbed by the reduction of the O_2 gas at the copper electrode. This unwanted reaction decreases the gas pressure and consequently the efficiency of the actuator. To reduce this effect, the copper electrode has to be protected against O_2 , which can be done with e.g. an ion-exchange polymer membrane like Nafion[®] [8]. Nafion[®] is permeable to polar compounds and many positive ions, so that the current loop during electrolysis is closed, but impermeable to negative ions and nonpolar compounds such as O_2 gas. A serious problem with this material, however, is that it does not adhere very well to metals, SiO_2 or Si_3N_4 .

The gas pressure developed by electrolysis is used to deflect a membrane. We modeled the pressure-deflection behaviour using the theory for small and large deflections of flat and corrugated membranes described in ref. [9]. For small deflections, the relationship between pressure and deflection is linear (only bending of the membrane occurs). The non-linearity which occurs for large deflections is the result of tensile stress caused by the stretching of the membrane. For a flat, square membrane of thickness h , length $2a$, Young's modulus E , Poisson's ratio ν , and initial stress σ , the relationship between the pressure difference P over the membrane and the corresponding centre deflection y is described by:

$$P = \frac{3.41\sigma h}{a^2} \cdot y + \frac{Eh}{a^4} \cdot \frac{1.98 \cdot (1 - 0.295\nu)}{1 - \nu} \cdot y^3$$

Analytical simulations for square, 1.2 mm wide and 1 μm thick silicon nitride membranes, $E = 300 \text{ GPa}$, $\nu = 0.3$, $\sigma = 100 \text{ MPa}$, and 8 μm thick polyimide membranes, $E = 5 \text{ GPa}$, $\sigma = 40 \text{ MPa}$, $\nu = 0.3$ were carried out. The deflection of all membranes was measured with the use of air pressure, and membrane deflections were recorded by a Sloan DEKTAK 3030 profiler.

Good agreement is found between calculated and experimental data (see Fig. 1). The amount of gas produced can be calculated from the deflection/pressure "calibration curve" in Fig.1, the volume of the cell cavity and measurements of the deflection during oxygen pressure build up. The deflecting membrane can be used in a micro-valve, e.g. designed in such a way that the membrane closes a (circular) hole in a plate above the membrane (called "disk" case), or the membrane is situated inside the channel (called "channel" case). In order to get an impression of the behaviour of such a valve, we estimate the pressure drop across the membrane for both two cases. In the simulation we assumed laminar flow, and fully developed velocity profile, with outer radius of 300 μm and inner radius of 150 μm for the "disk" case, and 150 μm the gap length for the "channel" case. Low volume flow rates were used, 1 $\mu\text{l}/\text{min}$ ("low flow") and 3 $\mu\text{l}/\text{min}$ ("high flow"). The behaviour of the pressure drop for the two cases is shown in Fig.2. The real situation in a valve of the design discussed above will be different; this situation can only be modelled accurately with numerical methods, e.g. with the aid of coupled fluid dynamically and mechanical finite element calculations.

3. Experiment

The microactuator of total size $5 \times 5 \times 1 \text{ mm}^3$ was fabricated with silicon micromachining and thin film techniques from two silicon wafers and consists of two main parts: the electrochemical cell and the deflecting membrane, which is used for pressure-to-deflection transformation (Fig. 3). The deflecting membranes are either made of low-stress LPCVD silicon nitride or of polyimide. The 1 μm thick silicon nitride membranes are either flat or with corrugations; the fabrication process can be found in ref.[6]. The process of polyimide membranes is as follows: a silicon wafer with a layer of 1 μm LPCVD silicon nitride is etched from the backside in KOH solution; on the front side a polyimide layer is spun and cured, over a 20 nm sputtered Cr adhesion layer, and finally the silicon nitride layer is removed by Reactive Ion Etching in an O_2/CHF_3 plasma, while the Cr layer is removed by wet etching. The two electrodes, Pt and Cu, are deposited by sputtering and patterned by lift-off. Full details of the complete fabrication procedure can be found in ref. [6].

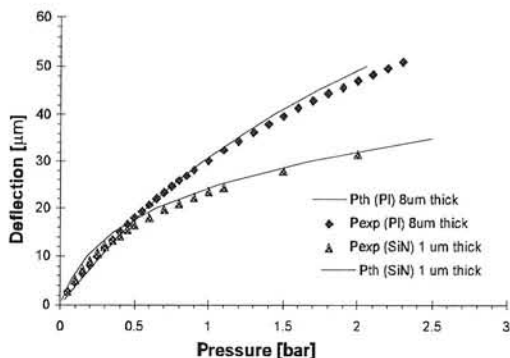


Fig.1. Comparison of calculated and measured membrane deflections (PI = polyimide, SiN = silicon nitride).

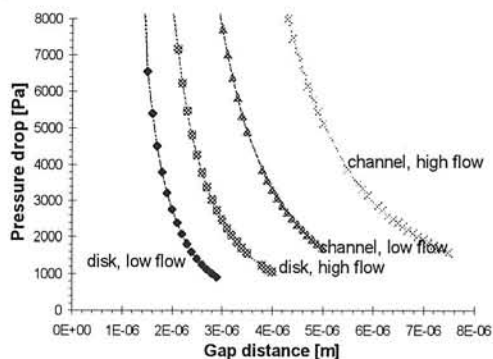


Fig. 2 Pressure drop across the membrane for "disk" and "channel" case and two values of volume flow rate (see text).

In order to improve the adhesion of Nafion[®] on the Cu electrode and to allow thicker Nafion[®] films with a smaller area, so that oxygen diffusion to the Cu electrode is reduced [6], a polyimide mesh was used (Fig.3). Tests have shown that the mechanical stability of this polymer membrane is sufficient for our application.

In principle the two processed wafers can be bonded at 300°C to form a perfectly sealed cavity, however, this temperature is not allowed because it would change the properties of Nafion[®]. Therefore bonding and closing of the electrochemical cell cavity were done at room temperature with epoxy. Some measurements of the electrochemical behaviour of the actuator were conducted at constant current. Using as little as 7 μ W for 100 s, a pressure of 20 mbar was easily obtained, which deflected

a flat membrane over 1.25 μ m. If the microvalve is actuated at 1.6 V and currents below 50 μ A, pressures of 2 bar could easily be obtained, causing membrane deflections in the range of 30 to 70 μ m. We also demonstrated that, by short-circuiting the cell or applying a reverse current, the membrane deflection can be reduced in an accurate way.

In conclusion, it was demonstrated that the electrochemical actuation presented here is an efficient and flexible method for the deflection of membranes, which can be applied in e.g. active microvalves with good characteristics.

ACKNOWLEDGEMENTS

This research project is supported by the Netherlands Technology Foundation (STW).

- [1] P. Gravesen, J. Branebjerg, O.S. Jensen, "Microfluidics - A review", *J. Micromech. Microeng.* 3, pp. 168-182, 1993.
- [2] M. Elwenspoek, T.S.J. Lammerink, R. Miyake and J.H.J. Fluitman, "Towards integrated microliquid handling systems", *J. Micromech. Microeng.* 4, pp. 227-245, 1994.
- [3] R. Zengerle, W. Geiger, M. Richter, J. Ulrich, S. Kluge, A. Richter, "Application of micro diaphragm pumps in microfluid systems", *Proc. Actuator 94*, Bremen, Germany, p. 25-29, 1994.
- [4] P.W. Barth, "Silicon microvalves for gas flow control", *Transducers '95 & Eurosensors IX*, Stockholm, Sweden, p. 276-279, 1995.
- [5] H. Janocha, "Neue Aktoren", *Proc. Actuator 88*, Bremen, Germany, p.389, 1988.
- [6] C. Neagu, J.G.E. Gardeniers, M. Elwenspoek and J.J. Kelly, "An Electrochemical Microactuator: Principle and First Results", *J. Microelectromech. Syst.* 5(1), March, 1996, in press.
- [7] A. J. Bard, L. R. Faulkner, *Electrochemistry methods: fundamentals and applications*, John Wiley & Sons, 1980.
- [8] Nafion[®] is a E. I. du Pont de Nemours & Co. Inc. registered trademark; product catalogue no. 27,470-4.
- [9] M. di Giovanni, *Flat and corrugated diaphragm design handbook*, Marcel Dekker Inc., New York, U.S.A., 1982.

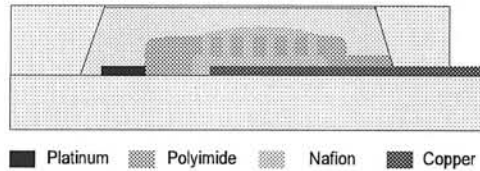


Fig.3.a Cross-section of the electrochemical microactuator.

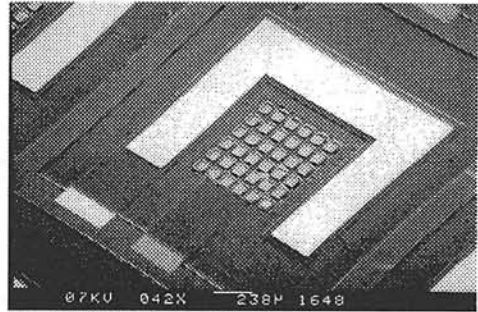


Fig.3.b SEM photo of the Pt, Cu electrodes, and the polyimide mesh.(top view).

Microsystems Activities at CSEM

Ted Smith, Hans van der Vlekkert, Felix Rudolf

CSEM, Centre Suisse d'Electronique et de Microtechnique SA
 Jaquet Droz 1, CH-2007 Neuchâtel, Switzerland
 phone: +41 38 205 111 fax: +41 38 205 700
 e-mail: sensing@csemne.ch

Abstract This paper describes a wide variety of mechanical, photonic and magnetic microsystems, as well as integrated circuits developed and fabricated by CSEM. Advanced research activities focus on perceptive systems. The microsystems development methodology addresses the design flow in an industrial environment.

CSEM in brief

CSEM is a Swiss center of international stature which provides the synergies necessary between research, industrial development and education, in order to successfully tackle the technological challenges of the future.

CSEM's principal mission is to generate new high-tech business, based on leading-edge know-how and expertise in microelectronics, microtechnologies, and related systems and materials. By assisting industry through a dynamic shuttle action between research and industrial production, CSEM contributes to the development of novel products. This is particularly the case in the framework of European programs.

CSEM is a private company, the shares in which are held by leading Swiss enterprises. Advanced research programs and capital equipment are supported by the Swiss federal government. Beside Switzerland, CSEM is internationally active in a dozen European countries, as well as overseas.

CSEM's core competencies are in the field of microtechnology:

- Integrated circuits and systems, especially for low-power applications
- Microsystem techniques
- Subsystems and instrumentation
- Bio-inspired techniques.

Strategic Areas Based on trends of the economy, CSEM's medium-term strategy focuses on :

- Analog and mixed analog/digital circuits and systems.
- Circuit design concepts to enable new breakthroughs in low power consumption.
- Extending the variety and performance of technological processes in silicon, particularly for sensors, actuators, and smart microcomponents.

- Mastering micro-system and subsystem technologies, both with respect to hardware (methods, tools, components, packaging, assembly and test), and software aspects (processing, learning, networking and interfacing).
- Bio-inspired technologies and architectures for perception and action, as well as smart nanostructure interfaces.

Creating a competitive advantage for new products. CSEM's front-edge know-how and core competencies rely on the combination of several key technologies. Since these are available from a single source, truly original and innovative product concepts are feasible.

Applications for micropower circuits and components extend from biomedical instruments to portable measuring equipment, through paging and time-keeping systems. Key elements are also being used more extensively for sensing and interfacing in industrial automation and process control units.

CSEM's approach to microsystems and subsystems relies on the integration of electronics, mechanics, optics, magnetics and materials to develop multicomponent devices with enhanced performance.

They address the strongly growing market of miniaturized and portable applications which have exacting technical requirements. They also include the aerospace and heavy industry sectors. Applications range from computer mice to subsystems for transport equipment, through novel printing systems and atomic-scale measuring equipment.

Technological means. At CSEM, projects are handled from the research phase, through technology feasibility studies, product design and development, to prototyping, production and testing. This unique feature is due to the full availability of in-house technological capabilities and services, as well as to the expertise and success in running projects from basics all the way to full industrialization.

In particular, CSEM, operates a versatile and modular silicon processing line with state-of-art production equipment for micromachining, optical microstructures, particle sensors, special microelectronic components, and other specialities.

LITOMASK is CSEM's own mask-shop facility with complete optical, e-beam and laser writing capabilities. As an external service, it has obtained quality certification according to ISO 9002 industrial standards.

Other technological services are also provided for chip integration, multi-project wafers, IC testing, and thin film deposition.

CSEM has been appointed by the European community as leader of one of the four Microsystem Manufacturing Clusters. In a joint collaboration with the Twente Micro Products (TMP) and Holland Signaal, both in The Netherlands, CSEM will offer microsystems development competence, technology service and microsystem production, as well as consulting.

Multi-disciplinary research and development

CSEM's microsystems development and production activities cover four main specialities: mechanical, photonic and magnetic microsystems, and integrated circuits.

The advanced research activity is concentrated on perception systems inspired on biology, bio-chemical sensors and process technology.

The following examples of products and research results will illustrate the multi-disciplinary aspects of the developments.

Firstly, *mechanical microsystems* combine low-power signal processing with capacitive sensing devices such as accelerometers and pressure sensors for high accuracy applications [1], [2], [3], [4]. Figure 1 shows a microsystem which measures the frequency of a differential pressure as part of a fluidic oscillator for flow measurements. Based on an oil-filled capacitive sensor, the system is capable of measuring frequencies from 0.15 to 45 Hz for differential pressures from 0.6 Pa to 60 kPa. The ASIC permanently compensates for large quasi-static pressure offsets in the presence of small differential pressure variations. Consuming less than 10 μA over 5 - 90 $^{\circ}\text{C}$, the microsystem can operate 10 years from a 3 V lithium battery. The development was carried out in the frame of the European ESPRIT project SLOPSYS [1].

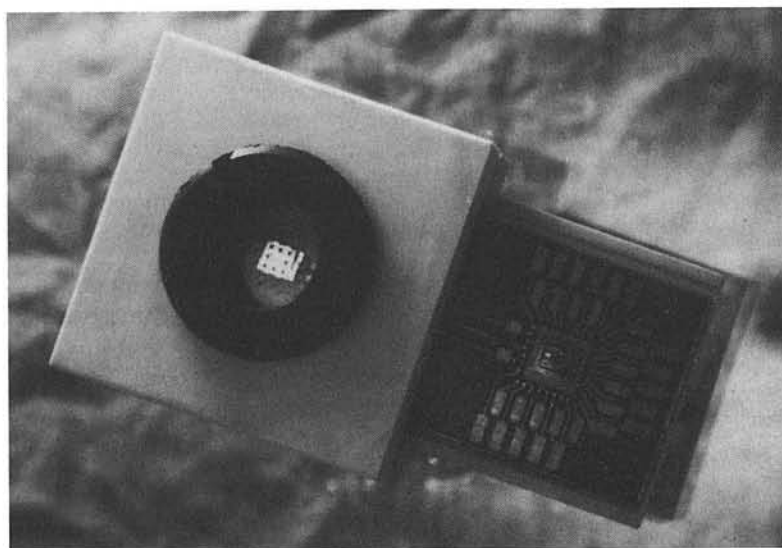


Figure 1 Differential capacitive pressure sensor with low power ASIC [1].

Classical and flexural mechanics are used to realise high precision actuators for fine-positioning devices, as is shown in Figure 2. Based on a silicon bulk micromachined flexible structure and a classical miniature motor, the microslit realises precision apertures in an optical application. The silicon device has been designed and

fabricated at CSEM, and the complete unit is assembled and functionally tested in house.

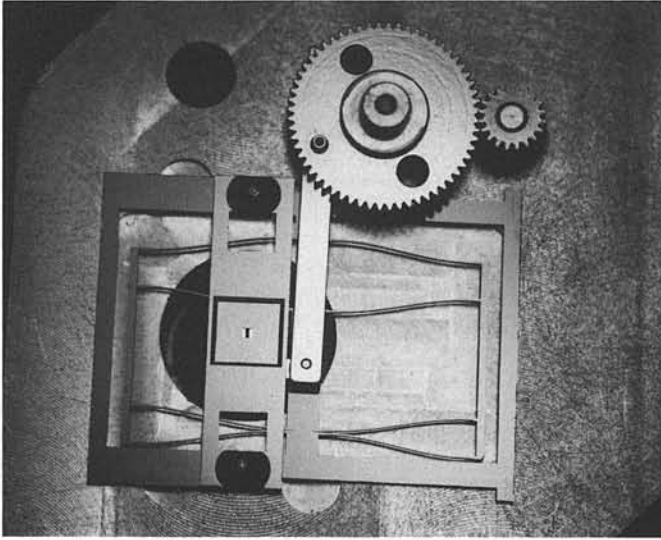


Figure 2 Microslit for precision optical application.

Magnetic microsystems combine integrated electronics with electroplated coils and magnetic materials to form dense arrays of magnetic actuators, antennas-on-chip, and coil-on-chip positioning sensors. Figure 3 shows a detail of a 1-inch silicon chip containing 480 electromagnets. The electromagnets are composed of FeNi writing poles, connected through a FeNi back plate, and are surrounded by gold coils which are addressed by on-chip multiplexing diodes. Several 1-inch silicon chips are assembled to form a magnetographic printer head [7].

Photonic microsystems may be composed of arrays of diffractive or classical microlenses, shutters and massive parallel analog signal processing based on arrays of photodiodes. They are used in light measuring and modulation systems and perceptive vision. Applications are found in colour, motion and obstacle detection, position encoders and optical imaging systems [5], [6].

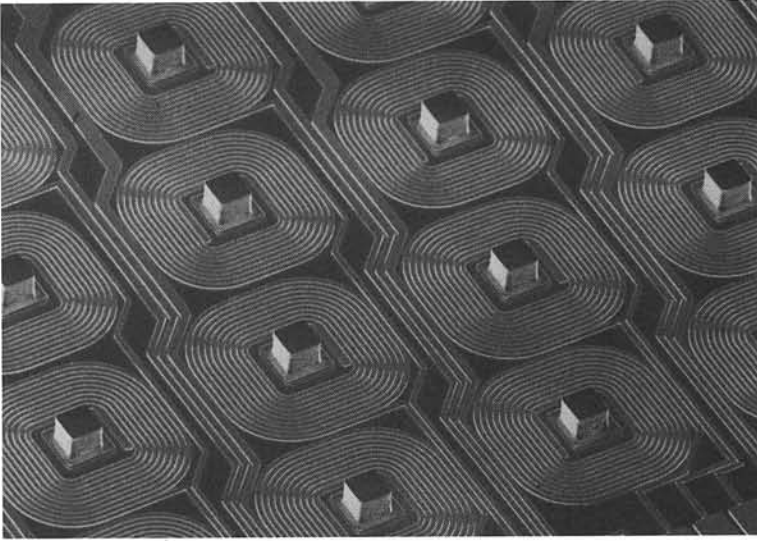


Figure 3 Detail of a 1-inch long silicon chip containing 480 electromagnets (1000 devices/cm²).

One of the early industrial applications of perceptive vision research is an encoder for a trackball, as illustrated in Figure 4. A displacement of the speckled image on the ball of the pointing device (trackball) is detected by an artificial retina mounted under a microlens. The silicon retina contains an array of 93 smart pixels, each based on a photodiode and associated analog read-out electronics. Inspired on the biological vision system, local and global information from the pixels are combined to extract displacement in a digital format. This feature is obtained without processing a sequence of sampled images, as would be the case in a CCD-based system. The result is a robust and low-cost encoder realised in standard CMOS technology [5].

A vital building block of microsystems is the *ASIC*, which may contain a combination of sensor and actuator interface electronics, A/D and D/A converters, power management functions, a micro-controller for calibration, communication protocol handling and self-test. High voltage drivers, bus interfaces as well as emerging wireless links are possible peripheral options which enable highly integrated intelligent microsystems [8], [9], [10], [11].

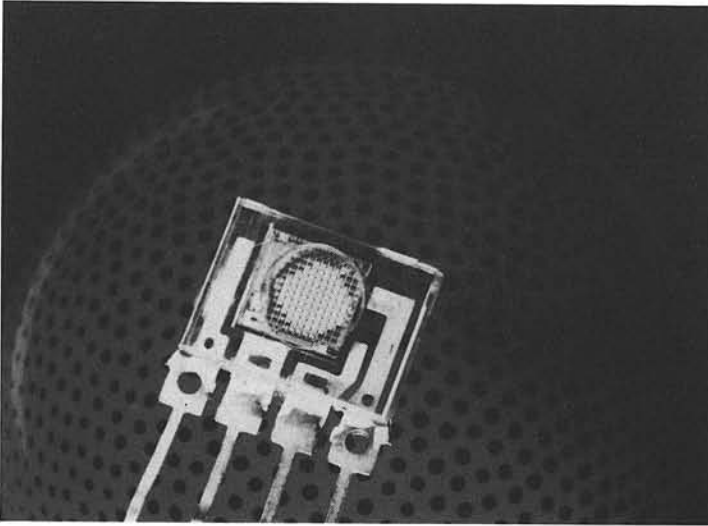


Figure 4 This pointing device (mouse) is based on a silicon retina which uses parallel analog signal processing to perform movement detection [5].

Low power consumption and/or low voltage operation becomes an issue in portable and remotely located applications, as well as in products with increasing functionality with a constantly reducing power budget. Figure 5 shows a detail of a 3-axes portable shock-detector with 10 years autonomy. The product is based on three CSEM capacitive accelerometers and an ASIC incorporating sensor read-out, programmable filtering, 11 bit per-channel A/D conversion, r.m.s.-to-DC converter, a real-time clock, built-in test features and a microprocessor interface. The circuit is powered at 3 V, consuming 450 μ W in standby mode, and 1.5 mW during full operation. The accelerometers and their interface assure a sub-ms wake-up to full functionality [8].

One of the driving forces in advanced research today is the study of how sensing, actuation and computational tasks are implemented in nature. This biological study teaches many things about robust, flexible and efficient techniques that can be implemented in microsystems.

The exploration areas include bio-inspired perception systems for vision, audition and olfaction (smell). VLSI (very large scale integration) circuit technology is used to conveniently interface cellular architectures of sensors and actuators with massively parallel electronics [12], [13].

In the area of bio-chemical microsystems research, CSEM focusses on bio-chemical sensitive layers, detection techniques, liquid handling and signal processing techniques.

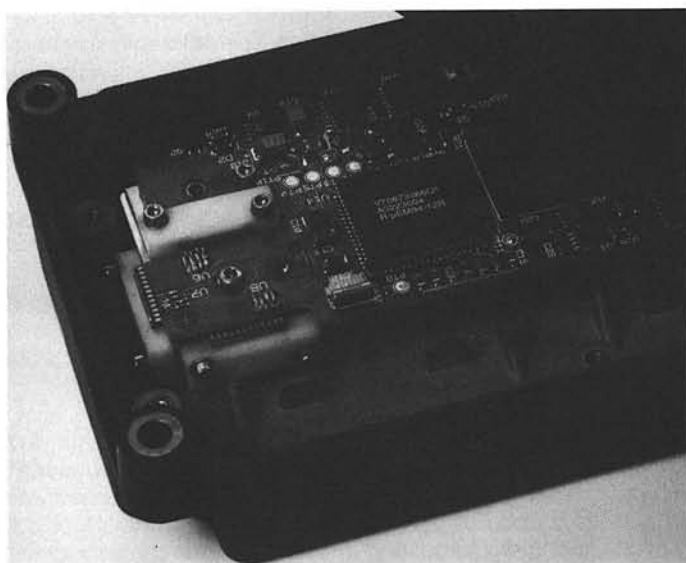


Figure 5 Detail of a 3-axes portable shock-detector with 10 years autonomy. Capacitive sensors and low power ASIC are CSEM developments [6].

Design methodology

Unlike in integrated circuit design, which relies on standard IC technologies, the microsystem designer has a virtually infinite liberty to combine a variety of semiconductor process steps and dedicated wafer technologies, assembly techniques and packaging concepts. In order to handle this freedom in an industrial environment, we have identified *three product creation phases*:

1. *the technology set-up phase*, in which the feasibility of new wafer processes and assembly and packaging concepts are proven and documented in a 'technology cook-book'.
2. *the development phase*, in which the actual microsystem design takes place, using proven and documented technology steps. This phase includes the manufacturability study.
3. *the production phase*, including the industrialisation phase during which test procedures and yield are determined.

Market introduction, distribution and sales are carried out by CSEM's customers.

In developments where the technical and commercial specifications are within reach using existing and well characterized technologies, the product development phase can be started directly.

For the product development phase, CSEM has defined a microsystem development methodology. Following the product definition and system design are addressed: detailed design, fabrication of components, prototype assembly and qualification. Upon customer approval, the definitive design, fabrication, assembly and test phases are accomplished.

The system design phase is vital for successful microsystems development, since it is in this phase that design concepts in terms of technical performance, manufacturability and production costs. Global specifications are translated into component specifications. Transducer physics, process knowledge, flexible packaging techniques, ASIC design and system simulation skills are required in this multi-disciplinary activity. Intensive project management and communication between development engineers are key success factors.

Behavioural microsystem simulation is becoming a valuable tool in development. By using HDLA, the analog complement of the digital hardware description language VHDL, it is possible to simulate together physical elements and electronic circuits, as to compare the performance of different microsystem architectures, and to assure that system specifications are translated into feasible sub-system specifications.

Conclusion

Microsystems represent a key technology for the future. CSEM's microsystems research, product development and production activities cover mechanical, magnetic, photonic and bio-chemical devices. Biological inspiration forms a driving force in today's microsystem research. Complemented by the in-house ASIC design skills, all microsystem development elements are available under one roof.

References

Selected publications by CSEM authors

Mechanical microsystems

- [1] M. Pierre, B. Steenis, J. Hermann, J.-P. Bardyn, "A battery operated microsystem for flow measurements," in: Proceedings of the 8th International Conference on Solid-State Sensors and Actuators (Transducers '95), Stockholm, Sweden, 1995, pg. 544 - 547.
- [2] T. Smith, Y. De Coulon, J. Hermann, F. Rudolf, "Low Power Precision Microaccelerometer," in: Proceedings Sensor'95, May 9-11, 1995, Nürnberg, Germany, paper A8.2.
- [3] F. Rudolf, H. De Lambilly, "Low cost pressure sensor microsystem," in: Proceedings of Micro System Technologies, October 19-21, 1994, Berlin, pp. 603.

- [4] Y. De Coulon, T. Smith, J. Hermann, M. Chevroulet, F. Rudolf, "Design and test of a precision servoaccelerometer with digital output," in: Proceedings of the 7th International Conference on Solid-State Sensors and Actuators (Transducers '93), Yokohama, Japan, 1995, pp. 832.

Photonic microsystems

- [5] X. Arreguit, F.A. van Schaik, F. Bauduin, M. Bidiville, E. Raeber, "A CMOS Motion Detector System for Pointing Devices," in: Proceedings of the International Solid-State Circuits Conference 1996 (ISSCC), San Francisco, USA, paper 6.4.
- [6] P. Debergh, P. Venier, O. Landolt, X. Arreguit, P. Roze, P. Biton, "Photonic microsystem for solar illumination monitoring," in: Proceedings of the 8th International Conference on Solid-State Sensors and Actuators (Transducers '95), Stockholm, Sweden, 1995, pp. 140.

Magnetic microsystems

- [7] F. Cardot, J. Gobet, M. Bogdanski, F. Rudolf, "Microfabrication of high-density arrays of microelectromagnets with on-chip electronics," in: Proceeding of the 7th International Conference on Solid-State Sensors and Actuators, 1993, (Transducers '93), Yokohama, Japan, pp. 32-35.

Integrated circuits

- [8] B. De Geeter, M. Pierre, O. Nys, V. von Kaenel, M. Chevroulet, M. Degrauwe, "A portable 3-axis 11-bit shock measurement circuit," in: Proceedings of the Custom Integrated Circuits Conference (CICC'94), San Diego, USA, May1-4, 1994, pp.331 - 334.
- [9] F. Maloberti, F. Francesconi, P. Malcovati, O. Nys, "Design Considerations on Low-Voltage, Low-Power Data Converter Design," IEEE Transactions on Circuits and Systems, Vol. 42, no. 11, November 95, pp. 853 - 863.
- [10] E. Vittoz, "Micropower Techniques," in: Design of VLSI Circuits for Telecommunication and Signal Processing, Editor J. Franca and Y.Tsividis, Prentice Hall, 1994, pp. 53 - 96.
- [11] E. Vittoz, E. Dijkstra, D. Shiels, Low Power Design, A Collection of CSEM Papers, Electronic Design Books, Penton Publishing, 1995.

Perception systems

- [12] X. Arreguit, E. Vittoz, F. A. van Schaik, A. Mortara, "Analog Implementation of low-level vision systems," in: Proceedings of the ECCTD'93, Davos, August 30 - September 3, 1993.
- [13] X. Arreguit, E. Vittoz, "Perception Systems Implemented in Analog VLSI for Real-Time Applications," in: Proceedings of the PerAc'94 Conference "From Perception to Action", Lausanne, September 5- 9, 1994, pp. 170 - 180.

Design, fabrication and characterisation of a planar microcoil inductor for power supply in and data exchange with implantable microsystems

*A. Smith, C.R. Neagu, J.G.E. Gardeniers,
M.C. Elwenspoek & J.H.J. Fluitman*

*Mesa Research Institute, University of Twente,
P.O. box 217, 7500 AE Enschede*

ABSTRACT

In this report a summary will be given of some considerations which are important when powering implants by telemetry. The fabrication process and electrical characterisation of planar receiver coils of small dimensions ($\sim 5 \text{ mm}^2$) will be described. Optimising the diverse variety of parameters, a receiver coil of sufficient efficiency has been developed.

1. INTRODUCTION

Over the last few years, interest and use of implants in the human body has increased. Permanent implants can be useful when there is a need for monitoring for example the insulin level, intraocular pressure or actuation of specific nerves. As the implants get smaller, much attention is directed towards downscaling of the electronics, data transmission circuitry and power supply. Considering the latter, the use of a battery is not always feasible or desirable because of size and lifetime limitations [1]. Wire connections can not be placed for long periods of time. An alternative for powering of implants is transmission of energy by inductive coupling of a pair of coils (fig. 1).

Making the receiver smaller has several consequences. First of all, as the area encapsulated by the turns of a receiver gets smaller, a more dense magnetic field is necessary to transfer the desired amount of energy. A dense field may induce eddy currents in human tissue, resulting in resistive heating or actuation of nerves. It has been reported that inductive heating can cause damage to the human tissue [2]. Coupling of coils by air (fig. 1), is inefficient compared to coils coupled by a core. Therefore, to increase efficiency, a small distance between transmitter and receiver is

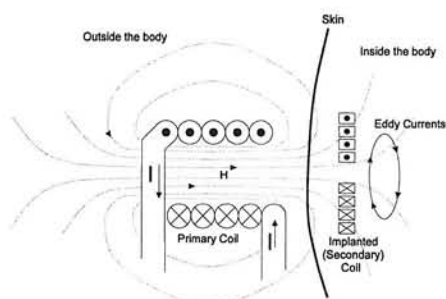


Figure 1 cross-section of a transmission-receiver set-up showing magnetic fieldlines.

preferred. For the same reason, a planar receiver coil is preferred over a solenoid.

In this paper we will concentrate on two configurations of a planar micro coil with dimensions of 4.5 mm in diameter, a wire thickness of 10 μm and more than 112 turns. The first coil has a wire height of 1 μm and the second a height of 11 μm . Insight has been gained in the importance of parasitic effects, which start dominating at frequencies of several megahertz.

2. DESIGN PARAMETERS FOR PLANAR COILS

A one layer planar coil deposited on a silicon substrate with a SiO_2 insulation layer (fig. 2) can be modelled by an electrical equivalent as shown in figure 3. The lower limit of the working frequency for transmission is determined by the physical size of the components in the electronic circuitry and the decrease of the quality factor, Q , of the coil, which, for $R_p \rightarrow \infty$, is determined by :

$$Q = \frac{\omega_0 L_r}{R_s}$$

The upper limit of the working frequency is not only determined by the absorption in human tissue, but also by the quasi-static condition and the change of resistance at higher frequencies. Regarding the quasi-static condition, it is necessary that the dimensions of the electronics are small compared to the wavelength in order to use conventional circuit theory [4]. To increase the inductance of a planar coil, many turns are necessary. The total length of the wire in our coils is about 1 m, implying that the working frequency should be much smaller than 300 MHz.

A theoretical prediction of the series resistance R_s of the coil was found to be difficult. As the operating frequency increases, the penetration depth of the current decreases, resulting in a redistribution of the current in the wire. This effect is amplified by the magnetic fields induced by neighbouring wires. Modelling of these effects indicates that the total series resistance may be several times the dc resistance, according to the formula [3]:

$$R_s = R_{dc} \left[1 + \frac{1}{48} \left(\frac{r_t}{\delta} \right)^2 \left[1 + u \cdot 12 \left(\frac{r_t}{d} \right)^2 \right] \right] \quad [\Omega]$$

δ is the penetration depth, r_t is half the width of a turn and d is the distance between the centre of two neighbouring wires. For a planar coil wound to the centre, the constant u is 8.64. The increase in resistance can be prevented by a careful choice of the dimensions of the coil and working frequency of the aimed circuitry.

The capacitance in the circuitry is dominated by the capacitance between the turns and the substrate. The self-inductance depends on the number of turns N and the mean diameter, a , and a factor P which depends on the coils dimensions[5]. P is 13.9 for the coils in this paper.

$$L_r \approx 0.1 \cdot N^2 \cdot a \cdot P \quad [\mu\text{H}]$$

3. POWER HANDLING AND DATA TRANSFER

To drive an implant's circuitry, the transmitted power needs to be rectified and smoothed to a dc voltage of at least 1.5 to 2.0 volts. Furthermore this voltage needs to be kept constant. An

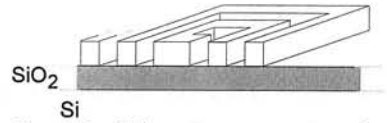


Figure 2 Schematic cross-section of a planar micro-coil.

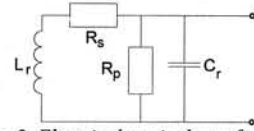


Figure 3 Electrical equivalent of a planar micro-coil.

accidental increase of the magnetic field strength should not result in a sudden voltage increase, risking damage to the implant. Besides voltage regulation, there needs to be some kind of feed-back from the implant to the external environment, because it is not always possible to see how and where the implant is placed. Therefore, a signal needs to be sent back as soon as the transmitter is correctly placed and enough power is coupled into the implant. Besides synchronisation, the implant may have to signal back when it is ready performing the desired action.

Passive rectification is done by using a bridge of Germanium diodes. They have the advantage over silicon diodes that the voltage drop is only 0.3 V, instead of 0.6 V, so that less power is lost. The circuitry can be protected from a (sudden) voltage increase by a zener diode (see figure 4).

Feedback can be given by changing the impedance of the receiver circuitry. A significant change of the impedance can be measured at the transmitter. The impedance can be changed by applying a signal on the gate of a CMOS or JFET. This technique prevents the need for transmitter circuitry in the implant.

4. FABRICATION

Two different fabrication techniques have been used to make planar coils. The first is preparation of a conductive wire by lift-off and sputtering. The second is by electroplating of copper. In both cases an oxidised silicon substrate is used.

To make a coil with the lift-off technique, conventional photoresist is patterned, a 1 μm layer of copper is deposited by sputtering. The sputtering set-up does not give perfect perpendicular incidence of copper atoms on the substrate, which is the cause for the ledges on the side of the turns (fig. 5).

Fabrication of a coil by electroplating was done by sputtering a blanket layer of 20 nm of chromium followed by 0.5 μm of copper. Two layers of 7.5 μm thick resist (Ma-P275, Micro allresist) were spun on the wafer with a 1 min. 90°C baking period in-between. After exposure, the resist was partially developed. It was then aligned, exposed and developed for a second time. This two step development was done because there seemed to be a significant change of refractive index between the upper and lower resist layer. An electroplating set-up was made using a commercial Cu electrode and electrolyte with surface active agents. A layer of 11 μm of copper was grown in 30 min. The resist was stripped with acetone in an

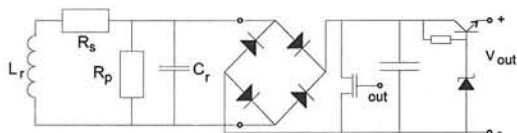


Figure 4 Schematic showing rectifying and voltage regulation circuitry.

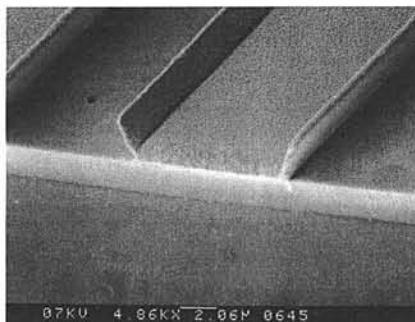


Figure 5 SEM photo of a 1 μm high turn made with sputtering and a lift-off technique.

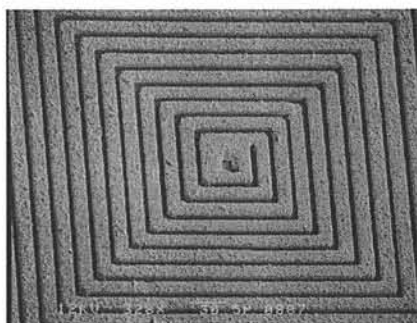


Figure 6 SEM photo of the centre of a 11 μm high electroplated planar coil.

ultrasonic bath. Finally the seed layer was removed by ion beam etching. Figure 6 shows the result.

Although fabrication of coils by sputtering produces much smoother surfaces, it is expected that it can not be grown as high as 10 μm due to the expected residual stresses in the copper. In fact, the rough surface on top of the electroplated layer ($\pm 0.5 \mu\text{m}$) does not seem to influence the electrical parameters very much.

5. MEASUREMENTS

Impedance measurements of the coils are shown in figure 7. The 1 μm high coil does not show inductance, due to the relatively high resistance. It has a resonance frequency at 2 MHz and a dc resistance of 2200 Ω . The other coil clearly shows inductance properties. The resonance frequency is 3 MHz and the dc resistance 130 Ω .

A transmitter-receiver set-up was made using the receiver circuitry from figure 3. The transmitter was placed at a distance of 3 mm. Using the electroplated coil, it was possible to have at least 1mW / 1.5V available on the output terminals. The efficiency between power delivered by the transmitter generator and available power on the output terminals was 0.1%.

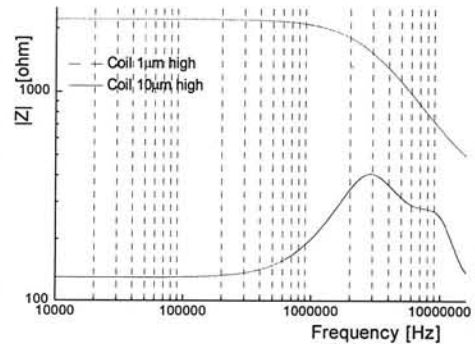


Figure 7 Impedance measurements of the two coils.

6. CONCLUSIONS

Coils have been fabricated which may find practical use for powering of implants as well as data exchange. Although the efficiency is low, the power transmission can be high enough to power electronics. At small dimensions it seems that not only absorption in human tissue is a limiting factor but also the quasi-static condition and effective resistance increase at higher frequencies.

Currently attention is directed to produce multi-layered planar coils with a more optimal ratio of winding depth and number of turns.

7. REFERENCES

- [1] R. Kadefors, E. Kaiser and I. Petersen, *Energizing Implantable Transmitters by Means of Coupled Inductance Coils*, IEEE transactions on Bio-medical Eng., vol. 16, 1969, p.177-183
- [2] J.F.Lehmann, *Therapeutic Heat and Cold*, third edition, Williams & Wilkins, Baltimore/London, 1982
- [3] S. Butterworth, *Effective resistance of inductance coils at radio frequency; part 1*, Experimental wireless & The wireless engineer, 1926, p. 203-210 and 309-316
- [4] J.R. Reitz, F.J. Milford and R.W. Christy, *Foundations of Electromagnetic Theory*, Addison-Wesley Pub. Company, USA, 1993
- [5] F.W. Grover, *Inductance calculations: working formulas and tables*, reprint, Dover publications, 1973

Range camera at 12-bits resolution and video speed

Michiel de Bakker¹, Piet W. Verbeek¹, Gijs K. Steenvoorden²

*¹Pattern Recognition Group of the Faculty of Applied Physics
Delft University of Technology
Lorentzweg 1, 2628 CJ Delft, The Netherlands*

*²Instrumentation Department, TNO Institute of Applied Physics
Stieltjesweg 1, 2628 CK Delft, The Netherlands*

e-mail: michiel@ph.tn.tudelft.nl

ABSTRACT

In the present paper we introduce a smart image sensor, the PSD-chip, designed for sheet-of-light range imaging. The sensor area consists of an array of Position Sensitive Detector (PSD)-strips. The on-chip signal processing electronics is built up from both analog and digital circuitry. Our aim is to be able to record 1.5 million range values (Rangels) per second at a 12-bits resolution.

I. INTRODUCTION

The urge for optical 3D scanning devices arises in fully automated processes or assembly cells, where image sensors can serve as inspection tools. The development of smart sensors is a natural result of the removal of people from the industrial process. A smart image sensor is a chip where an image sensor and signal-processing circuits have been put together on the same silicon die [3]. The smart image sensor of our investigations will be able to record 1.5 Mrangels/s at a 12-bits resolution.

3D information can be obtained with the aid of 3 reference points (in the human system two eyes and an object). The measurement technique that is based on this principle is called triangulation [see Fig. 1]: the beam of a laser diode is converted into a sheet of light. The light sheet cuts the object under observation in a profile-line. This intersectional line is projected onto an image sensor containing an array of Position Sensitive Detector (PSD)-strips.

A PSD consists of a planar p-n (or n-p) junction. Each PSD-strip produces two currents caused by the lateral photo-effect [1]: one to the left and one to the right side of the PSD. The ratio of these currents is a measure for the center of gravity of the incident light-distribution, from

which the range values can be computed. A complete range image can be obtained by recording a number of adjacent profile lines. An interesting property of the production of PSD's is that it is compatible with processing of bipolar transistors, and this creates the possibility to integrate PSD's and readout electronics on the same silicon die. We will exploit this for the PSD-chip to let on-chip electronics take care of amplification, and of demultiplexing of the sensor signals to a single output channel.

Several sensors have been reported that are able to perform the task of sheet-of-light range imaging [3-6]. The smart sensor of our investigations is the first that contains both a PSD-array and readout electronics on a single die, thus reducing the number of bonding pads to our chip (because demultiplexing of the sensor-signals occurs "on-chip").

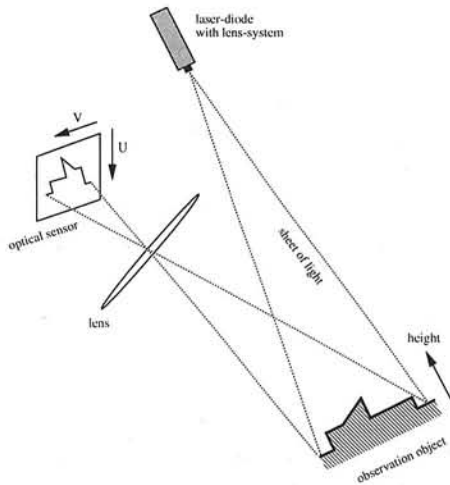


Fig. 1 Active triangulation.

II. THE SMART IMAGE SENSOR

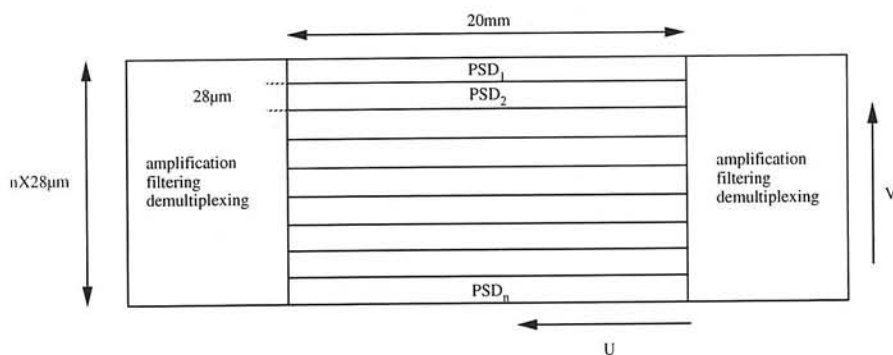
As mentioned in Sec. I, the smart image sensor that is presently being developed, will contain the PSD-strips as well as a part of the readout electronics [see Fig. 2a for a sketch of the PSD-chip]. The on-chip electronics consist of an analog as well as a digital part :

- Analog : amplification and low-pass filtering of the sensor signals
- Digital : demultiplexing (i.e. selection of the PSD-strips)

II-A Analog electronics (on-chip)

Amplification and low-pass filtering occurs using an operational amplifier, connected in a resistive and capacitive feedback circuit. The -3dB cut-off frequency of the opamp with feedback is 20kHz. Low-pass filtering is necessary to eliminate the high-frequency transistor-noise that is present in integrated circuits. The opamp is designed to deliver a large amount of gain using a minimum number of transistors. The high opamp gain will make sure that the (small) photo-currents will be lifted above the noise-level of the rest of the signal-processing electronics. The Signal to Noise Ratio must be sufficient to support 12-bits representation of the range values.

a).



b).

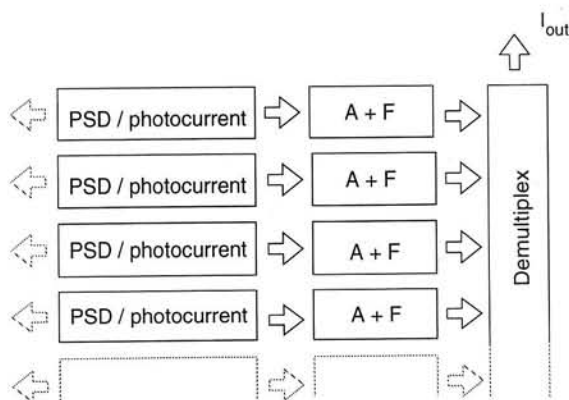


Fig. 2 a). sketch of the dimensions of the PSD-chip, b) sketch of the signal-processing that takes place on the sensor-chip : amplification (A), low-pass filtering (F) and demultiplexing of the signals to a single output-channel.

II-B Digital electronics (on-chip)

The strip-selection circuit will be implemented in Emitter Coupled Logic (ECL). Strip-selection proceeds with a ring-counter, which is designed from standard ECL OR/NOR-gates and D-type flipflops. Using ECL, switching speeds of over 10 MHz can be obtained. Each strip is selected once every 64 μ s, in order to make the PSD-chip compatible with video-standards. Fig. 2b) shows (schematically) the idea of the signal processing that takes place on the sensor-chip.

II-C Off-chip signal processing

Apart from supply voltage and ground-connections the only connections to the outside world are a clock signal "in", and an amplified, filtered and demultiplexed signal "out". The rest of the signal processing (off-chip) consists of :

- variable gain amplification
- 12-bits AD-conversion
- correction for amplifier off-sets, using look-up tables
- computation of the range values using Digital Signal Processors (DSP's)

II-D Concatenation of more PSD-chips

A special feature of the PSD-chip of our investigations is the possibility of increasing the number of PSD-strips with a multiple of n (i.e. the number of strips on a single die). This is achieved by making the dice (that contain n PSD-strip each) suitable for concatenation, which will give us the opportunity of increasing the number of samples in the V-direction [see Figs. 1 and 2a)] without the need of making a single, very large die. The digital electronics are designed such that two (or more) PSD-chips can be interconnected in order to form a ring-counter that selects between $2n$ (or a multiple of n) strips. This feature, of placing a number of PSD-chip next to each other, will also set high demands on the physical size of the dice (containing the sensors and the electronics) if periodicity in the V-direction has to be maintained.

III. CONCLUSIONS

The simulation results (simulations have been performed on Pstar 3.0, using DIMES01 transistor parameters) we have obtained so far provide a sound reason to believe that the PSD-chip will be able to meet the demands concerning accuracy (83 dB SNR) and speed (1.5MHz range frequency). A prototype of the PSD-chip is being processed at the Delft Institute for Micro Electronics and Submicrontechnology (DIMES).

REFERENCES

- [1] D.J.W. Noorlag, *Lateral-photoeffect position-sensitive detectors*, Thesis Delft University of Technology (Delft University Press, Delft, the Netherlands), 1982.
- [2] M. Johannesson, *SIMD Architectures for Range and Radar Imaging* Ph.D. Thesis, Linköping University, 1995.
- [3] A. Åström, *Smart Image Sensors* Ph.D. Thesis, Linköping University, 1993.
- [4] J. Kramer, P.Seitz and H. Baltes, "Inexpensive range camera operating at video speed," *Appl. Opt.* 32, 2323-2330 (1993).
- [5] K. Araki et al., "High speed and continuous 3-D measurement system," 11th ICPR, Conf. D : Architectures for Vision and Pattern Recognition, The Hague, The Netherlands 1992.

Light-to-Frequency Converter with a Digital Output

G. de Graaf and R.F. Wolffenbuttel

Delft University of Technology
Dept. of Electrical Engineering
Laboratory for Electronic Instrumentation
Mekelweg 4, 2628 CD Delft
The Netherlands
Phone: 15-2784707 FAX: 15-2785755
Email: G.de Graaf@et.tudelft.nl

ABSTRACT

An optical sensor for operation in the visible spectrum with integrated electronic read-circuits has been realised in a BIFET process. The output signal is a pulse series with a frequency proportional to the intensity of the incident light. Furthermore, the duty-cycle of the output pulses depends on the spectral distribution of the incident light, enabling measurement of colour. The electronic circuits have been designed for operating a large dynamic range and a relatively small chip area. No internal or external capacitor is needed for the current-to-frequency conversion, since the photodiode operates in a charge integrating mode. This enables fabrication of arrays of smart image detectors where a large area can be used for the photodetector.

INTRODUCTION

Light is generally characterised by its intensity (Luminance) and its spectral distribution (Colour). Utilising the very large dynamic range of sensors like silicon photodiodes in analog systems would require an expensive high-performance AD converter. Therefore recently several sensor interface circuits with a frequency output both in MOS [1] [4] and bipolar technology [2] [3] have been introduced. A frequency output generally allows a high dynamic range since frequencies from a few Hz up to several Mega-Hertz can be easily counted using simple logic. Modern microcontrollers have on-chip counter/timer logic allowing a direct interface of these type of sensors, also a digital output of the sensor allows a simple interface to bus systems. Commercially available Light-to-Frequency converters realised in MOS technology [4] consists of a current amplifier covering an input current range of about four decades followed by a current-to-frequency converter. The current amplifier is programmable in 3 steps of one decade to cover the entire dynamic range of the detector (10^{-9} - 10^{-1} W/cm²). These devices perform very well in terms of dynamic range and linearity, but in many

applications e.g. object recognition, also the spectral distribution of the incident light is needed. The circuit presented here uses the photocurrents of two stacked junction diodes in the epilayer. Due to the wavelength-dependent absorption of light in the epilayer these currents can be used to extract information on the spectral distribution of the impinging light [7].

INTEGRATING MODE OPERATION

One of the photodiodes in this novel sensor system is used in the Integrating Mode [5][6]. Figure 1 shows the basic circuit of the diode as the timing element in an astable oscillator configuration.

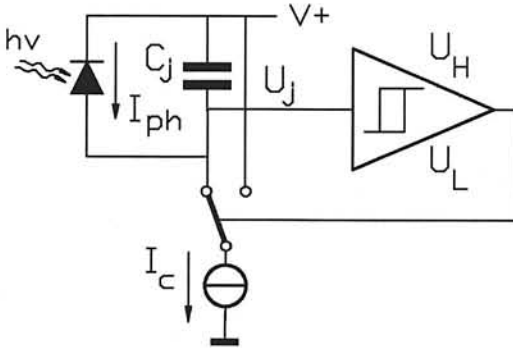


Figure 1 Integrating Mode Oscillator

The current source I_c charges the junction capacitance of the reverse biased photodiode. The voltage U_j across the diode is then given by:

$$\frac{dQ}{dt} = C_j \frac{dU_j}{dt} + U_j \frac{dC_j}{dt} = -I_c + I_{ph} \quad (1)$$

The depletion capacitance C_j of the diode depends on the voltage across the junction by the following relation: $C_j = kA_j U_j^m$, where A_j is the diode area, k is a constant and m is a constant depending the doping gradients of the P and N side of the junction (m equals $-1/2$ for an abrupt junction). Substitution in (1) yields:

$$-I_c + I_{ph} = kA_j U_j^m \frac{dU_j}{dt} + U_j k m A_j U_j^{(m-1)} \frac{dU_j}{dt} = kA_j U_j^m (1+m) \frac{dU_j}{dt}$$

If U_H and U_L are the high and low threshold voltage of the comparator, the charge time t_c can be derived from:

$$\Delta Q = \int_{t=0}^{t=t_c} (I_c - I_{ph}) dt = (I_c - I_{ph}) t_c = kA_j (1+m) \int_{U_j=U_H}^{U_j=U_L} U_j^m dU_j \quad \Rightarrow \quad t_c = \frac{kA_j}{(I_c - I_{ph})} (U_H^{m+1} - U_L^{m+1}) \quad (2)$$

After reaching U_L the comparator will switch I_c to ground and the photocurrent I_{ph} will discharge the junction capacitance again to the high threshold voltage U_H . The discharge time

$$t_d \text{ can be found by substitution of } I_{ph} = \frac{PA_j \lambda \eta_c}{\lambda c} \text{ in (2) giving: } t_d = \frac{k \hbar c}{\lambda \eta_c P} (U_H^{m+1} - U_L^{m+1}) \quad (3)$$

So the discharge time t_c is inversely proportional to the light intensity P . Also note that the discharge time t_d does not depend on the diode area A_j , and the voltage across the junction is non-linear. However since the threshold voltages V_H and V_L are constant this does not influence the linearity in the current-to-frequency conversion. A disadvantage of this circuit is that the fixed current I_c must always be larger than the photocurrent I_{ph} to be able to charge C_j again. This results in a large difference between the charge- and discharge times at a low

photocurrent, meaning a very low duty-cycle of the output pulses at low illumination levels. The circuit and sensor combination described in the next paragraph avoids this problem.

"STACKED-DIODE" STRUCTURE

The structure of the sensor is shown in figure 2a. It is a vertical PNP device consisting of a P-implanted layer, the epilayer and the substrate. Figure 2b shows the spectral responses of the reverse biased upper(a) and lower(b) photodiode.

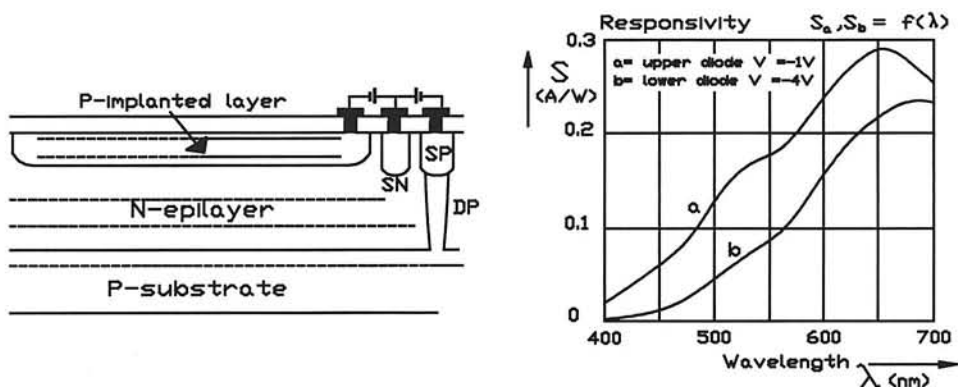


Figure 2 a) Sensor structure.
b) Photodetector responsivities.

Figure 3 shows the basic read-out circuit. The shallow PN diode is used in the charge integrating mode. The sum of both photocurrents $I_e = I_{ph} + I_s$ is mirrored by transistors Q_9 - Q_{10} and replaces the fixed charge current I_c in figure 1.

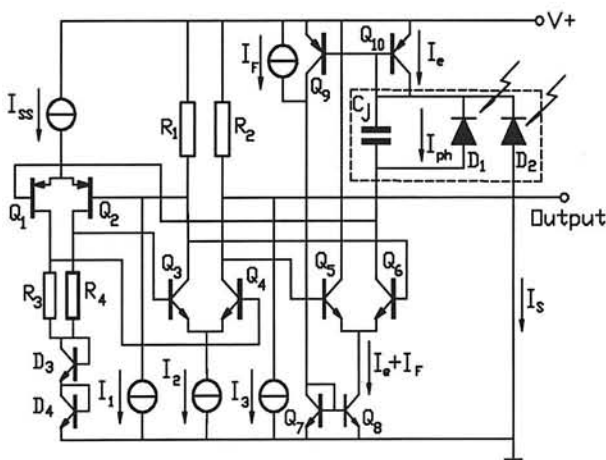


Figure 3 Electronic circuit

Substitution of $I_c = I_s + I_{ph}$ in equation (2) shows that the discharge time t_d is inversely proportional to the photocurrent generated in D_2 , while the charge time t_c is inversely proportional to the photocurrent in the shallow junction D_1 . From figure 2b can be seen that the responsivity at short wavelengths of the shallow PN junction is much higher than that of the epilayer-substrate junction. Since both the charge- and the discharge current are proportional to the incident light, the duty-cycle of the output pulses remains constant at a varying luminous intensity. Due to the wavelength-dependent absorption of light in silicon the ratio of these currents will change with the wavelength [7]. This results in a varying duty-cycle as a function of the average wavelength (colour) of the light on the sensor. The junction FET input pair (Q_1 - Q_2) of the comparator features a very low input current and a good noise performance. The positive feedback loop to the gate of Q_2 introduces the required hysteresis for astable oscillator operation. The fixed current sources I_1 and I_3 bias the JFET's and the output switches Q_5 and Q_6 . The comparator threshold voltages are given by: $U_L = R_1(I_1 + I_2)$ and $U_H = R_1 I_1$. The NPN current mirror (Q_7 - Q_8) as well as the output switches (Q_5 - Q_6) do not operate well at a collector current (= the total photocurrent I_c) lower than 1nA. Therefore, the fixed current I_f is added. Photo 1 shows the L-shaped photodiode with the electronic circuits in the lower left corner.

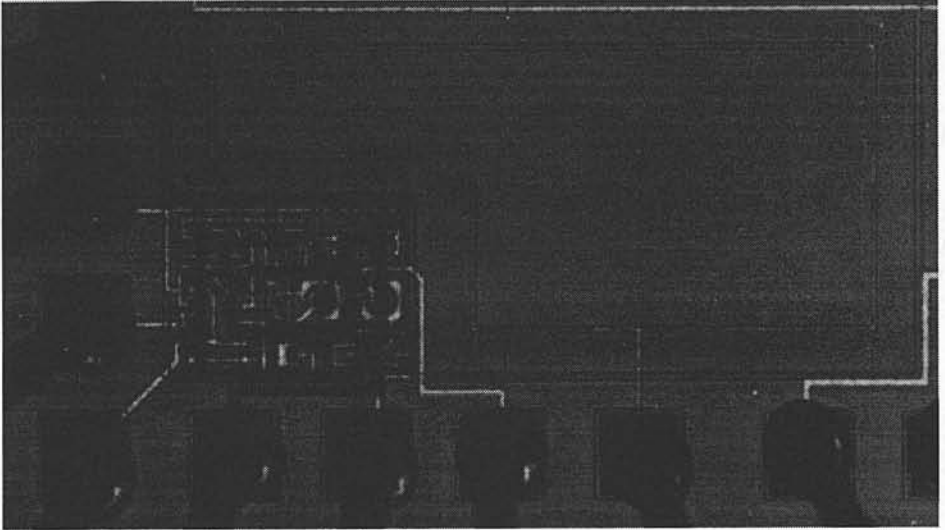


Photo 1 The sensor with electronic circuits.

MEASUREMENT RESULTS

Figure 4 shows measurement results of the output frequency of the converter using a 2x2 mm photodiode as a function of the light intensity. The lower and upper limit of the output frequency have been measured to be 0.1 Hz and 120 kHz respectively. Frequency scaling is possible by adding external capacitors.

The dynamic range mainly depends on the photodetector characteristics. The large series resistance of the epilayer, limits the charge- and discharge-time of the junction capacitance

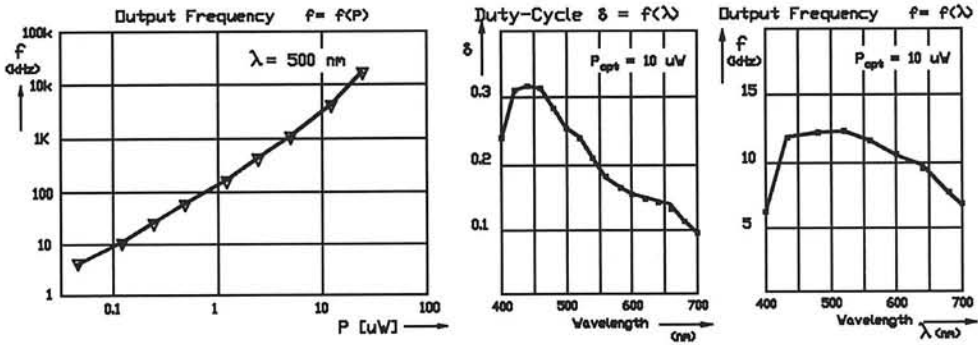


Figure 4 a) Output period = $f(P)$ b) Duty cycle = $f(\lambda)$. c) Output frequency = $f(\lambda)$

(≈ 500 pF @ 3V) resulting in an upper frequency limit. Devices with a lower series resistance would allow operation limited merely by the speed of the comparator. The lower limit of the output frequency is determined by the leakage current of the PN junction (≈ 65 pA). Figure 4b shows that the duty cycle of the output signal has an unambiguous spectral response from 450 to 700nm.

CONCLUSIONS

A fully integrated silicon light-to-frequency converter has been realised in a BIFET process without an external capacitor. Batch production is possible since no external components are needed and colour can be measured without the use of optical filters or extra mask steps. The system covers a measurement range of about 5 decades of intensity. Temperature compensation may be a next step in the development of the system. As many applications in the future require "plug-and-play" sensor systems, adding an interface for a bus system on the same chip is required.

ACKNOWLEDGEMENT

The authors would like to thank the IC processing section of the Delft Institute for Micro-Electronics and Submicrontechnology (DIMES) for fabrication of the devices.

References:

- [1] Jordan, J.R., Peter, K.W., Renshaw D., "A capacitance ratio to frequency converter using switched capacitor techniques", *Sensors & Actuators part A*, Vol. 29, no.2, pp.133-139, November 1991.
- [2] Meyer, G.C.M., van Gelder, R., Noorder, V., van Drecht, J., Kerkvliet, H., "A Three Terminal Temperature Transducer with Microcomputer Interfacing", *Sensors & Actuators, Part A*, Vol. 18, pp.195-206, October 1988.
- [3] Van Dijk, G.J.A., Huijsing, J.H., "Bridge-Output-Frequency Converter for Smart Thermal Air-flow Sensors", *IEEE transactions on Instrumentation and Measurement*, Vol. 44, no.4, pp. 881, August 1995.
- [4] Texas Instruments. Application Notes of the TSL230 Light-to-Frequency Converter.

- [5] Weckler,G.P., "Operation of p-n junction photodetectors in a photon flux integrating mode," IEEE Journal of Solid State Circuits, Vol. SC-2, pp. 65-73, September 1967.
- [6] S.G. Chamberlain, "Photosensitivity and Scanning of Silicon Image Detector Arrays," IEEE Journal of Solid State Circuits, Vol. SC-4, No.6, December 1969.
- [7] Wolffenbuttel, R.F., De Graaf, G., "Performance of an Integrated Silicon Colour Sensor with a Digital Output in Terms of Response to Colours in the Colour Triangle." Sensors and Actuators, A21-A23 (1990) pp. 574-580.

First Results on a New Type of Photon Counting Avalanche Photodiode

W.J. Kindt, N.H. Shahrjerdy and H.W. van Zeijl⁺

*Lab. for Electronic Instrumentation, Dept. of Electrical Eng., ⁺DIMES
Delft University of Technology, The Netherlands
Tel +31 15 2783342, Fax +31 15 2785755*

Abstract

APDs can be used to count single photons. To achieve this, they can be used in the so called geiger mode, in which the diode is operated above the breakdown voltage. The absorption of a single photon initiates an avalanche breakdown, which can easily be detected. Prototypes of geiger mode APDs were fabricated and tested. Initial results show that these diodes function correctly. However, because of trapping centers in the depletion layer, they show a considerable amount of afterpulsing.

Introduction

Photon counting is a technique that is used in many application areas for the detection of weak optical signals, for example in astronomy [1]. If not only very weak, but also very fast optical signals have to be analyzed *Time correlated* single photon counting can be used [2]. This technique is used in applications such as the analyses of fast fluorescent decays [2].

Usually, photomultiplier tubes and microchannel plates are used for (time correlated) photon counting. In some applications these conventional, photocathode based, devices can be replaced by avalanche photodiodes (APDs). Advantages of APDs are a larger quantum efficiency, smaller size, lower bias voltage and insensitivity to magnetic fields. Disadvantages are a limited active area and a larger number of false counts, both dark counts and counts resulting from afterpulsing.

APDs can be used in two operation modes, the multiplication mode and the geiger mode. Both modes can be used for photon counting [3]. Our work concerns the development of a new, geiger mode dedicated, silicon APD structure. This structure is area efficient and readout-electronics compatible, and therefore suited for the fabrication of arrays. In this paper we describe geiger mode operation of APDs, followed by a presentation of the first results on our own devices.

Photon counting in the geiger mode

In the geiger mode, the APD operates like a Geiger Müller counter [3]. The diode is biased a few volts above the breakdown voltage, which results in an instable situation. As soon as a single charge carrier enters the depletion layer of the diode, this carrier is multiplied infinitely by the

impact ionization process. This results in an avalanche breakdown, and a large breakdown current starts to flow. This process can be used to count photons. The absorption of a photon in the APD will trigger an avalanche breakdown. This breakdown is detected and subsequently it is quenched electronically. There are two ways to quench a breakdown: passive and active quenching.

Passive quenching [4] is illustrated in figure 1. The APD is connected to the power supply through a large series resistor R_s . If the current through the diode equals zero, the voltage across the diode equals V_{bias} which is larger than the breakdown voltage. If the diode breaks down, the series resistor reduces the voltage across the APD which quenches the avalanche. This can only be achieved with a large series resistor. A large resistor forces the current through the diode to be small; the number of charge carriers in the depletion layer will also be small and therefore statistical fluctuations will cause the current to drop to zero. After the breakdown is quenched, the diode is recharged to the bias voltage with a time constant that is determined by the depletion layer capacitance and the series resistor. Photons are counted by counting the number of voltage pulses at the at the output V_o .

Active quenching [5] uses an active electronic circuit to bias the APD and to detect the breakdown. As soon as a breakdown current starts to flow through the diode, the voltage is reduced to a few volts below the breakdown voltage for a well determined quenching time. Subsequently the diode is quickly recharged to the operation voltage to allow the detection of a new photon.

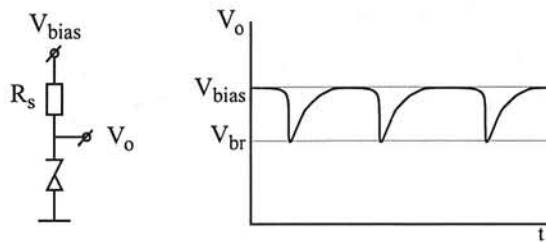


Figure 1: Passive quenching

Properties of geiger mode APDs

A few properties of geiger mode operated APDs deserve some attention here:

- Photoelectron detection efficiency

Not every photoelectron will initiate an avalanche. Some photoelectrons may traverse the depletion layer without ionizing any lattice atoms. Also, the avalanche may extinguish after a few ionizations. The probability that a photoelectron does initiate a breakdown increases with the applied bias voltage. At a few volts above the breakdown voltage, it approaches unity.

- Dead time

Geiger mode operated APDs always show a certain dead time after the detection of a photon. Photons absorbed within this dead time can not be counted. With passive quenching the photoelectron detection efficiency increases gradually from zero to its steady-state value during the recharge. With active quenching the dead time is determined by the quenching time of the electronic circuit. The dead time limits the maximum count rate of geiger mode APDs.

- Dark counts

Thermal generation of e-h pairs in the diode causes dark counts. These are false counts, not caused by a photon. The number of dark counts can be reduced by cooling the diode.

- Afterpulsing

During a breakdown a large number of charge carriers flows through the diode. Some of these

carriers may be captured by trapping centers inside the depletion layer. Later the captured carriers may be released, which causes another type of false count: an afterpulse. The probability that an afterpulse occurs increases with the amount of charge that flows through the diode during a breakdown. Because this charge discharges the APD from the bias voltage to the breakdown voltage, the afterpulsing probability increases with increasing bias voltage.

Fabrication of prototypes

Prototypes of geiger mode APDs were created in the DIMES processing facilities. The structure of the prototypes is given in figure 2. The diodes are fabricated in a p⁻-type epilayer on a p⁺-type substrate. The active area is defined by a Boron implantation (dp) followed by a drive in. The cathode of the diode is created by an Arsenic implantation (sn). This implantation is also used to create a guard ring around the diode. A boron implantation around the guard ring (sp) is used as an anode contact. After the implantations an anneal, oxidation and metallization are performed. The sn implantation overlaps the dp implantation to avoid very high field strengths at the junction edge.

To enable cooling of the APDs, the dies were glued to a small copper plate that is mounted in a hole in a small printed circuit board. Bond wires connect the bond flaps of the dies to the PCB. The resulting devices can be mounted on a peltier element inside a small vacuum chamber. The vacuum avoids condensation of water vapor on the diodes when the devices are cooled.

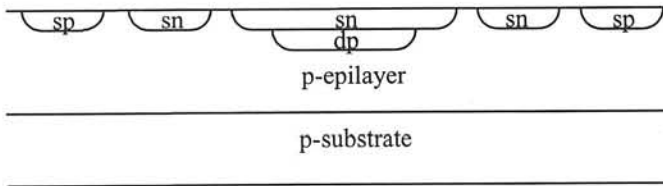


Figure 2: Structure of the fabricated prototype geiger mode APD

Measurement results

Counting experiments were performed at 20 °C and at -50 °C with passive quenching using a series resistor of 110 kΩ. An LED was used to illuminate the APDs. The area of the measured diodes equals 40*40 μm². During the experiments the bias voltage was varied between 25 and 35 volts. In another experiment the dark counts of a 20*20 μm² APD were measured at room temperature over the same bias voltage range. Figure 3 shows the resulting count rates.

Figure 3 clearly shows the increase of the photoelectron detection efficiency with increasing bias voltage. Because the breakdown voltage decreases with decreasing temperature, the curve for -50 °C is shifted to the left with respect to the curve for 20 °C.

At -50 °C the count rate saturates at 100 kHz. After dead time correction [6], the counted photon flux therefore equals $7.8 \cdot 10^9 \text{ cm}^{-2}\text{s}^{-1}$ (a dead time of 2 μs was determined with an oscilloscope). The photon flux measured using a regular photodiode was $1.38 \cdot 10^{10} \text{ cm}^{-2}\text{s}^{-1}$. The difference is not yet explained.

At room temperature the count rate does not saturate. This is assumed to be caused by afterpulsing. At -50 °C the decay time of the traps is very long. Therefore they always remain occupied and have no influence on the results.

The presence of trapping centers is also indicated by the measurement of the dark counts. At large voltages the afterpulsing probability becomes very large and the afterpulses become self-perpetuating. This results in a sharp increase of the count rate. This increase occurs for voltages

larger than 34 volt as can be seen in figure 3.

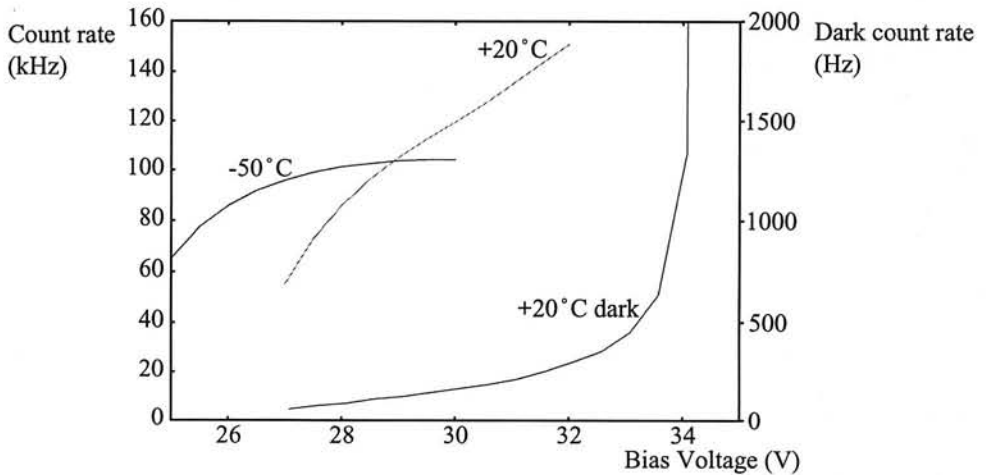


Figure 3: Illuminated count rate and dark count rate as a function of bias voltage

Conclusions

APDs can be used for photon counting. Geiger mode APDs were fabricated at DIMES. Initial measurements show that these diodes can be used for photon counting, but they are not yet optimal because they show a considerable amount of afterpulsing caused by trapping centers in the depletion layer of the diode.

Currently we are working on an improved measurement setup that includes an active quenching circuit. Future research will concentrate on processes to reduce the concentration of trapping centers in the APD.

Acknowledgments

This project is supported by the dutch technology foundation (S.T.W.) under project no. DEL 44.3294

References

- 1 J.G. Timothy "Photon-Counting detector systems: Current status and future prospects" *Photoelectronic Image Devices 1991*, pp. 85-96
- 2 D.V. O'Connor and D. Philips *Time Correlated Single Photon Counting*, London, Academic, 1984
- 3 A. Lightstone, A. MacGregor, D. MacSween, R. McIntyre, C. Trottier and P. Webb "Photon counting modules using RCA silicon avalanche photodiodes" *Electronic Engineering*, Oct. 1989, pp. 37-45
- 4 R.G.W. Brown, K.D. Ridley and J.G. Rarity "Characterization of silicon avalanche photodiodes for photon correlation measurements 1: Passive quenching" *Applied Optics*, vol. 25 no. 22, nov. 1986, pp. 4122-4126
- 5 R.G.W. Brown, R. Jones, J.G. Rarity and K.D. Ridley "Characterization of silicon avalanche photodiodes for photon correlation measurements 2: Active quenching" *Applied Optics*, vol 26 no. 12, jun. 1987, pp. 2383-2389
- 6 A. Sharma and J.G. Walker "Effect of deadtime in imaging detectors" *Instrumentation in Astronomy VII (1990)*, SPIE Vol. 1235, 1990, pp. 474-481

EXPLOITING A COULOMETRICALLY OBTAINED ACID-BASE TITRATION CURVE FOR AUTOMATED ACID CONCENTRATION DETERMINATION

J. Hendrikse, F. Pierdominici, W. Olthuis, P. Bergveld
 MESA Research Institute, University of Twente
 P.O. Box 217, 7500 AE Enschede, The Netherlands
 email: J.Hendrikse@el.utwente.nl

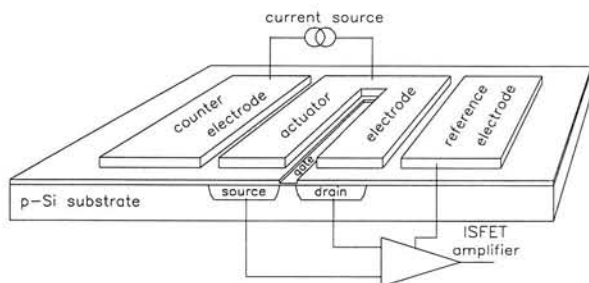
Abstract

The concentration of acids or bases is determined with an ISFET-based sensor-actuator device in two steps: First H^+ or OH^- ions are generated by the electrolysis of water and the resulting pH change is measured as a function of time. Then a part of the measured pH-time curve is fitted to an equation derived from a two-dimensional model describing the diffusion from the actuator to the sensor. It is shown that the concentration of strong acids and bases can thus be experimentally determined with an error of less than 5% when the concentration is between 1 and 30 mM. The whole procedure takes place in less than twenty seconds and can be automated easily.

1 Introduction

On-line determination of the concentration of acids and bases is required in a variety of production processes, but will only be useful if at least the following conditions are met:

1. The determination is fast and can be automated.
2. The measuring device can be miniaturised.
3. No knowledge about the specimen is needed beforehand.



Coulometric acid to base titration devices using the Ion Sensitive Field Effect Transistor (ISFET) as a sensor and a platinum film deposited around the ISFET-gate acting as a coulometric H^+/OH^- actuator were described by Olthuis in [1] (Fig. 1)

Fig. 1 Impression of the coulometric sensor actuator system

A constant flux of OH^- ions is generated coulometrically at the actuator surface, titrating the sample near the actuator and sensor. Originally, only the end point of the completely recorded titration curve was used to determine the acid concentration, a method well known from classical titrations. This method meets the first two conditions, but not the third one, since either the diffusion coefficient of the acid has to be known in advance or a calibration curve has to be made. In this paper we introduce a new approach that enables us to determine the concentration of both strong acids and bases by one measurement only, without the need of prior knowledge of the acid diffusion coefficient.

2 Theory

2a The pH change at the sensor surface

In a solution having a pH below 4 the concentration of the OH^- ions is negligible. When from $t=t_0$ until $t=t_0 + dt_0$ a concentration q [$\text{mol}/\text{m}^3\text{s}$] of OH^- ions is continually released from a volume $dx_0 dy_0 dz_0$ at $x=x_0, y=y_0, z=z_0$, the concentration of protons at a point (x, y, z) is described by subtracting Green's function $G(x-x_0, y-y_0, z-z_0)$ from the original proton concentration C_0 [2]:

$$C_{H^+}(x, y, z, t) = C_0 - G = C_0 - \frac{q dx_0 dy_0 dz_0 dt_0}{8(\pi D(t-t_0))^{3/2}} \exp\left(-\frac{(x-x_0)^2 + (y-y_0)^2 + (z-z_0)^2}{4D(t-t_0)}\right) \quad (1)$$

where D is the proton diffusion coefficient. In order to describe the temporal change of the proton concentration at the sensor surface at $(0, 0, z)$ by diffusion from the actuator plates, Green's function has to be integrated over the surface of the electrodes and in time (Fig. 2):

$$C_{H^+}(0, 0, z, t) = C_0 - 2 \int_{t=0}^t \int_{y=d}^{\infty} \int_{z=-\infty}^{\infty} G - 2 \int_{t=0}^t \int_{y=-\infty}^{-d} \int_{z=-\infty}^{\infty} G \quad (2)$$

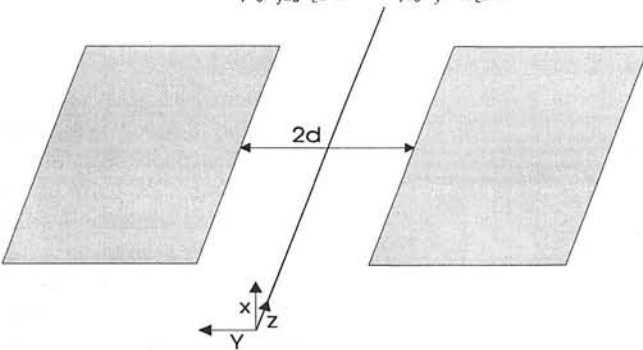


Fig. 2 Geometry used in the sensor-actuator model. The actuator surface (grey area) is assumed to be infinitely wide in the y and z directions. The pH-sensor is placed at the z -axis and has zero width.

The factor of two in equation 2 is caused by the inability of ions to diffuse out of the backside of the surface. It can be shown that:

$$C_{H^+}(0,0,z,t) = C_0 - \frac{q dx_0}{\pi D} \left(2\sqrt{\pi D t} \operatorname{erfc} \frac{d}{2\sqrt{D t}} - d \operatorname{Ei} \left(1, \frac{d^2}{4 D t} \right) \right) \quad (3)$$

where $q dx_0$ [mol/m² s] is the surface concentration released from the surface and $\operatorname{Ei}(1,n)$ is known as the exponential integral, which is equal to $\int_1^{\infty} \frac{e^{-nt}}{t} dt$.

2b Processing of the experimental data and fitting

The experimental data must be translated and scaled to enable a fit to equation 3. The ISFET amplifier output voltage V_{ISFET} depends linearly on the pH; $V_{\text{ISFET}} = a - b \log[\gamma H^+]$. Assuming a constant proton activity coefficient γ due to the large amount of background electrolyte, both the factor a and the activity coefficient cancel when the signal is normalised with respect to $V_{\text{ISFET}}(t=0) = V_0$. Thus we obtain:

$$\frac{C_{H^+}(t)}{C_0} = 1 - 10^{\frac{V - V_0}{b}} \quad (4)$$

In order to use equation 3 as a fitting formula, both sides are divided by C_0 and its series expansion is taken around $d/2\sqrt{D t} = 0$. The equation then is fitted to the measured data using $q/\pi d C_0$ and $d/4\sqrt{D}$ as fitting parameters. As q and d are known, both the value of C_0 and D are obtained as a result of the fit.

3 Experimental

Chemicals. Solutions of 2-10 mM HNO₃ in 1M KNO₃ were made by dilution of a (1±0.0025)M HNO₃ solution with a 1M KNO₃ solution. Demineralised water was used and all chemicals used were of analytical grade (Merck).

Equipment. The measuring device is shown in Fig 1, the measurement set-up is shown in Fig. 3. For the data acquisition we used the data retrieval program ASYST™.

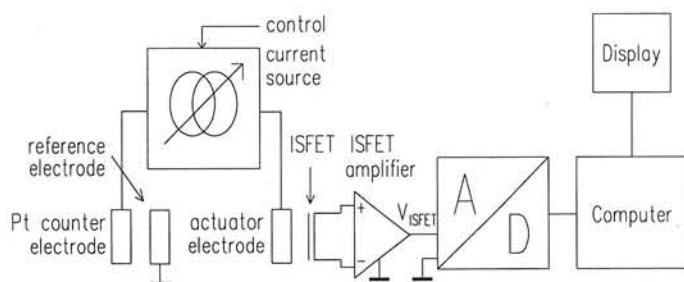


Fig 3
Measurement set-up

The ISFET pH-sensitivity was obtained by measuring the ISFET signal in Radiometer buffers with pH 4.01 and 7.00 and was found to be -58.4 mV/pH at room temperature.

4 Results and discussion

A constant current density of 50 A/m^2 ($q=0.52 \text{ mmol/m}^2\text{s}$) was applied between the actuator and the counter electrode. The ISFET signal, V_{ISFET} , was recorded for four seconds in HNO_3 solutions of different concentration at room temperature. This signal was processed using equation 4 and fitted to the series expansion of equation 3 using the Levenberg-Marquardt algorithm implemented in Slide Write[®] Plus. An example of the transformed signal measured in 5mM HNO_3 and the fit are shown in Fig 4. Note that for short times the fit fails due to the limited range in which the series expansion is valid, and that for longer times it fails because hydroxyl ion diffusion becomes significant. For this reason, only the part of the curve between $t=0.5 \text{ sec}$ and $C/C_0 = 0.4$ is fitted. It was shown that the quality of the fit did not depend on the number of points when at least three were used. When a fitting algorithm using three points was implemented in ASYST[™], the measurement and fitting procedure took less than twenty seconds. Fig 5 shows the acid concentration we found as a function of the actual acid concentration. The regression line shows that we have a good linear response but we have a small systematic error of 0.244 mM , possibly caused by oversimplifications in the model.

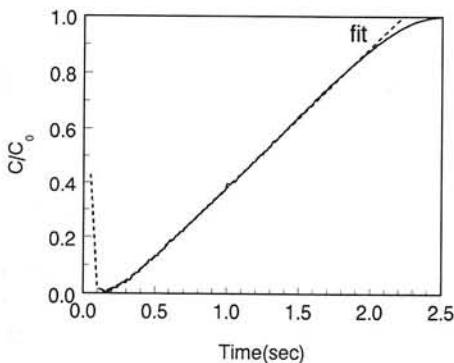


Fig. 4 Measurement in 5mM HNO_3 fitted with the series expansion of eq. 3

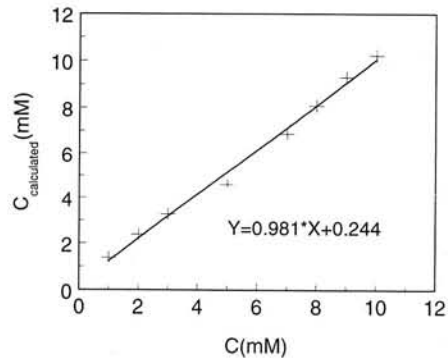


Fig. 5 Calculated acid concentration as a function of the actual concentration

5 Conclusions

We made a small device that is successful in fast and automated acid titrations. No prior knowledge of the sample solution is needed. By this method we can calculate both the diffusion coefficient and the concentration of the acid. Since only a small part of the titration curve is needed the pH change is limited to less than a decade, which is favourable for future use in biosensors.

- [1] W. Olthuis and P. Bergveld, Integrated coulometric sensor actuator devices, Mikrochim. Acta 121, 191-223 (1995).
- [2] H.S. Carslaw and J.C. Jaeger, Conduction of heat in solids, Chapter 10, Clarendon Press 1959

Bragg-reflector used as integrated chemo-optical sensor

G.J. Veldhuis, J.H. Berends, R.G. Heideman and P.V. Lambeck

MESA Research Institute, University of Twente
P.O.Box 217, 7500 AE Enschede, The Netherlands
e-mail: G.J.Veldhuis@el.utwente.nl

Abstract. This paper describes the use of an integrated optical Bragg-reflector as a chemo-optical sensor. It is shown that Bragg-reflectors for a wavelength of 630nm can be realised with a bandwidth smaller than 0.2nm in a $\text{Si}_3\text{N}_4/\text{SiO}_2$ optical waveguide. Measurements show that a refractive index change of the waveguide cladding of $dn_{c,\min}=2 \times 10^{-5}$ can be detected.

I. Introduction

The use of integrated optical devices for chemical sensing has several advantages [1], such as their high sensitivities and small weight and size. Furthermore, there is no electro-magnetic interference and remote sensing in harsh environments is possible using optical fibers. Finally, large sensor families can be created, whose individual members only differ by the applied chemo-optical transduction layer.

So far several types of integrated chemo-optical sensors have been investigated. Among them are the Mach-Zehnder interferometer [2], the surface plasmon sensor [3,4] and the grating in/output coupler [5]. In this paper we will concentrate on the use of a Bragg-reflector as a chemo-optical sensor. In contrast with the grating output coupler, where the light is coupled out of the waveguide into free space, the use of a grating as a Bragg-reflector, allows for all beams propagation inside the planar system. The sensor principle will be explained, the fabrication process of a Bragg-reflector in $\text{Si}_3\text{N}_4/\text{SiO}_2$ will be described and measurements on the sensor sensitivity will be presented.

II. Sensor principle

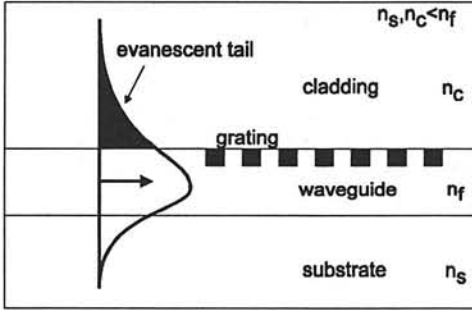
We will focus on a transduction layer which converts a change in analyte concentration into a refractive index change. If such a layer is applied on top of an optical waveguide, a change of the refractive index of this cladding layer will be felt by the evanescent tail of the guided optical field (see fig. 1a). This will result in a change in the effective refractive index, N , of the waveguide (N is a measure for the light velocity in the waveguide).

A Bragg-reflector is used to convert the change in effective refractive index of the waveguide into a shift in the reflection wavelength; a quantity which is easy detectable. In a Bragg-reflector, which is basically a periodic disturbance in a waveguide (see fig. 1a), a sinc-

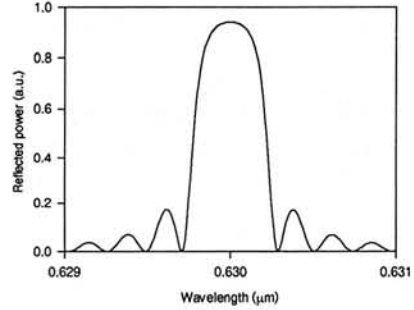
type behaviour of the reflected light is observed (see fig. 1b). The central wavelength, λ_0 , obeys the phase match condition

$$\Lambda = \frac{\lambda_0}{2N} \quad (1)$$

where Λ is the period of the grating. It is clear that (since the period is fixed) a change in N will result in a change in λ_0 .



a



b

Figure 1. (a) Schematic representation of the optical field in a waveguide with a grating. The evanescent tail penetrates the cladding. (b) Typical reflection spectrum for a Bragg-reflector.

The wavelength shift, $d\lambda$, resulting from a change in the refractive index of the cladding, dn_c , can be expressed as

$$d\lambda = \frac{\partial \lambda}{\partial N} \cdot \frac{\partial N}{\partial n_c} \cdot dn_c \quad (2)$$

In order to obtain a large wavelength shift, the two partial sensitivities need to be optimised. From the phase-match condition we can find

$$\frac{\partial \lambda}{\partial N} = \frac{\lambda_0}{N} = 2\Lambda \quad (3)$$

This means that for given central wavelength the effective refractive index of the sensing waveguide needs to be minimised. It can be shown [5] that for $n_c < n_s$, $\delta N / \delta n_c$ can be optimised by taking the difference $n_f - n_c$ as large as possible, while a waveguide thickness of approximately twice the cut-off thickness of the guided mode should be chosen. This last requirement will also result in a low value for N , which means that both partial sensitivities can be optimised at the same time.

The minimum shift in wavelength that can be detected, is strongly determined by the bandwidth of the reflection peak, $\Delta\lambda_{FWHM}$. Assuming that a wavelength shift of one bandwidth can be detected in Γ steps, the minimum detectable refractive index change, $dn_{c,min}$, can now be expressed as

$$dn_{c,min} = \frac{\Delta\lambda_{FWHM}}{\Gamma \cdot 2\Lambda} \cdot \left(\frac{\partial N}{\partial n_c} \right)^{-1} \quad (4)$$

III. Device fabrication

As a demonstrator we will concentrate on a sensor for measuring ethanol ($n=1.36$) concentrations in water ($n=1.33$). A cross-section of the used (channel) waveguide configuration, parallel to the propagation direction, is shown in figure 2. First a LPCVD Si_3N_4 waveguiding layer was deposited on a thermally oxidised silicon wafer. Then a $2.5\mu\text{m}$ wide channel waveguide was defined by etching a 2nm ridge in the waveguiding layer using a $\text{HF}:\text{NH}_4\text{F}=1:7$ etch liquid. The grating period was defined by holographic exposure [6] of a 60nm thick layer of photoresist. The pattern was transferred into the waveguide by exposing the system to an O_2 -plasma. In the short time it takes the plasma to remove the resist, it also introduces a very small disturbance by periodically oxidising the surface of the Si_3N_4 layer. Finally the waveguide was cladded with a PECVD deposited SiO_2 layer which was removed in the sensing area by the etch liquid mentioned before.

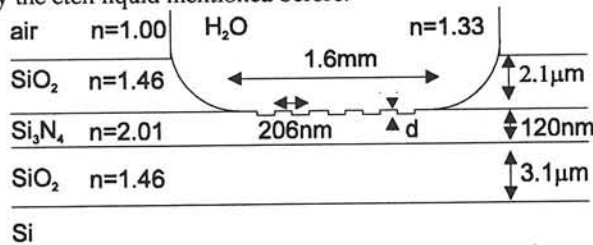


Figure 2. Cross-section of the used waveguide configuration.

The thickness of the waveguide was chosen to optimise $\delta N/\delta n_c$ for TM-polarised light at $\lambda_0=630\text{nm}$. The calculated partial sensitivity [5] is $(\delta N/\delta n_c)_{\text{TM}}=0.27$. For TE-polarisation we find $\lambda_0=670\text{nm}$ and $(\delta N/\delta n_c)_{\text{TE}}=0.15$.

IV. Experimental results

The Bragg-reflector was characterised using a dye laser tuneable between $620\text{nm}<\lambda<680\text{nm}$ with 0.03nm steps. The laser bandwidth is $\Delta\lambda=0.2\text{nm}$. Figure 3a shows the reflection spectra for TE-polarisation when the sensor is exposed to different mixtures of water and ethanol. The refractive indices of the mixtures were measured with an Abbe-refractometer for $\lambda=589\text{nm}$. The measured bandwidth is 0.2nm which is the same as that of the laser. This means that the bandwidth of the Bragg-reflector is smaller, $\Delta\lambda_{\text{FWHM}}<0.2\text{nm}$. It also explains the absence of a sinc-type behaviour. This extremely small bandwidth, is the result of the new method of grating implementation, that we have developed.

The relation between the reflection wavelength and the refractive index of the cladding is shown in figure 3b. From a least square fit on the measured data, $(\delta N/\delta n_c)_{\text{TE}}=0.17$ was found. For TM-polarisation $(\delta N/\delta n_c)_{\text{TM}}=0.24$. These values agree very well with the theoretical sensitivities. The large error bars are mainly caused by the temperature dependence of the refractive index of water and ethanol. The temperature dependence of the grating itself was measured to be $\delta\lambda/\delta T=0.01\text{nm}/^\circ\text{C}$.

When a mono-mode tuneable semi-conductor laser is used, a conservative estimate of the number of steps in which a shift of one bandwidth of the reflector can be detected is $\Gamma=100$,

provided the system is stabilised for temperature changes. Substituting the measured data in equation 4, the minimal detectable refractive index change of the cladding can be calculated to be $dn_{c,\min}=2\times 10^{-5}$. This is equivalent to a fraction of 0.02% sucrose in an aqueous solution [7]. Work is in progress for developing a detection scheme, where the tuneable laser can be replaced by a cheaper broadband light source.

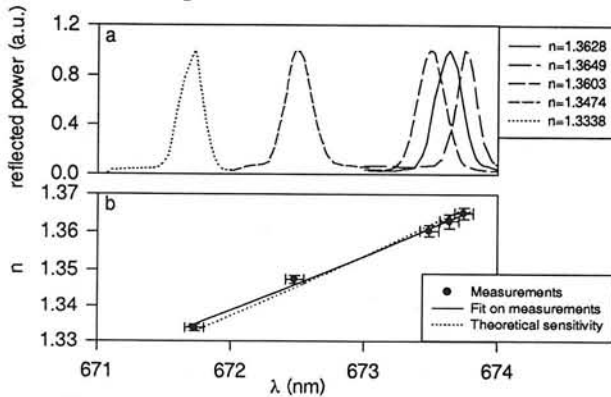


Figure 3. (a) Reflection spectra measured for different water-ethanol mixtures. (b) Measured relation between the reflection wavelength and the refractive index of the cladding. Also the theoretical sensitivity curve is shown.

V. Conclusion

A Bragg-reflector for a wavelength of 630nm was realised with a bandwidth smaller than 0.2nm in a $\text{Si}_3\text{N}_4/\text{SiO}_2$ optical waveguide. Furthermore it was shown that a refractive index change of the waveguide cladding of $dn_{c,\min}=2\times 10^{-5}$ can be detected. This makes the Bragg-reflector a suitable candidate for chemo-optical sensing. The specific sensitivity can be adjusted by selecting an appropriate transduction layer for the cladding.

Acknowledgements

The authors would like to thank Folkert Horst for his work on the holographic exposure technique and Toon Andringa and Lucie Hilderink for cleanroom assistance.

References

- [1] P.V. Lambeck, Sensors and Actuators B, 10 (1993) 209.
- [2] R.G. Heideman et al., Sensors and Actuators B, 8 (1992) 103.
- [3] B. Liedberg et al., Sensors and Actuators, 4 (1983) 299.
- [4] J. van Gent et al., Applied Optics, 29 (1990) 2843.
- [5] K. Tiefenthaler and W. Lukosz, J. Opt. Soc. Am. B, 6 (1989) 209.
- [6] X. Mai et al., Applied Optics, 24 (1985) 3155.
- [7] CRC Handbook of Chemistry and Physics, editor R.C. Weast, 53ed., (1972).

ACID-BASE TITRATION WITH AN ISFET MICROSENSOR AS A TOOL FOR PROTEIN DETECTION

J. Kruise, J.C.T. Eijkel and P. Bergveld

MESA Research Institute, University of Twente
P.O. Box 217, 7500 AE Enschede, The Netherlands
Phone: 00-31-53-4892755; Fax: 00-31-53-4892287
E-mail: j.kruise@el.utwente.nl

ABSTRACT

Protein molecules immobilized in a membrane deposited on top of an ISFET can be detected by performing acid-base protein titrations. Model simulations show a linear relation between titration time and immobilized protein concentration in the membrane. Experimental results of two different titration methods show a clear dependence of the titration curve on the incubation time in a protein solution.

INTRODUCTION

ISFET-based biosensors that can determine protein concentration have been extensively studied throughout the past decades. The acid-base behaviour of a protein is one of the properties that can be further exploited in ISFET-based protein sensors, by performing acid-base protein titrations.

After deposition of a membrane in which protein molecules can be bound, an ISFET-based coulometric sensor-actuator device can be used for this purpose. A device without a membrane was used for the measurement of acid or base concentrations by titration [1] and, after adding a porous gold actuator electrode, for the determination of protein buffer capacity [2]. Titrant is generated coulometrically by sending a current between the actuator electrode, deposited closely around the ISFET gate, and a distant counter electrode. The titrant causes a local change in the pH, which can easily be measured by the ISFET. The measured pH as a function of time results in a titration curve. We define the time needed to reach pH=7 at the ISFET surface as t_{pH7} .

As a second, more conventional method for titrant generation a step-wise change in pH can be applied at the membrane-electrolyte interface, after mounting the ISFET in a flow-through system. After a pH step from pH=4 to 10, hydroxyl ions will diffuse towards the ISFET, whereas protons will diffuse in the opposite direction. The pH at the ISFET surface will slowly change from pH=4 to 10. Again, we define t_{pH7} as the time needed to reach pH=7 at the ISFET surface.

By using a simulation model, for both titration methods the relation between protein

concentration in the membrane and t_{pH7} is obtained. Measurements that show the dependence of t_{pH7} on incubation time in a protein solution are presented.

MODEL DESCRIPTION

A one-dimensional model based on the Nernst-Planck and Poisson equations [7], in which all the acid-base reactions occurring in the membrane are taken into account, has been used to describe the titration process. Model simulations for both titration methods result in a linear relation between t_{pH7} and the concentration of lysozyme in the membrane, as shown in fig. 1. This linear relation may be understood by making use of a modified form of Fick's second law of diffusion [3], that describes the first part of our coulometric titration until the time at which the pH=7 at the actuator electrode, defined as t_a .

$$\frac{\partial c_{H^+}^m(x, t)}{\partial t} = D_{H^+}^m \cdot \frac{\partial^2 c_{H^+}^m(x, t)}{\partial x^2} - \frac{\partial c_{HProt}^m}{\partial t} \quad (1)$$

where $c_{H^+}^m$ is the concentration of mobile protons in the membrane, $D_{H^+}^m$ is the diffusion coefficient of these protons and c_{HProt}^m is the concentration of undissociated protein groups.

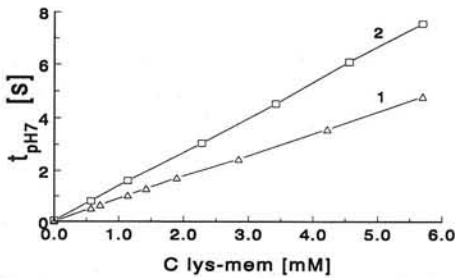


Fig. 1 Simulated t_{pH7} as a function of the lysozyme concentration in the membrane for (1) the coulometric titration and (2) the pH-step titration

According to eqn. 1, the change in the proton concentration at a location x in the membrane is a function of both diffusion (first term on the right-hand side) and dissociation reactions of protons with immobile protein groups (second term on the right-hand side). These immobile protein groups should be regarded as an extra source of protons. Our model simulations show that the proton concentration profile at $t=t_a$, and thus the depleted volume in the membrane is independent of protein concentration. Consequently, the time needed to deplete this fixed volume depends linearly on the total amount of protons in it. Since the amount of immobile protons is large compared to the concentration of mobile protons (at least several mM compared to 0.1 mM), a linear relation between t_a and the number of protein groups is found. The same line of reasoning can be followed for $t_a \leq t \leq t_{pH7}$ and for the pH-step method, resulting in a linear relation between t_{pH7} and the protein concentration. It should be noted that this linear relation could not be verified experimentally, since the concentration of immobilized protein in the membrane is a function of the incubation time in a protein solution via a complex adsorption process that is not included in the simulation model.

EXPERIMENTAL

ISFETs with a Ta₂O₅ gate insulator, having a sensitivity of 58.5 mV/pH, and a platinum actuator electrode deposited around the gate were fabricated in the MESA cleanroom following the usual processing steps. With a polyimide mask an active actuator area of 1 mm² was defined. After mounting the chips on a piece of printed circuit board, they were encapsulated using hysol epoxy, leaving a circular area around the gate with a diameter of 1.7 mm and a depth of 150 μm uncovered. Polystyrene beads/agarose membranes, with a

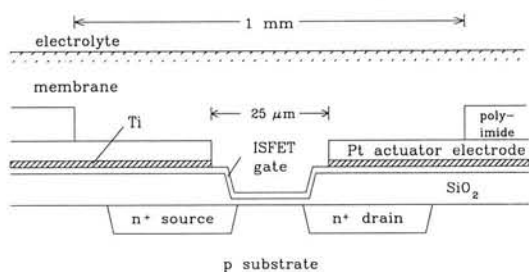


Fig. 2 Cross-section of the measuring device with actuator electrode deposited around the ISFET gate and the membrane covering both.

performed in an unbuffered 1M KNO_3 solution of $\text{pH}=4.0$, in order to avoid migration effects. After inserting the ISFET in the measurement solution, we waited 2 min. before starting the titration, in order to minimize convection. A current of $10 \mu\text{A}/\text{mm}^2$ was sent between the actuator and the counter electrode at $t=0$ for 10 to 25 sec.

For the pH -step measurements, the device is mounted in the wall-jet cell of a flow-through system. The liquid flow (5 ml/min) is perpendicular to the ISFET surface [6]. The pH -step can be applied in 0.1 s. All experiments were performed in 1 M KNO_3 , using HNO_3 and KOH to adjust the pH to respectively 4.0 and 10.0. After mounting the devices in the wall-jet cell, they were rinsed with the $\text{pH}=4$ solution for 3 min., before the pH step was applied. The ISFET response, measured with a source-drain follower, was recorded with a Nicolet 310 digital oscilloscope.

RESULTS AND DISCUSSION

Fig. 3a shows typical titration curves, as a function of the cumulative incubation time in a 0.5 mg/ml ($3 \cdot 10^{-5}$ M) lysozyme solution. A time shift of the titration curves, resulting in a clear dependence of $t_{\text{pH}7}$ (intersection with dashed line) on the incubation time in a lysozyme solution is found. The value $t_{\text{pH}7}=9.0$ s. before incubation (curve 1) indicates that the bare membrane already contains a large amount of proton-dissociating groups.

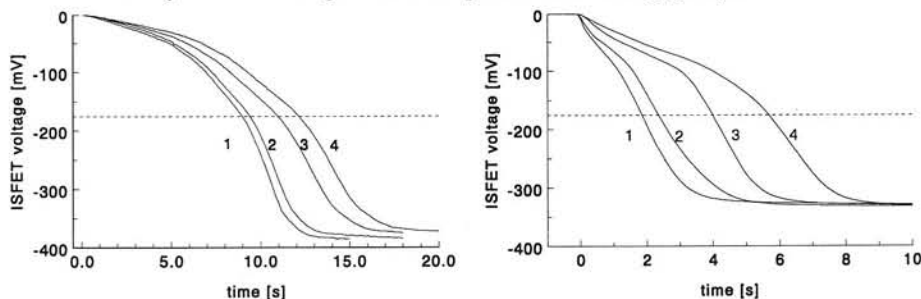


Fig. 3 Typical titration curves (a) measured with coulometric sensor-actuator device: before incubation (1), after 5 min. (2), 35 min. (3), and 95 min. (4) of incubation in a 0.5 mg/ml lysozyme solution. (b) measured with the pH -step method: before incubation (1), after 1 min. (2), 6 min. (3) and 21 min. (4) of incubation in a 0.5 mg/ml lysozyme solution. The dashed lines indicate the ISFET voltage at $\text{pH}=7.0$.

thickness of about $8 \mu\text{m}$ were casted in this area [4]. Fig. 2 shows a cross-section of this measuring device. Lysozyme (from chicken egg white, Sigma) was adsorbed in the membrane by incubation in a solution containing 0.5 or 5 mg/ml lysozyme in 100 mM KNO_3 , $\text{pH}=7.4$. After each incubation step the devices were rinsed for one minute.

The measurement set-up for the coulometric titrations is described elsewhere [5]. All measurements were

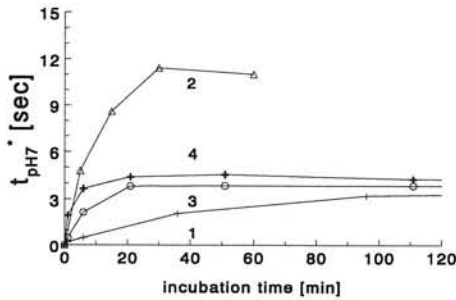


Fig. 4 t_{pH7}^* as a function of the cumulative incubation time for coulometric titration: (1) 0.5 and (2) 5 mg/ml and for pH-step titration: (3) 0.5 and (4) 5 mg/ml lysozyme.

by simulations (fig. 1). Using the linear relation between t_{pH7} and the protein concentration in the membrane found by simulations, the curves in fig. 4 clearly reflect the shape of adsorption isotherms.

CONCLUSIONS

Protein can be detected by means of acid-base titrations, after immobilization in a membrane. Model simulations show a linear relation between t_{pH7} , the time at which pH=7 is reached at the ISFET surface, and the immobilized protein concentration. With two different titration methods a clear dependence of t_{pH7} on the incubation time in solutions containing 0.5 and 5.0 mg/ml lysozyme is found. Using the simulation results, this dependence clearly reflects the shape of an adsorption isotherm.

ACKNOWLEDGEMENT

The authors thank Johan Bomer for the realization and encapsulation of the ISFET devices

REFERENCES

- [1] W. Olthuis, J. Luo, B.H. v.d. Schoot, P. Bergveld, M. Bos and W.E. v.d. Linden, Modelling of non-steady-state concentration profiles at ISFET-based coulometric sensor-actuator systems, *Anal. Chim. Acta.*, 229 (1990) 71-81.
- [2] W. Olthuis, J. Luo and P. Bergveld, Characterization of proteins by means of their buffer capacity, measured with an ISFET-based coulometric sensor-actuator system, *Biosensors & Bioelectronics*, 9 (1994) 743-751.
- [3] J. Crank, *The mathematics of diffusion*, Oxford University Press, London, 1975.
- [4] R.B.M. Schasfoort, R.P.H. Kooyman, P. Bergveld and J. Greve, A new approach to ImmonoFET operation, *Biosensors & Bioelectronics*, 5 (1990), 103-124.
- [5] W. Olthuis and P. Bergveld, Simplified design of the coulometric sensor-actuator system by the application of a time-dependent actuator current, *Sensors and Actuators B*, 7 (1992) 479-483.
- [6] J.C. van Kerkhof, P. Bergveld and R.B.M. Schasfoort, The ISFET based heparin sensor with a monolayer of protamine as affinity ligand, *Biosensors & Bioelectronics* 10 (1995) 269-282.
- [7] J.C.T. Eijkel, Potentiometric detection and characterization of adsorbed protein using stimulus-response measurement techniques, Thesis University of Twente, Enschede, The Netherlands, ISBN 90-9008615-3 (1995).

Typical results of pH-step protein titrations are shown in fig. 3b. Again a clear dependence of t_{pH7} on the incubation time in a lysozyme solution could be measured. Also here, curve 1 shows an offset in t_{pH7} (1.85s.) for the titration of the bare membrane.

Fig. 4 shows the titration results of both methods for incubation in 0.5 and 5.0 mg/ml lysozyme solutions. It shows t_{pH7}^* , being the measured t_{pH7} minus t_{pH7} of the bare membrane, as a function of the cumulative incubation time. It should be noted that the order of magnitude of the measured t_{pH7}^* values corresponds well with the values found

Detection of Staphylococcal Enterotoxin B employing a piezoelectric crystal immunosensor

by:

J.L.N. Harteveld, M.S. Nieuwenhuizen, and E.R.J. Wils
TNO Prins Maurits Laboratory
P.O. Box 45, 2280 AA Rijswijk, The Netherlands

ABSTRACT

There is a lack of modern biochemical sensors capable of real-time monitoring of biological warfare agents and related substances. The present family of detection equipment is rather slow, heavy and expensive and needs a lot of manpower for sampling, analysis and servicing. General requirements for this type of sensors are: high sensitivity, short response times and high selectivity resulting in low false alarm rates. This paper reports on a study concerning a biochemical sensor for Staphylococcal Enterotoxin B (SEB), a representative of a biological warfare agent.

A 20 MHz piezoelectric quartz crystal sensor device was employed in a flow injection system. The assay for SEB is based on a competition scheme. A detection limit of 0.1 $\mu\text{g/ml}$ is obtained, whereas at concentrations of SEB of 10 $\mu\text{g/ml}$ or higher the sensor response is completely inhibited.

1. INTRODUCTION

Biochemical sensors are measuring devices that transduce (bio)chemical signals into the appropriate electrical signals. There is a lack of modern biochemical sensors capable of real-time monitoring of biological warfare agents and related compounds. General requirements for this type of sensors are: high sensitivity, short response times and selectivity resulting in low false alarm rates. In addition, small size, light weight, ruggedness, long shelf life, long operational life and low cost are important. The present family of detection equipment is rather slow, heavy and expensive.

Biochemical sensors incorporate a biologically active sensing material: the biochemical interface, which interacts with the analyte as selectively as possible. For the biochemical interface, one can make use of either the selectivity of molecular biological systems such as enzymes, antibodies, DNA probes and receptors, or of integral biological systems such as a bacterium, an organelle or even a piece of an organism.

This paper reports on a study concerning a piezoelectric crystal sensor for a representative of a biological warfare agent: the toxin Staphylococcal Enterotoxin B (SEB). SEB is one of the toxins produced by the bacterium *Staphylococcus Aureus* and is known to cause food poisoning. Piezoelectric crystal sensors are simple to operate and because the sensor can be integrated with the signal transducing electronics on a single chip, they can be made at low cost.

The current literature includes a number of papers dealing with piezoelectric crystal biochemical sensors employing antibodies or antigens as the biochemical interface, some of which are dealing with the detection of pathogenic micro-organisms like viruses such as HIV (Aberl et al., 1994) or herpes (König & Grätzel, 1991) or bacteria such as *Escherichia Coli* (He et al., 1994). Only a few papers report on the detection of potential biological warfare agents with a piezoelectric crystal biochemical sensor. *Staphylococcus Aureus* was detected with a piezoelectric crystal sensor using antibodies (Le et al., 1995) and with the same kind of sensor in which one electrode was separated from the quartz disc measuring living bacteria. (He et al., 1995). *Vibrio Cholera* bacterium was detected with an antibody based piezoelectric crystal sensor (Carter et al. 1995). The same approach was used for ricin and goat anti-ricin antibody (Carter et al., 1995).

2. MATERIALS AND METHODS

2.1. Reagents

Affinity purified rabbit anti-SEB, lot 395BI, cat. no. LBI202 was obtained from Toxin Tech. Inc. Sarasota Florida (USA). SEB toxin, batch 16137, cat. no. 0734, was obtained from Makor Chemicals ltd. Jerusalem (Israel). Bovine serum albumine (BSA) was obtained from Sigma Chemie (Belgium). Phosphate Buffered Saline (PBS) was home made at pH 7.2. Anti-Rabbit-PO was obtained from Boehringer Mannheim Biochemica, product no. 1238850.

2.2. Sensor test system

The piezoelectric crystals are 20 MHz AT-cut quartz plates sandwiched between two gold electrodes obtained from Quarzkeramik, Stockdorf (Germany). The oscillator was purchased from Fraunhofer Gesellschaft-Institut für Festkörper Technologie (Germany). The frequency output of the oscillator was measured with a Hewlett Packard 5334B universal counter. The counter was connected to a Personal Computer via an IO-tech IEEE data acquisition board. Data were acquired, displayed real time in a plot on the computer screen and stored on disk. The experiments were performed in a flow through system. A pulse free flow was delivered by a Harvard 22 Syringe pump (Massachusetts, USA). Samples were injected through a six way valve and a sample loop of 40 μ l. The experimental set-up is pictured in Figure 1.

2.3. Sensor experiments

A new 20 MHz crystal was cleaned with hot methanol in a Soxhlet apparatus for about 20 minutes followed by mounting the crystal on the lower part of the flow cell (Figure 1). The electrical connections to the pins of the oscillator were made using conducting glue (Elecolit). A 5 μ l solution containing 1 mg/ml SEB was pipetted on the sensor surface. After one hour the upper part of the cell was connected and a flow rate of 25 μ l/min was adjusted. The carrier buffer was PBS containing 1% BSA to minimize unspecific effects.

The competition assay was performed as follows:

50 μ l of a solution of 100 μ g/ml anti-SEB was mixed with 50 μ l SEB solutions of different concentrations and incubated for twenty minutes. Hereafter the sample loop was flushed with the mixture (100 μ l) followed by injection of the sample. For the zero concentration of SEB

50 μl of the 100 $\mu\text{g}/\text{ml}$ anti-SEB solution was mixed with 50 μl buffer solution. The response of this solution was set to 100%.

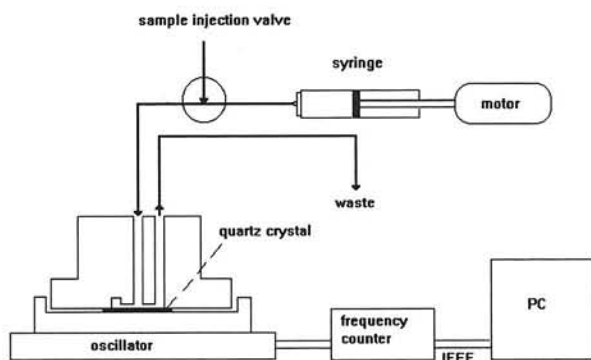


Figure 1: Experimental setup

3. RESULTS AND DISCUSSION

Preliminary experiments were carried out using a static measuring system testing the possible immune responses of the combination of SEB and antibodies on the sensor surface. No responses were obtained when antibodies were coated on the surface followed by addition of SEB. However the reverse approach demonstrated that immune responses were possible. Further experiments were performed in a flow injection system, in which SEB was detected by means of a competition assay. SEB was immobilized on the sensor surface by physical adsorption. Polyclonal antibodies were allowed to react with SEB in solution whereafter the remaining antibodies were allowed to bind to SEB on the sensor surface. The sensor response is thus inversely proportional to the concentration of SEB in solution.

To verify the sensor experiments an Enzyme Linked Immunosorbent Assay (ELISA) was performed using the same competition scheme.

In Figure 2 the normalised responses of both the ELISA and the sensor experiments are plotted on the Y-axis. The normalised response is the response of a certain sample divided by that of pure anti-SEB. At concentrations of SEB of 10 $\mu\text{g}/\text{ml}$ or higher the sensor response is completely inhibited meaning that all antibodies are bound to SEB in solution. The ELISA shows a somewhat smaller dynamic range. The detection limit of the sensor amounts to approximately 0.1 $\mu\text{g}/\text{ml}$ where the inhibition of the sensor response is in the order of 10 %.

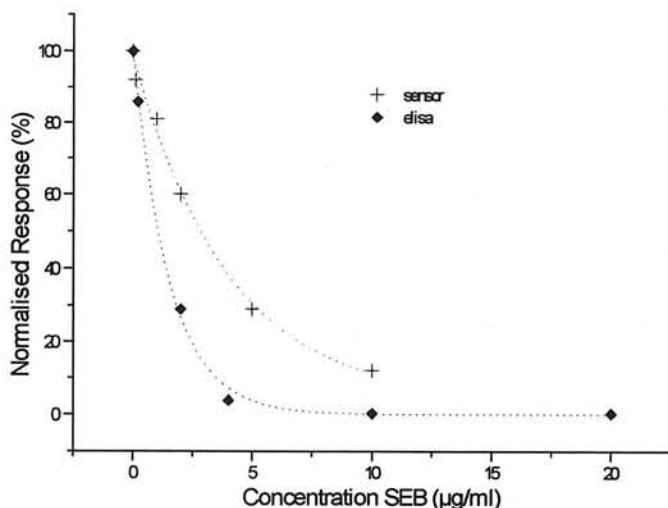


Figure 2: Response curves for the biosensor assay and ELISA of SEB

5. REFERENCES

- Aberl, F., Wolf, H., Koesslinger, C., Drost, S., Woias, P., & Koch, S. (1994). HIV serology using piezoelectric immunosensors. *Sensors and Actuators* **B18**, 271-275.
- Carter R.M., Jacobs, M.B., Lubrano, G.J. and Guilbault, G.G.(1995). Piezoelectric detection of ricin and affinity purified goat anti-ricin antibody. *Anal. Lett.*, **28**(8), 1379-1386.
- Carter, R.M., Mekalanos, J.J., Jacobs, M.B., Lubrano, G.J., Guilbault, G.G.(1995). Quartz crystal microbalance detection of *Vibrio Cholerae* O139 serotype. *J. Immunol. Methods* **187**, 121-125.
- He, F.J., Geng, Q., Zhu, W., Nie, L.H., Yao, S.Z. & Meifeng, C. (1994). Rapid detection of *Escherichia Coli* using a separated piezoelectric crystal sensor. *Anal. Chim. Acta* **289**, 313-319.
- He, F.J., Deng, H; Xie, Q.J; Nie, L.H; Yao, S.Z (1995). Rapid detection of *Staphylococcus Aureus* using a separated electrode piezoelectric crystal sensor. *Anal Lett.* **28**, 213-224.
- König, B. & Grätzel M. (1994). A novel immunosensor for herpes viruses. *Anal. Chem.* **66**, 341-344.
- Le, D; He, F.H; Jiang, T.J; Nie, L.H; Yao, S.Z (1995). A goat-anti-human igg modified piezoimmunosensor for *staphylococcus aureus* detection. *J. Microbiol. Methods*, **23**, 229-234.

THE INTEGRATED MACH-ZEHNDER INTERFEROMETER SENSOR FOR THE DETECTION OF BIOLOGICAL MOLECULES

E.F. Schipper¹, A.M. Brugman¹, C. Dominguez², L.M. Lechuga^{1,3},
R.P.H. Kooyman¹, J.Greve¹

¹MESA Research Institute, Department of Applied Physics, Bio-interface Group,
University of Twente, P.O. Box 217, 7500 AE Enschede (The Netherlands), Tel: [31] 53
893112, Fax: [31] 53 309549

²Centro Nacional de Microelectrónica, Campus UAB, 08193 Bellaterra Barcelona (Spain)

³Centro Nacional de Microelectrónica, Calle Serrano 144, 28006 Madrid (Spain)

ABSTRACT

We describe the realisation of a symmetric integrated channel waveguide Mach-Zehnder sensor which uses the evanescent field to detect small refractive index changes ($\Delta n_{\min} \sim 1 \cdot 10^{-4}$) near the waveguide layer surface. The feasibility of this sensor as an immunosensor detecting directly the binding of antigens to an antibody receptor surface is shown with immunobinding experiments.

INTRODUCTION

Optical evanescent wave sensors based on the Mach-Zehnder principle show a very high sensitivity for the detection of refractive index changes on the waveguide surface within the evanescent field of this waveguide. Due to this high sensitivity this type of sensors is suitable for direct detection of antigen binding to antibody receptor molecules immobilised on the waveguide surface. With a direct detection measurement the number of preparation steps in an immunoassay will decrease, and also on-line measurements will become possible.

A disadvantage of the earlier developed Mach-Zehnder sensors [1] is the 'bulky' construction, making them more complex in operation than for example SPR based evanescent wave sensors. Also the development of future multichannel sensors is impossible when this concept is used. In this paper we will demonstrate that with Si technology more integrated and, therefore, less complex Mach-Zehnder sensors can be made. The use of a channel Mach-Zehnder interferometer as a gas sensor has been demonstrated before [2,3]. It will be shown that with waveguiding channels consisting of 3 nm ridges also immunoreactions can be monitored. The device presented here could be the forerunner of a new generation of immunosensors capable of sensitive multichannel operation.

DEVICE STRUCTURE AND MANUFACTURE

The design of the Mach-Zehnder device can be seen in Fig.1. A 1.5 μm thermally oxidised SiO_2 layer with a refractive index of 1.46 is used as the lower cladding layer. On this SiO_2 layer a high index LPCVD Si_3N_4 waveguide layer with a refractive index of 2.0, and a 1.5 μm PECVD SiO_2 cladding layer with a refractive index of 1.46 is deposited. The high refractive index contrast between waveguide layer and cladding is chosen to obtain a maximum sensitivity

at a wavelength of 633 nm [4]. This is especially needed for immunosensing experiments where the average thickness of the layer grown on the surface will be smaller than 1 nm. For a TE₀ mode the highest sensitivity is found at a waveguide layer thickness of around 100 nm [1].

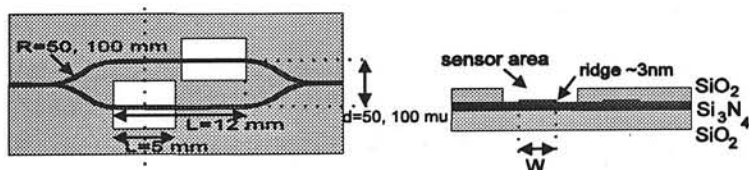


Fig. 1 The design of the integrated Mach-Zehnder sensor

The realisation of channel waveguides in this structure is not straightforward, in view of the very small ridge height of a few nm required for monomode operation. With RIE technology it turned out to be possible to make a ridge height of $\sim 3 \pm 1$ nm in the Si_3N_4 layer, as measured by atomic force microscopy. In this way (semi-monomode) waveguide channels with a width of 4.0 ± 0.5 μm could be realised.

The Y junction splitter and combiner are designed with S bend structures. In our design radii of 50 or 100 μm were used. With these bend radii no extra light losses due to the bending were observed. The total length of the Y junction splitter and combiner is kept at 30 mm. With this length the light is split in two branches that are 50 or 100 μm separated from each another. On both branches of the interferometer a sensor area is created with a length $L=5$ mm. This is done by removing the SiO_2 cladding in a HF etching step. A sensor area is created on both branches of the interferometric device to keep the optical differences between the branches as small as possible. In this way temperature drifts that normally limit the performance of a Mach-Zehnder sensor are kept small.

RESULTS AND DISCUSSION

1. Model verification

The Mach-Zehnder sensor as an immunosensor detects the binding of analyte molecules to receptor molecules immobilised on the sensor surface. The effect of the binding is comparable to a change of the bulk refractive index of the analyte medium itself [1]. Therefore, to verify the applicability of model calculations to the sensor response, the use of solutions with different bulk refractive indices is practical. To this end, solutions with different concentrations of glucose in water were used. The response of the Mach-Zehnder sensor to these solutions is measured and compared to the model expectations. The results of these measurements can be seen in Fig. 2. The line in this graph gives the theoretical response following from the slabguide model. As can be seen the measured phase change is in all situations comparable to the model calculations. This shows that the device works as prospected and that a 'simple' slab waveguide model can be used to calculate the sensitivity. This measurements also provides a calibration for immunoexperiments (see next section). The differential sensitivity $d\phi/dn$ was found to be $(1.4 \pm 0.1) \cdot 10^3 2\pi$.

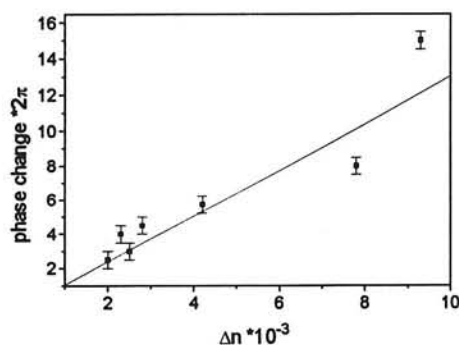


Fig. 2. Response of the Mach-Zehnder sensor as a function of bulk refractive index

2 Immunosensing experiments

According to Heideman [1] the binding of a 40 kD antigen to an antibody receptor surface, prepared by physical adsorption, results maximally in an average layer growth of ~ 0.3 nm. According to our calibration experiments this results in a phase change of $\sim 1 \cdot 2\pi$. This phase change should be detectable.

Experiments were done with human chorionic gonadotropin (hCG) as the antigen and (monoclonal) anti-hCG as the antibody. The preparation of the receptor surface is done by physical adsorption of $1 \cdot 10^{-6}$ M anti-hCG to the surface. After the preparation of the anti-hCG receptor surface the specificity of this surface for the immunosensing of hCG is tested. This is done by adding a high concentration of BSA to the surface. Adding of $1 \cdot 10^{-6}$ M BSA gives no response, as expected. After this test hCG is added in concentrations ranging from 10^{-8} to 10^{-7} M. In Fig. 4. we see the familiar binding curves, well known from previous reports. Both adding of $3 \cdot 10^{-8}$ M and subsequently $6 \cdot 10^{-8}$ M result in a response. Addition of $6 \cdot 10^{-8}$ M antigen almost saturates the receptor layer as is seen by the subsequent addition of $8 \cdot 10^{-8}$ M of antigen, where almost no response is found.

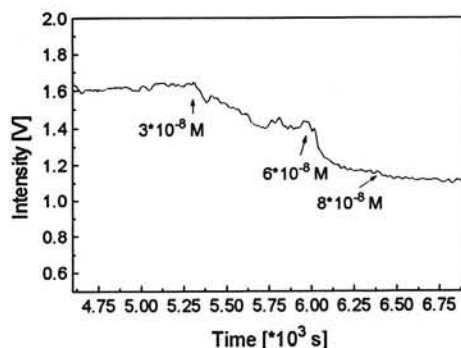


Fig. 3. Immunosensing experiment. The sensor surface is coated with anti-hCG. Before applying hCG the specificity of the surface is tested by adding $1 \cdot 10^{-6}$ M BSA. A response is seen upon adding of $3 \cdot 10^{-8}$, $6 \cdot 10^{-8}$, $8 \cdot 10^{-8}$ M hCG, respectively

These experiments show that it is feasible to use the integrated Mach-Zehnder sensor as an immunosensor for the direct detection of the binding of antigens to antibodies on the sensor surface.

CONCLUSIONS

We have demonstrated that it is possible to manufacture sensitive monomode channel waveguides by etching a small ridge of ~ 3 nm in Si_3N_4 waveguide layers. These waveguide layers have been optimized for the detection of optical changes at the waveguide layer surface. With glucose solutions with different refractive index it has been shown that the sensitivity of these devices can be calculated with a simple slab waveguide model. The feasibility of these devices as an immunosensor for the direct detection of antigens binding to an antibody receptor surface has been shown with hCG/anti-hCG measurements.

The compact and simple design of the sensor opens possibilities for future development of multi-channel devices, which are difficult to realise with slab waveguide based Mach-Zehnder sensors.

For a further improvement of the sensor a phase tuning system is desirable. Especially for the direct detection of the immunobinding of antigens to an antibody receptor surface, where the expected phase change is much smaller than 2π , fringe counting is not accurate enough. A measurement of a phase change smaller than 2π based on direct measuring the change in the intensity of the outcoupled light beam is highly non-linear and dependent on the initial phase difference between reference and signal beam. Only with a phase tuning system this problem can be solved.

LITERATURE

- [1] Performance of a highly sensitive optical Mach Zehnder interferometer immunosensor, R.G. Heideman, R.P.H. Kooyman, J. Greve, *Sensor and Actuators B* 10 209-217, 1993
- [2] N. Fabricius, G. Gauglitz, J. Ingenhoff, A gas sensor based on an integrated optical Mach-Zehnder interferometer, *Sensors and Actuators B*, 7, 672-676, 1992
- [3] A. Brandenberg, R. Edelhäuser, F. Hutter, Integrated optical gas sensors using organically modified silicates as sensitive films, *Sensors and Actuators B*, 11, 361-374, 1993
- [4] K. Tiefenthaler, W. Lukosz, Sensitivity of grating couplers as integrated-optical sensors, *J. Opt. Soc. Am. B*, 6, 209-220, 1989

DEVELOPMENT OF ON-LINE IMMUNOSENSORS FOR CORTISOL AND OTHER METABOLITES

W.A. Kaptein^{1,2}, J.J. Zwaagstra¹, K. Venema¹, M.H.J. Ruiters², J. Korf¹

University of Groningen, PO box 30.001, 9700 RB Groningen, the Netherlands

¹ Biological Psychiatry, University of Groningen, Hanzeplein 1, 9713 EZ Groningen, the Netherlands

² Biomedical Technology Centre, University of Groningen, Hanzeplein 1, 9713 EZ Groningen, the Netherlands

ABSTRACT

We describe a displacement immunosensor for the on-line detection of cortisol. The principle of the immunosensor is that cortisol displaces cortisol-HRP complex of the immobilized antibody. The cortisol-HRP can be detected on- or off-line with a colour reaction or electrochemically respectively. This displacement detection is a suitable method for on-line, *in vivo* or *ex vivo* detection of cortisol in physiological concentrations.

INTRODUCTION

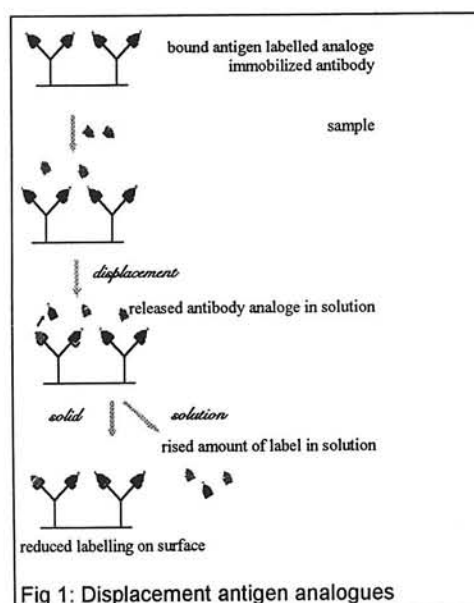
Biosensors can support biomedical research and clinical treatments. For clinical use, optimal biosensors are on-line and bed-site. Accordingly, delays caused by laboratory analysis are prevented and direct information of the parameters measured can be obtained.

For the detection of components in body fluids, it is often necessary to use immunological recognition of the component (1). Rabbany et al. (2) developed a flow immunoassay using the displacement technique for off-line analysis. Here we describe the development of an immunosensor for on-line and bed-site applications.

AIM

Our goal is to develop an immunosensor to measure on-line specific components in body fluids, either *ex-vivo* or *in-vivo*. As a

model system, we are aiming for an immunosensor for cortisol.

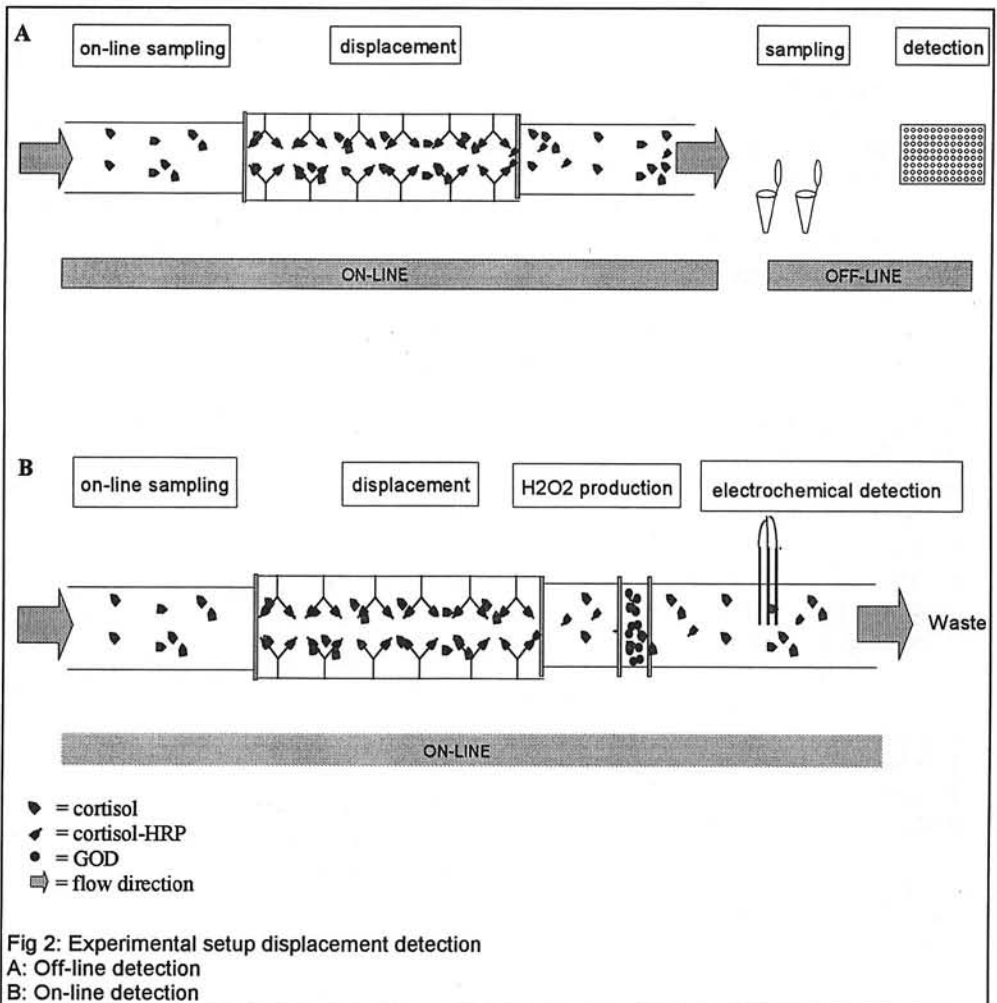


METHODS

Our cortisol immunosensor is based on a displacement detection. The displacement technique uses immobilized cortisol antibodies, saturated with a labelled analogue of the cortisol, cortisol-HRP (horse radish peroxidase). In a flow system, the cortisol-HRP will be displaced by the cortisol present in the fluid perfused, e.g. body fluids (fig 1).

The schematic structure of the off-line detection are showed in figure 2a. We determined the cort-HRP off-line with an enzymatic OPD colour reaction, normally used in ELISAs.

In the on-line detection (fig 2b), HRP is detected electrochemically. Immobilised glucose oxidase produces H_2O_2 from glucose in the buffer. The HRP reduces the H_2O_2 , giving electrons via ferrocene (present in the buffer) to the electrode.



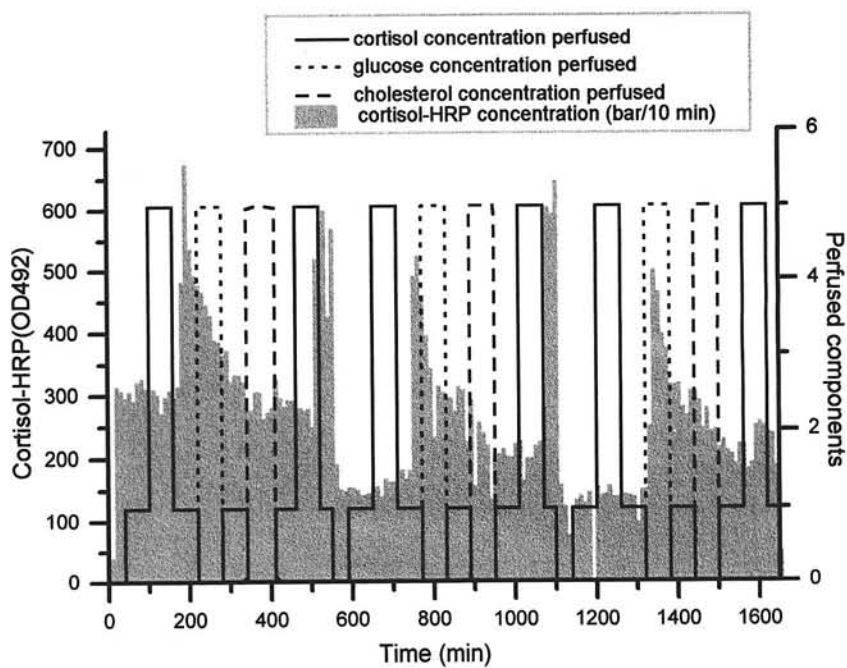
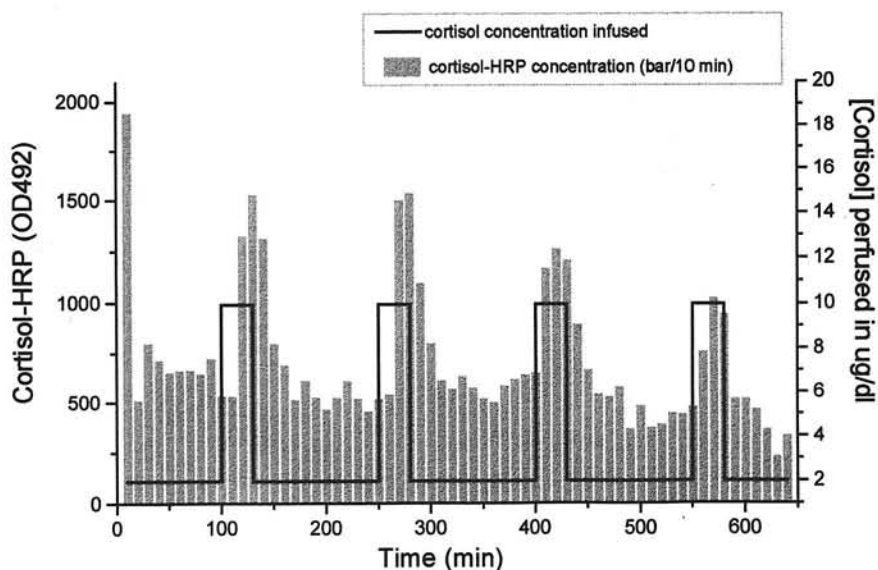


Fig 3: Results off-line displacement detection

RESULTS AND CONCLUSION

Figure 3 shows results of *in vitro* experiments of our off-line detection system, we were able to displace the labelled cortisol analogue at physiological cortisol concentrations, and this displacement was concentration dependent. Other components like glucose and cholesterol did not enhance the signal. Preliminary results are obtained with the on-line module.

These results show that displacement detection is a suitable method for on-line, *in vivo* or *ex vivo* detection of cortisol in physiological concentrations.

LITERATURE

1. W.A. Kaptein, J.J. Zwaagstra, K. Venema, M.H.J. Ruiters, J. Korf. Development of on-line displacement immunosensor for cortisol. *In preparation*.
2. Rabbany, S.Y., Kusterbeck, A.W., Bredehorst, R., and Ligler, F.S. Effect of antibody density on the displacement kinetics of a flow immunoassay. *J.Immunol.Methods* 168(2):227-234, 1994.

The project is supported by the Dutch Technology Foundation Project number GGN33.3103

Durable anion-selective sensors based on polysiloxane membranes

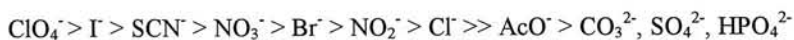
*Martijn M.G. Antonisse, Ronny J.W. Lugtenberg, Johan F.J. Engbersen,
David N. Reinhoudt*

Department of Supramolecular Chemistry and Technology and MESA
Research Institute, University of Twente, P.O. Box 217, 7500 AE Enschede,
The Netherlands.

In this contribution the development of durable anion sensors based on chemically modified field effect transistors (CHEMFETs) is presented. The ion-selective membrane in these sensors is made of well defined polysiloxane terpolymers which are synthesized according a new route. By this way the selectivity can be tuned by using different polar moieties in the polymer. This is shown for a durable nitrate-selective CHEMFET which is still well functioning after exposure for 190 days to running tap water.

1. Introduction

Ion-selective field effect transistors (ISFETs) have been used for the development of micro-sensors for many cations like sodium, potassium and heavy metal ions. For anion sensing only a small number of examples is known in literature. Most of these sensors make use of PVC based anion-exchange membranes. The selectivity of this type of sensors is governed by the relative dehydration energies of the anions (the Hofmeister series) and favours the more lipophilic ions over the hydrophilic ones, following the Hofmeister series:



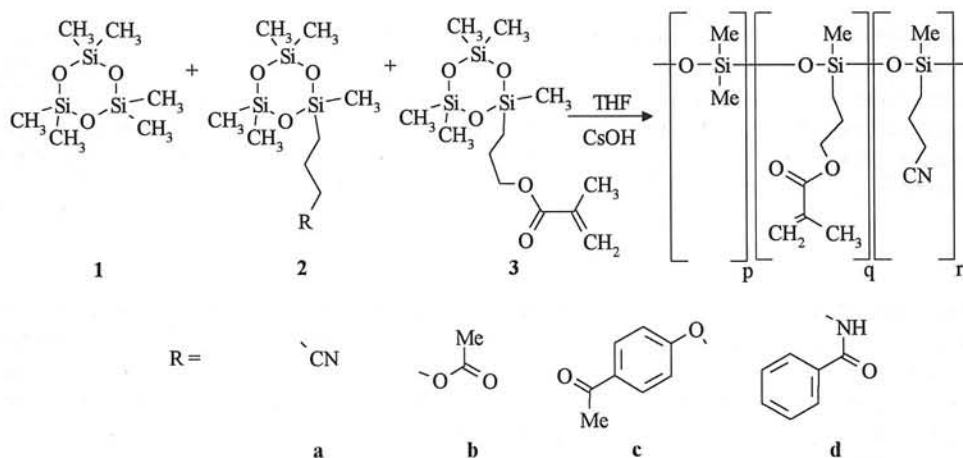
Plasticized PVC membranes have some major drawbacks. These membranes are physically attached to the chip surface and easily peel off after prolonged contact with water. Another reduction of the durability of these sensors is caused by leaching of the plasticizers into the sample, which changes the polarity and strength of the membrane during time. Also the positively charged anion-exchange sites slowly leach from the membrane deteriorating the sensor characteristics.

Many other membrane materials have been investigated in an attempt to improve the adhesion and the durability of the micro sensors. Examples are copolymers of PVC, poly(vinyl alcohol) and poly(vinyl acetate), Urushi, acrylate, nitrile rubber, and solid-solvents like octadecyl alcohol. These materials, however, still need plasticizers and it is not easy to link the ion-exchange sites covalently to the membrane matrix to prevent it from leaching. Polysiloxane rubbers have proved to be good, durable membrane materials for the development of cation sensors. This polymer does not need a plasticizer, and ion-exchange site and ion receptors can be covalently bound to the polymer matrix. However, in production only moderate yield of good working sensors was obtained because the used polysiloxanes were chemically not well defined and inhomogeneous.

In this contribution the synthesis and use of chemically well defined and homogeneous polysiloxanes will be presented. These polymers were used as membrane material for ion exchange membrane based nitrate-selective CHEMFETs (chemically modified field effect transistors). The durability of these sensors was further improved by the covalent attachment of the ion exchange sites. The characteristics of the nitrate sensors will also be presented.

2. Results

The polysiloxanes are made by the polymerization of three monomers (scheme 1). Monomer **1** forms the bulk of the polymer, poly(dimethylsiloxane). Because the polarity of poly(dimethylsiloxane) is too low to obtain a good working sensor, polar side chains (**2**) have to be introduced in the polymer. For cross-linking of the polymer chains monomer **3** is added. Besides increasing the mechanical strength of the membrane, the photopolymerizable methacrylate moiety of this monomer can also be used for covalent anchoring of the membrane to the chip surface and binding of receptors and ion exchange sites.



Scheme 1

To obtain a homogeneous random polymer the reactivity the three monomer has to be the same. Therefore all three monomers were synthesized based on a cyclotrisiloxane ring. This unit can be polymerized by the addition of CsOH as initiator. The obtained polymers were characterized by the use of GPC and NMR. The GPC chromatogram shows a molecular weight (M_w) of about 50000 and a distribution (M_w/M_n) of 1.5. This narrow distribution points out that the polymer is well defined. From the NMR spectra the relative amounts of the substituents in the polymer can be derived. These are almost the same as the relative amounts used in the monomers indicating that the monomers are all of the same reactivity. Besides the commonly used cyanopropyl polar moiety (**2a**) also other polar substituents like esters (**2b**), ketones (**2c**), and amides (**2d**) can be introduced in a similar way.

The above described polymers were used for the development of nitrate-selective CHEMFETs. Therefore 0.5 % w/w of lipophillic tetraoctylammonium bromide (TOAB) sites were added. In table 1 the characteristics of these sensors are given.

Table 1 *Sensor characteristics (FIM) of nitrate CHEMFETs based on polysiloxane polymers with polar cyano, ketone, ester or amide substituents (10 mol %) and mobile ammonium sites (0.5 % w/w TOAB)*

Log $K_{NO_3, j}^{Pot}$ [slope mV/decade]							
Polar monomer	Detection limit	Cl ⁻	Br ^{-†}	NO ₂ ⁻	OAc ⁻	SO ₄ ²⁻	Phosphate [‡]
2a	-3.7 [-57]	-2.2 [-56]	-1.0 [-55]	-1.2 [-50]	-2.5 [-54]	-3.0 [-58]	-2.7 [-56]
2b	-3.9 [-56]	-2.3 [-56]	-1.2 [-56]	-1.6 [-53]	-2.4 [-56]	-2.9 [-57]	-2.3 [-57]
2c	-3.7 [-60]	-2.2 [-57]	-0.9 [-54]	-1.2 [-51]	-2.8 [-49]	-2.6 [-50]	-2.7 [-55]
2d	-3.7 [-54]	-1.6 [-53]	-0.5 [-53]	-1.2 [-51]	-2.3 [-53]	-2.9 [-57]	-2.4 [-54]

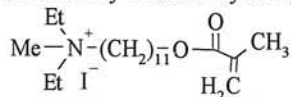
[j] = 0.1 M; [†][Br⁻] = 0.01 M; [‡]pH = 7.0

Using the common cyanopropyl polar substituent (entry **2a** in table 1) a sensor is obtained with an almost Nernstian response of -57 mV/decade and a detection limit of $10^{-3.7}$ M nitrate. The selectivity coefficients are clearly following the Hofmeisters series. The obtained selectivity coefficients for sulfate and phosphate are determined by the detection limit of the sensor.

By using the ester **2b** as polar substituent small deviations in the selectivity are obtained. In table 1 can be seen that nitrite is becoming less interfering and phosphate a little more compared to the cyanopropyl based polymer. The use of ketone moieties (**2c**) does nearly not influence the selectivity, and acetate and sulfate show minor changes in selectivity. However, the use of the amide moiety **2d** has a very strong effect on the selectivity of the halogenides tested. Chloride and bromide have become significantly more interfering to nitrate. Also for phosphate there is somewhat more interference measured.

The above described sensors are still limited in their durability by the possibility that the positively charged TOAB sites leach from the membrane. Therefore ammonium site **4** was synthesized. The photopolymerizable methacrylate moiety of **4** will polymerize with the

synthesized. The photopolymerizable methacrylate moiety of **4** will polymerize with the methacrylate substituents of the polysiloxane during the UV-induced cross-linking. This anchors the positive ammonium sites to the membrane matrix. The use of **4** in stead of TOAB does not affect the good sensor characteristics, like slope, detection limit, or selectivity, but does increase the durability as was shown by a durability study.



4

The durability of the sensors was investigated by placing them in running tap water. As can be seen in figure 1 the sensors based on immobilized ammonium sites **4** last for over 190 days (line ●). Compared with the response at the beginning of the experiment (line ◆) only a small shift in the detection limit appeared, the slope remains the same. Also the tested selectivities for nitrite and chloride did not change during this period. This is in contrast with the sensors based on mobile TOAB sites (line ×) where due to leaching of the positive sites a high noise level and a slope of less than -50 mV/decade was obtained.

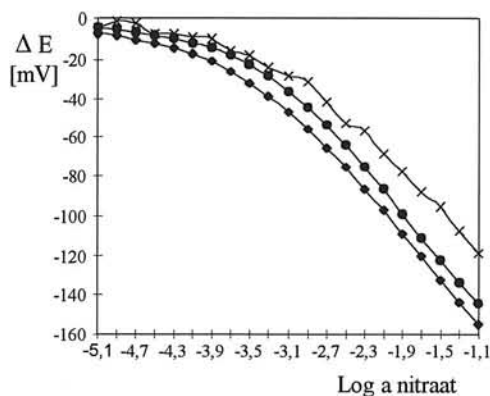


Figure 1 Response of nitrate CHEMFETs at the beginning of the durability test (◆), after 190 days with immobilized ammonium sites **4** (●) and after 190 days with TOAB (×).

3. Conclusions

The newly developed synthesis of siloxane terpolymers results in well defined polysiloxanes. The polymers can be used to produce in a reproducible way nitrate sensors with good characteristics. The selectivity of these sensors can be influenced by the type of polar moiety of the polymer. The durability of the sensors can be improved by covalent attachment of the ammonium sites to the membrane matrix. The fabricated sensors function well over a period of 190 days without loss of sensitivity or selectivity.

Durable Chemical Sensors for Heavy Metal Ions Based on Field Effect Transistors

R.J.W. Lugtenberg, R.J.M. Egberink,
J.F.J. Engbersen, and D.N. Reinhoudt

*Department of Supramolecular Chemistry and Technology
and MESA Research Institute,
University of Twente, P.O. Box 217, 7500 AE Enschede,
The Netherlands*

Abstract

In this contribution the development of polysiloxane based CHEMFETs for heavy metal ion detection is described. Well-structured polysiloxane membranes were synthesized and used as sensing membranes for Ag^+ , Cd^{2+} , and Pb^{2+} -selective CHEMFETs. Different polysiloxane based CHEMFETs were selective for these heavy metal ions in presence of different interfering ions. The intrinsic elastomeric properties of the polysiloxane membrane makes the use of a plasticizer superfluous and this should have favourable effect on the durability of these CHEMFETs.

Introduction

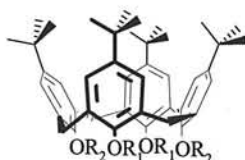
A chemical sensor connects the chemical domain and the physical domain. Our work is aimed at the design and synthesis of molecular receptors that can selectively recognize a guest species. When such a guest carries a charge, like in cations, the chemical recognition process converts the neutral receptor in a charged species. This allows us to use a Field Effect Transistor for the transduction of the (chemical) complexation reaction into an electronic signal [1].

Supramolecular chemistry involves the chemistry above the molecular level and allows to design molecules that *selectively* recognize certain species by using the principle of mutual complementarity of the receptor and the guest. Factors that determine the complementarity are the size of the species, the number of possible interactions between the receptor and the guest and the nature of the binding sites of both.

Cation selective receptors based on calix[4]arenes

Most of our work in the past decade has been focused on receptors for cationic guest species and we have been able to obtain receptors that can discriminate with a high degree of

selectivity between the different heavy metal cations (e.g. Ag^+ (1), Cd^{2+} (2), and Pb^{2+} (3)) [2]. The molecular platform that we use for the synthesis of such receptors is a calix[4]arene, a molecule with a high hydrophobicity and 4 positions for chemical modification. The latter introduces the desired selectivity.

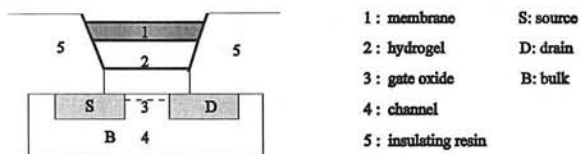


- 1 $R_1 = \text{OH}$; $R_2 = (\text{CH}_2)_2\text{SCH}_3$
 2 $R_1 = R_2 = (\text{CH}_2)_2\text{O}(\text{CH}_2)\text{C}(\text{S})\text{N}(\text{Et})_2$
 3 $R_1 = R_2 = \text{CH}_2\text{OC}(\text{S})\text{N}(\text{Me})_2$

Calix[4]arene derivatives

CHEMFET architecture

We have developed a new architecture for CHEMFETs which eliminates most of the existing drawbacks that have been reported in the literature [3]. The gate of the ISFETs has been covered with a buffered poly HEMA layer in order to eliminate CO_2 interference and pH sensitivity [4]. On top of this layer a hydrophobic membrane is cast. The membrane contains the selective molecular receptor (e.g. 1-3) and the hydrophobic anion that is commonly applied in ion selective electrodes to eliminate the interference of sample anions.



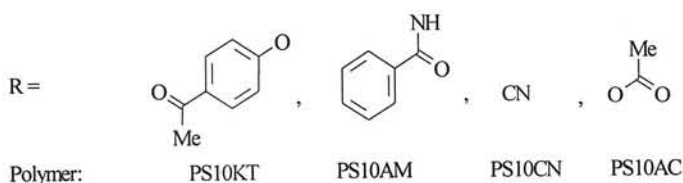
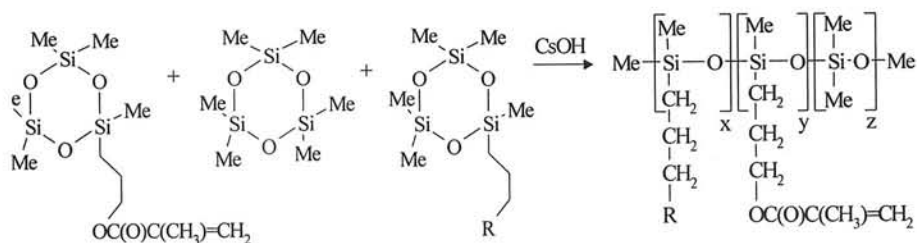
CHEMFET structure

CHEMFETs based on the calix[4]arene (1) responded selectively ($60 \text{ mV decade}^{-1}$) to a change in silver activity in the aqueous solution in the presence of potassium, calcium, cadmium, and copper ions ($\log K_{i,j} < -4$). The selectivity toward mercury ($\log K_{i,j} = -2.7$) is comparable to the best neutral carrier based ISE so far. The calix[4]arene (2), which has four

dimethylthiocarbamoylmethoxyethoxy substituents, was selective in a CHEMFET (30 mV decade⁻¹) toward cadmium in the presence of calcium and potassium ions. Tetrasubstitution of the calix[4]arene with thioamide groups (3) is a prerequisite for the selective detection of lead and leads to a highly selective CHEMFET ($\log K_{ij}$ -3.4 to -5.2) [2].

Novel membrane material

For the practical applications of this CHEMFET technology the lifetime of such a sensor should be at least 3 but preferably 6 months. The hydrophobic membranes should be very thin in order to reduce the electrical resistance and in the continuous contact with aqueous sample solutions, the sensors response deteriorates in time because of the leaching of the essential electroactive components. The attention was focused on polysiloxane membranes. Polysiloxanes possess suitable elastomeric properties, because low glass transition temperature (-120°C), which makes the use of an additional plasticizer superfluous. The synthesis of well-structured reproducible siloxane copolymer is possible, based on the anionic copolymerization of cyclic trisiloxanes. These cyclic trisiloxanes are monofunctionalized with either a methyl, a polar or a methacrylate side group [5].



This novel membrane material does not require additional plasticizer, is IC compatible and, in addition, can be covalently attached to the gate oxide of the ISFET or the polyHEMA hydrogel.

Polysiloxane based CHEMFETs for heavy metal ion detection

The siloxane copolymers with methacrylate side groups enable the covalent attachment of the membrane to the polyHEMA surface. The different siloxane copolymers can be used as a membrane material for selective heavy metal ion detection with CHEMFETs. The polysiloxane

based CHEMFETs have the advantage that no plasticizer is used in the membrane, which should have favourable effect on the durability of the CHEMFETs. The results are shown in Table 1. CHEMFETs with the cyanopropyl functionalized siloxane copolymers, incorporating a Ag^+ -selective ionophore **1**, are very selective for Ag^+ -ions in present of different ions. The interference of Hg^{2+} is most severe but still a selective response was found ($\log K_{\text{Ag,Hg}} = -2.4$). CHEMFETs with an acetoxypopyl functionalized siloxane membrane containing the Cd^{2+} -selective calix[4]arene derivative **2** gave the best Cd^{2+} -selectivity. Good $\text{Cd}^{2+}/\text{Pb}^{2+}$ -selectivity (-2.0) is obtained with these CHEMFETs, which is not possible using plasticized PVC membranes.

Table 1. Selectivity ($\log K_{i,j}$) and sensitivity (slope, mV/decade) of polysiloxane based CHEMFETs for heavy metal ions.

primary cation	membrane	K^+	Cu^{2+}	Cd^{2+}	Ca^{2+}
Ag^+	PS10CN	-4.3 (55)	-4.4 [58]	-4.0 [54]	-4.3 [54]
Cd^{2+}	PS10AC	-2.6 (27)	^a	----	-4.1 [29]
Pb^{2+}	PS10KT	-3.3 [28]	-3.0 [26]	-3.8 [22]	-4.3 [27]

^a Not selective for Cd^{2+} -ions in presence of Cu^{2+} .

CHEMFETs based on *p*-acetylphenyloxypropyl functionalized siloxane membranes with a Pb^{2+} -selective ionophore **3** were selective for Pb^{2+} -ions (Table 1, entry 3). The selectivities are similar to PVC/*o*-NPOE based CHEMFETs, but the polysiloxane based CHEMFETs should have an enhancement of the durability. Currently lifetime measurements are being carried out.

References

- [1] D.N. Reinhoudt, *Sensors and Actuators B*, 6, (1992), 179-185.
- [2] P.L.H.M. Cobben, R.J.M. Egberink, J.G. Bomer, P. Bergveld, W. Verboom, D.N. Reinhoudt, *J. Am. Chem. Soc.*, 114, (1992), 10573-10582.
- [3] E.J.R. Sudhölter, D.N. Reinhoudt, *Adv. Mater.*, 2, (1990), 23-32.
- [4] E.J.R. Sudhölter, P.D. van der Wal, M. Skowronska-Ptasinska, A. van den Berg, P. Bergveld, D.N. Reinhoudt, *Anal. Chim. Acta*, 230, (1990), 59-65.
- [5] R.J.W. Lugtenberg, M.M.G. Antonisse, J.F.J. Engbersen, D.N. Reinhoudt, submitted for publication.

Development of a low cost ventilation rate sensor combined with an ammonia sensor for ammonia emission measurement and control

D. Berckmans^(1,2); E. Vranken⁽¹⁾ and J. Ni⁽¹⁾; J. Roggen⁽³⁾;
G. Huybrechts⁽³⁾

1. Laboratory for Agricultural Building Research, Katholieke
Universiteit Leuven

Kardinaal Mercierlaan 92, B-3001 Heverlee, Belgium

2. National Fund for Scientific Research, Belgium

3. IMEC v.z.w, Heverlee, Belgium

Abstract:

A ventilation rate sensor is developed for the continuous measurement of ventilation rate in sections with turbulent flow. The measurement range of the sensor is 200 - 5000 m³/h and this for static pressure differences over the ventilation unit from 0 to 120 Pa. The accuracy of the sensor is + and - 60 m³/h. This low cost sensor is combined with a solid state ammonia sensor to measure the ammonia emission rate from eg. animal houses. The two sensors were installed in a pig compartment with hard environmental conditions. Ammonia concentration measured with ammonia sensor was compared with that obtained with an NO_x analyser. The field test of the two sensors shows positive results for the realisation of a new low cost device to monitor and to control ammonia emission from ventilated buildings.

1. Principle of the ventilation rate sensor

In many applications of mechanical ventilation axial fans are used because of their high performance and their low cost control possibilities (voltage control).

From the measurements of the characteristics of axial fans however, it is known that a back flow effect can appear if the static pressure drop over the fan increases.

Because of the high pressure difference to overcome, especially in winter time at low ventilation rates, the fan still keeps his rotational speed but takes the air back through its own impeller. The resulting total ventilation rate is decreasing while the fan still is using a high voltage and power input. As a consequence, it is concluded that the ventilation rate sensor should at least cover the whole duct section. Consequently a sensor that measures in one point of the section like a point in a pitot tube traverse is useless in these circumstances. Taking into account the required working environment of the sensor (temperature from -5 to 60°C, humidity up till 90%, high gas and dust concentrations,...) and the condition of a low price (to become a sensor for control purposes) the choice was made for the principle of a free running

turbine covering the whole ventilation duct section. In literature it is shown that a pressure correcting measurement can be realised with turbine meters of smaller diameters (Lee et al., 1981, 1982).

A flow rate sensor of the considered principle will be subject to changes in air flow rate and variations in pressure difference over the test chimney. Because of the principle of a free running turbine the calibration measurements are focused on the relationship between rotational speed of the turbine, the measured air flow rate and the pressure difference over the test section. Consequently the procedures for fan testing with variation of pressure difference can be applied for testing this air flow rate sensor as well. A test installation that has been built according to the German Standards DIN 1952, the Belgian Standard NBN 688 and the British Standard BS 848 has been used for the development of the sensor.

To measure the characteristics of the air flow rate sensor standardised ventilation chimneys are used with diameters varying from 0.35 m to 0.56 m and a length of 1 m. In this test chimney it was possible during the experiments to realise an air flow rate from 50 to 5800 m³/h and this for pressure differences (under pressures in the test room) from 0 to 120 Pa.

In 1982 a first prototype sensor has been developed, but some crucial adaptations were needed to improve its accuracy (see calibration curve in figure 1). A first step was the reduction of the number of blades of the sensor from 8 to 2 in order to minimize the resistance to the fluid flow. A second adaptation was the position of the sensor in relation to the fan. From measurements on a test installation it could be concluded that the upstream position of the turbine with regard to the position of the fan does have an important positive influence on the characteristics of the turbine meter.

The most important step was the design of the turbine impeller. Based on the concept of velocity triangles the blade angle was calculated and evaluated experimentally.

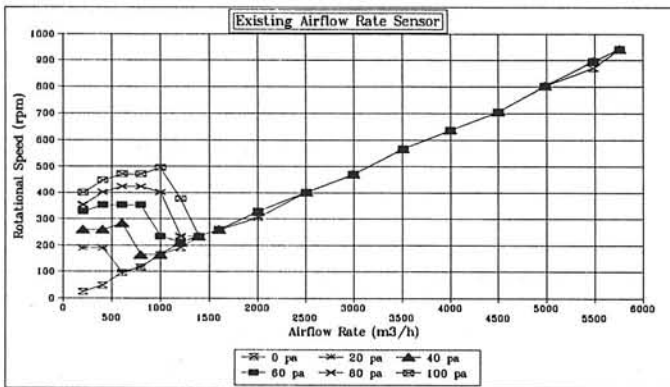


Figure 1: Calibration curve of an existing low cost sensor for ventilation rate measurement.

2. Principle of the ammonia sensor

The development of the NH_3 sensor was realised in IMEC v.z.w. (Interuniversity Microelectronics Center, Belgium). The sensor is a thick film semiconducting metal oxide sensor. These sensors are produced by a conventional screen printing technology on 96% alumina substrates. On these substrates a patterned multi-layer structure has been realised consisting of a heater element, a contact layer, a dielectric layer and a gas sensitive semiconductive metal oxide layer. On completion of the production process, the individual sensors are isolated from the substrate by laser scribing and suspended in a package by its contact wires. A typical sensor is illustrated in Figure 2.

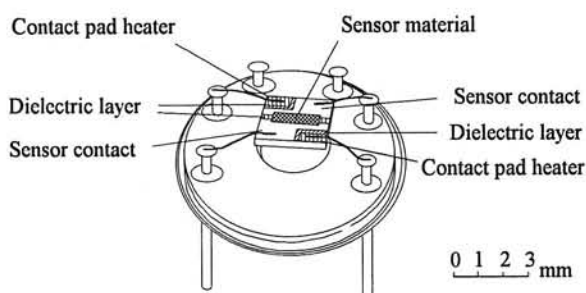


Figure 2. The ammonia sensor developed by IMEC

The operating temperature of the sensor element is 300-400 °C, after which the conductivity of the gas sensitive layer is determined. With the help of the improved electronic control system, the sensor temperature is kept independent from the air velocity on the sensor surface. At the constant operating temperature, the conductivity, σ_x , is dependent on the concentration of the pollutant, which is often presented by the following equation (Van Geloven, 1992; Van Muylder, 1992):

$$\sigma_x = \sigma_0 + \alpha \cdot [R]^b \quad (\text{Equation 1})$$

Where:

σ_x and σ_0 , the conductivity of the sensor material at a given temperature in the gas mixture under investigation and in un-polluted air respectively, in μ Siemens;

$[R]$, the concentration of the pollutant, ppm;

α and b , constants that depend on the composition and physico-chemical characteristics of the sensor material and the nature of the reducing gas.

The ammonia sensor was combined with a ventilation rate sensor and tested under field conditions in an animal house for a total of 279 days from September 1992-March 1994

(Berckmans et al., 1994). Within the framework of the on-going project of IWONL 5538A, which dedicates to the study of ammonia emission and abatement techniques in Belgium, the test of the ammonia sensor combined with the ventilation rate sensor is incorporated. The test installation is located in a commercial fattening pig house in Riemst which is described in previous work (Berckmans and Ni, 1993).

3. Test results

3.1. Ventilation rate sensor

The result of the design procedure was a new prototype sensor with a pressure independent calibration curve. Figure 3 shows the corresponding linear regression covering the complete flow rate interval from 0 to 5000 m³/h. It is clear that there is an improvement in the linearity of the steady state characteristics of the turbine meter used as an air flow rate sensor. The corresponding improvement in accuracy is important since the mean deviation has been reduced from 488 m³/h to 91 m³/h which value is 1.8% of the full scale (5000 m³/h). Since the maximum deviation is occurring for the very low air flow rates, the reduction of this value might be of importance for automation of the set points of minimum ventilation rate.

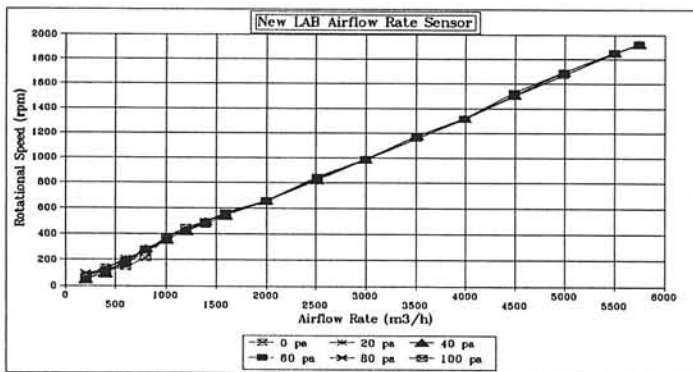


Figure 3: Calibration curve of new prototype sensor for airflow rate measurement

Finally a mould for a new prototype sensor for field use was developed and five prototype sensors of different diameters were tested on the laboratory test rig resulting in an overall accuracy of + and - 65 m³/h in the higher mentioned measuring range.

An overview of the technical results of the final sensor is given in table 1.

Table 1: Technical characteristics for a prototype air flow rate sensor (diameter 450 mm) suitable for field use.

Accuracy	+ and - 65 m ³ /h
Linearity	R ² = 0.998
Minimal rate	18 m ³ /h
Time constant	4 sec
Max. static pressure drop	10 pa
Max. noise production	81 dBa

In can be concluded that most of the requirements are fulfilled with this new prototype sensor.

3.2. Ammonia emission sensor

The ammonia sensor was installed in one of the control compartments on 16 December 1994 close to the ventilation chimney. The output of the ammonia sensor was sampled every second and averaged every 12-minute. This output is compared with the output of an accurate Chemiluminescence NO_x Analyzer (Thermo Instrument Systems, Model 42, measurement range 50ppm, Precision $\pm 0.5\text{ppb}$). With this "in situ $\text{NH}_3 \rightarrow \text{NO}$ converter with subsequent NO_x analyzer," ammonia concentration can be measured with an error of only 2 % as indicated by the manufacture. With the combination of the accurate ventilation rate sensor (error of 3 % at $2000 \text{ m}^3/\text{h}$), this test installation allows to measure NH_3 emission rate, which is the product of ventilation rate and the ammonia concentration in the outflow air, with an error of 3-5 %. Part of the measurement data (from 10 AM 11/03/1995 to 23 PM 14/03/95) is presented in Figure 4 as an example. The correlation coefficient between ammonia sensor output and ammonia concentration measured with NO_x analyzer is 0.675.

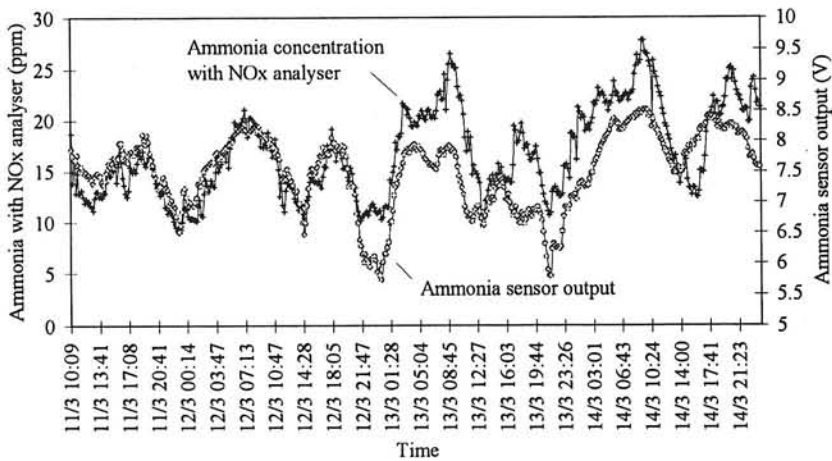


Figure 4. Ammonia concentration measured with NO_x analyzer and ammonia sensor output from 11/03/1995 to 14/03/95

Reference:

Berckmans, D. and Ni, J. Q. (1993). "Field test installation for on-line continuous measurement of total ammonia emission from animal houses." Proceedings of the International Conference for Agricultural Machinery & Process Engineering, October 19-22, Seoul, Korea. V. 2, pp. 393-402.

Berckmans, D., Ni, J. Q., Goedseels, V., Roggen, J., Huyberechts, G. and Van Overstraeten, R. (1994). "Haalbaarheidsstudie van de aanwending van bestaande sensoren voor de meting en de beheersing van NH₃-emissies in dierlijke produktie-eenheden (Feasibility study of the use of an existing sensor for the measurement and control of NH₃-emission from animal production unit)." Final report, K.U.Leuven and IMEC, Leuven, Belgium. 57p.

BS 848 Part 1 (1980) British Standards Institution. Fans for general purposes. Part 1 : Methods of testing performance, 80 pp.

DIN 1952 (1952) Deutsche Normen. Durchfluszmessung mit genommen Düsen, Blenden und Venturidüsen, 13 pp.

Huybrechts, G., Van Mulder, M., Honore, M., Desmet, J., Roggen, J., Berckmans, D., Ni, J. Q., 1993. Development of a thick film ammonia sensor combined with a ventilation rate sensor for livestock buildings. In "Sensors VI, Technology, Systemn and applications", Edited by Grattan K.T.V. and Augousti A.T., Institute of Physics Publishing, Bristol and Philadelphia, Series Editor Jones B.E., ISBN 0-7503-0316-6, pp. 85-90.

Lee, W.F.Z., Fisher H.W. and Montag, D.R. (1981) Development of a self-checking gas turbinemeter, In : Flow, its measurement and control in science and industry, Vol. 2, by W.W. Durgin. Instrument. Society of America, pp. 453-469.

NBN 688 NI (1966) "Belgische Norm. Debietmeting van fluïda door drukvalapparaten" - Algemeen, 32 pp.

Van Geloven, P. (1992). "Tin oxide gas sensors for the simultaneous determination of gas concentrations in mixtures." Ph.D. Thesis, Department of Electronics, K.U.Leuven, Belgium. 237p.

Van Muylder, M. (1992). "De invloed van koperoxide op de gasgevoeligheid van tinoxide gassensoren." Rega school, 43p.

Vranken, E., Berckmans, D. Goedseels, V. (1992) "Optimalisatie Fancom-meetturbine". Internal research publication Fancom-Katholieke Universiteit Leuven, 56 pp.

Silicon Fusion Bonding with Chemical Mechanical Polishing

C. Gui, H. Albers, J. G. E. Gardeniers, M. Elwenspoek and P. V. Lambeck

MESA Research Institute, University of Twente, P.O. Box 217, 7500 AE
Enschede, The Netherlands, Email: c.gui@el.utwente.nl

Abstract Silicon fusion bonding of wafers after KOH etching is almost impossible. The same is the case for wafers being heavily doped or having epitaxial layers of bad quality. In this contribution, we demonstrate that these wafers become spontaneously bondable after a very brief chemical mechanical polishing step.

1. Introduction

Silicon fusion bonding (SFB) is the joining of two silicon wafers without the use of any intermediate adhesives at room temperature (RT) and in ambient atmosphere, followed by a high temperature annealing. This technology has been used to fabricate silicon-on-insulator (SOI), silicon power devices, as well as silicon sensor and actuator (S&A) devices.

Chemical mechanical polishing (CMP) plays an important role in SFB in two ways: preparing very flat and smooth surfaces for successful room temperature bonding and mechanically thinning one side of the bonded wafer pair. While the latter is one of the key techniques in the fabrication of SOI wafers and silicon power devices [1-3], the first one, however, is a crucial and very critical process step for the fabrication of S&A devices, where bonding between a large range of materials and bonding silicon wafers with micro mechanical structures are of interest.

It has been reported that both the macroscopic surface flatness and the microscopic surface roughness are crucial for a successful wafer bonding[4-6]. Commercially available well-polished silicon wafers, with or without buried oxide layer or well grown epitaxial layers, having a flatness less than 10 μm and a micro roughness not exceeding 10 \AA , can be easily pre-bonded at RT in a particle-free environment, as has been done so far in the SOI community. Haisma and his group, for the first time, have extensively investigated the feasibility of direct bonding of a variety of materials, applying their dedicated optical polishing technology [7]. However, up to now CMP has not been developed as an *in situ* process for SFB, which may offer more freedom for the application of bonding technology in the fabrication of S&A devices.

As an initial effort to implement CMP in SFB, in this paper, we demonstrate that silicon wafers after KOH etching, very heavy boron diffusion and LPCVD silicon rich nitride ($\text{Si}_{3+x}\text{N}_4$) deposition, can be bonded yet after being shortly polished with a CMP machine, while normally such wafers are believed to be not spontaneously bondable (e.g. in [8]).

2. Experiments

Sample preparation: One side polished, 380 μm thick 3 inch (100) silicon wafers were used in the following experiments. Before KOH etching, boron diffusion or LPCVD $\text{Si}_{3+x}\text{N}_4$ deposition, the wafers were treated with a standard wafer cleaning (SWC) to remove both the organic and metallic contaminants, followed by a HF dipping step to remove the wafer surface native oxide. The SWC procedure consists of 10 minutes dipping in the fuming nitric acid 100% HNO_3 (5 minutes in beaker I, and another 5 minutes in beaker II), rinsing in the quick dump rinser (QDR), 15 minutes dipping in the hot nitric acid 70% HNO_3 at 90 $^\circ\text{C}$, again rinsing in QDR and spin drying. The HF dipping step consists of 1 minute dipping in 1% HF solution, rinsing in QDR and spin drying.

Then 8 wafers were etched in a 55 wt% KOH solution at 75 $^\circ\text{C}$ for 10 minutes. The etch rate of the KOH solution is about 1 $\mu\text{m}/\text{min}$.

Another 11 wafers were doped in a boron diffusion oven at 1100 $^\circ\text{C}$ for 3 hours. The boron oxide was removed from the wafers by BHF etching for 1 hour. The surface boron concentration is about $3 \times 10^{20} \text{ cm}^{-3}$, and the doping depth is about 2.5 μm .

Finally, a LPCVD $\text{Si}_{3+x}\text{N}_4$ layer was grown on 3 wafers from a gas mixture of SiH_2Cl_2 (70 sccm) and NH_3 (18 sccm), in 200 mT at 850 $^\circ\text{C}$. The thickness of the LPCVD $\text{Si}_{3+x}\text{N}_4$ layer is about 430 nm [9].

Polishing: For comparison, part of the samples were polished before being brought together for SFB, by using E460 CMP machine. A schematic drawing of the CMP set up is shown in Fig. 1. The CMP process was specially optimized for silicon wafer polishing. The polishing slurry was Nalco 2350 that was diluted in DI water at the ratio of 1 to 30. The pH value of the slurry is 11. The work pressure and the plate temperature of CMP were 1 bar and 25 $^\circ\text{C}$ respectively. The polishing pad was UR 100, which is very soft and specially made for silicon wafer final polishing. After polishing, the wafers were cleaned for removing the silica particles. The silicon removal rate of CMP was 30 nm/min. For a detail discussion of CMP process, readers are referred to [10].

For polishing LPCVD $\text{Si}_{3+x}\text{N}_4$, the same process was used as in silicon polishing. A removal rate of about 2.5 nm/min. was found, which is 12 times lower than the silicon removal rate. However, the LPCVD $\text{Si}_{3+x}\text{N}_4$ layer surface quality after polishing was comparable to that of silicon wafer polishing.

Before and after CMP, the wafer surface topography was characterized by using a surface profiler. Surface roughness of the heavy boron doped wafers before and after CMP was also measured by using atomic force microscope (AFM).

Bonding: The SFB experiment was conducted in a class 100 clean room environment at RT and standard atmosphere. Before bonding, all wafers were treated with a standard RCA ($\text{H}_2\text{SO}_4(1) +$

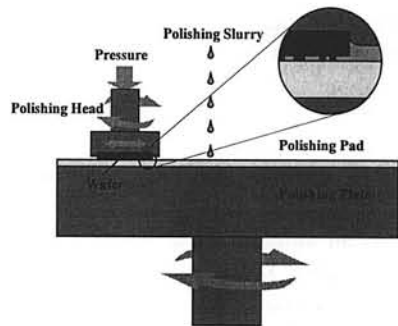


Fig. 1, Schematic drawing of the CMP set up

$\text{H}_2\text{O}(5) + 30\% \text{H}_2\text{O}_2(1)$) cleaning at 80°C for 20 minutes, followed by a SWC. After spin drying, the wafers were brought together immediately for RT bonding in a self-made bonding set up, which has an IR camera that enables us to monitor the RT bonding process. A slight pressure was necessary for the first point contact of each successful RT bonding. Then the bond wave propagated over the whole wafer automatically. Once the wafer pairs were successfully pre-bonded, they were annealed for 2 hours at 1000°C in N_2 . The bond strength after annealing was checked by inserting a razor blade. The particles and voids captured between the wafer pair were detected by using an IR camera.

3. Results and discussion

The SFB results are summarized in Table. 1.

Table 1, SFB of Silicon Wafers with Different Surface Conditions

Wafer No.	Surface	CMP treatment	Bondability
1	KOH etching	no	1+2
2	KOH etching	no	impossible
3	KOH etching	no	3+4
4	KOH etching	no	impossible
5	KOH etching	CMP 3 min.	5+6
6	KOH etching	CMP 3 min.	spontaneously
7	KOH etching	CMP 3 min.	7+8
8	KOH etching	CMP 3 min.	spontaneously
9	Boron diffusion	no	9+10
10	Boron diffusion	no	very difficult
11	Boron diffusion	no	11+12
12	Boron diffusion	no	very difficult
13	Boron diffusion	CMP 3 min.	13+14
14	Boron diffusion	CMP 3 min.	spontaneously
15	Boron diffusion	CMP 3 min.	15+16
16	Boron diffusion	CMP 3 min.	spontaneously
17	Boron diffusion	CMP 3 min.	17+20
20	LPCVD $\text{Si}_{3+x}\text{N}_4$	CMP 3 min.	impossible
17	Boron diffusion	CMP 3 min.	17+20
20	LPCVD $\text{Si}_{3+x}\text{N}_4$	CMP upto 20 min.	very well
18	Boron diffusion	CMP 3 min.	18+21
21	LPCVD $\text{Si}_{3+x}\text{N}_4$	CMP 20 min.	very well
19	Boron diffusion	CMP 3 min.	19+22
22	LPCVD $\text{Si}_{3+x}\text{N}_4$	CMP 20 min.	very well

The bond strength after annealing is so strong that it is impossible to insert a razor blade into the bond interface. We once tried to do so and the edge of one wafer was broken at a place other than the bond interface.

In each bonded wafer pair, several voids were found, which was due to the particles and air bubble captured in the bonding interface.

After KOH etching, many hillocks are produced that make the silicon wafer surface much rougher than before. The peak-valley values of the hillocks are about 25 nm, which is high enough to make the wafers unsuitable for SFB. The wafer surface roughness after 10 minutes of KOH etching is comparable to that after several hours of KOH etching. After a very short CMP step, all the pyramids were removed, the wafer surface became as smooth as the original ones (Fig. 2).

Silicon wafers after boron diffusion are significantly rougher than original one before removing the boron oxide. They are still too rough to bond after removing the boron oxide. However, it is impossible to measure the micro roughness by a conventional step profiler. AFM images reveal that many small peaks of several nm high are still on the wafer after boron diffusion and removal of the boron oxide (Fig. 3). After 3 minutes CMP, smooth surfaces are achieved (Fig. 4). The mean sheet resistance of the doped layer before and after CMP was 2.45 Ω /sq. and 2.46 Ω /sq. respectively. The electrical properties of the doping layer were not altered by polishing.

In the case of bonding $\text{Si}_{3+x}\text{N}_4$ to a heavy boron doped silicon wafer, the micro roughness on both surfaces was much too high to achieve an immediate bond. The surface topography of the LPCVD $\text{Si}_{3+x}\text{N}_4$ layer is shown in Fig. 5. Because the $\text{Si}_{3+x}\text{N}_4$ removal rate is much lower than that of silicon, 3 minutes of CMP was not sufficient to smoothen the micro hillocks. Instead, after removal of about 50 nm by 20 minutes CMP, the silicon nitride layer surface

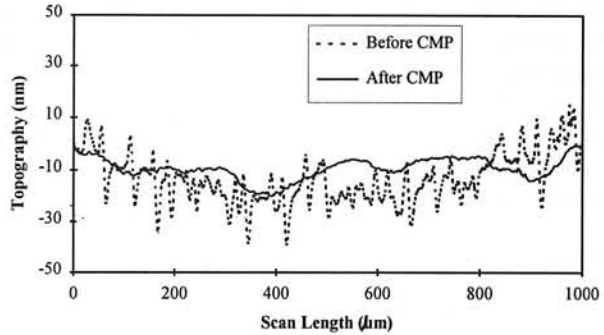


Fig. 2, Surface topography of Si (100) wafers, which were etched in 55 wt% KOH solution at 75 °C for 10 minutes, before and after 3 min. CMP.

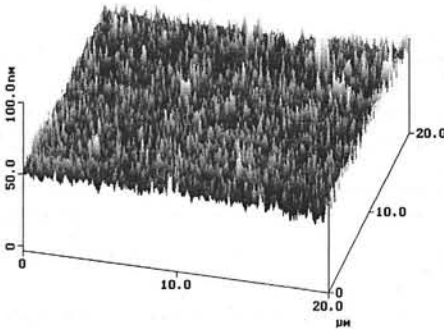


Fig. 3, AFM image of heavy boron doped silicon wafer surface before CMP

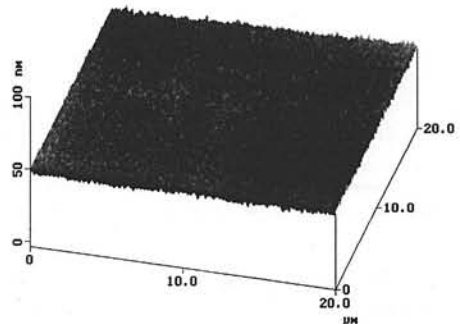


Fig. 4, AFM image of heavy boron doped silicon wafer surface after 3 min. CMP

becomes suitable for fusion bonding (Fig. 5).

4. Conclusion

Silicon wafers after KOH etching, very heavy boron diffusion and LPCVD $\text{Si}_{3+x}\text{N}_4$ deposition, which were not spontaneously bondable, have been successfully bonded after CMP. Since less than 100 nm of silicon has been removed by CMP, the electrical properties of the boron doped silicon wafers were not influenced.

CMP has been shown a very promising *in situ* technology for silicon fusion bonding.

Acknowledgements

The silicon nitride bonding experiment was conducted together with S. Sánchez. The authors also like to thank staff of the MESA clean room for technical support. This research is sponsored by the Dutch Technology Foundation (STW).

References

- [1] S. Blackstone, Mechanical thinning for SOI, *Proceedings of the 3rd International Symposium on Semiconductor Wafer Bonding: Physics and Applications*, Vol 95-7 (1995) 56-71.
- [2] J. Haisma, T.M. Michielsen and G.A.C.M. Spierings, High-quality by bonding standard Si wafers and thinning by polishing techniques only, *Jap. J. Appl. Phys. Vol. 28, No. 5*, (1989) L725-726.
- [3] J. Haisma, B.A.C. Spierings, U.K.P. Biermann, and J. A. Pals, Silicon-on-insulator wafer bonding-wafer thinning; technological evaluations, *Jap. J. Appl. Phys. 28*, (1989) 1426-1443.
- [4] W.P. Maszara, B-L. Jiang, A. Yamada, G.A. Rozgonyi, H. Baumgart, A.J.R. de Kock, Role of the surface roughness in wafer bonding, *J. Appl. Phys. 69 (1)*, (1991), 257-260.
- [5] M. Bergh, S. Bengtsson and M.O. Andersson, The influence of the surface micro-roughness on bondability, *Proceedings of the 3rd International Symposium on Semiconductor Wafer Bonding: Physics and Applications*, Vol 95-7 (1995) 126-137.
- [6] B. Roberds and S. Farrens, An AFM study on the roughness of silicon wafers correlated with direct wafer bonding, *Proceedings of the 3rd International Symposium on Semiconductor Wafer Bonding: Physics and Applications*, Vol 95-7 (1995) 326-341.
- [7] J. Haisma, B.A.C. Spierings, U.K.P. Biermann, and A.A. van Gorkum, Diversity and feasibility of direct bonding: a survey of a dedicated optical technology, *Applied Optics*, Vol. 33, No. 7 (1994) 1154-1169.
- [8] Y. Backlund, L. Rosengren, B. Hok and B. Svedbergh, Passive silicon transducer intended for biomedical, remote pressure monitoring, *Sensors & Actuators, A21-A23* (1990) 58-61.
- [9] S. Sánchez, M.J.M.E. de Nivelte, W. Michalke, E. Steinbeiss, M. Burnus, T. Heidenblut, B. Schwierzi, R. de Vries, P.A.J. de Korte and M. Elwenspoek, A high- T_c superconductor bolometer on a $\text{Si}_3\text{N}_4/\text{Si}$ membrane, Proceedings of this conference.
- [10] C. Gui, H. Albers, J.G.E. Gardeniers, M. Elwenspoek and P.V. Lambeck, Optimization of Si chemical mechanical polishing process using response surface methodology, to be published.

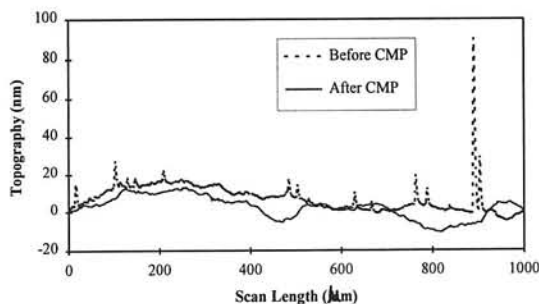


Fig. 5, Surface topography of LPCVD $\text{Si}_{3+x}\text{N}_4$ layer before and after 20 min. CMP.

A High- T_c superconductor bolometer on a $\text{Si}_3\text{N}_4/\text{Si}$ membrane

S. Sánchez⁽¹⁾, M.J.M.E. de Nivelles⁽²⁾, W. Michalke⁽³⁾, E. Steinbeiss⁽³⁾,
M. Burnus⁽⁴⁾, T. Heidenblut⁽⁴⁾, B. Schwierzi⁽⁴⁾, R. de Vries⁽²⁾,
P.A.J. de Korte⁽²⁾ and M. Elwenspoek⁽¹⁾.

⁽¹⁾*MESA Research Institute, P.O. Box 217, 7500 AE Enschede,
The Netherlands*

⁽²⁾*Space Research Organization Netherlands, Sorbonnelaan 2, 3584 CA
Utrecht, The Netherlands*

⁽³⁾*Institut für Physikalische Hochtechnologie, Helmholtzweg 4, D-07743
Jena, Germany*

⁽⁴⁾*Institut für Halbleitertechnologie und Werkstoffe der Elektrotechnik,
Universität Hannover, D-30167 Hannover, Germany*

Abstract

A high- T_c transition edge bolometer is being developed for remote sensing of atmospheric OH. By producing the bolometer on top of a Si_3N_4 membrane it should be possible to achieve a Noise Equivalent Power (NEP) smaller than 4×10^{-12} W/ $\sqrt{\text{Hz}}$. Two different routes are presented involving a fusion bonding step between Si_3N_4 and Si.

1. Introduction

Because of the central importance of OH in stratospheric chemistry, ESA and NASA are currently investigating different measurement techniques for remote sensing of OH from a satellite. One of the proposed techniques is the OH Interferometer Observations (OHIO) concept which includes a Fabry-Perot for selection of the 84.42 μm emission line of OH. This work is done in the context of the PIRAMHYD program (Passive Infra-Red Atmospheric Measurements of HYDroxyl). The concept of the OHIO instrument has been discussed in for example [1].

The OHIO instrument requires a far infrared detector with a high efficiency at 85 μm , a size of approximately 1 mm^2 , a timeconstant of less than 0.1 s, a Noise Equivalent Power (NEP) better than 4×10^{-12} W/ $\sqrt{\text{Hz}}$ and an operational temperature larger than 35 K [2]. None of the presently available semiconductor detectors can meet these requirements.

Detectors most likely to meet the stated requirements are superconducting membrane type bolometers. The bolometer is a thermal detector, which employs an electrical resistance thermometer to measure the temperature of a radiation absorber. The performance of a bolometer is usually indicated by the Noise Equivalent Power, NEP [W/ $\sqrt{\text{Hz}}$], the amount of power incident on the bolometer which creates a signal amplitude equal to the noise source. The specific detectivity D^* is often used as a replacement for the NEP. With A being the

detector area, D^* is defined as $D^* = \sqrt{A} / \text{NEP}$. A good review of the bolometer theory can be found in [3].

2. High T_c Bolometer on a Si membrane

Recently bolometers with a high- T_c superconductor transition edge thermometer have been prepared successfully on micromachined silicon membranes [4]. For the fabrication of these bolometer structures, a 50 nm thick yttria stabilized ZrO_2 (YSZ) bufferlayer was first epitaxially grown on top of a silicon membrane. After patterning the YSZ layer into a meander structure, a 50 nm thick $\text{GdBa}_2\text{Cu}_3\text{O}_{7.8}$ layer was deposited using magnetron sputtering. This inhibition technique resulted in good epitaxial GdBCO layers only there where the YSZ layer was present. On the parts where GdBCO was deposited directly on silicon it lost its superconducting qualities and became an insulator. Passivation of the GdBCO layer was done by sputter deposition of PtO_x . Electrical contacts were made by locally reducing the PtO_x to metallic platinum using laser heating.

The detectivity D^* of this bolometer was reported to be 3.8×10^9 ($\text{cm}\sqrt{\text{Hz/W}}$), at an operation temperature of 84.5 K. This D^* translates to a NEP of about 3×10^{-11} $\text{W}/\sqrt{\text{Hz}}$. This value is too large for our purpose due to the high thermal conductivity of the silicon and the resulting smaller sensitivity. Our investigations aim at the replacement of the membrane material by silicon nitride, while using the same inhibition technique. The thermal conductivity of Si_3N_4 is about 50 times smaller as compared to Si, so the required NEP limit should be feasible.

3. High T_c Bolometer on a Si/ Si_3N_4 membrane

Analysis of available data on the $1/f$ -voltage noise of high- T_c films shows that its contribution to the NEP of the detector remains within the requirements, provided that the superconducting film is of good epitaxial quality [2]. To enable epitaxial growth of the superconductor, a single crystalline Si layer is required on top of the Si_3N_4 membrane, of at most 100 nm to minimize the thermal conductance. A cross section of the obtained multilayer structure is shown in Fig. 1. The production of the Si_3N_4 membranes with a single crystalline Si top layer is one of the technological key issues in the production process.

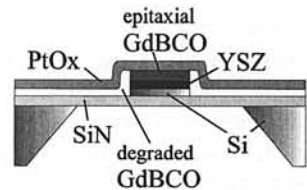


Fig. 1: Cross section of obtained multilayer structure of the bolometer.

4. Bond-And-Etch-Back Technologies

For the production of the $\text{Si}_3\text{N}_4/\text{Si}$ layer two bond-and-etch-back technologies are being investigated, both involving a silicon fusion bonding step between Si_3N_4 and Si. The first route involves the use of a high concentration boron layer, which can be used as an etch stop in KOH/IPA. The process scheme is shown in fig. 2. The second route involves the use of a SOI wafer. By transferring the thin silicon top layer to the nitride wafer it should be possible

to obtain the $\text{Si}_3\text{N}_4/\text{Si}$ layer. In initial bonding experiments it was found that both low stress Si_3N_4 (500 nm and 1200 nm thick) as well as high boron doped surfaces are too rough for fusion bonding. In literature successful bonding results between Si and Si_3N_4 have been mentioned [5,6], but these involved Si_3N_4 layers with a thickness of 300 nm or less. To make these surfaces bondable, a polishing step is needed. It was found that by using a Chemical Mechanical Polishing (CMP) step, previously unbondable Si_3N_4 and boron doped surfaces became bondable [7]. After bonding, the Si wafer is etched back until the etch stop is reached.

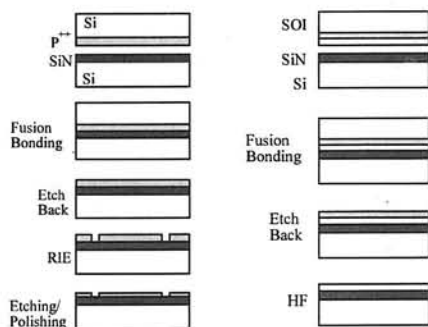


Fig. 2: Process schemes for routes 1 (left) and 2 (right)

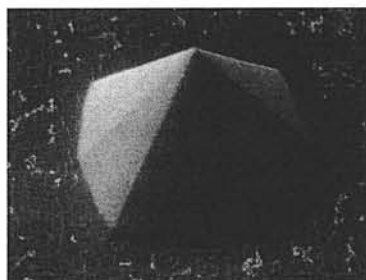


Fig. 3: Pyramidal hillock after KOH/IPA etching

5. Experimental

The first bond-and-etch-back experiments for route 1 were done with 380 μm thick 3" (100) wafers, 10-20 Ωcm . On one of the wafers a 430 nm thick low-stress LPCVD Si_3N_4 layer was grown. The other one was boron doped in a solid source dotation system, to a surface boron concentration of about $3 \times 10^{20} \text{ cm}^{-3}$ and a depth of 5 μm . Both the surfaces were given a CMP treatment, reducing the surface roughness to less than 1 nm, which is necessary for a successful bond.

Prior to bonding the wafers were given a standard clean, using fuming nitric acid (100%) and hot nitric acid (70%, 90° C). An IR camera was used to monitor the initial bonding of the wafers. Annealing was done for 2 hours at 1000° C in N_2 . Etching back was carried out with a mixture of KOH (23.4 wt%), IPA (13.3 wt%) and H_2O (63.3 wt%) at 80° C, resulting in an etch rate of approximately 0.9 $\mu\text{m}/\text{min}$ for undoped silicon. The etch rate of the high boron doped silicon at the surface of the etch stop (with a boron concentration of about $1 \times 10^{20} \text{ cm}^{-3}$) has not been determined exactly yet, but lies in the order of several nm/min. These results are in close agreement with literature [8].

After etching back, a thin silicon layer of 2.5 to 3 μm thick remained on top of the Si_3N_4 . Since the boron doped wafer was not completely bonded, parts of it came off during etching. The remaining silicon layer covered an area of about 40% of the wafer.

Another problem to be solved for route 1 is the formation of pyramidally shaped hillocks, and effect which is well known in anisotropic wet etching. In fig. 3 such a hillock is shown, after etching back and stopping on the high boron doped layer. This particular hillock is about 16 μm high, but also hillocks of 60 μm and higher were present on the surface. The

hillock density is about 3 cm^{-2} . On the surface next to the hillock small patterns are visible, which are believed to be crystal dislocations, caused by the high doping level. The bright structures on the surface are probably some kind of contamination. It is believed that these can be removed by a clean in $\text{H}_2\text{SO}_4/\text{H}_2\text{O}_2/\text{H}_2\text{O}$.

In route 2 the etch stop is provided by the buried oxide (BOX) layer from the SOI wafer. So the thin silicon layer is still unaffected by etching back the bulk of the SOI wafer. Removing the oxide layer with HF finally leaves the thin silicon layer on top of the silicon nitride. The advantage of route 2 is that by using SOI wafers with a Si top layer of several hundred nm only a small amount of Si has to be removed by either polishing or etching to obtain the required thickness. Experiments for route 2 will be carried out in the near future.

6. Conclusions

We expect that combining the $\text{Si}_3\text{N}_4/\text{Si}$ membrane fabrication with the existing technologies as presented in [4] it is possible to prepare HTS bolometers which meet the stated requirements. The proposed routes for the production of the $\text{Si}_3\text{N}_4/\text{Si}$ layers and membranes are still under investigation. The main points of attention at this moment are to increase the bonding yield, and achieve an etched-back surface without hillocks.

The combination of micromachining and superconductive films provides an interesting challenge, leading to new possibilities for the development of high T_c radiation sensors.

7. Acknowledgments

The authors would like to thank C. Gui for carrying out the CMP experiments. This project is funded by the European Space Agency under contract no. 11738/95/NL/PB. The contract manager is Dr. E. Armandillo.

8. References

- [1] J.J. Wijnbergen, P.J.A. de Korte, M.J.M.E. de Nivelle, "Instrumental aspects of a satellite-based fabry-perot equipped with a high- T_c bolometer for detection of stratospheric OH", European Symposium on Satellite Remote Sensing, Paris, 25-28 September 1995
- [2] P.J.A. de Korte, M.J.M.E. de Nivelle, J.J. Wijnbergen, "Bolometer detector for OH-observations", European Symposium on Satellite Remote Sensing, Paris, 25-28 September 1995
- [3] P.L. Richards, "Bolometers for infrared and millimeter waves", J. Appl. Phys. Vol. 76, pp1-24 (1994)
- [4] H. Neff, J. Laukemper, I.A. Khrebtov, A.D. Tkachenko, E. Steinbeiss, W. Michalke, M. Burnus, T. Heidenblut, G. Hefle and B. Schwierzi, "Sensitive high- T_c transition edge bolometer on a micromachined silicon membrane," Appl. Phys. Lett., Vol. 66 (18), pp. 2421-2423 (1995)
- [5] R.W. Bower, M.S. Ismail, B.E. Roberts, "Low temperature Si_3N_4 direct bonding", Appl. Phys. Lett. 62, pp3485 (1993)
- [6] C. Harendt, H.-G. Graf, B. Höflinger, E. Penteker, "Silicon fusion bonding and its characterizations", J. Micromech. Microeng. 2, pp113 (1992)
- [7] C. Gui, J.G.E. Gardeniers, M. Elwenspoek, H. Albers, P.V. Lambeck, "Silicon fusion bonding with chemical mechanical polishing", Proceedings of this conference.
- [8] J.B. Price, 'Anisotropic etching of silicon with $\text{KOH-H}_2\text{O}$ -Isopropyl alcohol', Semiconductor Silicon, Eds. H.R. Huff and R.R. Burgess, The Electrochemical Soc. Priceton, N.Y. pp339 (1973)

SILICON DRIFT DETECTORS FOR THE DETECTION OF X- AND γ -RAYS

H. Valk¹, E. A. Hijzen¹, J. Huizenga¹, C. W. E. van Eijk¹, R. W. Hollander¹,
L. K. Nanver², P. M. Sarro², A. van den Boogaard², J. Slabbekoorn²

Delft University of Technology, The Netherlands

¹Department of Applied Physics, Radiation Technology Group

²Delft Institute of Microelectronics and Submicron Technology (DIMES)

Abstract - Silicon drift detectors can be used for the detection of light, X-rays and charged particles. In combination with a scintillator also γ -rays can be detected. The energy resolution of drift detectors is better than p-i-n photodiodes with the same detection area, because of the low detector capacitance (less than 1 pF for detectors of 1 cm² and hardly scaling with the size). Integration of electronics is very beneficial for drift detectors, because stray capacitances of external bonds will always exceed the detector capacitance and this will limit the detector performance.

We present results obtained with detectors without integrated electronics and we describe the fabrication process which will lead to the incorporation of a JFET and a capacitor onto the detector. With this 'smart' process we aim to measure charge pulses consisting of down to 50 electrons.

1 - Introduction

In the interaction of radiation with matter some or all of the radiation energy is used to excite electrons. In (semi-)insulating materials this means electron-hole pairs. The average energy to create an electron-hole pairs is about 3 times the bandgap (3.6 eV for silicon). The number of electron-hole pairs therefore is a measure for the energy deposited in the detector. When particles or quanta are completely absorbed then the number of electron-hole pairs represent their energy, a main parameter in radiation detection. Other parameters are position and time. Free electron-hole pairs can only be measured if the electrons and holes are separated by an electric field, otherwise they will recombine. The depletion layer in a pn junction can be used for this purpose. For the detection of visible light where the penetration depth is short ($\sim 1 \mu\text{m}$), a normal wafer with a surface junction can be used. X-rays with larger penetration depths need thicker depletion layers. This can be obtained with high voltages over the junction or by reduction of the doping concentration, which will also increase the carrier lifetime [1]. With high-ohmic wafers (bulk concentration $\sim 10^{12} \text{ cm}^{-3}$) and moderate voltages ($\sim 100 \text{ V}$) it is possible to use the whole wafer thickness for radiation detection. With 400 μm thick wafers X-ray energies up to 10 keV can be detected with an efficiency of at least 90 % [2]. The

detection efficiency will drop considerably for higher X-ray energies to only a few percent at 60 keV.

For the detection of γ -rays, with even higher energies, silicon wafers are not the appropriate material. For this purpose a scintillator is often used. The scintillator converts with an efficiency of $\sim 10\%$ the radiation energy into light which can be detected by a silicon detector. With the combination of a silicon radiation detector and a scintillator a γ -ray detector can be made. Due to the low noise properties the drift detector may replace the now dominant photomultiplier tube for the read-out of scintillation light in some applications.

The simplest silicon radiation detection structure is the p-i-n diode where the i stems from the intrinsic (high-ohmic) bulk material. Straightforward derivatives of the p-i-n structure are the strip and pixel detectors with a one respectively two dimensional position resolution.

The following chapters describe the principle, fabrication and use of a special kind of p-i-n diode, the silicon drift detector and the work done to integrate electronics onto the detector.

2 - The drift detector

The silicon drift detector uses the complete wafer thickness for radiation detection. This is obtained with high-ohmic wafers and double sided processing. At this moment the best wafers available are n-type wafers with $\langle 100 \rangle$ orientation. In figure 1 a schematic of a linear and a circular drift detector is shown. The main difference between a p-i-n diode and a drift detector is the reduced area of the readout electrode (anode, n-implantation). The small anode effectively reduces the capacitance of the detector, resulting in an improved energy resolution. The circular drift detector in figure 1.a has no position resolution, the linear drift detector in figure 1.b with multiple anodes has a direct one-dimensional position resolution. With the measurement of the drift time in the detector two-dimensional position resolution can be obtained. The drift time is the time difference between the collection of the holes at the cathodes and the electrons at the anode(s).

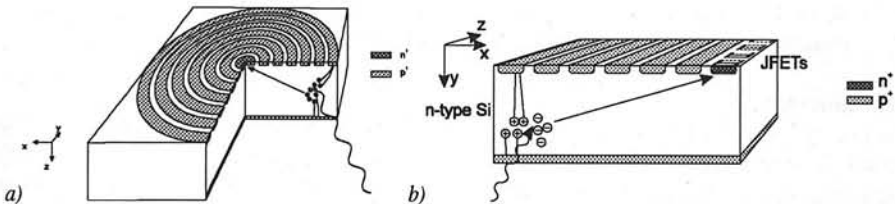


Figure 1 a) A circular drift detector with an anode in the centre of the cathode rings. This detector has no position resolution. b) A linear drift detector with a row of anodes at the side of the detector. In the anodes JFETs are placed. This detector has a 1 or 2 dimensional position resolution.

The drift detector is reversely biased with various voltages at the cathodes, the absolute voltage increasing with the distance from the anode. This will generate a drift field for electrons parallel to the surface in the direction of the anode(s). The holes on the other hand will drift towards the nearest cathode (p-implantation).

Gatti [3] calculated the noise behavior of a silicon detector connected with a preamplifier and filter-amplifier as

$$ENC^2 = \frac{a}{\tau} C_g^2 A_1 + 2\pi a_f A_2 + 2qI_{leak} \tau A_3 \quad (1)$$

where ENC is the equivalent noise charge [electrons], I_{leak} is the detector leakage current [A/cm^2], C_g is the total input capacitance ($= C_{\text{det}} + C_{\text{JFET}} + C_{\text{feedback}}$) [F], τ is the shaping time constant of the filter-amplifier [s], A_1 , A_2 , A_3 are filter constants and a and a_f are the white respectively $1/f$ series noise figures of a JFET, used at the input of the preamplifier.

From this formula it can be seen that the second term sets a constant noise level determined by the processing and the noise will decrease if both the leakage current and the input capacitance are low.

The sub-pF drift detector capacitance offers possibilities for a low ENC, but without integrated electronics the input capacitance always increases with some pF parasitic bonding capacitance. Leakage currents are an artefact of each silicon diode including the drift detector. This current is thermally generated and a function of the number of impurities or crystal disorientations in the bulk or at the interface. Cooling of the detector is a means of reducing this current, but requires a complicated measurement setup. Other ways to reduce the leakage current can be found in the processing of the detectors.

The leakage current is usually drained by a large feedback resistor ($\sim \text{G}\Omega$) in the preamplifier resulting in an increased ENC. A charge sensitive preamplifier circuit without a noisy feedback resistor is introduced by Bertuccio [4] and offers low noise possibilities. The leakage current is drained through the slightly forward biased gate-source junction of the input JFET, without additional components. If the JFET and the feedback capacitor are added onto the drift detector the preamplifier input is free of the parasitic bonding capacitance. A JFET can be built directly into the anode, where the anode now serves as the back gate of the JFET.

3 - Fabrication

The fabrication of 'standard' silicon drift detectors requires processing on both sides of n-type $\langle 100 \rangle$ high-ohmic wafers. After growing of a thermal oxide of 400 nm (8 hours at 1100 °C in O_2) the alignment marks are positioned on both sides of the wafer. Each side of the wafer has a p-type implantation through the oxide (boron, dose = $1 \cdot 10^{15} \text{ cm}^{-2}$, energy = 120 keV), the front side also receives an n-type implantation directly into the silicon (arsenic, dose = $1 \cdot 10^{15} \text{ cm}^{-2}$, energy = 40 keV). The implanted impurities are activated at 600 °C for 30 minutes. After activation contact holes to the p-implantations are made and a 600 nm thick aluminum layer (with 1% Si) is sputtered for contacting. Plasma etching is used during the whole process. The activation temperature is optimized for a low leakage current, but hampers the direct integration of electronics because of a low activation of the dopants.

For the 'smart' process the anode implantation is replaced by an n-type selective epitaxial layer containing a p-JFET. On top of this JFET a double metal feedback capacitor is placed. In the process schedule this JFET is processed before the detector implantations and is activated at 950 °C for 30 minutes. The processing of the JFET and the capacitor follows closely the DIMES-03 BiFET process [5], which contains a 1GHz p-JFET. The high temperature anneal only activates small areas of the wafer (the JFETs only) and a small influence on the leakage current is expected.

In previous process runs the feedback capacitor was formed by a MOS structure between the (top)gate and the aluminum. The dielectric consisted of a LPCVD oxide layer of 50 nm deposited at 700 °C. This process was not very successful, because of diffusion of boron from the drain and source contacts into the LPCVD oxide, what resulted in poor JFET contacts.

'Standard' silicon drift detectors can now be produced with success. The 'smart' drift detector process is still under development.

4 - Measurements

Up to now only the detection properties of 'standard' drift detectors could be tested. The leakage current of these detectors is 1 nA/cm^2 at room temperature, comparable with values of other manufactures [6]. Cooling reduces the leakage current with a factor of 2 per 10 K. The noise however did not diminish accordingly. This behavior is still under study.

The energy resolution, measured on one anode of a multianode drift detector is better than for a single anode drift detector of the same size since only a small fraction of the leakage current is collected per anode. Diffusion of electrons during the drift however causes a division of the total signal charge over several anodes. So measuring at one anode many events will be seen with only a fraction of the total charge, resulting in a low energy tail in the spectrum (figure 2, 1 anode). When some anodes are tied together the ratio of events with complete over incomplete charge collection will improve, resulting in a reduction of the low energy tail (figure 3, 3 anodes). When more anodes are tied together the energy resolution worsens, due to the increased leakage current (figure 2, 5 anodes). The collection area of each anode is $250\text{-}6000 \text{ }\mu\text{m}^2$ in this case. For the best case of '3 anodes' the noise level was about $\text{ENC} = 220$ electrons at room temperature, still far from the 13 electrons that Lutz [7] measured with a smart drift detector at 223K.

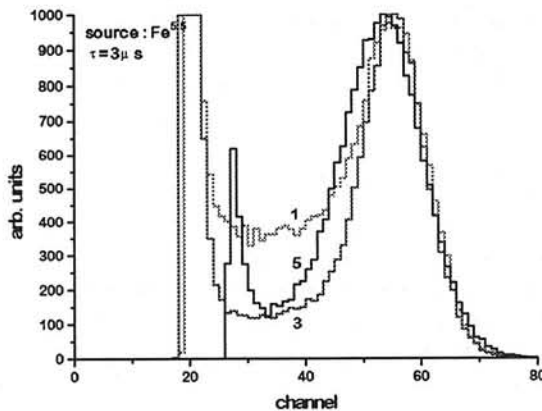


Figure 2 ^{55}Fe spectra (5.9 keV X-ray) measured with 1, 3 and 5 anodes of a linear drift detector. The collection area per anode was $250\text{-}6000 \text{ }\mu\text{m}^2$.

For a circular drift detector γ -rays have been measured using a CsI(Tl) scintillator crystal. The active area of the drift detector was 0.44 cm^2 . In figure 3 the energy spectrum is shown. The energy resolution of the 662 keV peak was 7.6 % FWHM, only slightly worse than the 6.7 % measured with a photomultiplier-tube using the same crystal. The current drift detector process is not optimized for light detection and e.g. a non-reflective entrance window and a shallow dead layer will improve the energy resolution. Olschner [8] has measured energy resolutions of 5 % for drift detectors using the same type of crystal and radiation source.

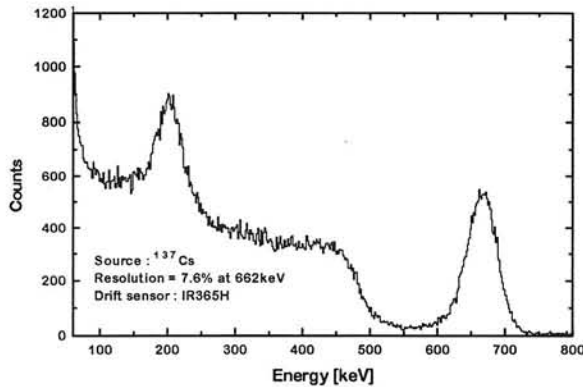


Figure 3 Energy spectrum of ^{137}Cs (662 keV γ -ray) measured with the combination of a CsI(Tl) scintillator and a circular drift detector with an active area of 0.44 cm^2 .

5 - Conclusions

At the moment a drift detector process has been developed and results demonstrated for X-rays and γ -rays. The energy resolution however is limited by the parasitic capacitance of external bonding. The first improvements therefore focus on integrated electronics, in parallel with reduced charge division in multi anode drift detectors. In later stages improvement of the light detection will be studied.

References

- [1] S. Wouters, *Diffusion-based silicon radiation detectors*, Ph.D. thesis, Delft University of Technology, 1992
- [2] E.M. Schooneveld, *Position Sensitive Silicon Radiation Detectors*, Ph. D. thesis, Delft University of Technology, 1993
- [3] E. Gatti, P.F. Manfredi, M. Sampietro, V. Speziali, *Suboptimal filtering of 1/f-noise in detector charge measurements*, Nucl. Instr. & Meth. A297, 1990, pp 467
- [4] G. Bertuccio, P. Rehak, D. Xi, *A novel charge sensitive preamplifier without the feedback resistor*, Nucl. Instr. & Meth. A326, 1993, pp 71
- [5] L.K. Nanver, E.J.G. Goudena, H.W. van Zeijl, *Optimization of base-link in fully-implanted NPNs*, Elec. Lettr. 29(16), 1993, pp 1451
- [6] G. Bertuccio, L.Fasoli, C.Fiorini, M. Sampietro, *Spectroscopy Charge Amplifiers For Detectors With Integrated Front-End FET*, IEEE Trans. Nucl. Sci. 42(4), 1995, pp 1399
- [7] G. Lutz, *Silicon radiation detectors*, Nucl. Instr. & Meth. A367, 1995, pp. 21-33
- [8] F. Olschner, *Silicon Drift Photodiode Array Detectors*, to be published IEEE Trans. Nucl. Sci.

ACTIVE INTERFERENCE FILTERS USING SILICON-COMPATIBLE MATERIALS

D.P. Poenar, P.J.French and R.F.Wolffenbuttel

*Electronic Instrumentation Laboratory,
Department of Electrical Engineering,
Delft University of Technology,
Mekelweg 4, 2628 CD, Delft,
The Netherlands.*

ABSTRACT

Colour sensors with a spectral response programmable by design that provides improved flexibility can be obtained using a structure that filters and detects light at the same time. Measurements of a simple test structure demonstrated the possibility of implementing such a thin film colour sensor.

1. INTRODUCTION

The spectral response of a photodiode depends on the transmission of impinging light through an optically optimized multilayer structure and the collection of photo-generated charge-carriers in a $p-n$ junction. Both effects can be used to control, by design, the spectral response of a colour sensor. With the first approach, an interference filter can provide a peaked response for a certain part of the spectrum [1, 2], or a flat response over a part of the spectrum [3], depending on the type and structure of the filter.

The second approach uses the dependence of the collection efficiency of photogenerated charge on the wavelength dependence due to the dispersion of the extinction coefficient k of monocrystalline silicon in the visible range of the spectrum which results from the indirect bandgap of silicon. This effect has been used for colour sensing by controlling the collection depth into bulk silicon using the reverse voltage across a shallow junction [4].

However, the disadvantage of a normal interference filter is that it does not realize any opto-electrical conversion and three different filters on top of separate detectors are required to provide the primary colour signals. On the other hand, the implementation based on the wavelength dependence of k lacks design flexibility and is also limited by the fabrication compatibility with standard microelectronic processing. A colour sensor with an 'active' multilayer structure which filters and detects light at the same time combines the advantages of the previous approaches and eliminates their drawbacks. The entire structure must be antireflectant (AR) to maximize the opto-electrical conversion efficiency. Consequently, a colour sensor using such an 'active' AR interference filter should be composed of:

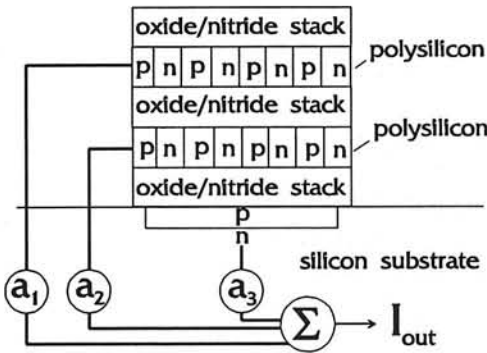


Fig. 1: Schematic structure of a colour sensor based on an 'active' thin film interference antireflectant filter.

1) a stack of Si compatible materials on top of a silicon wafer, with photodiodes in polysilicon layers and in the substrate (the 'active' regions) which provide the primary 'blue', 'green' and 'red' responses; and

2) weighting and summing circuits integrated in the substrate, which enable the programming of the overall response of the entire sensor.

Both flexibility and compatibility requirements are met when using such 'active' interference filters with on-chip weighting circuits. Furthermore, the 'active' regions are totally isolated from each other and the highly integrated approach makes on-chip integration of auxiliary signal conditioning circuits possible. Fig.1 shows schematically the structure of such a smart colour sensor.

2. PRACTICAL REALIZATION

Three steps are necessary to reach the final structure of an 'active' interference filter:

2.1. Determining the dispersion of the available materials.

For the different layers which must be used in the filter the literature data can be only orientative due to differences in deposition processes and equipment. Measurement data of dispersion of the refractive index n for two polysilicon layers in a multiple oxide-poly-oxide-oxide sandwich structure were carried out. The characteristics of the bottom polySi proved to be closer to those of monocrystalline Si [5] because its structure is recrystallized to a larger extent than that of the top polySi. This is due to the fact that it has suffered the effects of a higher thermal budget during the deposition and *in-situ* anneal of the top polySi.

2.2. Optimizing the technological processing for the best electrical characteristics of polySi diodes.

The polysilicon diodes are quite different from their monocrystalline counterparts and they are strongly influenced by the polysilicon grain structure and by the subsequent processing. Fig.2 shows measured Gummel plots for two types of lateral polysilicon diodes, together with the characteristic of a monocrystalline diode. The resistance in parallel with the diode is the most important parasitic component, due to the grain boundaries states that shortcut the $p-n$ junction. The "diffused" diode (obtained using a POCl_3 diffusion prior to the implant of the p^+ and n^+ regions) presents a better characteristic than the "implanted" diode, which was not subjected to such a treatment. This is due to the passivation of most of the carrier traps at the grain boundaries with phosphorus atoms which practically eliminates the parallel

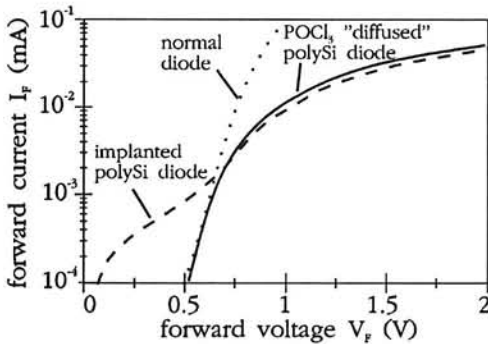


Fig. 2: Measured current-voltage characteristics of different diodes.

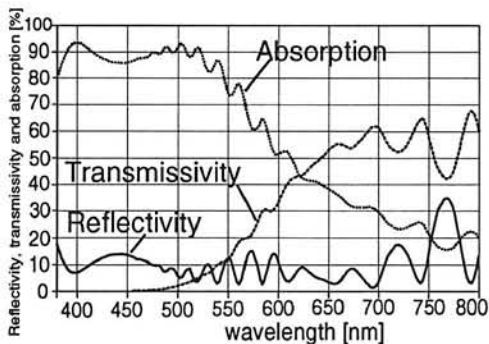


Fig. 3: Theoretical reflectivity, transmissivity and absorption of the multilayer resulted from optimization of an LHL structure.

parasitic resistance ($R_p \approx 1 \text{ k}\Omega$ for the "implanted" diodes, compared to $0.12 \text{ M}\Omega$ for the POCl_3 diffused polysilicon diodes) so that the series resistance ($R_s \approx 24 \Omega$) remains the only parasitic component.

2.3. Designing and optimizing AR filters.

Although an AR coating can be designed using several methods [6, 7], the simplest design approach is to start from an equivalent HLH or LHL layer (high and low refractive index materials are polySi and SiO_2 , respectively) and then to find matching structures with the substrate and the air. The simulated performance of a final structure obtained after computer optimization of such an LHL SiO_2 -polySi- SiO_2 combination is shown in Fig.3. It can be seen that it is characterized by good optical performances: the reflectivity in the entire visible range is $\sim 10\%$ whereas the transmissivity has an approximately linear increase up to $\sim 55\%$ for most of the 'red' region ($\sim 650\text{--}780 \text{ nm}$) of the spectrum.

Initial tests were performed with a simple structure in order to demonstrate the feasibility of the presented colour-detecting principle. The measured spectral power response of a lateral diode with a total area of about $1.26 \times 10^6 \mu\text{m}^2$ (realized in a polySi layer 4000 \AA thick) is shown in Fig.4. The shift of the measured curve relative to the theoretical one is due to different characteristics of the polySi as compared to the expected ones.

Present work is directed towards implementation of more complex structures, with better AR responses and improved sensivity of the polySi photodiodes.

3. CONCLUSIONS

'Active' antireflectant interference filters which detect light in polysilicon layers as well as in the substrate can be a solution to both flexibility and compatibility requirements.

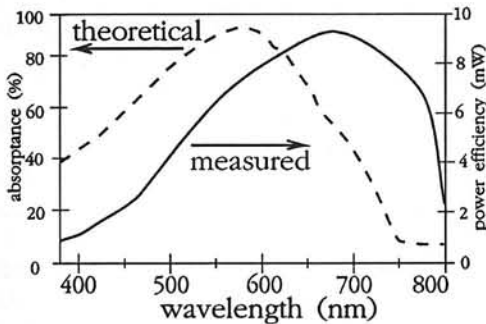


Fig. 4: Measured spectral response of a photodiode realized in the polysilicon layer of a test structure.

detection in photodiodes realized both in polysilicon layers and the monocrystalline substrate.

4. ACKNOWLEDGEMENTS

The authors are indebted to C. de Boer and P.M. Sarro of the Delft Institute for Microelectronics and Submicron-technology (DIMES) for their support in the practical realization of the structures.

5. REFERENCES

1. R.S. Popovic, K. Solt, U. Falt, Z. Stoessel, 'A Silicon Ultraviolet Detector', *Sensors and Actuators*, vol. A21-A23 (1990), pp.553-558.
2. A.S. Glass and R. Morf, 'Optimizing the Performance of Spectrally Selective Photodiodes by Simulated Annealing Techniques', *Sensors and Actuators*, vol. A21-A23 (1990), pp.564-569.
3. R.F. Wolffenbittel, 'Photodiodes in Polysilicon with an Electrically-programmable UV Response', *Sensors and Actuators*, vol. A21-A23 (1990), p.559-563.
4. M. Bartek, P.T.J. Gennissen, P. Sarro, P.J. French and R.F. Wolffenbittel, 'An integrated colour sensor using selective epitaxial growth', *Sensors and Actuators*, vol. A41-42 (1994), pp.123-128.
5. *Properties of silicon*, EMIS Datareviews Series No.4, INSPEC, The Institution of Electrical Engineers, London & New York, 1988, chapter 28.
6. H.A. Macleod, *Thin-film Optical Filters (the second edition)*, Adam Hilger Ltd, Bristol, 1986, chapters 2 and 3.
7. A. Thelen, *Design of Optical Interference Coatings*, McGraw-Hill Company, New York, 1988, chapters 2, 3 and 4.

Several different approaches can be used in order to design an AR interference filter with 'active' polysilicon layers but the simplest and therefore, the most feasible designs are obtained using the coatings resulted after optimization of an initial LHL structure (with 'L' = SiO₂ and 'H' = polySi). Their practical implementation is possible but it is strongly dependent on two technological factors:

a) the possibility of depositing thin dielectric layers with an accurate control of the desired refractive index and with good reproducibility; and

b) the capability of realizing *p-n* junctions in polysilicon with good electrical characteristics.

Initial experiments on simple test structures confirmed the possibility of implementing a colour sensor based on light

A Humidity Sensitive Capacitor Based on a Porous Silicon Dielectric

G.M. O'Halloran, M.Kuhl¹, P.J. Trimp, P.J. French

TU Delft, DIMES, Dept. of Electrical Engineering,
Laboratory for Electronic Instrumentation, Mekelweg 4,
2628 CD, Delft, The Netherlands.

Tel: +31.15-278-6518 Email: G.oHalloran.et.tudelft.nl
¹Dept. of Electrical Engineering, TU Chemnitz-Zwickau, Germany

Abstract. Porous ceramics have been used to make humidity sensors. The use of porous silicon allows the development of smart humidity sensors. This paper will focus on optimising the structure of the porous silicon layer to form capacitors with high sensitivity and fast response times. The effect of both HF concentration and current density on the porous structure will be examined. SEM is used for the structural characterisation of the porous layer.

1- Introduction

Porous silicon is essentially crystalline silicon with channels or pores preferentially etched into it, giving it a very large surface area. Porous silicon can be formed electrochemically by anodic dissolution of silicon in solutions containing hydrofluoric acid (HF). The structure of the resulting porous layer is highly dependant on; the doping type and concentration of the silicon substrate, HF concentration, and the anodic current density. Porous silicon has found applications in dielectric isolation [1], in micromachining as a sacrificial layer [2], and has been investigated for its photo and electroluminescent properties [3]. Some work has already been reported on the use of porous silicon as a dielectric material for capacitive humidity sensors [4,5]. In this application the porous silicon layer forms the dielectric in much the same way as porous alumina films have previously been used [6]. Figure 1 shows a schematic diagram of the test structure. If the pore diameters are small enough, water molecules will condense inside the pores causing a change in the permittivity of the layer. This change is then measured as a change in capacitance and related to the relative humidity change. In this paper the effect of changing the structure of the porous layer will be examined.

2- Experimental

Preliminary investigations have been carried out using p-type silicon 2-5 $\Omega\cdot\text{cm}$. Figure 2 shows a schematic diagram of the formation cell. The silicon forms the positive electrode (anode) of the cell, and the platinum electrode completes the circuit. The electrolyte is a mixture of hydrofluoric acid (HF) and an additive to reduce the surface tension in order to allow hydrogen gas to escape more freely. After formation of the porous layer, a gold coating of approximately 300 Å thickness is sputtered on top in a disc pattern. The area of the device is $7.85 \times 10^{-3} \text{ cm}^2$. The gold and backside aluminium contact of the silicon form the plates of the parallel plate capacitor. The depth of the porous layer was measured by stripping it away in a dilute KOH solution and measuring the step height using a surface profiler. The porosity of the layer was measured using the weight change method [7]. The test devices were tested in an environmental test chamber (Heraeus Vötsch HC 7020) where the relative humidity was stepped from 10% to 95% at a constant temperature of 40°C. The device capacitance was measured by a Hewlett Packard 4020 LCR meter at 100kHz.

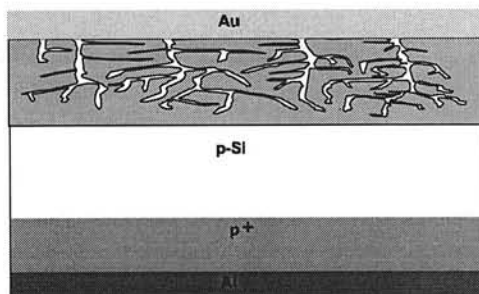


Figure 1 Schematic diagram of the test capacitor

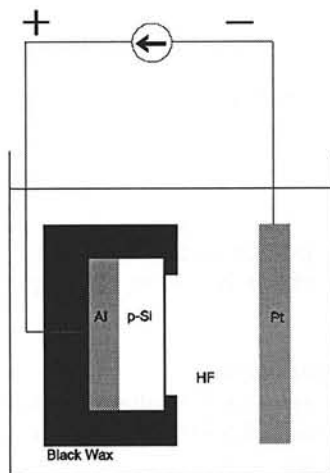


Figure 2 Porous Silicon Formation Cell

3 - Results

3-1 HF Concentration

In this set of experiments the HF concentration was varied between 30-70% in steps of 10%. In all cases, the electrolyte contains 1:1 HF:Ethanol (100%). Also, the current density was kept constant at 10 mA/cm^2 and reaction time at 1 minute. Under such conditions the depth of the porous layer formed was approximately $0.6 \mu\text{m}$. Table 1 summarises the result of these tests, which are also plotted in Figure 3. The sensitivity quoted in Table 1 refers to the total change in capacitance divided by the capacitance at 10% relative humidity. The time constant (τ) quoted is the time taken for the capacitor to reach 63% of its final value. SEM images of these layers revealed a wide distribution of pore diameters which did not change dramatically for different HF concentrations, although there seemed to be a slight increase in diameters at lower HF concentrations.

Table 1 : Summary of HF Variation Tests

HF%	Por%	τ /min	Sens%
30	70	15.0	749
40	65	13.5	543
50	60	16.0	474
60	55	18.0	143
70	50	13.0	15

Table 2 : Summary of Current Variation Tests

I /mA.cm ⁻²	τ /min	Sens	Depth/ μ m
5	12	840	0.32
10	15	749	0.66
20	11	695	1.52
40	9	530	2.84
60	9	199	4.12

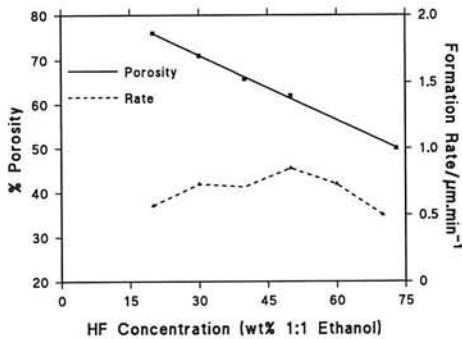


Figure 3 Effect of Changing the HF Concentration

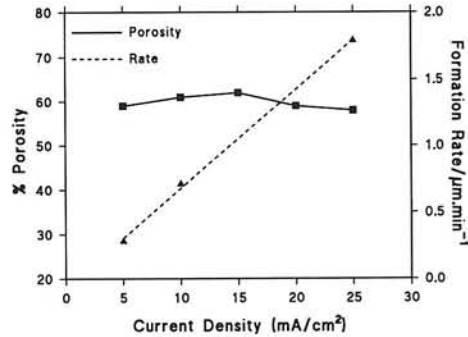


Figure 4 Effect of Changing the Current Density

3-2 Current Density

In this set of experiments the current density was varied between 5 and 60 mA/cm² while keeping the HF concentration at 30% (1:1 ethanol), and reaction time at 1 minute. Again the results are summarised in Table 2 and diagrammatically in Figure 4. SEM images of the porous layers formed using different current densities are shown in Figures 5 and 6. It can be seen that as the current density was increased the size of the pore diameters also increased.

3-3 Effect of Additives

Experiments have been carried out where the ethanol added to the HF solution was replaced by acetonitrile and iso-propyl alcohol. Using SEM it can be seen that these substances modify the shape of the pores. Initial results of capacitors formed using these additives seem to have higher response speeds. SEM images of these porous layers show that the shape of the pores, rather than the dimensions, change with different additives.

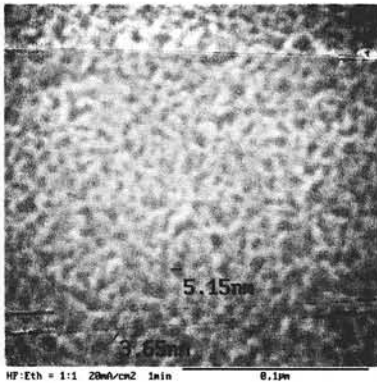


Figure 5 SEM of porous silicon prepared at $20\text{mA}/\text{cm}^2$ in $40\%\text{HF}(1:1 \text{ Ethanol})$

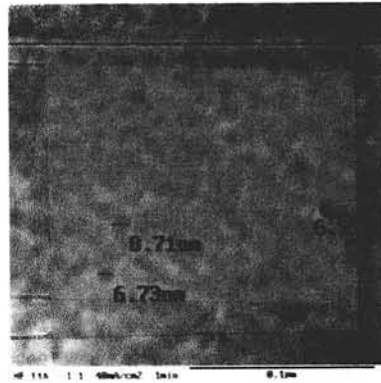


Figure 6 SEM of porous silicon prepared at $40\text{mA}/\text{cm}^2$ in $40\%\text{HF}(1:1 \text{ Ethanol})$

4 - Conclusions

From the initial structural characterisation of porous silicon formed in p-type substrates ($\sim 10^{17} \text{cm}^{-3}$) it was found that:

- (1) the porosity was a function of the percentage of HF in solution, and not current density, in the range 5 to $25 \text{mA}/\text{cm}^2$
- (2) the rate of formation depended more strongly on the value of current density than HF concentration
- (3) the pore diameter seems to be very dependent on the current density value, and to a lesser extent on the composition of the solution.
- (4) capacitors with the best response in terms of percentage sensitivity were formed using low current density and low concentration of HF
- (5) the response speed of the capacitors appeared to improve for larger pore diameters however from the results of the additives it seems the response speed may be more dependant on the shape of the nano-sized pores
- (6) it is possible that other additives, besides ethanol, can improve the structure of the porous layer in such a way that its capacitance response improves. Further investigation is required to establish the exact nature of these changes.

Acknowledgements

The authors are grateful to members of DIMES for their support in this project. This project is funded in part by STW Project number 55.3690.

References

1. Bomchil G. *et al*, Microelect. Eng., 8, (1988), pp.293-310
2. Gennissen P.T.J. *et al*, Proc. ESSDERC '95, Sept. 25-27, The Hague, The Netherlands pp.593-596
3. Kaneko H., French P.J., Wolfenbuttel R.F., J.Luminescence, 57 (1993), pp.101-104
4. Anderson R.C., Tobias C.W., Muller R.S., Sensors and Actuators A21-23 (1990), pp.835-839
5. Sweet J.N. *et al*, Proc. IEEE 41st Electronic Components and Technology Conf. (1991), pp.731-7376.
6. Khanna,V.K.,Nahar R.K.,Sensors and Actuators, 5 (1984), pp.187-198
7. Herino,R. *et al*, J.Electrochem.Soc., 134, 8, (1987), pp.1994-2000

On-chip micromachined corrector of a focal distance.

G. Vdovin, S. Middelhoek

Laboratory of Electronic Instrumentation, Delft University of Technology,
P.O.Box 5031, 2600 GA, Delft
E-mail: gleb@ei.et.tudelft.nl

P.M. Sarro, DIMES, P.O.Box 5053, 2600 GB Delft

G. Nützel, TNO-TPD, P.O.Box 155, 2600 AD Delft

Abstract

Simple electrostatically controlled on-chip corrector of the optical aberration of defocus is reported. The corrector is fabricated by means of bulk silicon micromachining. The device consists of a thin circular nitride membrane which is coated with a reflective layer of aluminum. The curvature of the membrane is controlled by applying the appropriate voltage to the aluminum electrode which is placed under the membrane.

Mixed (mechanical, optical, electrical) technologies are traditionally used for the fabrication of active and adaptive optical components [1, 2]. The combination of technologies leads to very high fabrication costs. Different approaches to the design and fabrication of adaptive mirrors have been reported, but still, high prices of adaptive optical components are considered to be acceptable.

Introduction of an inexpensive and uniform micro-fabrication technology [3] into the field of adaptive optics facilitates a rapid progress mainly because it reduces the fabrication costs and introduces the possibility of mass production. Silicon micromachining and hybrid packaging have been recently successfully applied to the fabrication of various adaptive optical components [4, 5, 6].

In our report we describe the technology and characteristics of a micromachined adaptive mirror with a variable focal distance. The device continues the line of micromachined optical devices developed in Delft: [6, 7, 8]. The mirror is controlled by a single voltage, ensuring simplicity together with a reasonably good quality of correction of the optical aberration of defocus in a wide range of focal distances: ($\infty \dots 1\text{m}$). The schematic section of the mirror is shown in Fig. 1.

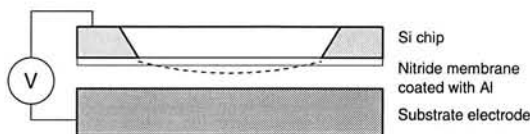


Figure 1: Cross section of the micromachined varifocal mirror.

A freely suspended deformable nitride membrane, forming the flexible substrate of the mirror, is fabricated by etching through the bulk of the wafer in a water/KOH solution. The main advantage of the KOH etching is the very slow etch rate of nitride, securing the high surface quality of the released membrane. Because of the directional selectivity, the final shape of the opening etched in a standard Si wafer is always rectangular. For correction of defocus, the deformed membrane must have a parabolic shape. A good approximation to the parabolic shape can be obtained by means of electrostatic deformation of a thin membrane stretched on a circular frame. Rectangular membrane has a cushion-like response and may not be used for correction of defocus. A special etch mask was developed to obtain a membrane with approximately circular aperture by means of a standard anisotropic KOH etching. The negative corner compensation applied resulted in a fabrication of "approximately circular" membrane with a diameter of 10mm, having RMS deviation from the circular contour of less than 0.1 mm. The absolute value of this error does not depend on the diameter, therefore larger circular membranes can be fabricated with relatively better approximation. The etching mask and a wafer with etched through circular openings are shown in Fig. 2.

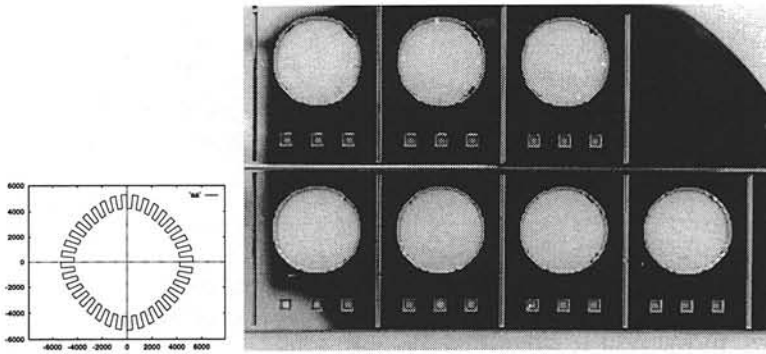


Figure 2: Example geometry of the etch mask used to obtain approximation to a circular contour, and Si wafer with circular openings etched with different compensation masks. Note the "normal" anisotropically etched rectangles below the circular openings.

Fabricated membranes demonstrate small stepwise deviation from a circular shape. For a membrane stretched on a contour with radius a and deformed by a constant pressure, the deviation from the nearest parabola with radius of curvature R due to the error in the contour shape δa is given by a formula: $\varepsilon = a\delta a/R$, or $\varepsilon/\delta a = a/R$. Substitution of numerical data into the last expression shows that practical requirements to the geometry of the membrane contour are very strict. For example, to achieve $\varepsilon = 0.1\mu\text{m}$ for a mirror with a diameter of 1 cm at the focal distance of one meter, the deviation of the etched contour from a circle must be less than $20\mu\text{m}$. Currently achieved value of deviation of $100\mu\text{m}$ corresponds to $\varepsilon = 0.5\mu\text{m}$.

The assembled mirror, consisting of a 10mm-diameter membrane mounted $50\mu\text{m}$ over the single control electrode was tested in a Twyman-Green interferometer with a plane $\lambda/20$ reference. The interferograms of both the initial and the deformed mirror surface are shown in Fig. 3.

Experience of the first experiments is summarized in the following conclusions:

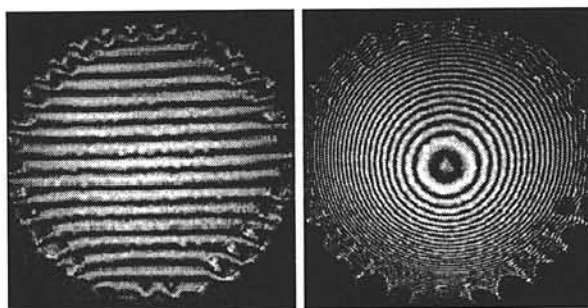


Figure 3: Interferogram of the initial mirror surface (left), the same for a membrane with the surface, deformed by a control voltage of 150V (right).

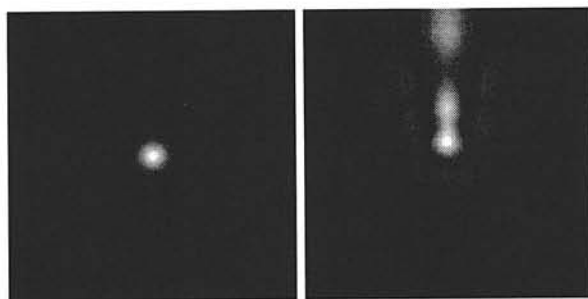


Figure 4: Focal distributions produced by the ideal membrane mirror (left) and by the mirror with 2.5% nonuniformity of the air gap (right)

- The high spatial frequency surface deformation, observed along the edge of the initially plain mirror, is caused by the bad quality of the evaporated *Al* coating. These regions were non-uniformly shadowed by the remnants of the compensation mask, which resulted in irregular variations of the coating thickness. The remnants of the compensation mask may be easily removed before coating, therefore this defect will not be observed in future runs.
- The high spatial frequency fringe deformation along the contour of the deformed mirror is caused by the stepwise geometry of the mirror edge. This defect is a feature of the technology used. It looks not very attractive on the interferogram, but the contribution of the edge aberration into the total wavefront RMS is comparatively low.
- The deformed mirror has asymmetrical coma-like aberration. The amplitude of the aberration reached 0.75λ at the focal distance of 1m. We have found that the aberration is caused by the initial nonuniformity of the gap between the membrane and the control electrode. Numerical simulation (see Fig. 4) showed that a simple tilt, causing 2.5% difference of the gap between the top and the bottom edges of the membrane produces an aberration which is very similar to the observed one. The spherical aberration, produced by the non-uniform electrostatic pressure in the gap under the deformed membrane [9] was at least an order of magnitude lower.

Experimental data concerning the possibility of correction of the aberrations caused by the misalignment will be present at the conference.

- The quality of the Al coating is not high enough for critical applications. We use a standard IC metallization step to produce Al coating. Deposition of an optical-grade Al coating will certainly reduce the amount of scattered light.
- Sharp edges of the steps, forming the membrane contour, concentrate the mechanical stress. A fatigue resistance of the mirror have to be proven by a long-term testing. At present we work on a technology of mixed anisotropic/isotropic etching, which will smooth the contour shape and therefore considerably improve the fatigue resistance.

Described varifocal mirror is simple, has a reasonably good optical quality and after some improvements can be fabricated in the line of standard IC process, including only one micromachining step of etching the bulk silicon in KOH. After obtaining additional proofs of its long-term reliability, the device may find many applications in modern optoelectronics.

References

- [1] R.K. Tyson, Principles of Adaptive Optics, Academic Press (1991)
- [2] R.P. Grosso, M. Yellin, The membrane mirror as an adaptive optical element, Journal of the Optical Society of America **67**, 399 (1977)
- [3] K.E. Petersen, Silicon as a mechanical material, Proc. IEEE **70**, 420 (1982)
- [4] M. Hisanaga, T. Koumura, T. Nattori, Fabrication of 3-dimensionally shaped Si diaphragm dynamic focusing mirror, Proc. IEEE workshop on Micro Electro Mechanical Systems, p. 30, (1993)
- [5] L.M. Miller, M.L. Argonin, R.K. Bartman, W.J. Kaiser, T.W. Kenny, R.L. Norton, E.C. Vote, Fabrication and characterization of a micromachined deformable mirror for adaptive optics applications, Proc. SPIE **1945**, 421-430 (1993)
- [6] G. Vdovin, P.M. Sarro, Flexible mirror micromachined in silicon, Applied Optics **34**, 2968-2972 (1995)
- [7] G. Vdovin, S. Middelhoek, L. Sarro, Deformable Mirror Display with Continuous Reflecting Surface Micromachined in Silicon, Proceedings IEEE workshop on Micro Electro Mechanical Systems, 61-65 (1995)
- [8] G. Vdovin, Spatial light modulator based on the control of the wavefront curvature, Optics Communications **115**, 170-178 (1995)
- [9] G. Vdovin, S. Middelhoek, M. Bartek, P.M. Sarro, D. Solomatine, Technology, characterization and applications of adaptive mirrors fabricated with IC-compatible micromachining, in Adaptive optical systems and applications, Proc. SPIE **2534**, 116-129 (1995)

FLEXIBLE PACKAGE FOR A TACTILE SENSOR ARRAY

Zhi Chu

Delft University of Technology, DIMES,
Laboratory for Electronic Instrumentation, P.O.Box 5031,
2600 GA Delft, The Netherlands,
Tel: 31-15-2786518, Fax: 31-15-2785755, E-mail: chu@ei.et.tudelft.nl

ABSTRACT

A package is designed to make a flexible tactile sensor array. Silicon/glass sensing islands are sandwiched between an elastomer layer and a polyimide substrate. Polyimide PI2611 from DuPont is selected as it is resistant to HF acid, which is used to separate the islands. The top elastomer can be a rubbery material with Young's modulus in the range of 0.1-10 N/mm². It has little influence on the sensitivity.

INTRODUCTION

A flexible package is essential for tactile array sensors. As many of them are designed to be functionally equivalent to the human finger skin, tactile sensors must be compliant to be able to mount on convex fingertips. The packaging design should be an integral part of the sensor design to satisfy the compatibility between the sensor fabrication and packaging techniques.

In 1988 Barth [1] proposed a flexible structure based on techniques developed for a thermometer array. A sensor array was sandwiched between two polyimide layers. Separated sensing islands were interconnected by gold leads embedded between the silicon and the bottom polyimide. The paper addressed the robustness and yield considerations, and no particular sensor structure or the correspondent processing were mentioned. In 1994, the same structure was further developed by Beebe [2] emphasising durability. Polyimide PI2611 from DuPont was evaluated as a suitable material. Epoxy was used to reinforce the connection between the rigid silicon islands and the flexible polyimide. The technique was developed without considering particular sensor structures.

A top elastomer layer is conventionally used for tactile sensors as a protection and force buffer. The materials used range from silicone resins [3] to polyimides [1]. This layer renders an important mechanical contribution to the sensor performance. However, study of the mechanical aspects is very limited.

This paper investigates a flexible package for a silicon capacitive tactile sensor. The process includes IC processing, Bulk MicroMachining (BMM) and flexible packaging. Prior to describing the process, the mechanical properties of elastomers are studied.

FLEXIBLE TACTILE SENSOR

The proposed structure consists of four layers: elastomer, silicon, glass and polyimide. The silicon and glass together form the sensing islands, which are interconnected by a metal layer embedded between the glass and the polyimide. Polyimide PI2611 is resistant to the isotropic etchant HF, and is therefore selected. The filling of the elastomer reinforces all the connection parts, and guarantees a high durability.

To date, silicon/glass chips ($1 \times 1 \times 0.1 \text{ cm}^3$) containing 3×3 elements have been made [4]. The sensing is based on the capacitive principle. For every sensing element there are four capacitors between the silicon and the glass. The capacitance changes in response to the applied forces. For devices without the top elastomer, forces are exerted directly on the silicon mesa. The sensitivity S_n to normal forces F_n is

$$S_n = \frac{\partial \Delta C}{\partial F_n} = \frac{2 \alpha \epsilon_0 \epsilon_r a^2 L^2}{E t^3 d^2} \quad (1)$$

where, E is Young's modulus of silicon, and α is a constant. For the current device, $a=900 \mu\text{m}$, $b=600 \mu\text{m}$, $L=600 \mu\text{m}$, $\alpha=0.0064$, $d=1 \mu\text{m}$, $t=10 \mu\text{m}$, and thus $S_n=2 \text{ pF/gf}$.

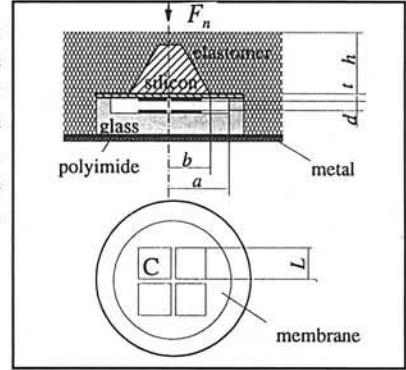


Fig.1 One sensing element.

ELASTOMER

The elastomer layer is substantially thicker than the deformation membrane. A stiff elastomer can considerably decrease the sensitivity. Material selection should be based on evaluating the mechanical behaviour of this layer.

Elastomers are a large class of materials ranging from nature rubbers to synthetics. These hyperelastic materials feature the ability of undergoing recoverable extensions of many hundreds of percent. Another important property is that most of the elastomers are nearly incompressible. These two features dictate a completely different method of modelling elastomers compared to more conventional materials.

First, stress is deviated from the energy function W of the element volume. The principle stress in Direction X for example is given by

$$\sigma_x = \frac{1}{\lambda_y \lambda_z} = \frac{\partial W(I_1, I_2, I_3)}{\partial \lambda_x}, \quad I_1 = \lambda_1^2 + \lambda_2^2 + \lambda_3^2, \quad I_2 = \lambda_1 \lambda_2 + \lambda_2 \lambda_3 + \lambda_3 \lambda_1, \quad I_3 = \lambda_1^2 \lambda_2^2 \lambda_3^2 \quad (2)$$

where, λ is the deformation ratio. Secondly, the function W is calculated based on statistic theories. The Moony-Rivlin energy density function is commonly used [5]

$$W = C_1 I_1 + C_2 I_2 + \beta I_3 \quad (3)$$

where, C_1 is a constant determined by the vulcanized network of the material, and C_2 is a constant determined by the volume ratio of the material. C_2 is constantly 0.1 N/mm^2 for dry materials. For most rubbery materials, $C_1 + C_2 = E/6$ holds.

SIMULATION

The above sensor structure is too complex for analytical formulae. Therefore, the finite element method (software ANSYS5.0) was used to estimate the force-deformation behaviour. The intention was to define suitable characteristics of the layer. Sensitivity dependence on parameters such as Young's modulus, Poisson ratio, and the thickness h were evaluated.

The simulated structure consists of a cone-shaped mesa, a ring-shaped membrane and an elastomer cover. The structure was presented by a 2-D axisymmetric model. Element plane82 was used to mesh the rigid silicon, and hyperelastic element hyper84 for the elastomer. Pressure loads were applied in a circular contact area with a diameter of 200 μm . Nonlinear calculation was used.

Elasticity C_1 was investigated from 10^{-1} to 10^4 N/mm^2 . In the range of 10^{-1} -10 N/mm^2 , the sensitivity decreases by 10 times. While when C_1 is greater than 10 N/mm^2 , the sensitivity is too small.

Thickness h was studied between 600-1000 μm . As expected, the sensitivity decreases as the elastomer gets thicker. However, the reduction is smaller than 25%. This implies that a uniform sensitivity can be expected even when the elastomer layer is uneven.

Rubber is not completely incompressible. The Poisson ratio ranges from 0.45 to 0.4999. However, the sensitivity difference is insignificant.

PROCESS

Chip with 3x3 tactels have been made using the BMM process and DIMES-01 bipolar process. Based on this, a packaging process is designed. Nonstandard steps are arranged after the whole standard IC process is finished, so that the two parts of processing are separated.

The process method is as follows: 1) Use DIMES-01 process to make a Si wafer, which contains a buried n -type layer (BN), an n -type epilayer, deep p -type (DP) channels, and a Si_3N_4 mask layer. Dryly etch the epilayer to partly open separation lanes. 2) Etch recesses in a Pyrex wafer. Evaporate and pattern Au layers on both sides of the Pyrex. 3) Bond the

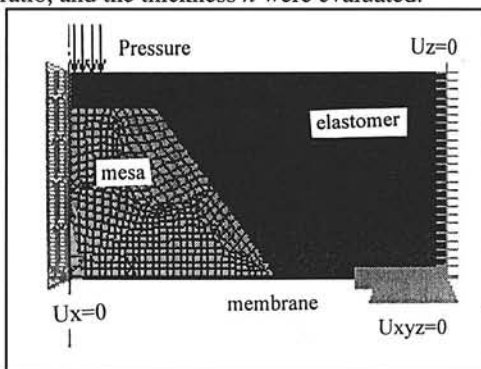


Fig. 3 The simulated axisymmetric model.

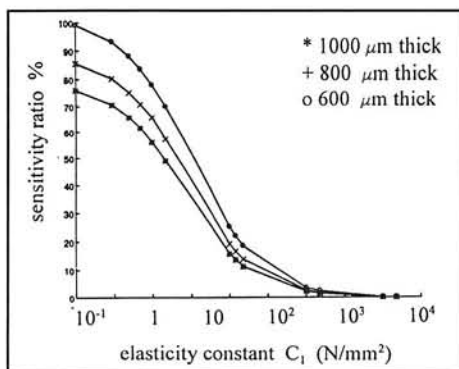


Fig.4 Sensitivity vs elasticity.

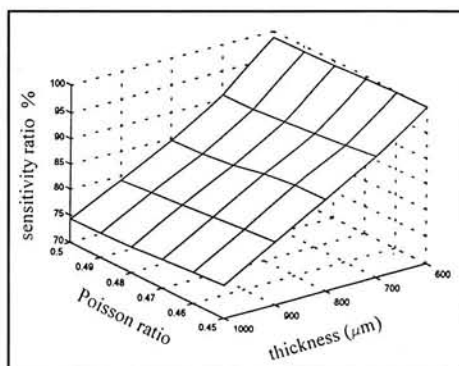


Fig. 5 Sensitivity vs thickness and Poisson ratio.

two wafers together using anodic bonding. Use electrochemically controlled etching to remove the unnecessary Si part till the separation lanes are opened. 4) Spin a polyimide PI2611 layer (8 μm thick) on the glass side using a spinning speed of 2000 rpm[6]. 5) Separate the sensing islands by etching in a 20% HF solution. The isotropic glass etching goes through the lanes as both the polyimide and Si are resistant to the HF solution. 6) Perform wire bonding between the two Au interconnection layers. 7) Mould an elastomer layer on the top of the whole device. Many of the silicone rubbers can flow easily in a cast before cure, and therefore, can be selected.

Several features can be summarized: 1) No mechanical sawing is used. As sawing is considered as the primary cause of the fragility of silicon chips [7], its elimination will largely improve the robustness of the silicon part. 2) The process is on a whole wafer scale. Devices can be as large as the wafer. 3) The device has a total thickness of 1-2 mm. This film-like device can be bent over a wide range without mechanical damage to the hard chips.

CONCLUSION

Behaviour of the elastomer layer was studied. Sensitivity depends more on the elasticity than on the layer thickness. The influence of Poisson ratio is insignificant for highly elastic elastomers. It is possible to make a flexible tactile sensor array. Development of unconventional processes are needed for packaging microsensors.

ACKNOWLEDGEMENT

I wish to acknowledge the staff of DIMES for the fabrication of the devices.

REFERENCE

- [1] P.W. Barth, "Flexible tactile sensing arrays for robotics: architectural robustness and yield considerations", *Proc. IEEE Solid-State Sensor and Actuator Workshop*, Hilton Head, 1988.
- [2] D.J. Beebe, *et al*, "A flexible polyimide-based package for silicon sensors", *Sensors and Actuators, A* 44, p. 57, 1994.
- [3] S. Hackwood, *et al*, "A torque-sensitive tactile array for robotics", *The International Journal of Robotics Research*, Vol. 2, p. 46, 1983.
- [4] Z. Chu, *et al*, "A silicon three axial tactile sensor", *Proc. Transducers'95*, p. 656, Stockholm, June 25-29, 1995.
- [5] L.R.G. Treloar, *The physics of rubber elasticity*, J.W. Arrowsmith LTD, Bristol, 1975.
- [6] *DuPont product information bulletin*.
- [7] K.E. Petersen, "Silicon as a mechanical material", *Proc. IEEE*, Vol. 70, p. 420, 1982.

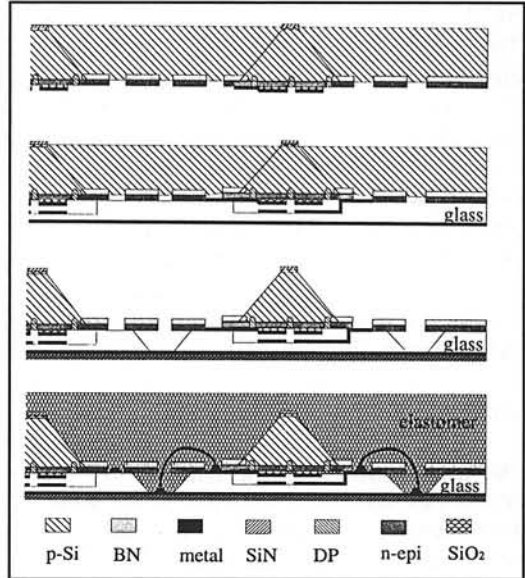


Fig. 6 The designed process flow.

A smart voltage processor for thermocouples

Saleh H. Khadouri, Gerard C. M. Meijer and Frank M. L van der Goes

Delft University of Technology, Department of Electrical Engineering,

Mekelweg 4, 2628 CD Delft, The Netherlands

Fax: 0152 785922, E-mail: G.C.M.Meijer@et.tudelft.nl

Abstract: This paper presents a novel interface for voltage-generating sensors, such as thermopiles and thermocouples. The processor converts sequentially a DC input voltage and three internally generated voltages into a period-modulated square-wave output signal. The internal signals are required to provide auto-calibration for offset and gain and to measure the interface internal temperature. Dynamic Element Matching is applied to generate an accurate and reliable PTAT voltage. The applied modulator used in the circuit has a 2nd-order filtering which suppresses low-frequency (1/f) noise. This filtering property enables the use of a low-cost CMOS process for the implementation of the circuit. The interface is able to measure a voltage (V_x) in the range of -27 mV to 100 mV, the measured accuracy of the system over a temperature range of -25°C to 75°C is 550 ppm of V_x . The inaccuracy in determining the reference-junction temperature is 0.6 K. The measuring time is ≤ 50 ms.

1. Introduction

This paper presents a novel design and implementation of an interface for DC voltage sources. The interface is capable to condition the signals of thermocouples and of a built-in temperature sensor. The output signal is readable by a micro-controller. To insure the accuracy and reliability of the circuit, auto calibration for offset and gain, is applied. The interface acts as an asynchronous converter for DC voltages employing a relaxation oscillator whose output is a period-modulated signal. Only one wire is needed between the micro-controller and the interface. The micro-controller converts the period-modulated signal into a digital number by simply counting the number of pulses within each period. Finally, from the obtained data, the micro-controller calculates the measuring-junction temperature of the thermocouple.

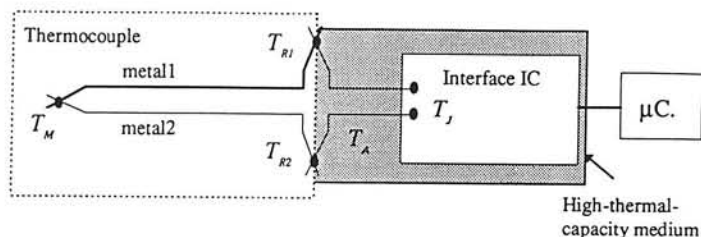


Fig. 1 The system set-up

The system set-up is shown in Fig. 1. The interface measures the thermocouple signal (V_x) which is directly related to the difference between the measuring-junction temperature (T_M) and

the reference-junction temperature ($T_{R1}=T_{R2}=T_R$) of the thermocouple. The interface also measures its own temperature T_j to compensate for the reference temperature of the thermocouple. Due to the self heating, the internal temperature of the interface is higher than the ambient temperature T_A . This limits the maximum allowable power dissipation. The reference temperature of the thermocouple is kept equal to the ambient temperature, by fixing the reference-junction and the interface with a low mutual thermal resistance at a high-thermal-capacity object, as indicated in Fig. 1, so that $T_R \approx T_A \approx T_j$. The thermocouples themselves are absolutely offset-free. Therefore any additive error degrades the performance. This is especially important for small measurement ranges of (T_M-T_R). For the larger ranges it is desirable that the maximum error of the interface is less than that of the thermocouple itself. The relative accuracy for different types of thermocouples is in the range of ± 2500 ppm to ± 7500 ppm [1].

2. Measuring approach

In addition to the thermocouple voltage, the interface generates two other voltages internally. One is a base-emitter voltage (V_{BE}) and the other is a PTAT voltage (V_{PTAT}). Both V_{BE} and V_{PTAT} are temperature dependent. Linear combinations of these two voltages are used to obtain a reference signal (V_{ref}) and a temperature-dependent signal (V_T), as follow [2] :

$$V_{ref} = V_{BE} + c_1(V_{BE2} - V_{BE1}) = V_{BE} + c_1 V_{PTAT} = V_{BE0} \quad (1)$$

$$V_T = V_{BE} - c_2 V_{PTAT} = \frac{V_{BE0}}{T_r} (T - T_r) \quad (2)$$

where T_r is the temperature at which $V_T=0$, and V_{BE0} is the extrapolated value of the linear approximation of V_{BE} at 0 K, as indicated in Fig. 2.

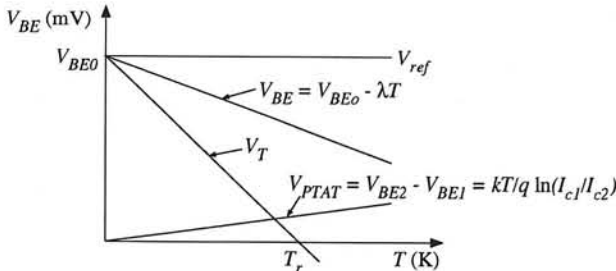


Fig. 2 A linear approximation of V_{BE} versus T for three transistors operating at different collector-current densities.

In Fig 3(a) the measurement set-up is shown. A divider is used to divide V_{BE} by a constant division factor (α_d) to make the voltage (V_{BE}/α_d) fitting within the range of (V_{PTAT} and V_x). The interface converts the four basic voltages V_{ex} , V_{PTAT} , V_{BE}/α_d and O_{ff} to the time domain using a linear voltage (V) to period (t) converter. The output voltage of this converter (Fig. 3(b)) is period modulated in such a way that $t_{ap} = a(O_{ff} + V_{pi})$, where O_{ff} and a are the equivalent offset and the conversion factor of the system, and V_{pi} ($i = 1, \dots, 4$) represents the four basic voltages to be converted.

Since the basic voltages are converted in an identical way to time intervals, it becomes possible to implement the algorithms (1) and (2) by the μC in the time domain. Moreover, the three-signal technique [2] can be applied to find the following dimensionless ratios:

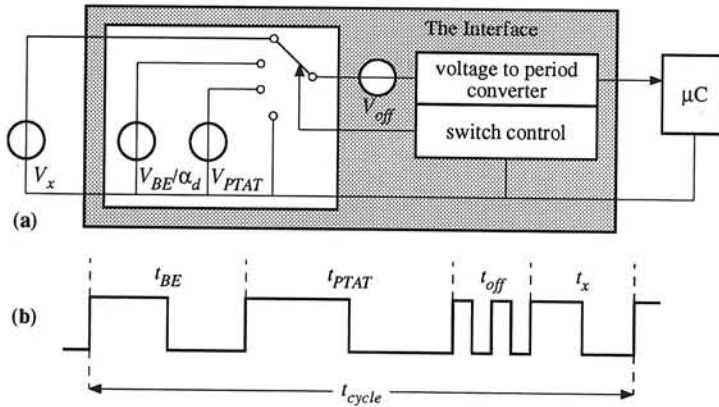


Fig. 3(a) Measuring approach of the interface, (b) the period-modulated output signal.

$$M_1 = \frac{(t_x - t_{off})}{(\alpha_d t_{BE} + c_1 t_{PTAT}) - (\alpha_d + c_1) t_{off}} = \frac{V_x}{V_{ref}}, \quad (3)$$

$$M_2 = \frac{(\alpha_d t_{BE} - c_2 t_{PTAT}) - (\alpha_d - c_2) t_{off}}{(\alpha_d t_{BE} + c_1 t_{PTAT}) - (\alpha_d + c_1) t_{off}} = \frac{V_T}{V_{ref}}. \quad (4)$$

In these ratios the influence of the additive and the multiplicative parameters (a and V_{off}) are eliminated, and the only requirement for the converter is that of linearity.

Once the ratios M_1 and M_2 are found, the μC calculates the measured thermocouple signal (V_x) by multiplying M_1 by V_{ref} , from which the temperature difference ($T_M - T_R$) of the thermocouple is found using a look-up table for the values of the thermocouple voltages and the corresponding temperature differences. Similarly, V_T is found by multiplying M_2 by V_{ref} , from which the interface temperature (T_J) is calculated using (2). Since the reference-junction temperature of the thermocouple (T_R) is approximately equal to the internal temperature of the interface (T_J), the measuring-junction temperature can simply be found using: $T_M \approx T_J + (T_M - T_R)$.

3. Realization

The schematic diagram of the interface circuit, shown in Fig. 4, contains the following main parts:

- A first-order oscillator to convert the analogue signals to be measured into a period-modulated signal.
- A circuit to generate the two voltages (V_{PTAT} and V_{BE}/α_d) required to obtain the reference and the temperature-dependent signals.
- A logic circuit to control the phase selection and the switching operations of the interface and to start up oscillation.
- A circuit to generate the alternating integration current.

Dynamic element matching is applied to obtain a high accuracy for the attenuation factor α_d and of the generated PTAT voltage V_{PTAT} [3] - [5]. The micro-controller measures the duration of each phase and calculates the ratios M_1 and M_2 using Equations (3) and (4). To enable the micro-controller to identify the different phases of the output signal, it is necessary to synchronise the interface and the micro-controller. One method to do this is to enable the micro-controller to identify the offset phase, by making the interval of the offset pulse shorter than the intervals of the others. The offset pulses is

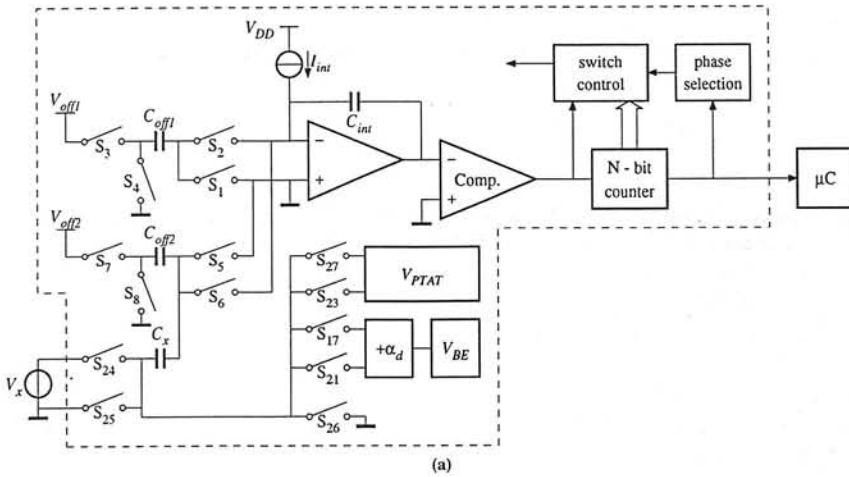


Fig. 4 Schematic diagram of the interface.

doubled to achieve that t_{off} is not beyond the range of the other intervals. A logic circuit is required to control the phase selection and the switching operations of the circuit.

4. Measurements and results

The complete circuit is realised on a single chip in a 0.7 μm CMOS process. The chip area, for the total IC including its bond pads, is 3.2 mm^2 . A photomicrograph of the chip is shown in Fig. 5.

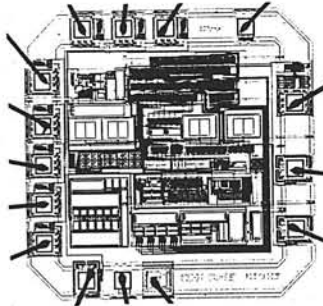


Fig. 5 A photomicrograph of the chip.

Table 1 The main measurement results

parameters	value		
Supply voltage	3.5- 6 V		
Input voltage range	-27 + 500 mV		
Measurement time	50 ms		
Power dissipation	4 mW at 5 V		
	250 K	300 K	350 K
inaccuracy in V_x	550 ppm		
$\sigma_{V_{ex}}$, due to noise	0.013 mV	0.014 mV	0.013 mV
inaccuracy in T_R	0.6 K		
σ_{TR} , due to noise	0.06 K	0.05 K	0.05K

The applied μC is of the type D87C51F8 with internal 8 kbytes EPROM and 256 bytes RAM, the clock frequency is 12 MHz and the sampling frequency of the μC is 3 MHz. The digital output signal of the interface is applied as input to the μC . The data available from the μC are applied to the computer, by which the calculations of the ratios M_1 and M_2 according to (3) and (4) and the calculations of the input signal and the reference junction temperature are performed. Before making the measurement test for the interface, the base-emitter voltage is calibrated by using an accurate test voltage as an input signal. The value of this voltage is calculated using the data provided by the μC which correspond to the output signal of the interface. The emitter area is adjusted such that the calculated voltage is as close as possible to the applied test voltage. After the calibration of the base-emitter voltage, voltage and temperature measurements have been performed to check the accuracy of the circuit in measuring the thermocouple signal and its own temperature. To test the interface an accurate test voltage (V_x) is applied to the input of the chip. The measured scaled error is found to be -550 ppm of V_x . This error is due to the inaccuracy of the internal bandgap reference. Although the interface has been designed for the voltage range of (-27 mV to 100 mV), large positive values of V_x up to +500 mV can be applied as well without a decrease of the relative accuracy. Also the accuracy of the internal temperature sensor has been tested. The inaccuracy of this sensor was found to be 0.6 K over the temperature range of -25°C to +75°C. Table 1 list the main measurement results at room temperature and at the temperature extremes (250 K and 350 K) of the chip.

5. Conclusion

A low-cost interface for a thermocouple has been designed and realised using a CMOS process. The main properties of this interface are its ability to measure small input voltages together with its own temperature. Moreover, the application of the three-signal technique in the measuring approach has guaranteed the accuracy and long-term stability against the deviation in the offset and gain. Also the application of a special DEM has enabled the generation of an accurate and reliable V_{PTAT} .

The main causes for the limited accuracy in the measured results are the inaccuracy of the generated base-emitter voltage and the deviation of the reference junction temperature of the thermocouple from that of the interface itself due to self heating. The change in V_{BE} due to the inaccuracy in the reference current and the process parameters is reduced by calibrating a

transistor with multi-emitter area, while the inaccuracy due to the non-linearity is limited by applying a specific method in processing the signal by the micro-controller. The error of the internal temperature sensor amounts to 0.6 K for a power dissipation of about 4 mW.

The application of an oscillator with 2nd-order filtering to suppress the low-frequency (1/f) noise has enabled the use of low-cost CMOS process for the implementation of the circuit.

REFERENCES

- [1] "Manual on the use of thermocouple in temperature measurement," American Society for testing and materials, Fourth printing, April 1987.
- [2] G.C.M. Meijer, J. van Drecht, P.C. de Jong and H. Neuteboom. "New concepts for smart signal processors and their application to PSD displacement transducers," Sensors and Actuators, no. 35, pp. 23-30, 1992.
- [3] G.C.M. Meijer, Patent appl. 1000222, April 1995.
- [4] F.M.L. van der Goes, G.C.M. Meijer "A simple and accurate dynamic voltage divider for resistive bridge transducer interfaces," in Proc. of IMTC., Hamamatsu, Japan, May 1994, pp. 784-787.
- [5] F.M.L. van der Goes, "Low-cost sensor interfacing," PhD. thesis, Delft University of Technology, Electronics Research Laboratory, April 1996.

Micro System Technology: Status and Infrastructure

Job Elders and Vincent Spiering

Twente MicroProducts,

P.O. Box 217, 7500 AE Enschede, the Netherlands

tel. xx31 53 489 4264

fax. xx31 53 435 8259

e-mail. TMP@eltn.utwente.nl <http://utep.el.utwente.nl/ mesa/tmp/tmp.html>

0. ABSTRACT

The status of micro system technology (MST) and its production facilities is described shortly and it is concluded that there is of lack of proper infrastructure to come to products. Clustering as a solution to shorten the trace from productdevelopment-prototyping-production is offered as an alternative for complete integration in one organisation. Within the EC, the programme *EUROPRACTICE* has been founded to make MST accessible for the industry in Europe. This article concludes with the presentation of the production infrastructure based on the four EC Manufacturing Clusters in this programme.

1. INTRODUCTION

Micro System Technology (MST) is recognised as an important (future) product technology. A large added value can be created by applications of batch processes with sub-micron tolerances. A wide variety of products have been invented that can be fabricated well with the use of MST, and there is a general recognition of the powerful potential of this technology. From the development of the MST [1] it is clear that the technology becomes mature, which means that industrial demands and motivations are getting more important. In this paper the status of the production technologies and the infrastructure to come to products within Europe are outlined.

2. DEFINITION AND STATUS OF MICRO SYSTEM TECHNOLOGY

The diversity of technologies seems to increase every day, so a definition of the terminology will be given. Silicon micromachining is a technology that has its origin in IC-technology, but it has also evaluated into a non-compatible technology. In general one can work in silicon (bulk micromachining) or on silicon (surface micromachining). With the latter technology deposited layers will be processed selectively in such a way that it is possible to release free hanging microstructures.

Especially a difference is made between IC-compatible processes and processes that have to be used in a MST-fab. IC production facilities have process constraints, to protect the material functionality necessary for the electrical components, which can be in conflict with the constraints (or advantages) of micromachined components. Experiences do conclude that many microstructures can be fabricated in a MST-fab only. This (lack of) infrastructure will be addressed in this article.

Foster's S curves [2] are utilised to analyse the potential of a new technology relative to an existing technology. Traditionally the curves are a performance plot of an existing and an invading product. These curves are based on the traditional and new technology's historical, existing and projected performance usually along a single dimension (cost, performance etc.). The trick is to know where on the curves you are. For example, if a firm or a government funds a new technology at the lower region of maximum slope, far superior technological advances will be obtained when compared to funding the technology late in the cycle. The curve of silicon micromachining [3], see figure 1, shows that the current status can still be qualified as a young technology [4]. This means that a growth in potential and specifications is to be expected. It also means that there are hardly any standard processes, generic test facilities or standardisation of functional tests for a structure. Moreover there is yet no large diversity of production facilities.

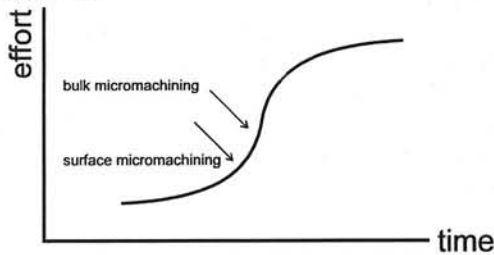


Figure 1. The status of bulk and surface micromachining in the Foster's S curve.

A lot of alternative possibilities to manufacture microstructures, like laser structuring, ion milling, micromoulding, microelectroforming, microembossing, spark erosion, exist. Techniques, originating from precision technology have an evident importance, since the number of products defines the choice between precision technology and MST. The precision technologies will not be worked out in detail here, but they could be applied in certain parts of the production trace, which increases the range of possibilities to come to a product.

An example of an interesting combination between precision technology and MST is DEEMO (Dry Etching, Electroplating, and Moulding) [5]. With this technology the IC-related tolerances are combined with economical mass-fabrication technologies like moulding. Basically the process starts with deep dry etching in silicon. This can be proceeded by filling the trenches with a metal by means of electroplating. This results in a mould for mass-production of plastic microstructures.

A part of the risks depend on the production infrastructure: back-ups are needed, technologies need to be standardised, and the location of the production as a function of the number of products has to be made clear.

3. PRODUCTION INFRASTRUCTURE AND EC MANUFACTURING CLUSTERS

Within the EC these barriers for innovation have been recognised and an ambitious programme *EUROPRACTICE* has been founded to make MST accessible for the industry. The *EUROPRACTICE* project is aimed at [6]:

- facilitating *access* to MST and know-how for enterprises in all industrial sectors
- promoting the *applications* of MST
- enhancing the capacity of industry and academia for *training* of engineers in the MST area

3.1 Structure of EUROPRACTICE

In this program three manufacturing and testing services (IC, Multi-Chip-Module, and Microsystems) are supported by training and best practice, and software support services. Overall co-ordination and management is done by a Global Manager, see also figure 2.

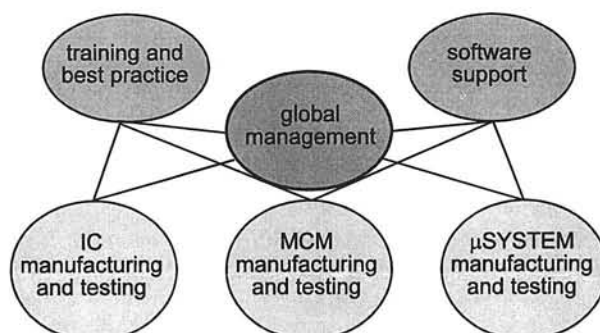


Figure 2. The structure of EUROPRACTICE.

The objectives of EUROPRACTICE with relation to microsystems are realised by:

- *transfer of expertise* from research to industry
- *creating services* which can supply MST to users covering design, simulation, process capabilities, manufacturing, packaging and assembly of MST products.
- *lowering entry costs and risks* associated with design and manufacturing of microsystems.

EUROPRACTICE will only meet its objectives if its clients (i.e. users) are attracted to, and use, the basic services on offer. Therefore much attention is paid to the users interface and many ways to access the microstructures services are possible for them.

3.2 Methodology

The methodology to push the transfer of expertise from research to industry is to create consortia which are led by industrial oriented partners, but which include the research laboratories and universities which are at the forefront in developing microsystem technologies. So clustering is offered as a solution to shorten the trace from product-development→prototyping→production instead of complete integration in one organisation. In the clusters, standards have to be defined to reduce the total production costs. In this way not only the innovative silicon component is offered, but the whole functionality, including the packaging, housing, and assembling.

3.3 Manufacturing Clusters (MC's)

Four Manufacturing Clusters (MC's) are established, with the task to fasten the prototype-to-production path. The 4 MC's are each led by an industrial led partner, in table 1 they are presented with the MC leaders on top.

MC1 (Germany)	MC2 (France)	MC3 (UK)	MC4 (Switzerland & The Netherlands)
Robert Bosch GmbH Fhg-ISit Fhg-IMS HL Planar GMA Microparts	Sagem CEA-LETI SEXTANT LAAS-CNRS	GMMT (GEC) RAL CRL TWI Epigem Ltd	CSEM Twente MicroProducts Holland Signaal

Table 1. The four Manufacturing Clusters as defined within EURO PRACTICE.

The cluster MC4 with Twente MicroProducts (Enschede), Holland Signaal Apparaten (Hengelo) and CSEM (Neuchâtel) is a good example of the offer of vertical integration: this cluster offers MST production of 1 piece to 2 million pieces.

Twente MicroProducts focuses on bulk and surface micromachining; design and prototyping of custom designed products like flow sensors, pressure sensors, micropumps and passive structures, e.g., high performance microchannels; production up to about 100.000 pieces (depending on the size of the structure).

CSEM handles production from about 100.000 to 2.000.000 pieces, silicon micromachining, galvanic processes, ASIC design, microsystem assembly and testing with special expertise in the field of capacitive sensors, magnetic sensors and electrochemical sensors.

HSA provides a range of complementary processes for the production of thin film substrates, including laser drilling and trimming, packaging and testing.

4. CONCLUSIONS

Clustering as a solution to shorten the trace from productdevelopment-prototyping-production is offered within the programme EURO PRACTICE to make MST accessible for the industry in Europe. Twente MicroProducts and all others cluster partners are open to inform the industry about the (im)possibilities of MST products and production.

REFERENCES

- [1] J. Fluitman, *jaarboek NVPT*, 1995.
- [2] R. Foster, Timing technological transitions, *Technology in Society*, 7, 1985.
- [3] S.T. Walsh, R. Boylan, R. Warrington, W. Carr, J. Elders, The strategy development of HARM manufacturing technologies, *proc. HARMST95*, Karlsruhe, 3-6 july 1995.
- [4] E. Schumann, Creating the market for MEMS devices, *workshop MEMS in the USA and Canada*, Düsseldorf, Germany, 3 nov. 1995.
- [5] J. Elders, H.V. Jansen, M.J. de Boer, M.Elwenspoek and J.H.J. Fluitman, DEEMO: Dry Etching, Electroplating and Moulding, *proc. HARMST95*, Karlsruhe, 3-6 july 1995.
- [6] D. Beernaert, M. Wilkinson, EURO PRACTICE: μ systems in the 4th framework programme, *MST news*, 14, 1995, 2-10.

Model-based parameter estimation from eddy-current images and application in a multi-sensor waste separation system

N.H. Gorte-Kroupnova, Z.Houkes, P.P.L.Regtien

Department of Electrical Engineering
University of Twente
The Netherlands

Abstract

The paper describes a multi-sensor waste separation system, in particular the system which finds certain components on printed circuit boards(PCB). A general framework for such a system is suggested. The general structure is concretized for a system consisting of a color camera and an eddy-current sensor. Components on a PCB are classified on the basis of features, extracted from eddy-current and color images. The paper describes methods for model-based extraction of necessary features from the raw sensor data.

1 Introduction

In most of the present bulk waste separation systems sensors and actuators are inseparable, being based on the same physical principle. In the proposed system, the classification of the waste objects and the removing of recognized objects from the stream are separated actions. The information necessary for the classification is obtained by multiple sensors. Sensor fusion allows to improve the performance of the system, reducing the errors and resolving ambiguities. As an example, recycling of printed circuit boards (PCB) is taken. At present, they are crushed into small pieces and then mechanically separated or just melted. Our intention is to design a system which finds certain components on a PCB before they are destroyed. The components in question are harmful for the environment (electrolytic capacitors) or for further processing (cadmium batteries), or they can be brought on the market again (memory chips).

A general framework of the classification system is proposed. This general structure is given concrete form for the case of a system, consisting of a color camera and an eddy-current sensor. Such a system is especially suitable for finding high conductive components on a PCB, like electrolytic capacitors.

2 Structure of a multi-sensor classification system

The proposed framework is presented on Fig. 1. Physical sensors provide raw sensor data. Their task is to transform the measured physical value into another one (voltage) and to digitize the result. In our system physical sensors include a color camera and an eddy-current sensor.

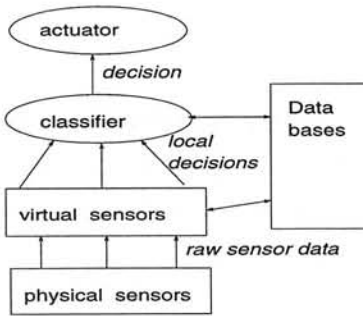


Figure 1: Multi-sensor system structure

Virtual sensors make conclusions about object characteristics on the basis of measurement models. They are actually computer programs that have raw sensor data as input and local decisions, such as object features or class hypothesis, as output. In this particular case components are found on the PCB from the color image and the parameters of every object, such as color, size and shape of its parts, are estimated. From the eddy-current image, such parameters as local conductivity and distance to the sensor are estimated.

Classifier makes a final decision based on local ones and the information in a DB, in this case a decision whether or not the component must be removed.

There are two DB's in such a system. A DB of objects, containing information about the objects we want to classify. In our case - DB of components on PCB's and their features: color, shape and size of their parts and electro magnetic image. The second DB is a DB that contains models and parameters of the available sensors and algorithms.

3 Eddy-current imaging

As known, an eddy-current sensor is a coil carrying an alternating current. When in the vicinity of a conductive object, the impedance of the coil changes depending on the electro magnetic characteristics of the object, and also on the sizes, shapes and relative positions of the coil and the object.

A PCB is scanned with a probe coil in a regular, rectangular grid. In every point the real and imaginary parts of the coil impedance over a frequency range are measured. The measurements are carried out with an impedance measurement device, the HP4194.

Several models describing changes in a coil impedance in the vicinity of a conductive object can be found in literature. Dodd and Deeds [2] and Cheng [3] gave an analytical solution for the coil impedance in vicinity of the layered object. Blitz in [4] describes a simplified variant of the same model, valid for certain conditions. Vernon in [5] builds an experimental model for ferrite cup-core coils, and in [6] a general computational model for this type of coils is described.

In our case, an application-specific requirement is, that the model must be as simple as possible to make it possible to estimate parameters in nearly real time. For this reason, an equivalent circuit model was chosen. As described in [1] and [5], in this case the probe and the object are represented as a simple coupled circuit, in which the coil plays the role of a primary circuit and the workpiece the secondary.

Since possible conductivities in this application can vary considerably, the measurements are implemented over a wide frequency range. At higher frequencies, the resonance starts to play a role. The resonance occurs in a circuit consisting of the probe coil and the capacity

of the coaxing cable and eventually the capacity of the turns of the coil. The frequency and amplitude of the resonance are defined by the coil and cable parameters and the electro magnetic parameters of the workpiece. The values of the equivalent resistivity and inductance of the coil in the vicinity of the object can be obtained using any model, and so the resonance model can be joined with other models. For this application, the coupled circuits model was used together with the resonance model as represented on Fig. 2. The capacity C_{add}

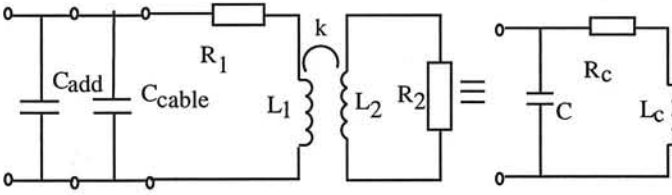


Figure 2: Resonance eddy-current sensor modeling

was added to make the resonance frequency lower in order to reduce the influence of random factors. Here, R_1 is the resistance of the probe and L_1 the self inductance. R_2 is the equivalent resistance of the workpiece and L_2 the equivalent inductance. The workpiece manifests itself in the ratio L_2/R_2 . The coupling coefficient k is linked to the distance between the sensor and the object: it decreases when the distance increases. The equivalent impedance of the coil can be written as:

$$R_c = R_1 + \frac{k^2 L_1 \omega^2 L_2 / R_2}{1 + \omega^2 (L_2 / R_2)^2}, \quad L_c = L_1 - \frac{k^2 L_1 \omega^2 (L_2 / R_2)^2}{1 + \omega^2 (L_2 / R_2)^2}$$

The impedance that we measure can be written as:

$$R_{meas} = \frac{L_c R_c / C - R_c / \omega C (\omega L_c - 1 / \omega C)}{R_c^2 + (\omega L_c - 1 / \omega C)}, \quad X_{meas} = -\frac{R_c^2 + L_c / C (\omega L_c - 1 / \omega C)}{R_c^2 + (\omega L_c - 1 / \omega C)}$$

where $C = C_{cable} + C_{add}$

Let's consider parameters of the model from Figure 2. In this model, R_1 , L_1 and C are parameters of the coil and the measurement circuit, which stay the same from one measurement to another, and L_2/R_2 and k are the measured values, that characterize the workpiece and its distance to the sensor. The parameter estimation is implemented as follows. First the sensor parameters are adjusted by measuring the coil impedance when an object is absent. The obtained resonance curves for the real and imaginary parts of the impedance are compared to the model curves and the parameters of the coil are estimated by a least-squares estimator. Then measured parameters are estimated in every point of the image, with the coil parameters considered constant.

An example of the parameter estimation can be found on Fig. 3 - 5. In this experiment, parameters were estimated in every scanning point. The local electro magnetic parameters were separated from the lift-off effects and represented as grey-values (white = $4.9 \cdot 10^{-6} H/\Omega$, black = $0 H/\Omega$ for electro magnetic parameters and white = 0.55, black = 1 for the coupling.)

4 Processing of color camera images

The parameters, obtained from the eddy-current image, are combined with those from the color camera image: size, shape and color of the parts of the object, position and orientation. An image is segmented, as described in [7], then objects are extracted from it. Every object

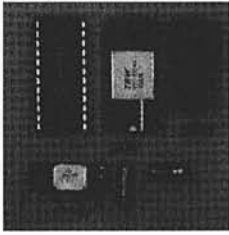


Figure 3: Camera image of a PCB

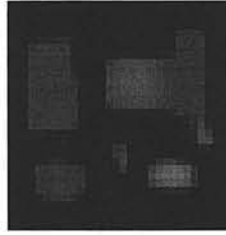


Figure 4: Estimated local conductivity

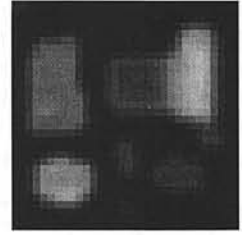


Figure 5: Estimated distance sensor-object

consists of several regions (parts). The description of an object is made in the form of attributed graph with relations 'adjacent' and 'surrounds' and the following attributes of every region: average color, compactness, rectangularity, area, as described in [8].

Every object in the color image is used to extract a local conductivity image of this object from the whole image of the board. The extracted image is added to the object description. The obtained descriptions are compared to references in the DB of waste objects to decide whether or not the object must be removed from the stream.

5 Conclusions and future work

The paper demonstrates model-based extraction of information from the combination of raw sensor data. The example considered in the paper concerns extraction of features of electronic components on a PCB for the classification during the recycling process. The used combination of a color camera and an eddy-current sensor is especially suitable for high conductive components (electrolytic capacitors).

Topics of future research include further verification of eddy-current sensor models, comparison of different coils (ferrite cup-cores, for example), further development of the sensor fusion methods. One of the points of interest is building of a pilot-system, where practical questions, like using of eddy-current coils arrays instead of scanning, can be tested.

References

- [1] Dufour, I., Placko, D. "Separation of conductivity and distance measurements for eddy current nondestructive inspection of graphite composite materials., J. Phys. III France, 3(1993), 1065-1074
- [2] Dood, C.V., Deeds, W. E. "Analytical solution to Eddy-Current Probe-Coil Problems," Journal of applied physics", 39(6), 1968
- [3] Cheng, D. H. S. "The Reflected Impedance of a Circular Coil in the proximity of a Semi-Infinite Medium", IEEE trans. on instr. and meas., 14(3), 1965
- [4] Blitz, J., "Prediction of Impedance components of Eddy-Current Coils using a PC", NDT International, 1(1989)
- [5] Vernon, S., "The Universal Impedance Diagram of the Ferrite Pot Core Eddy Current Transducer", IEEE trans. on magnetics, 25(3), 1989
- [6] Bowler, J. R., Sabbagh, L. D., Sabbagh, H. A., "A Theoretical and Computational Model of Eddy-Current Probes Incorporating Volume Integral and Conjugate Gradient Methods", IEEE trans. on magnetics, 25(3), 1989
- [7] Gorte, B., Gorte-Kroupnova, N., "Non-parametric classification algorithm with an unknown class", submitted to IEEE symposium on computer vision and visual motion, Florida, November 20-24, 1995
- [8] Sonka, M., Hlavac, V., Boyle, R., "Image Processing, Analysis and Machine Vision", London:Chapman & Hall Computing, 1993

NEW METHODS FOR NON-DESTRUCTIVE STERILITY TESTING OF ASEPTICALLY PACKED FOOD PRODUCTS

Stoyan Nihtianov, Gerard Meijer, Harry Kerkvliet, Eric Demeijer

**Electronics Research Laboratory, Faculty of Electrical Eng.,
Delft University of Technology, Mekelweg 4, 2628 CD Delft**

ABSTRACT

The results from experimenting three different new ways for non-invasive sterility testing are presented. The first two are based on monitoring the heat production and the volume of the food container, when there is a bacterial growth in the contained food. The third one is based on impedance measurement of the food product with only one of the electrodes in direct contact with it.

A new prototype of equipment for sterility testing by measuring the temperature variation of 49 cuvettes with food samples and another prototype of equipment for sterility testing by simultaneous control of temperature and volume differences between two 1L Tetra pak containers (a tested one and a reference one), are described.

I - INTRODUCTION

In microbiology society it is well known that for sterility testing of food products still there is no method discovered - universal enough to detect all kinds of bacteria in all kinds of food products. It is because of the enormous diversity of microorganisms and food products, that metabolism can lead to variety of possible physical effects on the infected food. The problem becomes even more difficult when the sterility testing of packed food products has to be accomplished in non-destructive way.

In the last few years in The Electronics Research Lab. of Delft University of Technology a research work has been carried out to develop different methods for non-destructive sterility testing of aseptically packaged food products, that can be efficient for detecting of as much bacterial species as possible, in reasonable time and with good reliability.

Here we would like to introduce the results from experimenting three different ways for non-invasive sterility testing. The first two are based on monitoring some physical effects on the food container, when there is a bacterial growth in the food product. These are heat production and volume change. The

This work is supported by the Dutch Government and the companies UNILEVER and LUMAC within an European EUREKA project.

third one is based on impedance measurement of the food product with only one of the electrodes in direct contact with it.

Prototypes of equipment, designed and developed for carrying out the experiments, are described.

II - CALORIMETRIC METHOD

A new calorimeter, sensing the temperature variations of 49 cuvettes (seven rows with seven cuvettes in each row) with food samples, has been designed - Fig.1. The temperature is measured by Smartec temperature sensors. The data from the sensors is collected by an Intel 87C51 based microcontroller and processed by a consumer friendly LabVIEW Virtual Instrument, installed on a personal computer. A block diagram of the electronic circuit is depicted in Fig.2.

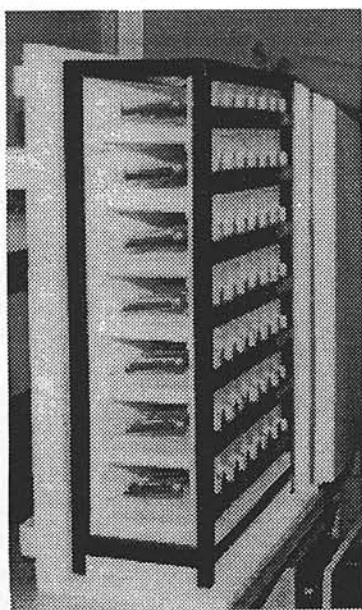


Fig.2

all cuvettes - regarded that normally only a very few of them are infected).

The cuvettes with infected food are located by detecting the temperature difference between them and some reference. Looking at the absolute temperature is not the best solution in this case, because of the room temperature fluctuation, which affects the temperature of all cuvettes.

A special post-processing LabVIEW program is developed to ease and to speed up the processing of the output data from the experiment. The operator can choose as a reference the temperature of every other single cuvette or the average temperature of more cuvettes (i.e. all cuvettes from one row or

A pre-view of seven thermal diagrams is ensured on seven different

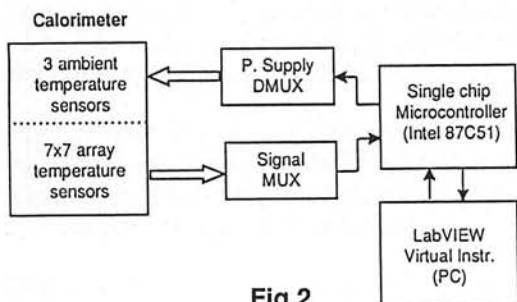


Fig.2

small graphical displays. On another large graphical display ten thermal diagrams can be displayed simultaneously and easily examined. With this new calorimeter temperature differences of less than 10 mK can easily be sensed at room temperature variations within $\pm 0.5K$, which allows the detection of a number of heat-producing bacteria.

III - VOLUME-TEMPERATURE MONITORING METHOD

Bacterial growth in aseptically packaged food products often influences the density of the infected food or gives metabolic products (CO_2), which change the total volume of the flexible TETRA BRIK container. So, simultaneous monitoring of the temperature and the volume of the package is expected to be more universal method than the calorimetric method.

A prototype of a new device, for simultaneous monitoring of the

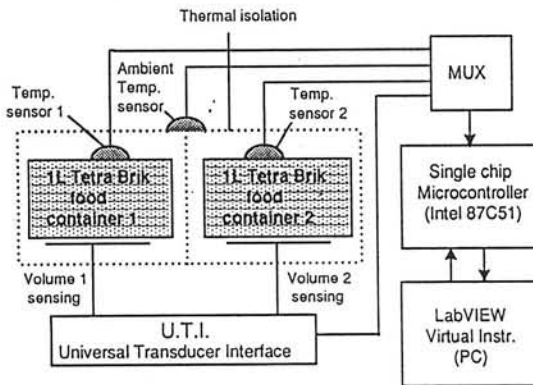
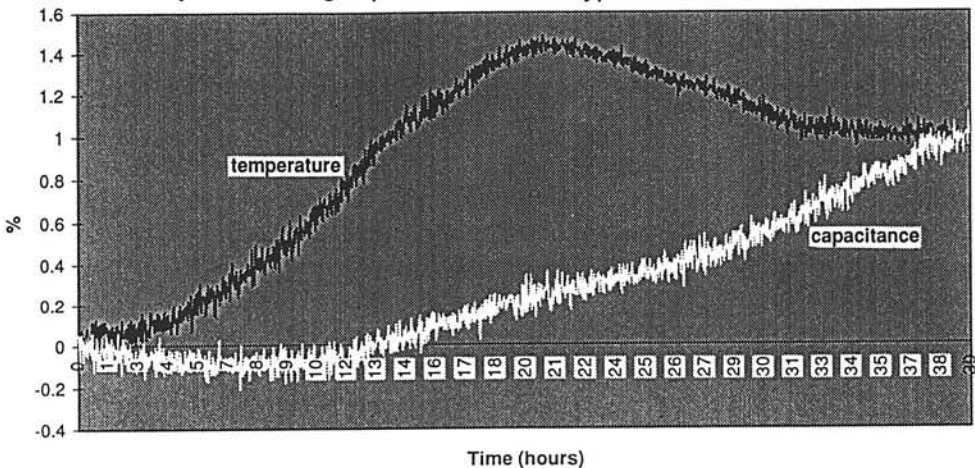


Fig.3

temperature and the volume differences between two 1L TETRA packages has been designed (a tested one and a reference one). The temperature is measured by Smartec temperature sensors. The volume variation is transduced into capacitance change between two conducting plates, pressing the package from two opposite sides, and measured by special universal transducer interface circuit (UTI), designed in the Electronics Res. Lab.. The data from the sensors is processed in the same way as it is done with the calorimetric method. In Fig.3 is depicted the block diagram of the electronic circuit and in Fig.4 are displayed the relative change of the temperature difference and the capacitance difference between inoculated with *E. coli* milk package and a sterile milk package, versus time. The volume increase in this case is mainly due to the gas production of this type of bacteria.



Time (hours)

Fig.4

IV - IMPEDANCE METHOD

A new way of implementing the impedance method, intended for sterility testing of the food in TETRA PAK containers, has been investigated with only one small electrode (1) in direct contact with the food. The value of the total impedance, measured, is influenced directly by the impedance of the food and indirectly, because of the electric field effects between the inner electrode (1) and the aluminium layer of the packaging material, when the food impedance is changing. In Fig.5 a cross-section of a TETRA food container is depicted with electric field lines in it, when voltage is applied between electrode (1), placed on the inner side of the container wall, and a big electrode (2), pressing the container from outside.

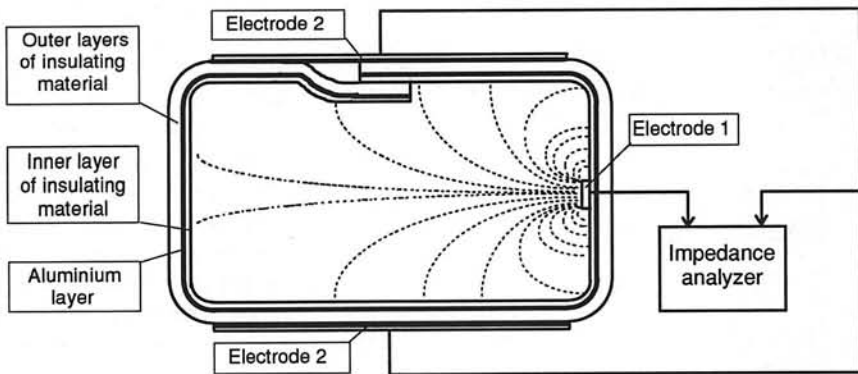


Fig.5

In this way of implementing the impedance method, better sensitivity is achieved for the absolute value of the measured impedance. Also, inserting one, instead of two electrodes, in the package decreases the possibility for leakage and lowers the price of this type of food containers.

A series of experiments has been carried out with milk packages, inoculated with different types of bacteria, to test the sensitivity, the rapidity and the reliability of the method. The obtained results show that within less than 72 hours the following bacteria can easily be detected: *E.coli*, *L. lach's subsp.*, *Bacillus cereus*, *Salmonella arizonae*.

ACKNOWLEDGEMENT

We would like to acknowledge with thanks the generous assistance given by our colleagues Ir. B. H. A. van Kleeff and Ir. W. Ovaa

A μ sensor array in a fluidic system for space applications

Vincent Spiering, Piet Bergveld, Miko Elwenspoek and Albert van den Berg

*MESA Research Institute, University of Twente,
P.O. Box 217, 7500 AE Enschede, the Netherlands
tel: xx31 53 489 2805 fax: xx31 53 435 9047*

email: v.l.spiering@el.utwente.nl

<http://tdm116.el.utwente.nl/tdm/mmd/projects/mutas/mutas.htm>

0. ABSTRACT

The development of a hybrid integration method for a multi μ sensor array unit in a fluid channel on a breadboard is presented. The method is illustrated by means of the fabrication of a demonstrator micro fluid analysis system, also called a Micro Total Analysis System (μ TAS), containing a pressure-, temperature-, pH-, pO_2 and pCO_2 -sensor. This system is designed for a multi-user and multi-purpose application in life science, biotechnology research, and life support systems according to the technical requirements for space.

1. INTRODUCTION

Over the past few years there has been an increasing interest in the development and realisation of miniaturised total analysis systems (μ TAS) [1-3]. This growth is partly due to the rapid developments in fluid handling devices such as micropumps, -valves, -filters and -mixers [4], but is also explained by the need for complex (bio)chemical sensor systems with integrated self-test and calibration features. This has led to attempts to fabricate miniaturised flow systems [2,3] and microfabricated parts for separation systems. However, since such systems typically would comprise a variety of components, materials and technologies, considerable attention should be paid to the integration-concept of such systems. The two extreme forms of integration are hybrid and monolithic. An example of a completely hybrid analysis systems is the stacked phosphate analyser, as developed by Van der Schoot *et al.* [2], whereas the liquid dosing system of Lammerink *et al.* [5] is an example of a monolithic system. In practice, most systems will consist of a combination of these two forms. In [6], Lammerink *et al.* showed a concept that enables a modular mixed integration of different system components or subsystems on a planar backplane: the Mixed Circuit Board. This MCB serves at the time as mechanical support for the system components (modules), it has the necessary electrical connections (Printed Circuit Board) and contains the microchannels for fluid transport connecting the different modules (Channel Circuit Board).

Standardization of components, materials and technology is important to make the modular concept successful. One of these issues is a general connection technology from components to the planar backplane or carrier. In this project the development of such technology that enables with fluid tight sealing, mechanical support and electrical contact of sensors, is presented and illustrated by means of a demonstrator μ TAS.

2. SYSTEM

An overview of the system layout is given in figure 1. The system has (on a flow system board) a conventional miniature pump and valves together with the sensor array carrier containing the micro channels and micro sensors. Analog electronics for sensor read-out are located on a separate printed circuit board which can be stacked under the flow system board. Control is done with a PC and belonging AD control electronics.

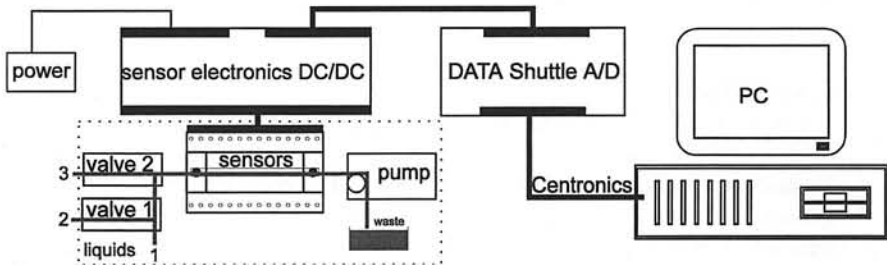


Fig. 1 System configuration.

2.1 sensors

The sensors used to demonstrate the technology are a capacitive pressure sensor, a temperature sensor, a pH ISFET and a chip containing the pO_2 sensor together with a pCO_2 sensor. Figure 2 shows a chip (4.8×6 mm) containing two ISFETs. The ISFETs contain a Ta_2O_5 layer on the gate for maximum sensitivity and minimum drift. On one of the two ISFETs, polymers are deposited and patterned to create a longer diffusion time [7]. During this time, the pH is measured differentially between the fast and slow response ISFET [8].

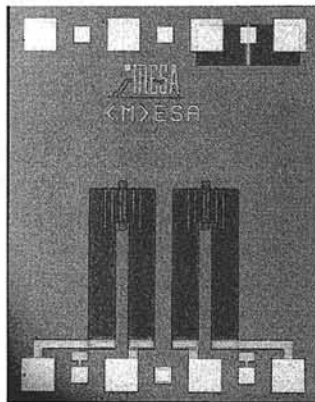


Fig. 2 Photograph of dual ISFET chip.

2.2 sensor carrier

The sensor carrier contains the sensor chips (pH, pO_2 , pCO_2 , P and T) on top and *fluid channels* inside (see fig. 3). It consists of a silicon layer with etched holes anodically bonded on a glass layer with machined channels. The channels have a minimum of sharp corners to prevent places with low-velocity of the fluid.

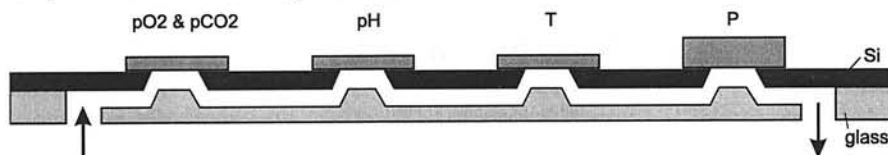


Fig. 3 Cross section of sensor carrier.

The sensors are sealed with epoxy to the glass/silicon substrate, while holes in the carrier allow wire bond connections (fig. 4 and 5). The epoxy is deposited by a programmable dispenser, after which the sensors are placed by a pick and place machine. The bio-compatible epoxy is room-temperature curable.

In a next generation the electrical contacts will be made by a kind of flipchip bonding technique, and this technology is then integrated with the sealing technology in one contact step. The holes in the carrier are not required anymore in that case.

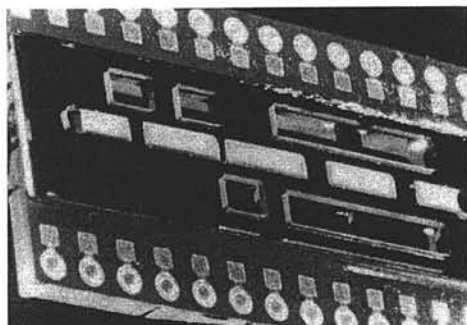
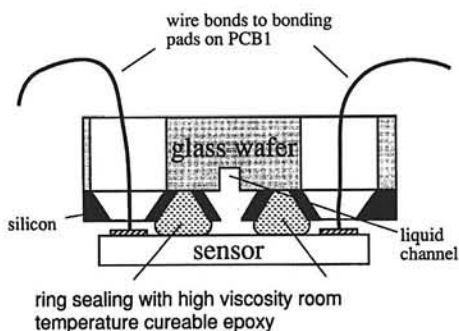


Fig. 4 Photograph of Si-glass sensor carrier. Fig. 5 Sensor to carrier connection technology.



2.3 flow system board (credit card size)

The flow system consists beside the carrier of 2 valves and a pump, connected by tubes (fig. 6). By switching the valves, sample-peaks can be injected in a (calibrant) carrier fluidic. Pump and valves are (semi-)commercial miniatures.

2.4 analog electronics; AD control electronics and PC

A printed circuit board with the *analog electronics* for sensor read-out is connected to the flow sensor board. The electronics and flowsystem can be stacked, or connected via a flatcable to separate electronics and fluids.

Control and read-out is done with the software package MS Visual Basic under windows.

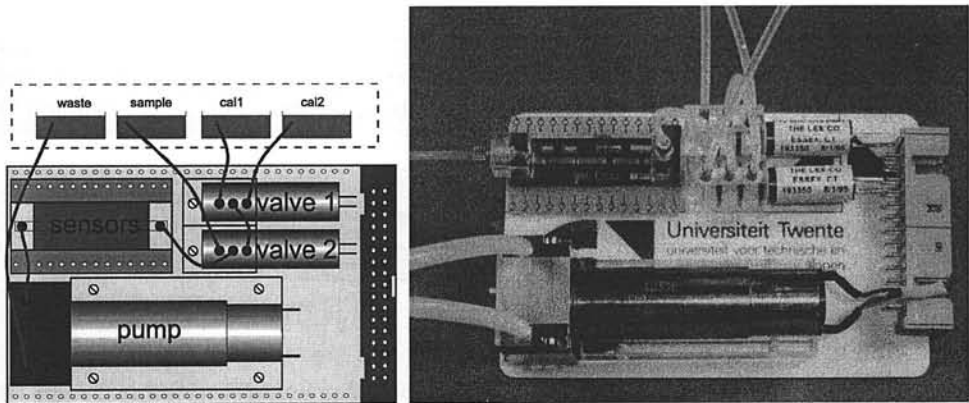


Fig. 6 Layout and mock-up of flow system board with components (credit card size).

3. CONCLUSIONS

The development of a hybrid integration method for a multi μ sensor array unit in a fluid channel on a breadboard is presented. A demonstrator micro fluid analysis system is designed and fabricated according to the technical requirements for space. The biotechnological experiments are carried out in the direct future.

ACKNOWLEDGEMENTS

This project is financed by ESA/ESTEC and the direct partners are IMT (Neuchâtel, CH), IMEC (Leuven, B), and Dornier (Friedrichshafen, D). Philip Arquint and Bart van der Schoot (IMT) are responsible for the pO_2 and pCO_2 -sensor. Kris Baert and Filip van Steenkiste (IMEC) take care for the P- and T-sensor and the carrier with sealing technology. MESA is responsible for the pH-sensor and the flow system.

REFERENCES

- [1] A. Manz, N. Graber, H.M. Widmer, *Sensors and Actuators B1*, (1990), 244.
- [2] B.H. van der Schoot, E.M.J. Verpoorte, S. Jeanneret, A. Manz, N.F. de Rooij, *Micro Total Analysis Systems*, A. van den Berg and P. Bergveld (eds.), Kluwer Academic Publishers, Dordrecht, the Netherlands, (1994), 181.
- [3] J.H.J. Fluitman, A. van den Berg and T.S.J. Lammerink, *Micro Total Analysis Systems*, A. van den Berg and P. Bergveld, (eds.), Kluwer Academic Publishers, Dordrecht, the Netherlands, (1994), 73.
- [4] M. Elwenspoek, T.S.J. Lammerink, R. Miyake and J.H.J. Fluitman, Towards integrated microliquid handling systems, *J. Micromech. Microeng.*, 4, (1994), 227-245.
- [5] T.S.J. Lammerink, M. Elwenspoek and J.H.J. Fluitman, Micro liquid dosing system, *Proc. MEMS '93 conference*, 7-10 February 1993, Fort Lauderdale, FA, USA, 25-29.
- [6] T.S.J. Lammerink, V.L. Spiering, M. Elwenspoek, J.H.J. Fluitman and A. van den Berg, Modular concept for fluid handling systems, a demonstrator micro analysis system, *Proc. MEMS '96 conference*, 11-15 February 1996, San Diego, CA, USA.
- [7] A. van den Berg, M. Koudelka, B.H. van der Schoot and A. Grisel, A universal on-wafer fabrication technique for diffusion limiting membranes for use in microelectrochemical amperometric sensors, *Sensors and Actuators B*, 5, (1991), 71-74.
- [8] Ph. Arquint, *Integrated blood gas sensor for PO_2 , pCO_2 and pH based on silicon technology*, thesis, University of Neuchâtel, IMT, Switzerland, 1994.

A Low-cost Universal Measurement System for Resistive (bridge) and Capacitive Sensors

Guijie Wang, Frank M.L. van der Goes, Gerard C.M. Meijer
and Harry M.M. Kerkvliet

*Faculty of Electrical Engineering Delft University of Technology
Mekelweg 4, 2628 CD Delft, The Netherlands
Phone 015-2786460, Fax 015-2785922 E-Mail: wang@duteela.et.tudelft.nl*

Abstract

A low-cost universal measurement system for resistive (bridge) and capacitive sensors is presented. It is based on a new designed universal transducer interface (UTI). The system includes sensors, interfaces and a microcontroller. The UTI is a signal-to-time converter, which has a microcontroller-compatible output and which is equipped with front-ends for resistive (bridge) and capacitive sensors. The microcontroller performs the measurement of the UTI output signals, the processing of the data and the communication with the outside digital world, such as a personal computer. A prototype of the measurement system which can measure humidity, temperature, pressure (or strain) and positions has been built and tested. The measurement results for various types of sensors are presented.

1. Introduction

Resistive and capacitive sensors are often employed to measure various physical quantities, such as pressure, temperature, humidity, position, strain, acceleration, etc. The appreciation of these sensors in industry is due to the fact their signals can accurately and easily be processed by low-cost and simple interface circuits. Many processing circuits for resistive and capacitive sensors have been presented [2-5]. Recently, by TU Delft and Smartec, a universal transducer interface (UTI) has been developed [1] which is also available as a market product now [6]. This interface is a sensor-signal-to-time converter, based on a period-modulated oscillator, which is equipped with front-ends for many types of resistive (bridge) and capacitive sensors and which generates a microcontroller-compatible output signal. By applying continuous autocalibration, the additive and multiplicative errors of the interface are eliminated. The accuracy and resolution can be up to 16 bits.

Based on this new interface, a universal measurement system is realized and tested in this paper. In this system, UTIs are employed to perform the interfaces for five types of sensor elements: capacitive humidity sensors, Platinum resistors and thermistors for temperature measurements, resistive-bridge

This work is supported by Smartec BV, The Netherlands.

pressure sensors and potentiometric position sensors. A single microcontroller is used to perform the measurement of the output signals from the interfaces, the data processing and the communication with the outside digital world.

2. Universal Transducer Interface (UTI)

The universal transducer interface (UTI), consists of a signal-to-time converter based on a period-modulated oscillator [1]. The UTI provides interfacing for:

- capacitive sensors 0-2pF, 0-12pF, 0-300pF,
- platinum resistors Pt100, Pt1000,
- thermistors 1k Ω -50k Ω ,
- resistive bridges 250 Ω -10k Ω with unbalance in the range of $\pm 4\%$ or $\pm 0.25\%$,
- potentiometers 1k Ω -50k Ω ,
- combinations of the above mentioned.

In order to perform the continuous autocalibration of offset and gain in the UTI, the three-signal method [7] has been adapted, which requires that a reference signal, an offset signal and a sensor signal are measured in exactly the same linear way. The selection of the measurements of these three signals is controlled by the interface itself. Fig.1 shows the output signal of the UTI in the 3-phase mode.

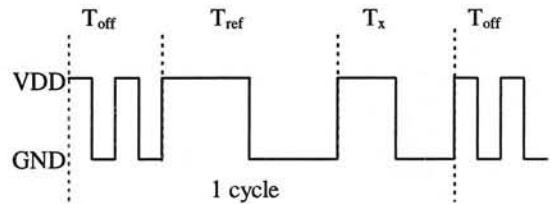


Figure 1. The output signal of UTI in the 3-phase mode.

The period of each phase can be measured by the microcontroller. The final measurement result is:

$$M = \frac{T_x - T_{off}}{T_{ref} - T_{off}} = \frac{S_x}{S_{ref}} \quad (1)$$

where S_{ref} is the reference signal and S_x is the sensor signal to be measured. In the result M , the influence of the additive and multiplicative parameters is eliminated. An important advantage of this technique is that the temperature independence and long-term stability of the signal processing are obtained automatically. The offset measurement with two short intervals is also used as a synchronization signal for the microcontroller.

Important features of the UTI are: measurement for many types of sensors, a single power supply (3.3V-5.5V), low current consumption (<2.5mA), being a low-cost device, continuous autocalibration of offset and gain, high resolution and accuracy (up to 16 bits), a microcontroller compatible output and suppression of 50/60Hz interference. Additional features are the power down mode, the fast/slow mode and the sixteen function modes for different applications which are controlled by four selection pins.

3. Measurement system for resistive (bridge) and capacitive sensors

Based on the features of the UTI, a universal measurement system for the resistive (bridge) and capacitive sensors can be realized in three ways: Firstly, one UTI is employed for one sensor element and the power down mode on the UTI is used to set the working situation of the UTI. Secondly, one UTI is employed for multiple sensors, but an extra multiplexer is used to select the sensor to be

measured. Thirdly, a combination of the above mentioned methods is applied. The best choice is trade-off between costs and simplicities. Here we have chosen the first way because of its simplicity. Fig. 2 shows the measurement system.

Five UTIs are employed for five types of sensors: a capacitive humidity sensor, a resistive-bridge pressure sensor, a Pt100 temperature sensor, a thermistor and a potentiometric position sensor. A microcontroller is used to select the sensor to be measured via the power down mode. The microcontroller also performs the measurement of the output signals from the UTIs, the data processing and the communication with computer. The software program LabView is used to display the measurement results in real time.

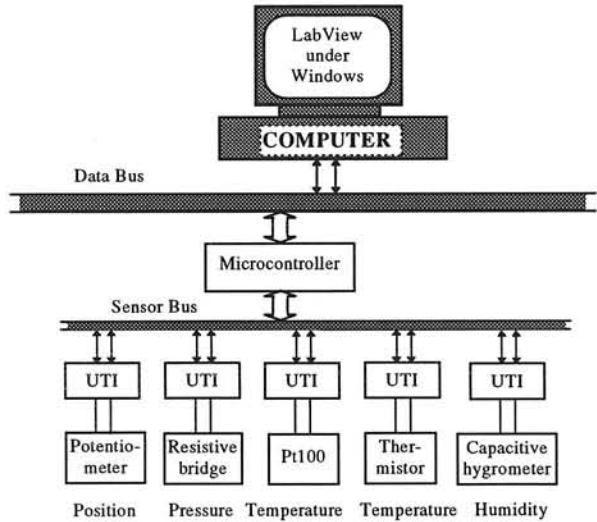


Figure 2. A universal measurement system for resistive and capacitive sensors.

4. The program in the microcontroller

The universal measurement system has six options. It can measure five sensor signals sequentially and continuously or it can only measure a selected one continuously. The selection of the measurement options is performed by the program in the microcontroller. The program is mainly composed of the measurement of the periods of the UTI output signals by counting of the number of internal clock cycles fitting in each phase, calculation of the quantities to be measured by using three-signal method and communication with a computer. Fig. 3 shows the flow diagram of the program.

5. Experimental results

A prototype of the universal measurement system has been built according to the diagram in Fig. 2. The complete system was supplied with single power supply of 5V. A microcontroller (Intel 87c51FB) was used with a 3MHz sampling frequency. In

the measurement of the capacitive humidity sensor, a reference capacitor is required, which was chosen

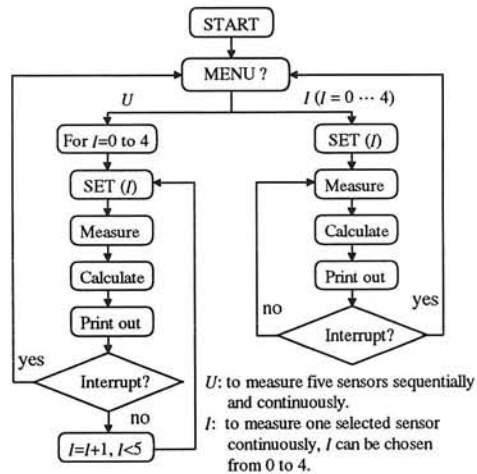


Figure 3. The flow diagram of the program in microcontroller

to be about 100pF. Two external resistors are used to set the voltage swing at the transmitting electrode of capacitors [6].

In the measurement of resistive (bridge) sensors, four-wire connection has been used to eliminate the effect of the parasitic resistance of the connecting wires. Reference resistors are applied for the measurements of the platinum resistor and thermistor. An extra serial resistor R_i is used to limit the current through the platinum resistor, thus the temperature error due to self-heating can be limited [6].

For the different applications, the resolutions and relative non-linearity's are tested in both slow and fast mode (SF=0 and SF=1). For the resistive-bridge pressure sensor and the potentiometer, the relative resolution are tested over the measurement ranges of $\pm 4\%$ and $10k\Omega$, respectively. The measurement results are listed in table 1.

Table 1. Experimental results for five typical sensors

Sensors	Resolution		Non-linearity	Measurement time	
	SF=0	SF=1		SF=0	SF=1
Humidity sensor	0.01 %RH	0.05%RH	0.01%	110ms	14ms
Pt100 temperature sensor	9 mK	96mK	0.02%	100ms	12.5ms
Thermistor	2 mK	8mK	0.02%	100ms	12.5ms
Resistive-bridge pressure sensor	5 ppm	25ppm	0.1%	120ms	15ms
Potentiometer	50 ppm	100ppm	0.02%	175ms	22ms

5. Conclusion

A low-cost universal measurement system has been presented. The system is designed to measure bridge unbalances, resistors and capacitors. The system has been built and tested as a measurement system for various physical quantities, such as, humidity, strain, force, displacement, temperature, etc. An evaluation of the results shows that the system is able to perform precision measurements at rather low costs and that it is suited for consumers as well as industrial applications.

References:

- [1] F. van der Goes, "Low-cost sensor interfacing", Ph.D thesis, Delft University of Technology, to be published, 1996.
- [2] Motorola, "Pressure sensors", USA, BR121/D REV 6, 1992.
- [3] Analog Devices, "Design-in reference manual", USA, 1994.
- [4] Crystal, "Crystal semiconductor data acquisition databook", USA, 1995.
- [5] F.N. Toth and G.C.M. Meijer, " A low-cost, smart capacitive position sensor", IEEE Trans. Instrum. Meas. Vol. 41, pp. 1041-1044, 1992.
- [6] "Universal transducer interface", application note, Smartec B.V. and Delft University of Technology, Dec. 1995.
- [7] G.C.M. Meijer, J. van Drecht, P.C. de Jong and H. Neuteboom, "New concepts for smart signal processors and their application to PSD displacement transducers", Sensors and Actuators A, 35 (1992) 23-30.

A Low-Cost High-Performance Capacitive Absolute Angular Encoder

Xiujun Li and Gerard C.M. Meijer

*Dept. of Electrical Engineering, Delft University of Technology,
Mekelweg 4, 2628 CD DELFT, The Netherlands
Telephone 015-2783836, Fax 015-2785922,
E-mail lixj@duteela.et.tudelft.nl*

Abstract

In this paper, a capacitive absolute angular encoder for the measurement of the position is presented. Its advantages are low-cost, high accuracy and resolution, and having a serial communication output. The encoder is mainly composed of the capacitive sensing element, a signal processor and a microcontroller. Using an appropriate algorithm, the effects of the main undesired influences are eliminated or significantly reduced. The remaining errors are further reduced by a self-calibration technique. The resolution of the angular encoder amounts to 1.5 arcsec, and the accuracy achieves to ± 27 arcsec for a measurement time of 140 ms.

1. INTRODUCTION

Angular encoders can be found in many measurement and control systems, such as liquid level gauges, robots, automobiles and so on. In industry, usually optical encoders are used to measure (angular) positions. The cost of optical precision encoders is relative high. The capacitive encoder presented in this paper can form an attractive alternative for the optical ones: By using multi-capacitive sensing elements and smart processing, a high precision can be obtained with rather relaxed requirements for the mechanical construction and consequently at low cost.

The new design presented in this paper uses a capacitive sensing element to sense angular position, a new algorithm to accurately calculate the position, a self-calibration technique, a high-performance signal processor and a microcontroller.

2. BASIC PRINCIPLE AND SENSING ELEMENT

2.1 Basic Principle

Figure 1 shows a diagram of capacitive encoder system. It is mainly composed of the capacitive sensing element, a signal processor and a microcontroller. The capacitor's values of the multi-electrode sensing element are sensitive to the position. The signal processor has a multi-capacitance input and a microcontroller-compatible output. It can linearly convert the capacitor's values of the

This project is supported by ENRAF (Delft Instruments), Smartec and the Dutch Technology Foundation (STW), The Netherlands.

sensing element to period-modulated signals. The microcontroller performs the measurement of the periods and calculates the position. It also enables the communication with the outside digital world. The system is inherently auto-calibrating for the linear systematic errors of the processing circuitry.

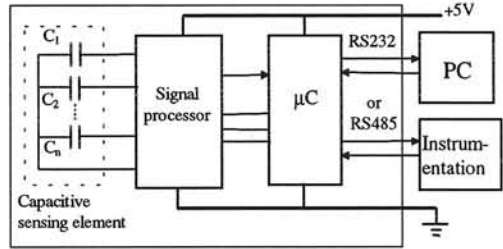


Fig. 1 A diagram of capacitive encoder.

2.2 The Sensing Element

A simplified structure of the capacitive angular sensing element is shown in Fig. 2 [4]. It is mainly composed of two fixed-plane electrodes and one rotating screen electrode. The nine capacitors are formed by using 27 electrode segments on the fixed segmented electrode. The 24 outer segments are used for a very accurate fine measurement over a range of one segment width (15°), and a first coarse measurement over a range of six segment widths (90°). Three inner segments are used for a second coarse measurement to determine in which quadrant the inner window is positioned and which completes the measurement range of 360° .

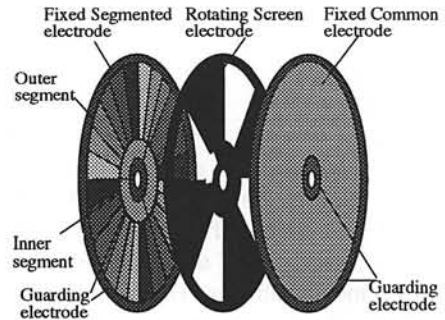


Fig. 2 A simplified structure of the angular sensing element.

The use of the cross-quad configuration in the sensing element significantly reduces the influence of both the stochastic mechanical errors and the systematic errors, such as the eccentricities, the nonflatness and the obliqueness of the electrodes. This technique has been described in [3, 4].

For the structure of the sensing element given in figure 2, the relation of the measured angular position φ_m and the capacitances ($C_{i+1} \dots C_{i+6}$) between the segmented electrode and the common electrode is represented by the following formula [3, 4]:

$$\frac{\varphi_m}{\varphi_s} = i + \frac{(C_{i+5} + C_{i+6}) - (C_{i+2} + C_{i+3})}{2(C_{i+4} - C_{i+1}) + \alpha(C_{i+2} + C_{i+4} + C_{i+6} - C_{i+1} - C_{i+3} - C_{i+5})}, \quad i = (0, 1, \dots, 5), \quad (1)$$

for $-1/2 \leq (\varphi_m / \varphi_s - i) \leq 1/2$. Where φ_s is the angular width of an electrode segment ($\varphi_s = 15^\circ$), α is called the fine-tuning factor ($0 \leq \alpha < 1$). The appropriate fine-tuning factor will reduce the influence of the electric-field-bending effect. Many undesired influences, for instance, gain errors and offsets of the sensing elements and the signal processor, are eliminated or significantly reduced on the measured angular position because of using the ratio of two linear combinations of the capacitances.

3. CALIBRATION

Although the effect of the mechanical errors is significantly reduced by using a symmetrical and redundant configuration in the electrode structure, some mechanical errors, for instance the nonflatness, and the pattern errors of the segmented electrode will still affect the equality of the segment-capacitance values between the outer segments and the common electrode. Here the influence of the local nonflatness of the electrode surface is integrated over the area of one segment. This results in a systematic inaccuracy with a period of six segment widths (90°) on the measured angular position because the outer window on the rotating electrode repeats itself after six segment widths [4].

In order to further reduce these remaining errors, the following relationship between the measured position and the capacitances is used:

$$\frac{\varphi_m}{\varphi_s} = \begin{cases} \left(1 - \frac{C_{i+2,\max} + C_{i-1,\max} - 2C_{i,\max}}{2C_{i,\max}} \right) \frac{\varphi_m(C_i)}{\varphi_s} - \frac{C_{i+1,\max} - C_{i-1,\max}}{2C_{i,\max}}, & \frac{\varphi_s}{2} \geq \varphi_m > 0 \\ \left(1 - \frac{C_{i+1,\max} + C_{i-2,\max} - 2C_{i,\max}}{2C_{i,\max}} \right) \frac{\varphi_m(C_i)}{\varphi_s} - \frac{C_{i+1,\max} - C_{i-1,\max}}{2C_{i,\max}}, & -\frac{\varphi_s}{2} < \varphi_m \leq 0, \end{cases} \quad (2)$$

for the measurement range of one segment width. Where $\varphi_m(C_i)/\varphi_s$ represents the relationship described by the formula (1). $C_{i,\max}$ ($i = 1, 2, \dots, 6$) represents the capacitance between the outer segments on the segmented electrode and the common electrode without the rotating electrode. Formula (2) includes the correction terms and factor for scale and offset errors. Those correction terms are found by calibration. This calibration can be performed without using a reference encoder, which is a very attractive point of this calibration technique. This calibration is called a self-calibration. The values of six capacitors ($C_{i,\max}$, $i = 1, 2, \dots, 6$) should be measured beforehand for applying the calibration. The scale and offset errors are automatically eliminated by using formula (2).

4. THE MEASUREMENT METHOD

The microcontroller is used to measure the periods, to calculate the position, to calibrate remaining errors and to communicate with the outside digital world. The calculation of the absolute angular position from the measured nine periods is performed in three steps: an accurate fine measurement over a range of 15° , and a first and a second coarse measurement over ranges of 90° and 360° , respectively. For applying the self-calibration technique, six periods representing six capacitances ($C_{i,\max}$, $i = 1, 2, \dots, 6$) and one offset period (T_{off}), are measured beforehand. The accurate fine measurement is performed using formula (2). With the first coarse measurement it is found in which circle segment i the angular position is situated. This is done by comparing the six measured values of the periods ($T_{s1} \dots T_{s6}$). After the first coarse measurement, the position is accurately known over a range of 90° . The second coarse measurement determines in which quadrant q ($q = 0, 1, \dots, 3$) the angular position is situated. The measured absolute angular position φ_m is found using the equation

$$\varphi_m = \varphi_{mi} + \left(i - \frac{1}{2}\right) \times 15^\circ + q \times 90^\circ, \quad (3)$$

where φ_{mi} is the result of the accurate fine measurement within one segment width from formula (2). Figure 3 shows the procedure of this measurement algorithm.

5. EXPERIMENTAL RESULTS

An absolute angular encoder based on the system described in section 2 has been built and tested. The common electrode and segmented electrode were made using simple printed-circuit-board technology. Guarding electrodes, surrounding the segmented electrode and common electrode, were used to reduce the influence of the electric-field bending. Both guarding and shielding are used to reduce the effect of

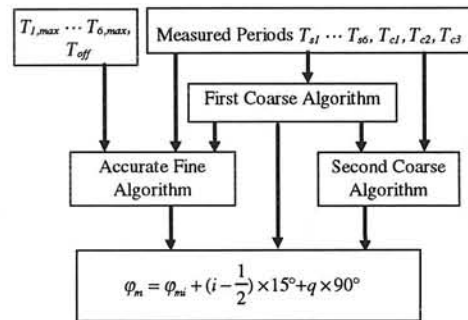


Fig. 3 The procedure to perform the measurement algorithm.

electromagnetic interference. The rotating electrode was made out of stainless steel by spark erosion technology and is grounded by using a sliding contact. All the electrodes were mounted in a metal housing, which is connected to ground and shields against external interference.

The signal processor has been implemented with two discrete chips, for the oscillator and the multiplexer, respectively. The oscillator chip is mounted at the common electrode PCB and the multiplexer chip at the segmented electrode PCB. This specific way of assembling is used to minimize undesired cross-talk effects. Seven periods were measured beforehand and loaded in the EPROM of the microcontroller. The nine periods were measured in a total measurement time of about 140 ms. The microcontroller directly gives a digital output signal representing the measured position. Table 1 lists some important experimental results and parameters.

Table 1 Some important experimental results and parameters.

Power supply	5V±10% / max. 30mA
Measurement range	0 – 360°
Resolution	19.7 bits (1.5 arcsec)
Repeatability:	18.4 bits (3.56 arcsec)
Reproducibility:	19 bits (2.54 arcsec)
Accuracy:	15.5 bits (26.2 arcsec)

6. CONCLUSION

A low-cost, high-performance capacitive angular encoder with a digital output has been presented. The applied algorithm reduces the influences of the major systematic nonidealities of the sensing element and the signal processor in a very effective way. In addition to this, a self-calibration technique has been applied for a further reduction of the remaining influence of the mechanical errors and pattern errors of the electrodes. A prototype of the encoder has been built using low-cost material. The inaccuracy of this angular encoder is less than ±27 arcsec for a measurement time of about 140 ms. This remaining inaccuracy is mainly due to the noise of the processing circuit, the sampling noise of the microcontroller and the asymmetry of the rotating electrode.

7. ACKNOWLEDGEMENTS

The authors greatly thank Jo W. Spronck, of the Dept. of Mechanical Engineering and Marine Technology, Delft Univ. of Technology, Ferry N. Toth, of the Dept. of Electrical Engineering, Delft Univ. of Technology, and M. van der Lee and Dorus A.J.M. Bertels, of Enraf Delft Instruments for their helpful discussions.

REFERENCES

- [1] F. Zhu, J.W. Spronck and H.F. van Beek, "A capacitive absolute position transducer," In Proc. of the 7th International Precision Engineering Seminar, Kobe, Japan, 1993.
- [2] F.N.Toth and G.C.M. Meijer, "A low-cost, smart capacitive position sensor," IEEE Trans. Instrum. Meas., vol. 41 no. 6, pp.1041-1044, Dec. 1992.
- [3] G.W. de Jong, "Smart capacitive sensor (physical, geometrical and electronic aspects)," Ph.D. Thesis, Electronics Research Lab., Delft Univ. of Technology, Dept. of Electrical Engineering, 1994.
- [4] X.J. Li, G.C.M. Meijer and G. W. de Jong, "An Accurate Smart Capacitive Angular-Position sensor with a Full Circle Range," in Proc. IEEE IMTC/95, pp. 80-83, USA. Apr. 1995.

SENSOR INTERFACE ENVIRONMENT

F.R.Riedijk, M. Balijon, E. van Kampen, M. de Groot, J.H. Huijsing

*Electronic Instrumentation Laboratory, Department of Electrical Engineering,
Delft University of Technology, Mekelweg 4, 2628 CD Delft, The Netherlands
Tel.: +31-15-785747, Fax: +31-15-785755.*

Abstract

A sensor interface environment is shown in which sensors can easily interface with a microcontroller or a Personal Computer. The system is based on a new sensor bus which is able to transmit both analog and digital signals. Bus control software has been developed and will be demonstrated with a number of smart sensor projects.

I. Introduction

A new generation of cheap and "easy to use" sensors is developed and is finding its way into professional applications such as satellites, and into consumer products, such as vacuum cleaners. These mostly silicon (chip) sensors are equipped with analog signal conditioning circuits, A-to-D converters and a two-wire bus interface. A new sensor bus, called Integrated Smart Sensor bus (IS²), has been developed in collaboration with Philips, also holder of the patent[1],[2]. The bus is closely related to the worldwide standard inter IC bus (I²C), used in domestic appliances such as video an tv. The bus protocol allows the transmission of analog, duty-cycle, frequency and digital sensor signals. In this way most commercial and the new developed sensors can be interfaced with microprocessors and a PC in a very easy and cheap way. "Normal" bus features such as error detection, alarms, conflict handling are also supported. The entire bus protocol is implemented in a small chip without any external components.

To show the possibilities of such smart sensors, an very cheap interface to a Personal Computer has been developed. This interface will be used to demonstrate a number of projects in which prototypes are build for commercial use or for research [3].

Also "stand alone" systems are shown in which one or more smart sensors are connected with a micro-controller using software for bus control or for sensor calibration. Such systems will be the centre of many future products.

II. Sensor-Computer interface environment demo

A system will be demonstrated in which smart sensors can directly communicate with a Personal Computer using the Integrated Smart Sensor bus. For this purpose the parallel printer output port (LPT1) is reprogrammed to drive this new bus. For protection purposes an additional buffer IC is used external from the Computer. Except for this IC, the total bus protocol and the bus control is software driven. This software can run on each 386 compatible PC. The bus configure data as well as the sensor output data is organised in files. These files can easily be read by programs as LabView, which offer a very nice graphical representation of the data and which can also be used to control the bus in automated measurement systems.

The interface environment is capable of dealing with analog signals, duty-cycles, frequencies and digital signals, without bothering the bus user with the actual used signal format.

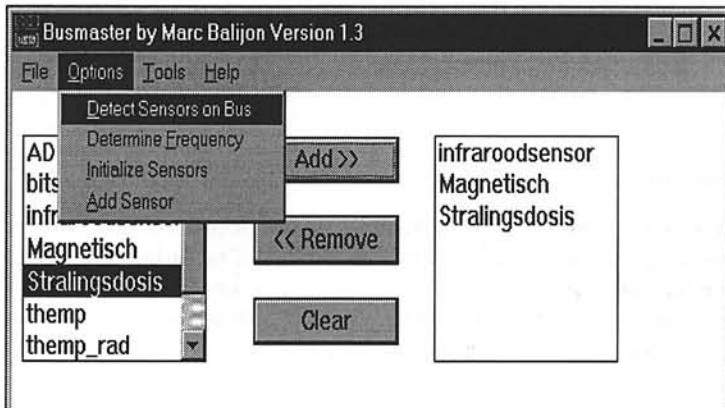


Figure 1. A snap shot of the busmaster program, working with windows. The program can configure the bus system and control the sensor read-out. Also it can be used in an automated measurement environment using for example LabView

III. Pyranometer bus interface for weather pole

In collaboration with Kipp&Zonen a sensor interface for thermocouples is developed for use in pyranometers (solar radiation). The pyranometer is based on a conventional thermal principle in which a black painted disc is heated by solar radiation. The temperature rise is measured by a thermocouple, which delivers a voltage between μV and tens of mV . The interface chip is therefore equipped with a very low offset integrated amplifier. The output signal of the amplifier is converted into a digital signal using a sigma delta A-to-D converter. Also an integrated temperature sensor with an accuracy of a few degrees is integrated for the calibration of the pyranometer. On the sensor interface chip a bus interface block is added, capable of addressing the temperature sensor, the pyranometer or the offset calibration circuit. The output format to the bus is a pulse rate. The pyranometer with discussed interface chip will be demonstrated using the described Personal Computer software setup.

IV. Smart Flow sensor for vacuum cleaner

In collaboration with Philips (Domestic Appliances Group) a smart flow sensor is developed for use in a vacuum cleaner. Information on the flow is used for motor control. A thermal flow sensor with bus output is realised. It is interfaced with a micro-processor already incorporated in the vacuum cleaner. The flow sensor is also used in wind meters and gas flow sensors.

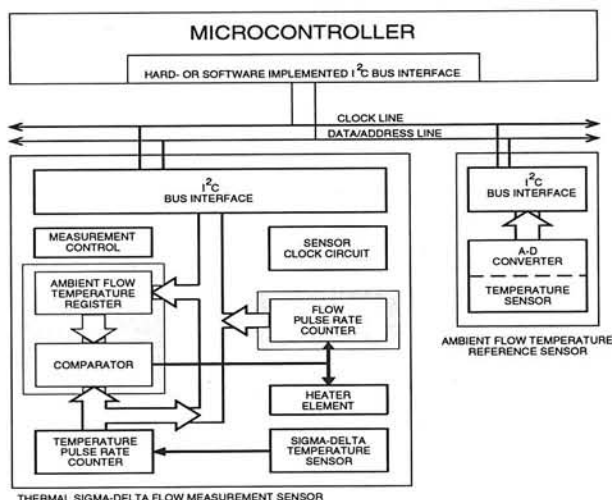


Figure 2. The setup of the thermal flow sensor system in a vacuum cleaner. One chip is heated and measures the power needed, which is a measurand for the flow. The other chip is needed as a reference. Both chips communicate via the I²C bus with a microcontroller, which calculates the flow and controls the motor.

V. Radiation sensor for satellites

In collaboration with ESTEC/ESA a smart sensor is developed for use in a satellite. For the control of a satellite it is needed to monitor the temperature and radiation on several places. A low-power, low-weight and radiation-resistant (bipolar) system was required. The radiation dose sensor is based on a large MOSFET, which is gradually degrading with the total radiation dose. This sensor has to be biased with a small current and its threshold voltage will vary between 0.8 and 5V with increasing radiation dose. For the temperature sensor an integrated bandgap sensor is used, which has an accuracy of several degrees Celsius. A single chip (ASIC) with the temperature sensor, biasing and read-out circuits for the radiation sensitive FET, interface electronics and bus output is realised. The chip can be directly interfaced to a microprocessor and a PC environment. This project is also included in the demonstration.

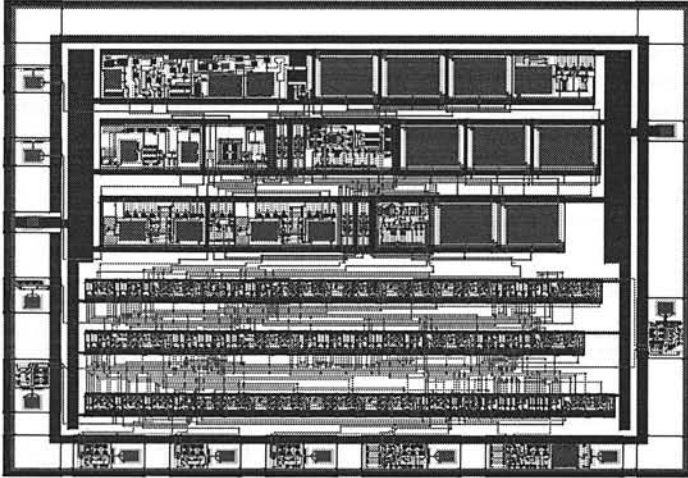


Figure 3. Interface chip developed for ESTEC, containing sensor signal conditioning, temperature sensor, A-to-D conversion and a bus interface. This chip is totally generated by automatic tools.

VI. Connecting commercial sensors

Many commercial sensors have an analog output such as 0-5V or a frequency/duty-cycle output. These sensors can be connected to the IS² bus using a very small analog interface chip containing some tens of logical ports. The duty-cycle or frequency signals can easily be interpreted by the microprocessor or by the PC with busmaster software. The pure analog signals are converted in a digital signal by using a separate A/D converter connected to the bus. This device recognises an analog transmission and takes a sample of the value. By reading out this device after each analog transmission a digital representation is available for the bus user. The user of the bus is shielded from the actual sensor signal on the bus and will only cope with the digital numbers, which can for example be displayed in LabView.

VII. References

- [1] J.H.Huijsing, R.F.Tuk, F.R.Riedijk, M. Bredius, G. v/d Horn, Mixed Analog/Digital two line Bus System, Dutch patent Nr 93201595-1, June 1993.
- [2] F.R.Riedijk, R.F.Tuk, M. Bredius, J.H.Huijsing, A bus controlled interface environment for an accurate read-out and flexible interconnection of integrated smart sensors in local systems, proc. transducers 1993, Yokohama, Japan, 7-10 June, 1993.
- [3] F.R. Riedijk, Analoge sensoren nu digitaal, Delft Integraal 95-2, June 1995.

Optical and Acoustic Sensor Systems for Autonomous Mobile Robots

P.J.Trimp, G.Buis and P.J.French

Delft University of Technology, DIMES
Faculty of Electrical Engineering
Lab. for Electronic Instrumentation
Postbus 5031, 2600GA Delft, The Netherlands.
Tel +31-15-2784707, Fax +31-15-2785755

Abstract

With the increasing need for autonomous robots has come the need for new advanced sensor systems. In the Laboratory of Electronic Instrumentation an autonomous mobile robot system called SIMON has been developed. SIMON stands for Sensor Intelligence for Mobile On-board Navigation. The aim of this project is to develop a range of sensor systems to implement intelligence and therefore autonomy into the robot. In this paper two systems will be discussed. The first is a homing system which enables the robot to find the charging station and the second is the collision avoidance system. The robot can therefore move autonomously in the laboratory by using both optical and acoustic sensor systems. The information from the sensors is read-out using a 80C552 microcontroller which has been incorporated into the robot.

Introduction

Modern autonomous robots require a range of sensor systems [1,2]. The mobile robot system comprised several modules such as motor control and remote control. The homing and the anti-collision system are also included in the mobile robot system. The mobile robot has a diameter of 44 cm. It has two drive wheels driven separately and can accelerate within 30 seconds to a maximum speed of 3 m/s. Horizontal stability is established by two swivel castors.

Homing

In normal operation the robot needs to be recharged at regular interval. Having decided that recharging is necessary the processor automatically starts the homing program. The homing program makes use of an IR-distance measurement system implemented on the mobile robot system. The homing system comprises the IR-distance measurement system and a fixed IR-beacon placed in the workspace of the robot. The current through the LED's is modulated with an arbitrary frequency of 2.5 kHz. In figure 1 the basic principle of the homing system is shown. The detection of the IR-signal is achieved using two photo diodes which are placed at a fixed distance, b , apart on the mobile robot system. Because of sunlight and other unwanted illumination sources the photo diodes are used in

the linear mode (Figure 2). The photo diode currents are directly related to the distance and the light intensity of the beacon. The illuminance ,E, of the photo diode, at a distance d from the IR-beacon:

$$E = \frac{I}{d^2} \quad (1)$$

where I is the luminous intensity.

The distance d can vary between 0.1 to 50 metres yielding a maximum to minimum illuminance of $2.5 \cdot 10^5$. The output signals from photo detectors are accompanied by unwanted noise and interference that set limits to the maximum detectable distance d. In particular, when the total noise power exceeds the signal power, special techniques are needed to recover the signal. These techniques are based on an improvement of the signal-to-noise ratio by the measuring system. It is proven that coherent detection provides an optimum technique for recovering the amplitude of the measurand by maximizing the signal-to-noise ratio [3]. This technique can be used when the frequency and phase of the signal are known.

The principle of the coherent switching demodulator [4] is given in figure 3a. $x(t)$ consists of the information carrying signal $s(t)$ and additive white noise $n(t)$. The noise is already band-limited by a pre-demodulation band-pass filter with a noise bandwidth B_n . A frequency converter that fulfills this demand is the double-balanced switching demodulator [4,5], which is essentially a reversing switch being thrown between input signal $-x(t)$ and the non-inverted input signal $x(t)$ at the rate of the reference frequency. If MOSFET's are used for the switches, the quadratic nonlinearity will be very small. Further, the dynamic range of this kind of demodulators is very large ($10^5 - 10^6$). Finally, the output signal of these demodulators is independent of the reference signal amplitude.

The operation of a switching demodulator can be described by the product of the input signal and a symmetrical square wave $y(t)$ with a unity amplitude and a frequency equal to the switching frequency. The square wave can be described by a Fourier series

$$y(t) = \frac{4}{\pi} \cdot [\cos \omega_r t - \frac{1}{3} \cdot \cos 3 \omega_r t + \frac{1}{5} \cdot \cos 5 \omega_r t - \dots] \quad (2)$$

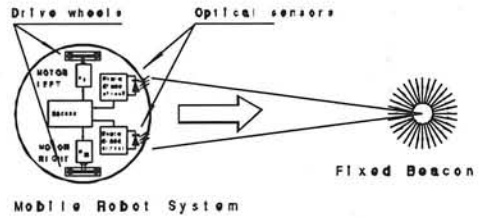


Fig.1 Basic principle of the homing system.

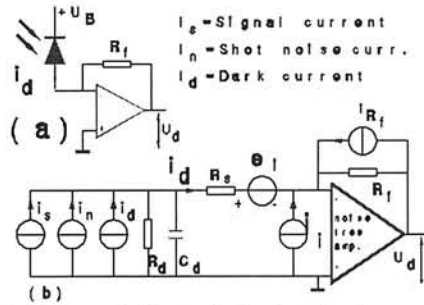


Fig.2 a) Photodiode circuit. b) Noise eq. circuit.

That means that the detector not only responds to the fundamental frequency of the reference signal but also responds to the odd harmonics as illustrated in figure 3b. When the mark-space ratio of the switching signal is not exactly unity, the detector will also become sensitive at even harmonics of the switching frequency. However, the detection is no longer sensitive to sub-harmonics.

The harmonic sensitivity will degrade the signal-to-noise ratio as given in (3) at the detector output.

$$(SNR)_o = \frac{\overline{s^2(t)} \cdot \cos^2 \phi}{N_o \cdot \Delta f_{nLP}} \quad (3)$$

If the circuit of figure 3a is used with an input signal and reference signal that are in phase, the circuit is usually referred to as a synchronous detector. For both the photo diode signals a coherent switching demodulator circuit is used. The two analogue output signals contain information over the distance d and the direction of the beacon. The analogue signals are processed by the 10 bit AD-converter on-board of the micro-processor.

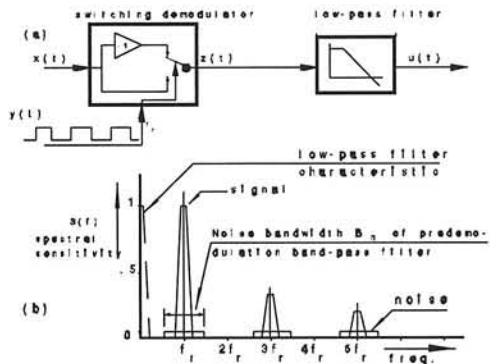


Fig.3 Coherent switching detector and demodulator circuit.

Anti-collision system

The mobile robot system is equipped with three ultrasonic distance sensor systems. These three sensors are positioned to cones 180° as shown in figure 4. To also avoid moving obstacles, the algorithm needs to be fast and thus simple.

The algorithms make use of only three directly measured quantities, obtained from two distance sensors. These sensors are wide beam and are mounted on the left (L), middle (M) and (R) sides of the robot. The distance sensors measure the distance to the nearest object in their angle of sight. The measured distance is directly related to the time-of-flight from the first received echo. Symbol d_L is defined as the distance between the centre of the left sensor and the edge of the nearest object. If there is no object within a distance m , d_L is set to m . The same holds for d_M and d_R . The quantities, d_L , d_M and d_R , determine the motor velocities v_L and v_R to rotate the robot. This

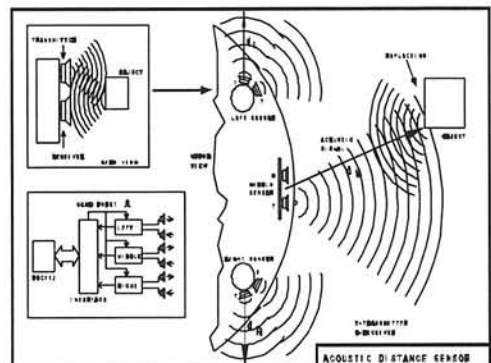


Fig.4 Acoustic distance sensor system.

will steer the robot to the left or right until the object is out of sight and therefore avoided. For every sample taken at time t , the values v_L and v_R are computed and as velocity setpoints fed into the motor controllers. Other movement control units, as map guided navigation or human remote control, produce setpoints σ_L and σ_R . Finally, a mathematical relationship has to be derived between the measured distances (d_L, d_M, d_R) and the velocities (v_L, v_R). The figure of merit is the ability for the robot to drive successfully into and through a corridor of a width c . The derived control rules are based on; a) the side sensors L and R mainly influence the robot's steering and b) the middle sensor (front sensor) M diminishes the overall speed if an object is encountered in front of the robot.

The settings of the side sensors determine the minimum corridor width and the safety margin can be set via the parameters of the middle sensor.

The control rules are given in the formulas;

$$v_L(t+1) = \sigma_L \frac{d_R(t)d_M(t)}{m.m_M} \quad (4)$$

$$v_R(t+1) = \sigma_R \frac{d_L(t)d_M(t)}{m.m_M} \quad (5)$$

which gives the robot full autonomous control over speed and direction.

Conclusions

The homing system is implemented on the mobile robot system and is able to locate the beacon within 10 metres. This distance is presently being increased by further reducing noise interference levels. The anti collision system ensures that the robot is able to travel to the beacon in safety.

References

- [1] A.M.Dudar; D.G.Wagner; G.D.Teese; Mobile autonomous robot for radiological surveys, 1992, 12p, Westinghouse Savannah River Co., Aiken, SC.
Funder: Department of Energy, Washington, DC. Patent Number 5,324,948
- [2] H.R.Everett; Intelligent battery charging system. Department of the Navy, Washington, DC, Filed 14 nov.'89, Patented 3 sept.'91 15p. Patent Number 5,045,769
- [3] A.J.Viterbi, "Principles of coherent communication". McGraw-Hill Book Company, New York, 1966
- [4] J.R.Anderson, D.R.Zrudsky, "A nanovolt MOSFET reversing switch for low temperature applications". Rev. Sci. Instrum., Vol.44, 1973, p136.
- [5] P.P.L.Regtien/ed, "Modern Electronic Measuring Systems", Delft University Press 1978, The Netherlands, pp 119-139

SIMULATION AND DEVELOPMENT OF A 1-BAR CAPACITIVE DIFFERENTIAL PRESSURE SENSOR

M. Pedersen, M.G.H. Meijerink, W. Olthuis and P. Bergveld

MESA Research Institute, University of Twente,
P.O. Box 217, NL-7500 AE Enschede, The Netherlands
Phone: +31 53 4892722, Fax: +31 53 4892287
e-mail: M.Pedersen@eltn.utwente.nl

ABSTRACT

A capacitive differential pressure sensor has been developed. The process used for the fabrication of the sensor is IC-compatible, meaning that the device potentially can be monolithically integrated on one chip with a suitable signal conditioning circuit. A sensor for a differential pressure range of ± 1 bar was fabricated and tested with two different detection circuits, and good agreement was found with the theoretical model of the sensor. A nominal sensitivity $\Delta C/C$ of 18 % has been measured for a positive differential pressure of 1 bar. The resolution of the complete detection system was 0.25 mbar (25 Pa).

I. INTRODUCTION

It is well acknowledged that the capacitive detection principle is superior concerning sensitivity and power consumption. However, a major problem of this type of sensors is that the source capacitance is very small, causing the sensitivity to parasitics and noise to be relatively high. The best approach to minimise these effects is to make the electrical connections between the sensor and the signal conditioning circuit as short as possible. The furthest implementation of this is to integrate the sensor on the same chip as the signal conditioning circuit. The problems arising from this desire to integrate sensor and electronics are, however, very complicated. If a sensor is to be made on the same piece of silicon as for instance CMOS circuits, one has to consider the compatibility between the sensor process and the CMOS process. It is well known that important parameters, such as threshold voltages and g_m -factors of the CMOS components are very sensitive to variations or changes in the fabrication process. Therefore, the introduction of any additional process steps for the fabrication of the sensor must be carefully considered in order to maintain the device properties of the CMOS circuits. In this paper we report on a capacitive pressure sensor, which may be fabricated directly on substrates already containing CMOS circuits. The fabrication process of the sensor only contains low temperature (<300 °C) spin-on, evaporation, and etching processes, which are all considered to be harmless to CMOS. The fabrication process has been derived from previous developments on silicon condenser microphones [1].

II. SENSOR STRUCTURE AND SIMULATION

The structure of the sensor is shown in figure 1. It essentially consists of a polyimide diaphragm, made on a silicon substrate. Between the diaphragm and substrate, an air gap has been created by deposition and subsequent removal of an aluminium sacrificial layer. On both the diaphragm and the substrate a metal electrode is attached. When, in operation, a pressure difference is applied across the diaphragm, it deflects due to the load, and a change of electrical capacitance between the electrodes may be observed.

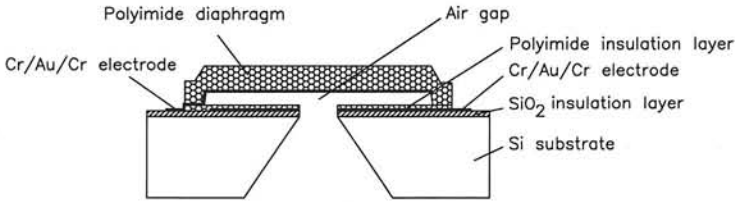


Figure 1: A cross-sectional view of the capacitive differential pressure sensor.

The theoretical behaviour of the sensor can be separated in two parts. One concerns the mechanical characteristics, which determines the deflection properties of the diaphragm under the load of an external pressure. The second part relates to the translation of the mechanical deflection of the diaphragm into a change of capacitance between the two electrodes. The polyimide diaphragm has a built-in tensile stress of about 40 MPa. For these values of built-in stress, it may be assumed that the deflection of the diaphragm is dominated by this stress, and that the additional stress introduced from bending may be neglected. The error introduced by this assumption can be compensated for with a linear matching factor K . For deflections much smaller than the thickness of the diaphragm, the deflection profile can be approximated by [2]:

$$w(x, y) = w_0 \cdot \cos\left(\frac{\pi x}{a}\right) \cos\left(\frac{\pi y}{a}\right) \quad (1)$$

where a is half the side length of the diaphragm, x and y are principal directions with the origin in the centre of the diaphragm, and w_0 is the centre deflection given by:

$$w_0 = K \cdot 0.3284 \cdot \frac{pa^2}{\sigma h_d} \quad (2)$$

in which σ is the built-in stress, h_d is the thickness of the diaphragm, p is the applied pressure, and K is the matching factor. This factor was determined by comparing the simple model with a more complex model [3], which includes both bending and built-in stress. For a diaphragm with side length 700 μm and thickness 16 μm , a matching factor of 0.57 was calculated.

The capacitance of the sensor can be derived by integration over the surfaces of the two electrodes, of which one is flat (the substrate) and one has the deflection profile of the diaphragm. The capacitance is given by:

$$C_{\text{sensor}} = \epsilon_i \epsilon_0 \int_{-a}^a \int_{-a}^a \frac{1}{h_i + \epsilon_i [h_g + w(x, y)]} dx dy \quad (3)$$

where ϵ_i and h_i is the relative permittivity and the thickness of the polyimide insulation layer, and h_g is the height of the air gap.

For the sensor, a diaphragm with a side length of 700 μm and a thickness of 16 μm , was chosen. The thickness of the insulation layer was 0.5 μm , and the height of the air gap was 5 μm . According to (2), the diaphragm will have a deflection of 3.6 μm for a pressure load of 1 bar. Therefore, the sensor can work with both negative and positive pressure differences. In figure 2, a simulation result is shown of the sensor capacitance as function of the applied differential pressure.

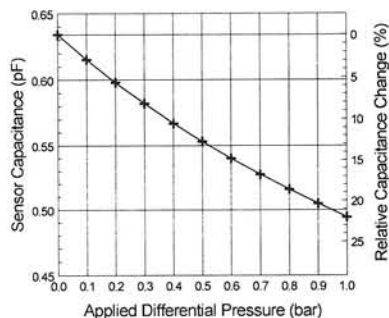


Figure 2: Simulated sensor capacitance vs. applied differential pressure.

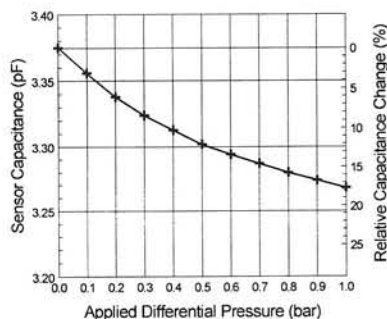


Figure 3: Measured sensor capacitance vs. applied differential pressure.

As it may be seen from figure 2, the theoretical sensor capacitance decreases more than 20 % in the pressure range from 0 bar to 1 bar.

III. MEASUREMENTS AND RESULTS

Since the capacitance of the sensor is very small (≈ 0.63 pF), the influence of the parasitic capacitance from the interconnection wires is significant. To illustrate this, a measurement on a completed device is shown in figure 3. The sensor was mounted on a test chuck, whereby a pressure could be applied to the backside. The sensor capacitance was measured using a Hewlett-Packard 4194A Impedance Analyzer. As it can be seen, the measured capacitance is much larger than the theoretical (≈ 3.37 pF). However, if one considers this extra capacitance (≈ 2.74 pF) to be caused by a parasitic capacitance in parallel with the sensor, the corrected measured relative capacitance change is in good agreement with the theory. The remaining differences between measurements and theory can be explained by deviations of the assumed built-in stress in the polyimide diaphragm.

The pressure sensor was also tested with two different detection circuits, shown in figures 4 and 5. The first circuit is a simple oscillator, in which the sensor determines the frequency of the signal on the output of the amplifier [4]. The simplicity of this circuit is appealing for a possible monolithic integration. The other circuit is a capacitance-to-voltage converter, previously developed for accelerometers [5]. In this circuit, the amplitude of a frequency carrier is modulated by the capacitance of the sensor. After demodulation, a DC voltage remains, which is in direct relation to the ratio between the sensor capacitance C_x and C_f .

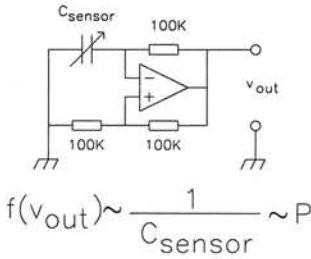


Figure 4: Oscillator detection circuit.

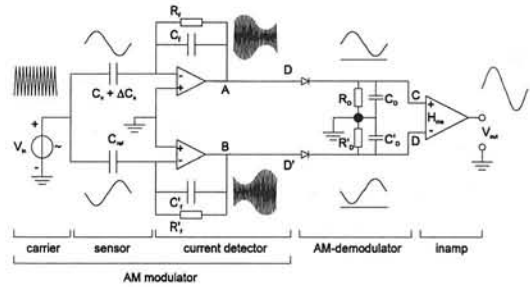


Figure 5: Capacitance to voltage converter.

The results of the measurements are shown in figures 6 and 7. It is characteristic that the behaviour of both systems is in close correlation. For the oscillator circuit a full-scale sensitivity of 4.2 kHz/bar with a resolution of 2.4 mbar was measured, whereas the C-V converter had a sensitivity of 4.5 V/bar and a resolution of 0.25 mbar. The resolution is determined by the signal-to-noise ratio. Consequently, the selection of detection circuit is a choice between simplicity and performance.

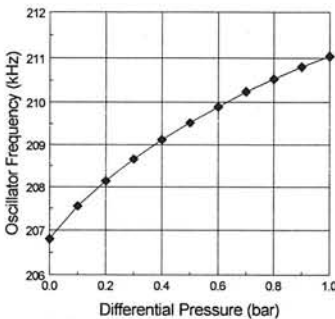


Figure 6: Oscillator frequency vs. applied pressure.

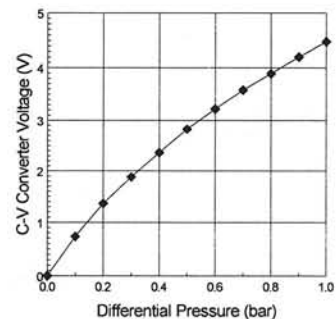


Figure 7: C-V converter output voltage vs. applied pressure.

IV. CONCLUSIONS

A capacitive differential pressure sensor containing a polyimide diaphragm has been developed. The fabrication process of the sensor is IC-compatible, and can be made directly on the substrates with completed integrated circuits. The sensor was tested, and good agreement was found with the theoretical performance. Future developments are focused on monolithic integration with CMOS circuits.

REFERENCES

- [1] Patent application no. 1001733, November, 1995, Rijswijk, The Netherlands.
- [2] S.P. Timoshenko, S. Woinowsky-Krieger, *Theory of Plates and Shells*, 2nd edition, McGraw-Hill, USA, 1959.
- [3] M. Pedersen, W. Olthuis, P. Bergveld, "Modelling and Simulation of the Quasi Static Behaviour of Silicon Condenser Microphones", *Proceedings of MME'95*, Copenhagen, Denmark, September 1995.
- [4] M. Meijerink, *Development of an IC-compatible capacitive pressure sensor*, Master's thesis, University of Twente, January, 1996.
- [5] J.C. Lötters, W. Olthuis, P.H. Veltink, P. Bergveld, "A sensitive differential capacitance to voltage converter for sensor applications", *Submitted for publication in IEEE Instrumentation and Measurement*.

Development of a high temperature resistance thermometer using noise thermometry

M.J. de Groot ✓, J.F. Dubbeldam ✓, H. Brixy X, F. Edler †, G.S. Dhupia ‡, M.V. Chattle ◆.

✓ NMI Van Swinden Laboratorium Postbox 654, NL-2600 AR DELFT The Netherlands; tel +15 2619661 fax. +15 2612971, email mdegroot@nmi.nl.

X Forschungszentrum Jülich GmbH, IWE 2, D-52425 Jülich, Germany

† Physikalisch Technischen Bundesanstalt, Abbestraße 2..12, D-10587 Berlin, Germany

‡ Brands GmbH, Zum Mühlengraben 16-18, D-52355 Düren, Germany

◆ National Physical Laboratory, Queens Road, Teddington, Middlesex, United Kingdom TW11 0LW.

This project is supported by the European Community Standards Measurements and Testing Program.

A thermometer is described for industrial use that uses a ceramic material as the temperature dependent resistive element. This new thermometer was developed and tested for its stability in the short term and the medium term. It is found that the stability of the thermometer can be compared with that of thermocouples. The obvious advantage of a resistance thermometer over thermocouples is that it can more easily be calibrated. A noise temperature system has been designed and used to characterise the thermometer resistance between 1000 °C and 1500 °C. Below 1000 °C the thermometer resistance was characterised by comparison with standard thermometers.

Introduction

This project aimed at the development of two prototype resistance thermometers based upon a ceramic with Mo and Si as its primary constituents. The material is regularly applied for heater applications. The design of the second prototype series was based upon experience obtained from testing the first series. Two laboratories were involved in testing the prototype thermometers. These were National Physical Laboratory and NMI Van Swinden Laboratorium. The company Brands GmbH had produced these thermometers. The aim of these phases of the project was to characterise the thermometers below 1000 °C and to evaluate the thermometers stability upon (prolongued) heat treatment up to 1500 °C.

Meanwhile the Forschungszentrum Jülich developed a new noise thermometer system to be used for the characterisation of the temperature dependence of the thermometer resistance between 1000 °C and 1500 °C. Use of a noise thermometer has the advantage that there is no need for a critical calibration furnace: the noise from the resistive element itself is used to assess its temperature. This temperature can then be compared with the resistance value of the thermometer.

Thermocouples

Temperature measurement above 1000 °C is realised mainly by the use of thermocouples. There are base metal thermocouples like W-Re (for use up to 2000 °C) or Chromel Alumel (up to 1300 °C) or noble metal thermocouples like Platinum-10%(or 13%)Rhodium versus platinum (up to 1580 °C) or platinum-6%rhodium versus platinum-30%rhodium (up to 1750 °C)¹. Development is under way on other platinum based thermocouples Pt-Au² and Pt-Pd³ for use up to 950 °C and 1300 °C respectively. Nicholas and White⁴ describe K-type thermocouples to change their thermal EMF to the equivalence of some 10 °C after heating for 1000 hours at 1000 °C in ideal circumstances. Long term (one year = 8500 hours) instabilities can exceed 10 °C at 1000 °C for even noble metal (platinum-rhodium) based thermocouples.

The disadvantage of thermocouples lies in their inability to be calibrated once irreversible ageing has taken place due to inhomogeneous ageing. These ageing effects will make the calibration characteristic sensitive to variations in immersion depth during calibration and use. Especially base-metal thermocouples show irreversible ageing effects that make them less suitable for re-calibration.

Resistance thermometers

For a long time, research has been conducted to find a resistance thermometer that can replace thermocouples in critical production facilities. When these facilities operate under an ISO-9000 system, traceability to national standards and thus calibration is required. Resistance thermometers can be made and used such as to eliminate lead wire effects: four wire measurement and AC-measurement techniques allows for elimination of lead resistances and spurious EMF's. Contamination problems with thermocouples create immersion effects which cannot be removed or treated. Resistance thermometers are not sensitive to contamination in this way. If the resistance thermometer is contaminated this affects only the measurement through the sensor element. The resistance drift that is caused by this contamination can easily be corrected for through calibration of the thermometer.

Most research for high temperature resistance thermometers is based upon platinum as the sensing element. While platinum resistance thermometers are now commercially available for use up to 850 °C, investigations are under way⁵ to produce platinum resistance thermometers for use up to 1100 °C. The

disadvantage of platinum resistance thermometer lies in the sensitivity of the platinum resistive wire to stress. Such stress will result from the difference in thermal expansion of the platinum wire and its ceramic insulating support following thermal cycling. Also the platinum will become soft at high temperatures.

This study uses a conductive ceramic based upon Molybdenum and Silica as

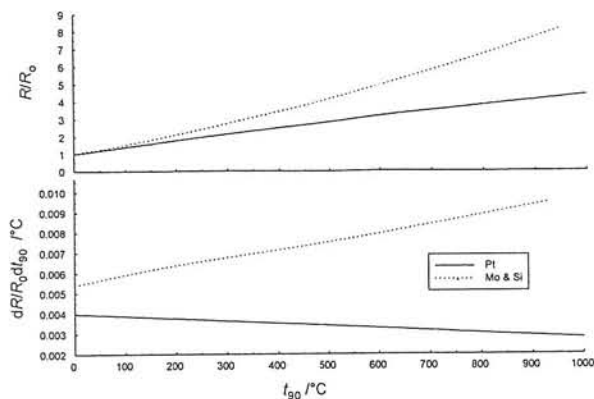


figure 1. thermometer resistance and temperature dependence of thermometer resistance as a function of temperature for Pt100 thermometers and the Mo/Si thermometers.

resistive element. This material has been in use as heater material up to 1800 °C for a long time, generally with relatively large diameters: between 3 mm and 18 mm. We applied material with diameters of the order of 1 mm. The advantage of this material also lies in the strong temperature dependence of its resistance when compared with platinum (figure 1). The resistance data of the MoSi based thermometers in figure 1 follows from calibration measurements by one of us (De Groot) in an early phase of this project. At higher temperatures the silica will form a protective layer around the sensing wire that protects the wire from oxidation and other atmospheric influences. It is anticipated that this effect will cause the thermometers to age with time during its initial use at high temperatures.

Noise thermometry

In 1928 Nyquist derived from general thermodynamic considerations the temperature dependence of noise in a resistor caused by thermally induced fluctuations of the conduction electrons:

$$\overline{V_{in}^2(t)} = 4kTR\Delta f$$

The intensity $\overline{V_{th}^2(t)}$ at any time t of this thermal noise only depends on the frequency interval Δf of the noise and not on the frequency itself. Thermal noise is proportional to the temperature T and the resistance R . A more accurate description would replace the resistance by the real part of the complex impedance $\text{Re}(Z(f))$. The constant k is that of Boltzmann. Because Johnson experimentally confirmed the same year as its theoretical description, thermal noise is also called Johnson noise.

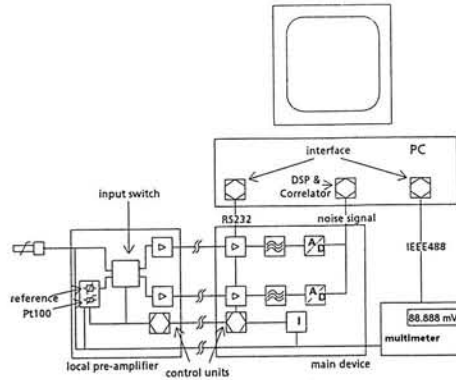


figure 2 block diagram of the noise thermometer system

The thermal noise to be measured is very small: $\sqrt{V_{th}^2(t)}$ is of the order of $1 \mu\text{V}$. Therefore, strong, low noise amplifiers are needed to measure it. To reduce lead wire noise, we use a system with two parallel amplifiers (see figure 2). Each amplifier consists of two stages: the first stage is located very close to the sensor. The main amplifier located in the control system, is controlled by the computer, and passes its output signal on to a band pass filter (frequency range 20 kHz to 200 kHz). The filtered noise signal is then digitised in two ADC's and processed in the computer. This allows the amplifier noise and lead wire noise to be eliminated in real time by cross correlation. Simultaneously the Digital Signal Processor performs Fast Fourier Analysis on both signals in the frequency domain. Comparison of the noise levels from temperature sensor and reference resistor gives the relative noise levels. From periodic measurement of the resistances and the temperature of the reference resistor, the unknown temperature can be evaluated. Thus, this thermometer is insensitive to ageing effect of the sensor element.

Measurements and discussion

The thermometers of the first and second series were first tested for their stability upon heat treatment. The following schedule was used:

1. The resistance was monitored during a prolonged near 1000°C using a thermocouple as a reference;
2. Thermometers were cycled progressively from

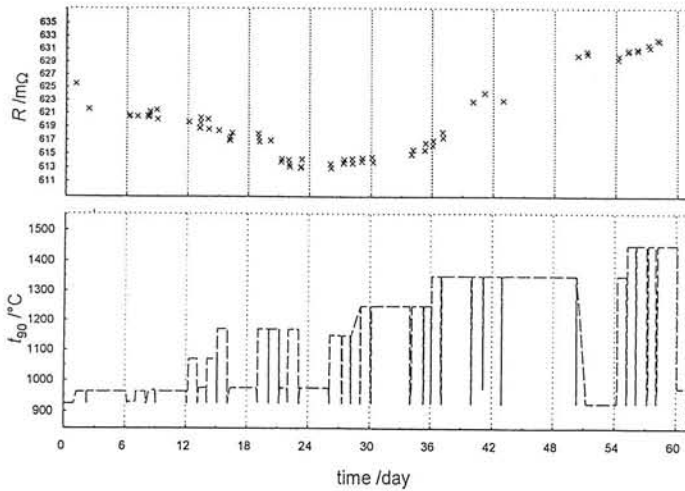


figure 3. The anneal procedure for thermometer with ID number 4-03: In the lower graph the thermal treatment is shown, while the upper graph shows the resistance measured at 950 °C in between the high temperature anneals. A thermocouple served as reference thermometer.

1000 °C to 1400 °C and as high as 1500 °C repeating every step. The thermometer resistance is measured near 1000 °C with reference to the thermocouple in between every high temperature excursion.

An example of such a stability test of the thermometers during this heat treatment can be found in figure 3. The measurement uncertainty for this series of measurements is within 0,1 °C. The temperature derivative of the resistance is 0,8 mΩ·°C⁻¹. The vertical scale of figure 3 is therefore 30 °C. A relaxation process can be seen to recur every time the thermometer is exposed to higher temperatures. For temperatures lower than 1200 °C ageing causes the resistance to decrease: initially this change is large, equivalent to some 10 °C this change reduces to within 1 °C. At temperatures higher than 1200 °C the resistance

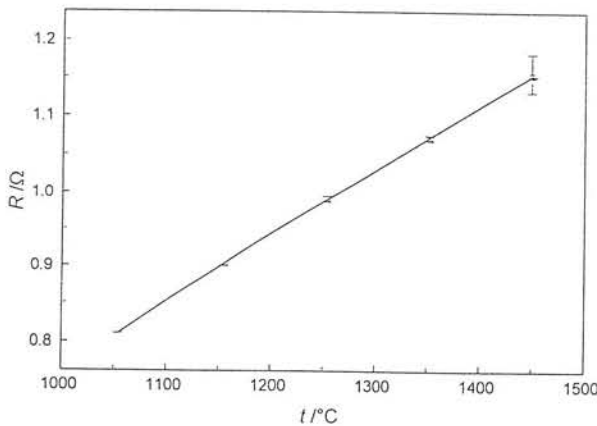


figure 4. Measurements of the resistance made with the thermometer noise as a reference for temperature measurement.

increases again initially to the order of and shows a trend to decrease with time. Further measurements are needed to study this effect on a longer time scale.

Similar effects can be seen to occur from the noise temperature measurements where two calibration cycles were performed, starting at 1450 °C decreasing down to 1050 °C. The measurement uncertainties were within 0,1% at two standard deviations: that is between 1,3 °C at 1050 °C and 1,7 °C at 1450 °C. The first measurement at 1450 °C shows that the thermometer changes resistance significantly (as indicated by the large "error"-bar). Later measurements show a more stable thermometer. This confirms results of the earlier stabilisation measurements: Once annealed at high temperatures, the thermometers remain stable at lower temperatures. Moreover, the strong resistance increase with temperature is continued up to high temperatures: the resistance is almost proportional to temperature. This shows that the thermometer remains a very sensitive thermometer up to high temperatures. Also, the thermometer has the possibility of replacing thermocouples as industrial thermometers in view of its reproducibility.

References

1. G.W. Burns et al, *Temperature-Electromotive Force Reference Functions and Tables for the Letter-Designated Thermocouple Types Based on the ITS-90*. NIST monograph 195, 1993.
2. M. Gotoh et.al. *A gold/platinum thermocouple reference table*, Rev. Sci. Instrum. 62, 2778-2791 (1991).
- G.W. Burns et.al., *Gold versus platinum thermocouples: performance data and an ITS-90 based reference function*. Temperature its Measurement and Control in Science and Industry volume IV pp 531..536, AIOP ,1992
3. F. Edler et. al. *A provisional reference function for platinum versus palladium thermocouples in the range 0 °C to 1084 °C*. CCT document: CCT/93-5, Bureau International des Poids et Mesures, (1993)
- L. Crovini et. al. *On the behaviour of platinum Palladium thermocouple from 600 °C to 1300 °C*, CCT document: CCT/93-17, Bureau International des Poids et Mesures, (1993)
4. Nicholas & White D.R , "Traceable Temperatures", John Wiley & Sons 1994.
5. M Arai, H. Sakurai, *Development of industrial platinum resistance sensors for use up to the gold point*, Temperature its Measurement and Control in Science and Industry volume IV pp 439.442, AIOP ,1992

Superconductive tunnel junctions for X-ray spectroscopy

M.L. van den Berg, M.P. Bruijn, J. Gomez, F. Kiewiet,
H.L. van Lieshout, O.J. Luiten, N. Snijders, and P.A.J. de Korte
*Space Research Organization Netherlands,
Sorbonnelaan 2, 3584 CA Utrecht, The Netherlands*

A.W. Hamster, C.G.S. Brons, and J. Flokstra
*University of Twente, Faculty of Applied Physics,
P.O. Box 217, 7500 AE Enschede, The Netherlands*

Abstract

We report on the development of a detector for X-ray astronomy based on superconductive tunnel junctions. Besides a very high energy resolution, these devices offer the possibility of almost 100% detection efficiency and intrinsic imaging properties. We discuss the detection principle and production techniques, and we present recent measurements with prototype devices.

I. INTRODUCTION

At present spectroscopic X-ray astrophysics is performed with dispersive instruments. Notwithstanding their good spectral resolution these instruments suffer from a low detection efficiency ($\simeq 10\%$), limited bandwidth, and the fact that they are unsuitable for spectroscopy of extended sources.

Currently, there is a strong interest in cryogenic detectors for future instruments, which is due to their potential to combine: (1) high detection efficiency over a wide range of photon energies, i.e. about 0.5 - 20 keV, (2) good spectral resolution, i.e. 10 eV FWHM energy resolution at a typical photon energy of 6 keV, (3) imaging properties. Two types of detectors have the prospect to deliver such a combination of characteristics, i.e. bolometers and detectors based on Superconductor-Insulator-Superconductor (SIS) tunnel junctions.

Other potential applications are in the field of materials analysis by means of X-ray fluorescence, high resolution Rutherford backscattering, and plasma diagnostics of fusion reactors. All these applications have in common that they require a proof of concept before to be considered seriously.

We are developing a superconductor detector, based on a 1 cm^2 single crystal niobium absorber. The absorber should be at least $30\ \mu\text{m}$ thick to obtain the required $> 90\%$ efficiency, and will be read out by a few SIS tunnel junctions on top, typically $100 \times 100 \times 0.5\ \mu\text{m}^3$ in size.

II. DETECTION PRINCIPLE

When a superconductor is cooled below the critical temperature T_c , the electrons condense into a ground state of so-called Cooper pairs, which is due to a weak phonon-mediated attractive interaction between the electrons. The elementary excitations are the so-called quasiparticles, electron and hole-like particles, which require for excitation a minimum energy Δ , the superconducting energy gap ($\Delta_{Nb} = 1.5$ meV). Absorption of an X-ray photon in a superconductor causes the generation of a photo-electron and/or Auger electrons. Through a cascade of electron-electron and electron-phonon interactions they relax to a population of quasiparticles and phonons. The part of the photon energy deposited in these excess (non-thermal) quasiparticles can be used for subsequent readout. In Nb a photon with energy E_x creates $N_{ex} = E_x/1.7\Delta$ excess quasiparticles [1].

The (sub-Poissonian) RMS statistical variation on this number of quasiparticles equals $\Delta N_{ex} = \sqrt{FN_{ex}}$ with F the so-called Fano-factor. Monte-Carlo simulations indicate $F \simeq 0.2$ for Nb [1]. The resulting limit on the achievable energy resolution thus becomes:

$$\Delta E_{FWHM} = 2.355(F\epsilon E_x)^{1/2},$$

with $\epsilon = 1.7\Delta$. For Nb $\Delta E_{FWHM} = 4.4$ eV at $E_x = 6$ keV. This relation has its analogy in similar relations for proportional counters and semiconductor detectors. The huge difference is the fact that the mean energy ϵ required for the creation of one free charge carrier typically amounts to 2.5 meV, compared to 3.6 eV for silicon. It is this small value for ϵ that allows for high resolution X-ray spectroscopy with these types of detectors.

After absorption of an X-ray photon in a superconducting slab, typically a few million excess quasiparticles are created, which diffuse outwards from the absorption site. By collecting all excess quasiparticles and measuring their total charge, the *energy* of the absorbed photon can be deduced. If the quasiparticles are collected during the diffusion process at several distinct positions on the absorber substrate simultaneously, the *position* of the X-ray impact can be inferred as well, thus enabling both spectroscopy *and* imaging.

To realize such a versatile detection scheme it is necessary to deposit efficient quasiparticle traps on top of the absorber substrate (see Fig. 1). The quasiparticle trapping mechanism is based on the fact that the quasiparticles dwell at an energy $\geq \Delta$ above the Fermi level E_f . A reduction of Δ is therefore experienced as a potential well, in which the quasiparticles may be trapped. This is illustrated in Fig. 1, where a tantalum trap ($\Delta_{Ta} = 0.7$ meV) is put on the niobium ($\Delta_{Nb} = 1.5$ meV) absorber substrate. In the case of a Nb absorber a second trapping stage of aluminium ($\Delta_{Al} = 0.18$ meV) is necessary. In addition, a niobium nitride protection layer ($\Delta_{NbN} \approx 2.5$ meV) on the outer surfaces of the Nb absorber keeps the quasiparticles confined to the absorber.

For our detector it is necessary that the time it takes for the quasiparticles to diffuse across a distance of ~ 1 cm is shorter than the quasiparticle lifetime. The latter is probably limited by surface catalyzed relaxation to the Cooper pair ground state, and is at least of the order of tens of microseconds. The diffusion is mainly determined by impurity scattering, so in order to obtain a diffusion time < 10 μ s, the absorber should be a single crystal of extremely high purity (residual resistance ratio $RRR \approx 10^4$).

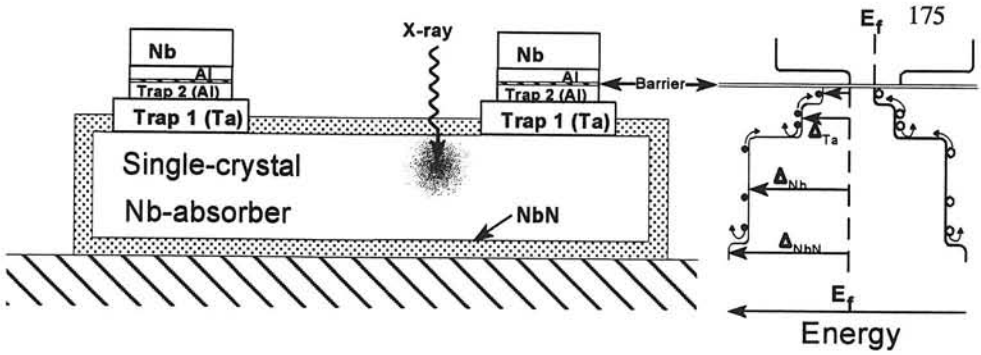


FIG. 1. Schematic representation of the detector concept and quasiparticle potential as a function of position.

After trapping, the number of collected quasiparticles is measured with SIS tunnel junctions, which are deposited on top of the quasiparticle traps (see Fig. 1). The junction operation is based on quantum mechanical tunneling of quasiparticles through the insulating barrier. If at sufficiently low temperatures ($T \ll T_c$) a bias voltage $V_{\text{bias}} < 2\Delta/e$ is applied across the junction, the tunneling of thermal quasiparticles is suppressed. Integration of the excess tunnel current then yields the number of trapped quasiparticles.

Our research efforts in the past few years were mainly focussed on the last detection stage, i.e. the fabrication of and the X-ray measurements on niobium based SIS junctions on silicon wafer substrates. Recently, we have started manufacturing the niobium absorber.

III. FABRICATION OF THE ABSORBER/JUNCTION DETECTOR

Fabrication of the complete detector is a complex technological challenge. First of all an absorber must be prepared with a very high bulk and surface quality. The surface roughness must be low enough to allow preparation of tunnel junctions with a barrier of only 1-2 nm thickness. Next, the absorber must be mounted on a substrate, structured and the edges passivated. The mounting must withstand all the lithographic processing and cryogenic operation. Finally a set of high quality tunnel junctions must be deposited, electrically well connected to the absorber. From this process we have investigated the following parts so far:

High purity single crystals of Nb were obtained from another research program [2] and from a commercial supplier. Slices of 200 μm thickness were cut from these crystals by spark erosion. With mechanical polishing [3] in principle a RMS-surface roughness (determined using AFM) of about 1 nm was obtained. However, a sufficiently good electrical contact to these surfaces has not yet been demonstrated. Much effort has been put in the development of a combined mechanical and electropolishing process. Another process, using reactive ion etching, is presently under study. With electropolishing very smooth surfaces with sub-nm roughness were obtained. A contact to such a Nb-surface was made ($2 \times 3 \mu\text{m}^2$ area) with a critical superconducting current density $> 300 \text{ kA/cm}^2$.

Development of tunnel junctions on Si-wafer substrates has been going on for a number of years already and has been reported before elsewhere [4]. We will very soon apply this junction process to one of the polished crystals.

IV. X-RAY MEASUREMENTS

In Fig. 2 a typical X-ray spectrum is shown, recorded with a $140 \times 140 \times 0.5 \mu\text{m}^3$ Nb junction with an Al-oxide barrier. The junction is sputter-deposited on an oxidized silicon substrate. The measurements have been performed at a temperature of 1.1 K, using a ^{55}Fe radioactive source emitting 88% Mn- K_α (5.89 keV) and 12% Mn- K_β (6.49 keV) radiation.

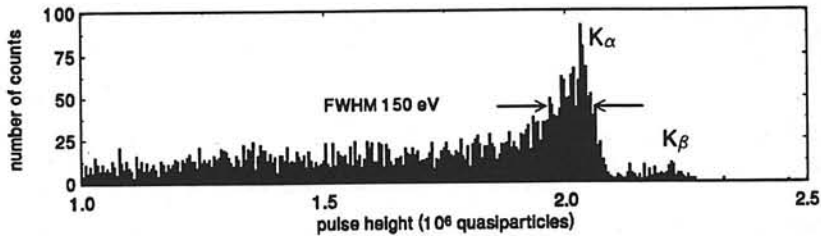


FIG. 2. X-ray spectrum recorded with a single Nb/AlO_x SIS junction on a silicon wafer.

The doublet structure due to the Mn- K_α and Mn- K_β peaks is clearly visible. The FWHM of the Mn- K_α peak amounts to approximately 150 eV. A particularly striking feature is the asymmetric shape. A risetime analysis [5] reveals that the asymmetric broadening to the left is due to faster charge collection events, which yield less charge. These are attributed to X-ray events in regions with a shorter quasiparticle lifetime, e.g. near the edges. By filtering out the fast events, the FWHM resolution can be reduced to below 100 eV.

The best resolution so far, 29 eV at 5.89 keV photon energy, has been obtained by Mears et al. [6]. By reducing the barrier thickness and passivating the edges, we believe we can improve our energy resolution to well below 100 eV. Whether a resolution of 10 eV at 6 keV can be achieved is still an open question.

ACKNOWLEDGEMENTS

This work is financially supported by the "Nederlandse Organisatie voor Wetenschappelijk Onderzoek (NWO)".

REFERENCES

- [1] M. Kurakado, Nucl. Instrum. and Meth. **196**, 275 (1982); N. Rando et al., Nucl. Instrum. and Meth. **A313**, 173 (1992).
- [2] Max-Planck-Institut für Metallforschung, Institut für Physik, Stuttgart.
- [3] Surface Preparation Laboratory, AMOLF, Amsterdam.
- [4] For a collection of papers, see: Proc. 6th Int. Workshop on Low Temperature Detectors, to be published in Nucl. Instr. and Meth. in Phys. Res. A (1995).
- [5] O.J. Luiten et al., *ibid.*
- [6] C.A. Mears et al., *ibid.*

Micromechanics@MIC.DTU.DK**Siebe Bouwstra****Mikroelektronik Centret
Technical University of Denmark
bldg. 345 east
DK-2800 Lyngby
Denmark****Abstract**

Mikroelektronik Centret is described briefly: status, mission and funding, organization, facilities, education and collaboration with Danish industry and the research areas. Next, the paper focuses on the Micromechanics research programme. A rough outline is given of the strategy of the programme, followed by an example of innovative processing, two examples of device oriented projects, as well as two examples of technology platform projects. Finally, a future outlook is presented.

Mikroelektronik Centret

Mikroelektronik Centret (MIC) is a brand new Danish national research institute on semiconductor materials and devices. MIC was founded in 1990 as an autonomous institute directly under the Ministry of Education. The charter for MIC defines a 3-fold mission: scientific research at an internationally competitive level, education of engineers and PhDs within the framework of the Technical University of Denmark (DTU), and technology transfer to Danish industry. MIC has a temporary status, which started with a 5 year period. In the first year a board was formed, in the second year the director was recruited, in the third year staff was recruited, in the fourth year processing facilities were built up. In the fifth year, MIC was extensively evaluated and was granted a new temporary status of another 4 years. MIC received a start-up grant of 130 Mkr from the Ministry of Education, supplemented with another 50 Mkr from the Ministry of Industry. The latter was associated with a collaboration project called Materials Centre for Microelectronics (MCM) of MIC with 5 major Danish companies: Danfoss, Grundfos, Brüel & Kjær, NKT and Topsisil. The total of 180 Mkr was roughly evenly divided between construction work (of offices and laboratories, in particular a clean room for silicon wafer processing), investment in new equipment (again in particular for processing, but also for analysis and design), and recurrent expenses (salaries, consumables). For the extended period of 4 years, MIC requested and was awarded a grant of 25 Mkr per year. On top of that, externally financed projects bring in more than 10 Mkr per year. All in all MIC has built up facilities worth more than 30 MDM, and now operates with an annual budget of approx. 10 MDM.

Organization

The organization of MIC is shown in Figure 1. The management of MIC consists of a director, a vice-director and a director of operations. Above this sits a board with 5 members from industry (including the board's chairman), 2 representatives from DTU, and 2 representatives from MIC's staff. The management is advised on the scientific programme by an international Scientific Council. MIC has a small administrative staff of 4 employees (financial and personnel administration is run through the system of DTU) and a technical staff of 7 engineers and 6 process specialists, the latter with high qualifications and long experience in research. The scientific staff consists of 8 full and associate professors, leading a research programme of a total of more than 50 researchers: 10 industrial co-workers, 7 postdocs, 22 PhD students, and several master's students and visiting scientists.

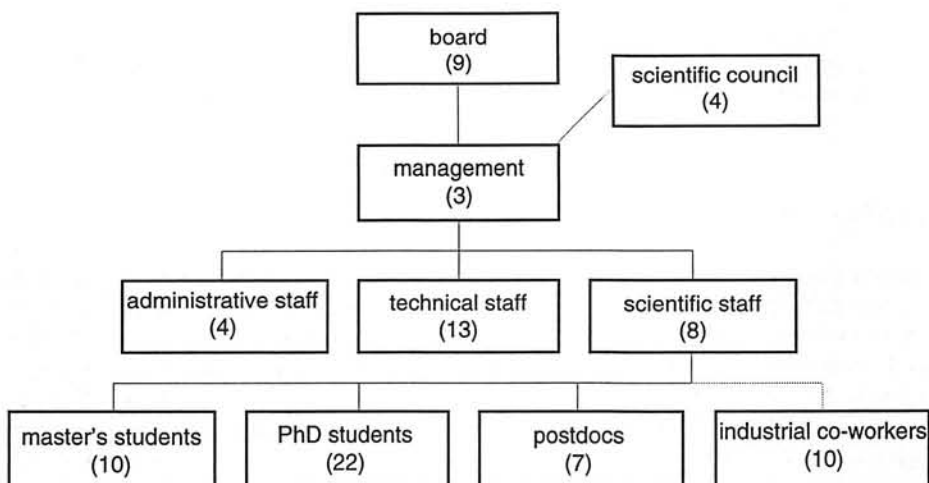


Figure 1: Organization plan of MIC

Laboratory facilities

The facilities are the responsibility of the director of operations and his technical staff. A class 10 clean room was constructed with a floor space of 600 m². Facilities were built up for processing 4" silicon wafers, with state-of-the-art equipment for basic competence, extended with specific equipment for innovative processing. The design of the clean room, the equipment and procedures lean heavily towards safety, as well as to large batch processing. Still, the conditions are optimum for development of specific process sequences with large flexibility. Researchers do their own processing. In the basement below the clean room (for Microtechnology) MIC has equipped a laboratory for Nanotechnology. Further MIC has several laboratories for device characterization, as well as for surface analysis, including Secondary Ion Mass Spectroscopy (SIMS).

Education

The education programme consists of lecture courses, including a Micromechanics lecture course, for students ranging from undergraduate students to PhD students, as well as small experimental projects for undergraduate students. All these are aimed at supporting the research programme. Master's projects last 12 months, while PhD projects last 3 years, both with the possibility of a stay abroad. The PhD projects have a wide range of funding possibilities, including government financed funds for frame programmes and for individual projects, university grants for individual candidates, as well as a government financed fund for subsidising industrial PhD education. Originally the latter stems from a programme of post-doctoral education of industrial researchers, which included research as well as an extensive programme of academic and industrial courses, while since recently the candidates also have the possibility to fulfill the requirements of the ordinary PhD examination. The latter includes the defence of the PhD thesis as well as an examination on general scientific knowledge. Examination in lecture courses and master's projects is carried out by an external evaluator, a so-called censor, usually from Danish industry. Examination in a PhD defence is the responsibility of 3 censors, at least two of whom come from another institute, usually from abroad. In industrial PhD examinations one of the censors is from industry.

Collaboration with Danish industry

One programme for private-public collaboration is the above-mentioned government-funded scheme for industrial PhD projects. These projects are bilateral: proposals are prepared jointly. The industrial partner initially covers the project costs; about half of these are refunded by the above scheme. The company recruits the candidate, who is stationed at the institute most of the time. In the case of MIC, these projects typically concern the development of a demonstrator for a transducer or for a packaging technology, and are often pilot projects for innovative product development or for larger technology development projects.

The latter are carried out in government-funded programmes, in which usually 2 or 3 ministries contribute towards the funding of the programme, and where the private-public partners both carry typically 50% of the financial burden themselves. The MCM collaboration is a relatively large project in one of these programmes, the so-called MUP programme, which started at the beginning of 1992. Five of MIC's process specialists work in this project full time. Each of the five industrial partners has one employee stationed at MIC full time for the duration of the project. Together with additional commitments of the companies this project amounts to a total of 100 man-years.

More recent are the so-called MUP2 programme, which started late in 1994, and the Centre Contract programme, which started at the end of 1995. In these programmes MIC has several large industrial collaborations of typically 10 to 30 man-years. Also in these projects, MIC contributes typically 30 to 40% of the manpower, while some of the industrial co-workers are stationed at the centre. These programmes and the practice of having industrial PhD students and industrial researchers stationed at the centre is expected to provide ideal conditions for effective collaboration. Most of the above private-public collaborations at MIC are within the area of Micromechanics.

Research areas

The research areas at MIC cover a broad spectrum ranging from fundamental research to applied research. MIC has an internationally renowned Theory group, dealing mainly with transport in mesoscopic devices. In MIC's Semiconductor Physics research programme gallium arsenide is studied by laser spectroscopy using a femtosecond laser semiconductor. The material is grown epitaxially using a Molecular Beam Epitaxy (MBE) facility MIC runs together with Copenhagen University. The Nanotechnology programme at MIC focuses on manipulation of surfaces with nanometer resolution ("nanolithography") using tunneling current tips. One technique is based on removing hydrogen atoms on hydrogen passivated silicon surfaces in ultra-high-vacuum, another one on electric field enhanced local oxidation of silicon in air. The patterns obtained are transferred into the underlying silicon by *e.g.* Reactive Ion Etching. The nature of the research is primarily fundamental, but also has a strong commitment to the development of a potential future technology. The MIC's Integrated Optics programme has focused so far on technology development for telecommunication, including passive and active waveguides, diffractive optics and fiber-pigtailing. Because of the demands of the application area the waveguide structures need to be thick, up to 36 microns. This is achieved by PECVD processes. To enable diffractive optics, germanium doped planar waveguides have been developed. The IC-technology programme at MIC focuses on two technologies for high-performance semiconductor devices: hetero-junction bipolar transistors (HBTs) and CMOS-on-insulator. HBT devices provide the possibility for silicon based electronics to compete with gallium arsenide on speed. The HBT programme includes growth of silicon germanium superlattices with sharp transitions. For this, MIC runs an MBE system together with Aarhus University, as well as a UHVCVD system. The MBE system is a flexible research system, which enables fast process sequence development and the study of different HBT devices. The UHVCVD system is being developed at MIC in order to create a batch process, which will be necessary for this technology to become interesting for industrial applications. The CMOS-on-insulator is being developed for robust semiconductor devices, with the transistors dielectrically isolated from each other. Also, the process sequence, using only 5 to 6 masks thanks to self-alignment steps, is very elegant and highly suitable for flexible hybrid or monolithic integration with micromechanical transducers. MIC's Microfluidics programme has so far dealt mainly with components for Microliquid Handling, such as check valves, active valves, diffuser/nozzle structures, filters and mixers. For future chemical analysis systems technologies are now under development for the monolithic integration of Integrated Optics and Microliquid Handling functions. One of the largest research areas at MIC is that of Micromechanics.

Micromechanics research programme

The strategy of the Micromechanics research programme is schematically shown in Figure 2. Basic competence is being built up within the MCM project: this concerns more or less conventional silicon processing, including improved zinc oxide deposition with *in situ* annealing and *in situ* passivation [1], e-beam evaporated borosilicate glass and subsequent thin film-anodic bonding, as well as low-stress sputter deposited silicon thin films with large thicknesses.

The technology platform at MIC for wafer processing is broadened by the development of innovative processing, which is carried out in close collaboration with other research programmes at MIC, e.g. laser micromachining of silicon with high resolution, high speed and large travel range [2,3], Reactive Ion Etching (RIE) of silicon, in particular deep etching with very good uniformity and shallow etching with controlled side-wall profiles, Plasma Enhanced Chemical Vapour Deposition (PECVD) of thick glass layers of several kinds with low stress, highly boron-doped epitaxial growth of silicon, and thick photoresist technology for electroplating molds. The boundary between basic competence and innovative processing is not sharp.

Development of application-specific transducers such as a piezoelectric tri-axial accelerometer and piezoresistive pressure sensors is done within the MCM collaboration [4,5], while Atomic Force Microscope (AFM) probes [6,7,8], microphones [9,10] and others [11,12], are being developed mainly in industrial PhD projects. Most of the applications are very demanding on signal-to-noise ratio, selectivity and long-term stability. These projects involve a great deal of structural design to optimize the performance, a careful development of a process sequence, as well as elaborate characterization. All this is supported by undergraduate students and master's projects [13,14,15].

The applicability of these devices in the real world is enhanced by larger collaboration projects with industry on advanced technology platforms, such as advanced packaging of aggressive media exposed sensors, funded in the MUP2 programme, and system integration for intelligent transducers and micro-electro-mechanical systems in the project called Micro System Centre (MSC), funded in the Center Contract programme.

Although not included in Figure 2, a similar strategy is followed at MIC for Micro-Opto-Mechanical Systems. Examples of optomechanical transducers are a uniaxial optomechanical accelerometer based on a Bragg grating strain gauge in planar waveguide technology, developed in an industrial PhD project together with Brüel & Kjær [16], and an optomechanical pressure transducer based on a Mach-Zehnder interferometer based on the elasto-optical effect in a planar waveguide integrated on a membrane [17]. This is supported by the development of basic competence and innovative processing for example for planar waveguide technology, UV-writing of Bragg gratings in germanium doped glass layers, and fiber-pigtailing, all within the Integrated Optics research programme.

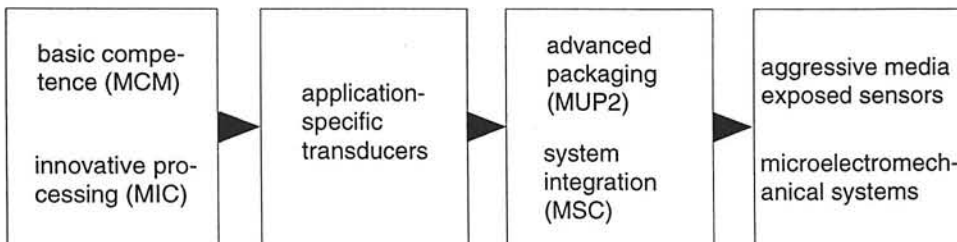


Figure 2: Micromechanics research programme

Laser micromachining of silicon

MIC has designed and built up equipment for laser micromachining of silicon, see Figure 3 (left) [2,3]. The process is based on focussing light of 0.5 W power to a very small spot, typically sub-micron in diameter, on the silicon surface. The high intensity leads to local melting of the silicon. This is done in a chlorine ambient under reduced pressure. A reaction occurs between the gas and the molten silicon, forming silicon chlorides, which are pumped off. This way a small volume of silicon, typically submicron in dimensions, is removed. By moving the sample using a computer controlled xy-stage, a whole sheet can be etched. By switching the beam on/off the shape of the removed sheet is determined. Next, the objective is translated to have the focus in the next plane, and the next sheet is removed. This 3D scanning concept yields a very high freedom of obtainable 3D structures. The stages we apply combine a repeatability of 25 nm with a travel range of 100 mm, and a speed of 100 mm/s. The size of the removed volume can be taken down to 50 nm by reducing the power. In practice the resolution in 3D micromachining is 300 nm.

We have applied this technique for the realization of diffuser/nozzle structures [12], see Figure 3 (centre), and compliant structures [11], see Figure 3 (right). Diffuser/nozzle structures have different (non-linear) flow resistances in the two directions. By loading them with an alternating differential pressure, a net flow will result. Therefore, they can be used in micropumps, replacing the particle sensitive check valves. The characteristics of these flow diodes depend on their length, width and taper angle, while sharp corners should be avoided. Using laser micromachining these parameters can be varied with a large freedom, and a taper in the depth direction can even be included. Moreover, design, realization, and characterization of new structures can be done within two days.

In a collaboration with the Institute of Solid-State Mechanics at DTU, we have developed a technology for the realization of compliant microstructures. These convert the magnitude and direction of a force or displacement, and can replace friction and wear sensitive microscale sliders and bearings. Figure 3 (right) shows an example of such a structure. The realization is based on Reactive Ion Etching of a low stress thick layer of silicon oxinitride, through a silicon thin film mask patterned by laser micromachining. Again, this provides the large freedom of shapes, albeit 2D, as well as the possibility of design, realization and characterization of new structures within a few days.

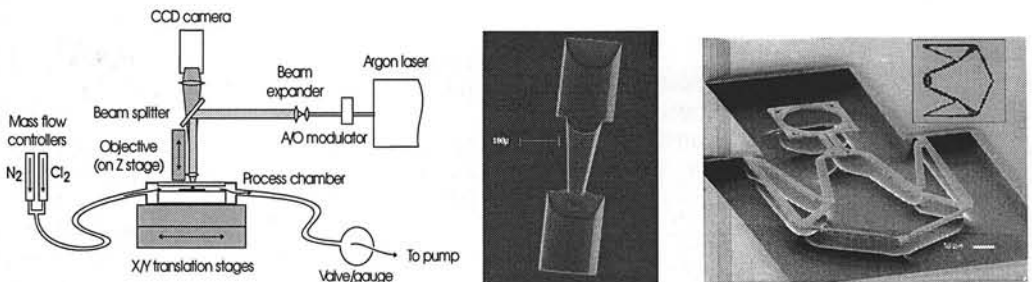


Figure 3: laser micromachining set-up (left), diffuser/nozzle structure (centre) and compliant microstructure (right)

AFM probe

In 1994 MIC started an industrial PhD project in collaboration with the company DME - Danish Micro Engineering. The primary goal is to develop a technology for versatile shapes of tips integrated with AFM cantilevers, so-called passive probes with external read-out, which can replace such probes in existing Scanning Probe Microscopes. The second goal is to develop an active probe, *i.e.* with integrated read-out, for a wide range of applications. The dimensions of the cantilevers are dictated by the required minimum value of the resonance frequency and maximum value of the stiffness, and are typically 1 micron thick, 50 micron wide and 180 micron long in the case of a silicon cantilever. For the tip technology we distinguish between direct [7] and indirect [8] technologies. In the direct technology a tip is etched from silicon. We have developed a sequence of Reactive Ion Etching process steps for the realization of so-called rocket-tips™, see Figure 4. First the mask (of silicon oxide) is undercut in an isotropic RIE process. In the second RIE step, the shadowed surfaces are coated with a polymer layer. In the third step a column is etched in an anisotropic RIE process. In the fourth RIE step the polymer is removed. Optionally, an isotropic RIE process is carried out for prolonged undercutting of the mask. All these steps are performed without breaking vacuum. Finally, the structure is oxidized and the oxide is etched, yielding tips with sharp radii of curvature of less than 20 nm, with good uniformity over the wafer. Heights of rocket-tips™ can be varied by varying the length of the anisotropic etch step, diameters can be varied by choosing between different sizes of the mask patterns. These tips combine robustness and slenderness, making them suitable for scanning on highly stepped surfaces. Tips have been integrated with silicon cantilevers of a variety of shapes, see Figure 4, using ion implantation of boron and RIE for the definition of the cantilevers, oxidation for additional protection, and KOH etching from the back side. Thicknesses of the cantilevers can be varied by adjusting process parameters of the ion implantation and subsequent annealing.

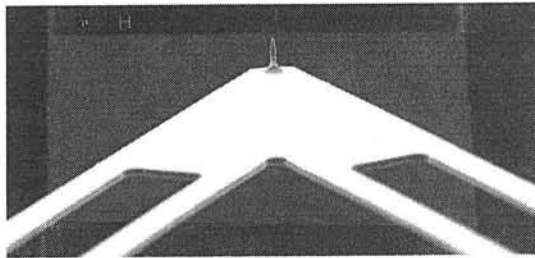


Figure 4: Rocket-tip™ on a passive AFM probe cantilever.

These probes have been demonstrated on a number of test samples. They are now routinely produced for DME's product range. Also, they are applied in MIC's Nanotechnology programme for surface manipulation. Currently, the active probe is being developed.

Microphone

Also in 1994 MIC started an industrial PhD project in collaboration with the company Microtronic, for the development of a silicon microphone for hearing aid applications. Earlier designs by other groups, making use of capacitive read-out, showed promising results, but none of them could fulfill the requirements for this demanding application: small size, low power consumption, low supply voltage, low noise level, large dynamic range, and robust against humidity, sweat and ear wax. Our feasibility study showed that a differential capacitive read-out with force balance, and with sealed parallel plate capacitors will be able to fulfill the above requirements [9]. Figure 5 shows a sketch of a microphone consisting of a so-called backplate sandwiched between two membranes, forming two parallel plate capacitors. The two membranes seal off the capacitors, preventing ambient media from entering. A sound inlet and a backchamber provide acoustic isolation between the front and back of the sensing element. The differential load due to an acoustic pressure leads to deflection of the two membranes and to a difference between the two capacitances. However, a common load due to a fluctuation of ambient pressure or temperature, which can be 3 orders of magnitude larger than the acoustic loads, will inflate or deflate the sandwich structure, and thereby change the sensitivity of the sensor. This inflation is prevented or reduced by mechanical connections between the two membranes, the pillars in Figure 5, in the area with the electrodes. Ambient fluctuations are now buffered in the compliant periphery.

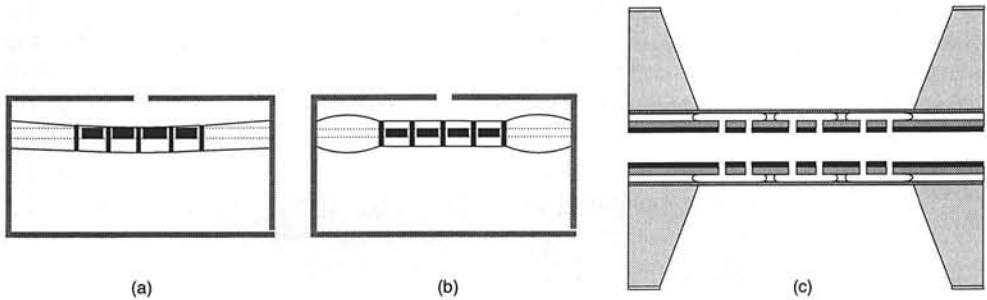


Figure 5: double membrane microphone a) acoustic load b) ambient fluctuation c) suggested realization in silicon technology, prior to bonding.

Moreover, the design makes use of force balance, which provides several advantages [10]. The bandwidth can be extended, while dynamic instabilities can be suppressed by adding zeros to the feedback loop. The response becomes nearly independent of the stiffnesses of the membrane and the backchamber, further reducing the influence of batch-to-batch variations and ambient fluctuations. These stiffnesses now only determine the equivalent noise pressure level.

CMOS based electronic interfaces are designed in a collaboration with the Electronics Institute at DTU. A low-voltage, low-power, low noise level preamplifier has been designed and tested [18]. Currently, a feedback loop in CMOS technology is being designed.

Advanced packaging of aggressive media exposed sensors

Many applications of micromechanical sensors involve exposure to aggressive media. For example alkaline solutions at elevated temperatures may be mild media for stainless steel and glass, but for silicon they pose a problem, considering that these kinds of media are used as etchants for silicon! Also, passivation by a thin film of silicon oxide or nitride may not suffice for exposure times longer than 10 years [19]. Not only the sensing element and the chip material need to be protected, but also the electrical connections to the outside world. Today, protection is achieved by a labour intensive hybrid encapsulation involving the assembly of a corrugated stainless steel or rubber membrane and a sealed-off reservoir with silicone oil for passivation and pressure transmission [20]. In collaboration with the companies Grundfos and Danfoss MIC is developing a technology platform for integrated protection, see Figure 6 (left). Deposition of passivation layers, for example silicon carbide, is carried out at wafer scale, whenever feasible. The chip is to be mounted onto a variety of substrates, either by a conventional die bonding approach (active side facing the surroundings) or by a flip-chip approach (active side facing the substrate). Area bonding has to provide a perfect seal, but may have to allow lateral feedthroughs. Contacting of membranes from the back side may be required. For this MIC has developed a technique using electrodepositable photoresist, see Figure 7 (left) [21]. This technique has also been demonstrated for multiple vertical feedthroughs with high wiring density in throughholes, see Figure 7 (right) [22]. A similar technology platform is being developed for encapsulation of lithium niobate based Surface Acoustic Wave devices, in an industrial PhD project together with Ferroperm Components [23].

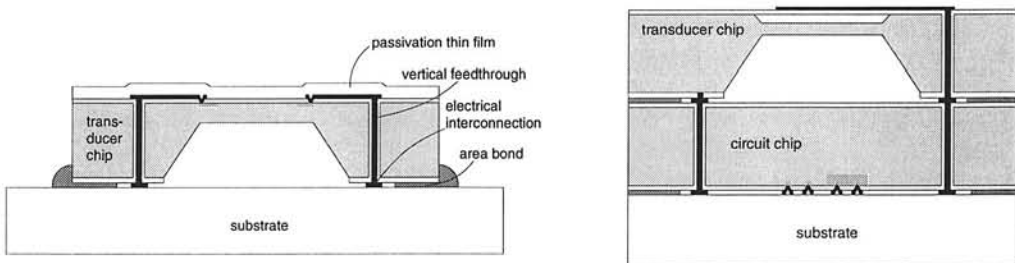


Figure 6: advanced packaging of aggressive media exposed sensors (left), and system integration of micro-electro-mechanical systems (right)

System integration of integrated circuits and micromechanical transducers

Within the project Microsystem Centre (MSC) together with the companies Microtronic and DELTA Danish Electronics, Light & Acoustics, MIC is developing a technology platform for hybrid integration of integrated circuits and micromechanical transducers. The idea is to physically bond a transducer chip and a circuit chip, while at the same time establish electrical connections between the two, see Figure 6 (right). Different techniques are being investigated, including the application of eutectic bonds, solder bumps, and isotropic and

anisotropic conductive adhesives. Furthermore, we have the ambition to develop these technologies on a wafer scale, thereby postponing dicing and handling of individual chips. This approach provides a hybrid technology for intelligent transducers. Next, this intelligent transducer will have to be mounted on a variety of substrates, again including electrical interconnections. The assembly may have the transducer facing the environment and the circuit facing the hosting system, while depending on the circumstances other orientations may be preferred. In either case, vertical feedthroughs will again be required. This hybrid approach is expected to be superior for space-constrained microsystems comprising high performance transducers with possibly also high performance circuits, with a minimum of compromises.

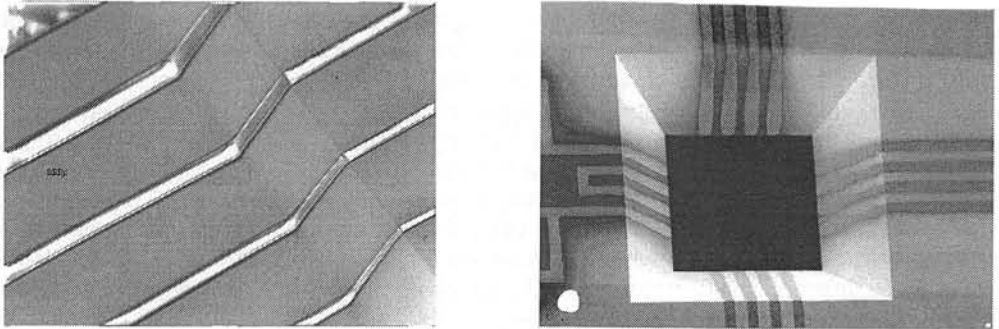


Figure 7: photoresist patterns after development, deposited by electrophoresis in a KOH-etched hole in silicon (left), and concept of vertical feedthroughs with very high wiring density realized by metal thin film deposition, photolithography and subsequent etching (right)

Future outlook

In the start-up phase of the Micromechanics programme, much effort has been devoted to basic competence, innovative processing, and high performance sensors. Since recently, technology platforms are being developed for implementation into larger systems. In the future, additional functions may be included in these systems, *e.g.* remote control. Also, Integrated Optics will be exploited further, either with electrical communication, requiring the integration of laser diodes and photodiodes, or with fiber optic communication links.

The close collaboration between MIC and Danish industry that is possible in the national industrial landscape, is expected to be effective. The first commercial success in a low volume application, passive AFM probes, is encouraging. The combination of a Micromechanics and a Nanotechnology research activity within a small institute like MIC will also yield a new challenging areas of application for both technologies. The Micromechanics research programme is now ready to take part in European collaboration projects.

References

1. E. Mikkelsen, R. de Reus and S. Bouwstra
"Improved quality zinc oxide thin films by *in situ* annealing"
Accepted for publication in J. Micromechanics and Microeng., 1996.
Procs. Micromechanics Europe 95 (MME 95), Copenhagen, Denmark,
September 1995, pp. 80-81.
2. M. Müllenborn, H. Dirac, J. W. Petersen and S. Bouwstra,
"Fast 3D laser micromachining of silicon for micromechanical and microfluidic
applications"
Accepted for publication in Sensors and Actuators A.
Procs. Transducers 95, Stockholm, Sweden, June 1995, vol. 1, pp. 166-169.
3. M. Müllenborn, M. Heschel, H. Dirac and S. Bouwstra
"Laser direct etching of silicon on oxide for fast prototyping"
Accepted for publication in J. Micromechanics and Microeng., 1996.
Procs. at MME 95, Copenhagen, Denmark, September 1995, pp. 64-67.
4. P. R. Scheeper, J. O. Gulløv and L. M. Kofoed
"A piezoelectric triaxial accelerometer"
Accepted for publication in J. Micromechanics and Microeng., 1996.
Procs. MME 95, Copenhagen, Denmark, September 1995, pp. 230-231.
5. O. Søndergaard-Jensen and P. Gravesen
"A new piezoresistive pressure transducer principle with improvements in
media compatibility"
Accepted for publication in J. Micromechanics and Microeng., 1996.
Procs. MME 95, Copenhagen, Denmark, September 1995, pp. 152-155.
6. J. Bay, S. Bouwstra, E. Lægsgaard and O. Hansen,
"Micromachined AFM transducer with differential capacitive read-out",
J. Micromechanics and Microengineering, 5 (1995) 161-165.
Procs. MME 94, Pisa, Italy, September 1994, pp. 145-150.
7. A. Boisen, O. Hansen and S. Bouwstra
"AFM probes with direct fabricated tips"
Accepted for publication in J. Micromechanics and Microeng., 1996.
Procs. MME 95, Copenhagen, Denmark, September 1995, pp. 76-79.
8. A. Boisen, J. P. Rasmussen, O. Hansen and S. Bouwstra
"Indirect tip fabrication for scanning probe microscopy"
accepted for publication in Micro- and Nanoengineering, 1995.
Procs. MNE 95, Aix-en-Provence, France, September 1995.
9. J. Bay, O. Hansen and S. Bouwstra,
"Design of a silicon microphone with differential capacitive read-out of a
sealed double parallel plate capacitor"
Accepted for publication in Sensors and Actuators A, August 1995.
Procs. Transducers 95, Stockholm, Sweden, June 1995, vol. 2, pp. 700-703.
10. J. Bay, O. Hansen and S. Bouwstra
"Modelling of microphones with differential capacitive read-out and force
balancing"
Accepted for publication in J. Micromechanics and Microeng., 1996.
Procs. MME 95, Copenhagen, Denmark, September 1995, pp. 221-224.

11. U. D. Larsen, O. Sigmund and S. Bouwstra
"Design and fabrication of compliant micromechanisms and materials with negative Poisson's ratio's",
submitted for publication in J. Micro-Electro-Mechanical-Systems, Dec. 1995.
Procs. MEMS-'96, San Diego, CA, February 1996.
12. M. Heschel, M. Müllenborn and S. Bouwstra
"Truly 3-dimensional diffuser/nozzle structures in silicon"
submitted for publication in J. Micro-Electro-Mechanical-Systems, Jan. 1996.
13. J. Bastue and S. Bouwstra
"Closed form formulas on linear membrane behaviour"
Procs. MME 95, Copenhagen, Denmark, September 1995, pp. 234-238.
14. M. Heschel and S. Bouwstra
"Robust, compliant silicon nitride membranes"
Procs. MME 95, Copenhagen, Denmark, September 1995, pp. 84-87.
15. J. Jonsmann and S. Bouwstra
"On the resonance frequencies of membranes"
Procs. MME 95, Copenhagen, Denmark, September 1995, pp. 225-229.
16. T. Storgaard-Larsen, S. Bouwstra and O. Leistiko,
"Opto-mechanical accelerometer based on strain sensing by a Bragg grating in a planar waveguide"
Accepted for publication in Sensors and Actuators A.
Procs. Transducers 95, Stockholm, Sweden, June 1995, vol. 2, pp. 667-670.
17. K. Hoppe, L. U. A. Andersen and S. Bouwstra,
"Integrated Mach-Zehnder interferometer pressure transducer"
Procs. Transducers 95, Stockholm, Sweden, June 1995, vol. 2, pp. 590-591.
18. C. E. Fürst
"A very-low-noise, low-power preamplifier for capacitive microphones"
Proceedings Norchip, November 1995, Copenhagen, DK, pp. 230-237.
19. G. F. Eriksen and K. Dyrbye
"Protective coatings in harsh environments"
Accepted for publication in J. Micromechanics and Microeng., 1996.
Procs. MME 95, Copenhagen, Denmark, September 1995, pp. 72-75.
20. K. Dyrbye, T. Romedahl-Brown and G. F. Eriksen
"Packaging of physical sensors for aggressive media applications"
Accepted for publication in J. Micromechanics and Microeng., 1996.
Procs. MME 95, Copenhagen, DK, September 1995, pp. 315-323.
21. P. Kersten, S. Bouwstra and J. W. Petersen,
"Photolithography on micromachined 3D surfaces using electrodeposited photoresists"
Sensors and Actuators A 51 (1995) 51-56.
Procs. EMRS 95, Strassbourg, France, May, 1995.
22. C. Christensen, P. Kersten, S. Bouwstra and J. Wulff Petersen,
"Wafer through-hole interconnections for high vertical wiring densities"
Procs. EuPac, Essen, Germany, January 1996.
23. F. K. Christensen and M. Müllenborn
"Sub-band-gap laser micromachining of lithium niobate"
Appl. Phys. Lett. 66 (21), 1995, 2772-2773.

Thick polysilicon microstructures by combination of epitaxial and poly growth in a single deposition step

P.T.J. Gennissen, M. Bartek, P.J. French, P.M. Sarro+

Lab. for Electronic Instrumentation, Dept. of Electrical Eng., +DIMES
Delft University of Technology, The Netherlands
Tel +31-15-2783342, Fax +31-15-2785755

Abstract

Thick polysilicon microstructures were fabricated by combination of epi and poly growth in a single deposition step in an epitaxial reactor. The fabrication process allows the combination of bipolar electronics and polysilicon mechanical structures on the same chip with reasonable process complexity. The process is fully planar up to the last sacrificial etch. Initial mechanical strain problems were found to be caused by oxidation of the polysilicon during bipolar processing. These problems were limited by the use of a process similar to LOCOS processes.

Introduction

Polysilicon has found extensive applications in surface micromachining. The thickness of this poly layer is limited by the low growth rate if standard LPCVD is used. This problem has been solved by use of an epitaxial reactor to form the polysilicon [1,2,3]. The most promising approach is the process where not only polysilicon is grown on the substrate [1,3], but where polysilicon and crystalline growth are combined in a single deposition step [2]. In the polysilicon layer microstructures are built and in the monocrystalline silicon layer electronics are fabricated [2]. After poly growth the layer is practically strain free, but bipolar processing steps after poly growth lead to compressive mechanical strain. Despite this undesirable property microstructures can be made by careful design [2]. In contrast this work proposes techniques to minimise the cause of this mechanical strain problem.

Fabrication process

The process starts with (100) oriented p-type wafers in which Sb is implanted on areas where transistors are projected and on areas where vertical capacitive read-out of mechanical struc-

tures is planned. The oxide layer resulting from the Sb drive-in step is covered by a thin layer of polysilicon. In the next step the poly and oxide are removed on areas where no mechanical structures will be fabricated (Fig. 1a), followed by epitaxial growth. During epi growth monocrystalline silicon is grown bare substrate and poly is grown on areas which contain the poly seeds. The process is continued according to a standard bipolar flow sheet (Fig. 1b). These steps are also used to make the electrical contacts to the micromechanical structures. After metallization a layer of LPCVD nitride is deposited followed by a $1\mu\text{m}$ thick plasma oxide as a masking layer for silicon trench etching. Trenches are etched through the epi-poly layer to the buried oxide (Fig. 1c). The structures are released during a sacrificial etch step in hydrofluoric acid or an alternative etchant followed by removal of the protection nitride (Fig. 1d).

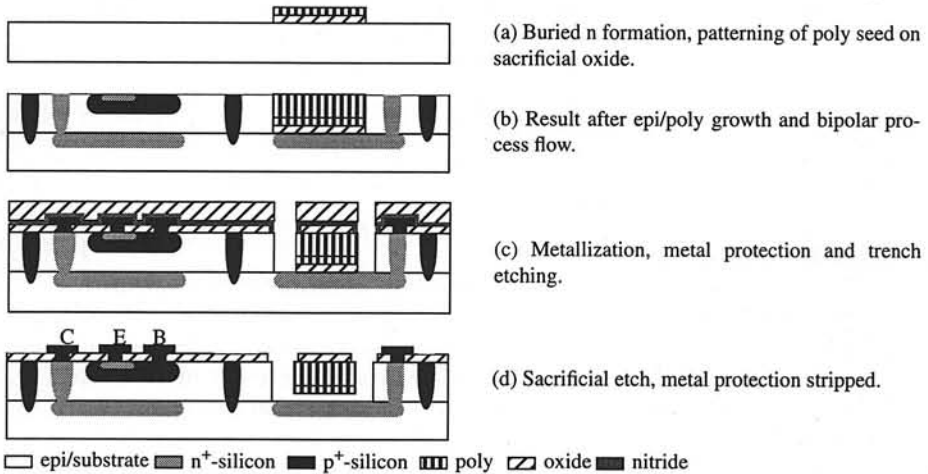


Fig.1 Fabrication scheme for micromechanical structures using epi-poly.

Experiments

Experiments were performed to study the strain level of the epi-poly layer as a function of growth conditions, doping level and annealing. Areas of 1 cm^2 with and without poly seeds on sacrificial oxide were distributed on the wafer in a chessboard pattern. Then epi was grown, doped and annealed using various growth, doping and annealing conditions. Finally the trench etch mask was applied and the structures were released by a 15 min. sacrificial etch in 20% HF. Compressive strain levels were estimated using an array of double clamped beams of different length. The shortest buckling beam is a measure for the strain.

In all experiments epi was grown using an ASM Epsilon One epitaxial reactor and a HCl/DCS gas system. A 5 min. in situ prebake in hydrogen at 950°C was performed. After this prebake epi growth was performed at a pressure of 60 Torr. Four experimental runs were performed:

1. In the first experiment the HCl to DCS flow ratio was varied between 0 and 4 at a constant growth temperature of 950°C and constant DCS flow of 100slm. This was done to study the possibility of selective growth of epi and poly in future processes. On 6 wafers $4\mu\text{m}$ epi-poly was grown in pairs at a HCl/DCS ratio of 0, 2, and 4. Half of the wafers was oxidised at 1100°C for 10 min. It is expected that the properties of the poly will not significantly change after they have been subjected to this highest temperature in the bipolar process flow.
2. In the second experiment wafers were grown at 1050°C at a DCS flow of 360slm without HCl addition which is the standard epi recipe for the bipolar process. The polysilicon layer

was doped using the standard deep boron insulation diffusion or the deep phosphorus collector contact diffusion of the bipolar process.

3. In the third run two wafers were grown at standard bipolar epi conditions, followed by an annealing step of 10 minutes, one in oxygen and one in argon ambient.
4. In this experiment a $4\mu\text{m}$ poly layer was grown at 1050 and 1150°C. The upper left quarter of the wafer was implanted with boron and the upper right with phosphorus, both at an energy of 100keV and dose of $5 \times 10^{15}\text{cm}^{-2}$. Then 300nm LPCVD nitride was deposited on the wafer followed by all bipolar oxidation and diffusion steps. The lower left quarter doping was defined by POCl_3 diffusion. In this case the nitride was stripped prior to the deep n collector contact diffusion. The remaining quarter received only the in-situ doping of the epi growth.

Results

In the first experiment the compressive strain levels were all in the same range of $20\mu\epsilon$ for the unannealed wafers and $200\mu\epsilon$ for the oxidised wafers. No strain dependence on HCl/DCS ratio was observed. The relative growth rate of the poly to monocrystalline silicon decreased with increasing HCl/DCS ratio, resulting in a different step height at the epi/epi-poly interface. The results are shown in Fig. 2. The difference in growth reaches its minimum when no HCl is added during growth. At these conditions the growth rate of the poly is about 70% of the growth rate of the monocrystalline silicon.

The surface of the wafer was scanned using an alpha step profilometer. It was found that the surface of the poly areas was convex and the surface of the epi was concave. This phenomenon is believed to be caused by non-uniformity of the temperature at the wafer surface during growth. Since the wafers are heated by halogen lamps the temperature in the middle of the poly-on-oxide areas will be higher than the temperature in the middle of the bare silicon areas due to the insulating properties of the oxide. To check this explanation epi-poly was grown on a wafer without oxide underneath the poly seed layer. The resulting surface was flat, confirming this hypothesis.

The second set of experiments showed no significant difference for the strain levels of the wafers which were doped and annealed according to the bipolar process flow sheet. Strain levels were compressive and in the $700\mu\epsilon$ range. No dependence on doping level or type was observed. From this experiment it was concluded that the annealing process has a higher influence on the strain level than dopant type and concentration.

In the third experiment the strain of the wafer which was annealed in oxygen ambient was much higher ($300\mu\epsilon$) than the strain of the wafer which was annealed in argon ($80\mu\epsilon$). This indicates that the strain is caused by oxidation of the poly and not by the temperature treatment. It is assumed that oxygen penetration into the polysilicon and formation of silicon oxide causes the compressive strain.

This assumption was confirmed by the results of the fourth experiment. Implanted areas which were covered with nitride during further bipolar processing showed no difference in strain level compared to wafers without thermal treatment. Strain levels were in the $20\mu\epsilon$ range. The dif

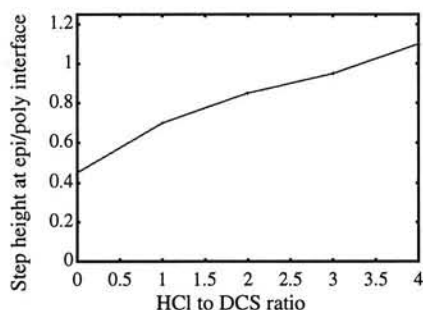


Fig.2: Step height at the epi/epi-poly interface for an epi thickness of $5\mu\text{m}$, a poly seed thickness of $0.5\mu\text{m}$ and an oxide thickness of $0.7\mu\text{m}$.

fused area, however, showed a high strain level of about $750\mu\epsilon$.

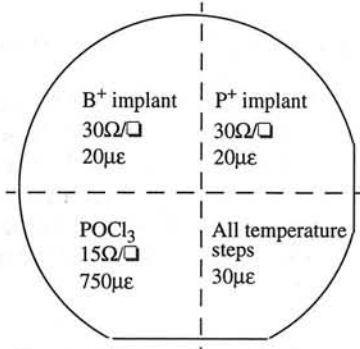


Fig.3: Summary process and results of the experiments in the fourth run.

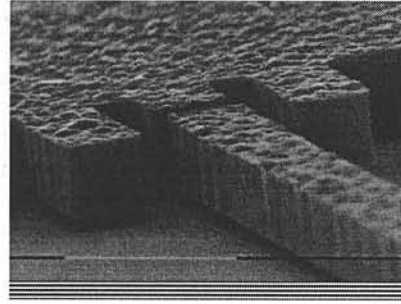


Fig.4: SEM photograph of a free etched $4\mu\text{m}$ thick epipoly structure.

The resistivity of the doped poly was measured and found to be $30\Omega/\square$ for the poly which was doped by implantation and $15\Omega/\square$ for the poly doped by diffusion.

The results are summarized in Fig. 3. A photograph of a fabricated structure is shown in Fig. 4.

Conclusions

Polysilicon has been deposited in an epitaxial reactor. Compressive strain levels in the epipoly have been estimated using arrays of double clamped beams. It was found that the strain in the epipoly increases dramatically when the epipoly is subjected to oxidation. Oxygen penetration in the epipoly layer forming silicon oxide at the grain boundaries is the likely cause. High temperature steps without oxidation showed no visible influence on the strain levels in the polysilicon. If the epipoly has to survive bipolar processing it needs to be protected for oxygen penetration by the use of a nitride layer. This solution, which is similar to LOCOS processes leads to polysilicon layers with acceptable resistance and strain levels for the fabrication of microstructures. When the poly is implanted before it is covered with nitride the whole thermal budget of the bipolar process is used to drive in and activate the dopants. This should minimize strain gradient problems. Another advantage of the LOCOS process is that the thickness of the polysilicon does not change during bipolar processing, while the thickness of the monocrystalline silicon decreases due to the oxidation steps. This compensates the difference in growth rate of the epi and epipoly.

Acknowledgments

The authors wish to thank the staff and processing crew of DIMES for assistance in fabricating the devices, especially Alex vd Bogaard and Cassan Visser. This work is supported, in part, by FOM/STW, project DEL 44.3758.

Literature

- [1] P. Lange, M. Kirsten, W. Riethmüller, B. Wenk, G. Zwicker, J.R. Morante, F. Ericson, J.A. Schweitz, Proceedings Transducers '95, Stockholm Sweden, pp. 202-205
- [2] M. Offenber, F. Lärmer, B. Elsner, H. Münzel, W. Riethmüller, Proceedings Transducers '95, Stockholm Sweden, pp. 589-592.
- [3] M. Kirsten, B. Wenk, F. Ericson, J.A. Schweitz, W. Riethmüller, P. Lange, Thin Solid Films, 259, 181 (1995).

Problems of sacrificial etching in a combined surface micromachining and electronic process.

J.F.L. Goosen, B.P. van Drieënhuizen, P.J. French and R.F. Wolffenbuttel

Lab. for Electronic Instrumentation, Delft University of Technology, Mekelweg 4, Delft.
Phone: 015-2785026, Fax: 015-2785755, e-mail: goosen@ei.et.tudelft.nl

Abstract

In a surface micromachining process that is design to be compatible with microelectronic processing, problems arise during the etching of the sacrificial layer. To prevent the aluminium present during the etching to be attacked by the etchant, two possible solutions are investigated.

The aluminium can be protected using a photoresist layer. When using photoresist, problems that arise are etching of the resist, peeling of the interconnect and underetching due to poor adhesion. Using baking of the resist, thin oxide layers and reflow of the resist this can be limited but not avoided.

Other etchants such as BHF with glycerol and glycerine additions and so called pad-etchants can be used. These etch the aluminium slowly and can be used for sacrificial etching with exposed aluminium.

Introduction

When combining surface micromachined elements with electronics on the same chip, many new possibilities for sensors arise. However, the combining of these two technologies also introduces many technological problems. One of the problems encountered is the protection of the aluminium interconnect during the sacrificial etch step which releases the mechanical structures.

Combined surface micromachining and electronic processing

The sacrificial material most often used in micromachining is silicon oxide or Phospho Silicate Glass (PSG). The most commonly used etchant for these materials is hydrofluoric acid (HF) or buffered hydrofluoric acid (BHF). These etchants have a high selectivity between the sacrificial oxide and the mechanical layers, which most often consist of polycrystalline silicon (poly silicon) and silicon nitride, and a high etch rate, which is necessary to perform the large under-etchings in a reasonable length of time.

It is difficult to do any patterning steps when the structures are freestanding due to the destructive effects of the spinning of resist to the delicate structures and the metal getting lodged underneath the freestanding structures during deposition. Therefore, the release of the structures most often takes place after all other processing has been performed, unless all cavities are sealed [1]. When the sacrificial etching takes place, the aluminium interconnect will usually be present on the wafer. However, the sacrificial etchants HF and BHF attack the aluminium very quickly and no interconnect will be left unless special measures are taken. Although it is possible in most cases to protect the aluminium using a PECVD nitride layer, this complicates processing to a large extent and this possibility is not considered in this paper.

Photoresist protection

One possible solution and the simplest and most obvious one, is the protection of the interconnect with photoresist, leaving access to the surface only around the mechanical structures, where no aluminium is present [2]. However, during etching problems will arise.

Photoresist etching

First of all, most modern photolithography lines are designed for electronic technologies such as CMOS, where patterning is done exclusively by plasma etching. The bake time used is insufficient to remove all the solvents present in the resist leaving the resist relatively soft. The etchant will etch the resist, limiting the maximum etch time to around 10 minutes. For the long wet etches needed for sacrificial etching, the resist needs a complete postbake of 110°C for 30 minutes to harden it, depending on the type of resist. For the same reason BHF is used instead of HF as the former etches the resist more slowly, giving a possible etch time of one and a half to two hours. If more time is needed, intermediate drying of the resist layer will lengthen this time even further.

Photoresist adhesion

The adhesion of the photoresist layer to the surface of the chip is another problem. The adhesion promoters used are designed to bind to the resist and to the dangling hydrogen bonds of a silicon oxide layer, which is most commonly used as a patterning layer in the fabrication of electronic devices. However, the layer on which the resist is deposited after the micromachining has taken place, consists of either nitride or silicon, which lack these hydrogen bonds. The resulting weak bond can cause the resist to separate from the surface, allowing etchant to seep underneath and attack the underlying aluminium (see figure 1). The attacked aluminium expands and pushes the resist upward, allowing new etchant to reach the aluminium. Figure 2 shows this clearly. The light grey area around the micromotor, is the part of the resist that has dislodged from the surface. The porous nature of the aluminium allows this to happen before the aluminium is fully etched by absorbing the etchant like a sponge, extending the area around the aluminium interconnect.

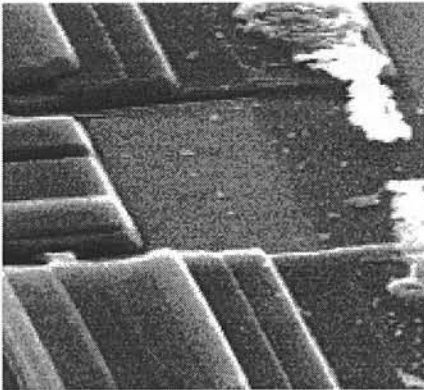


Figure 1. Attack of aluminium interconnect by sacrificial etchant

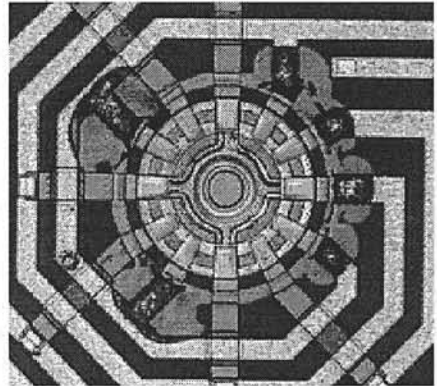


Figure 2. Etched aluminium causing delamination of resist (light grey area)

Furthermore, because the bond between resist and aluminium is as good as the bond between aluminium and nitride, the peeling of the resist can also cause the interconnect to be ripped off the wafer, resulting in broken wires (see figure 3). This effect can be observed after about 10 minutes and is therefore the most critical problem, as this time is insufficient to release most structures in a general surface micromachining process.

Different adhesion promoters have been tried to improve the adhesion. Although there are slight differences between different adhesion promoters, the etchant seeps under the resist within minutes and no adequate agent was found.

Tests have been performed using very thin oxide layers deposited using PECVD on the whole wafer to promote adhesion. No peeling of the resist has been observed when using this oxide. However, underetching of this layer can cause interconnect layers close enough to the etch cavities to be attacked, even when using layers as thin as 50nm. Underetching of this thin layer is as fast as, or even faster than the etching of the sacrificial layer due to the poor quality of the plasma oxide.

To reduce the underetching, the oxide layer was etched for a short time, removing the oxide from the etch window and allowing a slight underetching of the edges. The resist was then reheated at 150°C for 30 minutes to reflow the resist and to seal the access to the oxide (see figure 4). This increases the possible etch time, but is insufficient to protect the oxide and the aluminium indefinitely as the seal will start to leak as well. This will occur after around 5 minutes, but it reduces the underetching considerably due to the slow admission of fresh etchant in the cavity. Underetching rate of the resist mask is in the same order as the underetching of the structures.

Alternative etchants

The above mentioned photoresist layer is not sufficient to provide adequate protection for the interconnect, unless short etch times are sufficient. Another possible solution is the use of different etchants, which have a large selectivity between aluminium and the sacrificial oxide. Ways to increase the selectivity of BHF reported in literature is by the addition of glycerine or glycerol. Etch rates reported in literature of 0.55 nm/min. of aluminium and an etch rate of 95 nm/min. of thermal oxide for the glycerol [3] (40g NH₄F + 60ml H₂O + 20ml HF + 40ml



Figure 3. Peeling of the aluminium interconnect due to poor adhesion of the resist.

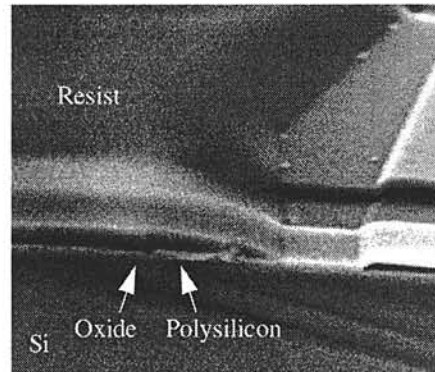


Figure 4. Reflow of resist to prevent underetching of the adhesion promoting oxide layer.

glycerol). The etch rate of glycerine is reported to be 6 nm/min. of aluminium and 200 nm/min. of thermal oxide [4] (4 parts-NH₄F (40%); 1 part-HF (48%); 2 parts glycerine (87%)).

Another possible sacrificial etchant investigated is the, so called, pad-etchants used to open contact holes in oxides on contact pads [5]. It consists of 1/3 acetic acid and 1/3 ammoniumfluoride and 1/3 water (Riedel-de Haen AEW 33-33-33). Etch rates of 5 nm/min. of aluminium and 200 nm/min. of PSG are found.

All etchant mentioned above etch the sacrificial material slower than BHF (500 nm/min. for PSG) and thus longer etch times are required. The etchants slowly attack the aluminium roughening the surface as shown in figure 5. If the two hours of possible etching are not enough to release the structures, it can be combined with the resist protection.

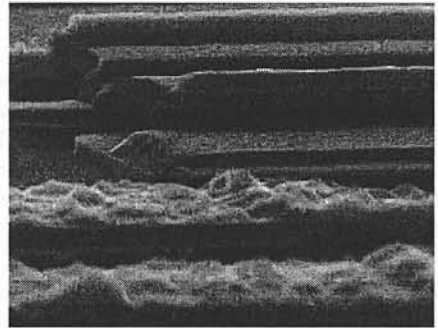


Figure 5. Roughening of the aluminium by the pad-etchant

Anchoring of the interconnect

The aluminium used for the interconnect contains 1% silicon to prevent junction spiking. When patterning the interconnect, a polysilicon dip etch is used to remove the silicon gains that remain after the etching of the aluminium. An oxide layer is necessary to protect the structural polysilicon layer from this dip etch. This oxide layer will be etched if the etchant seeps this far under the resist protection or if no photoresist protection is used. This can result in freestanding aluminium wires (see figure 6). As there is already a mask to etch openings in the oxide layer around contact holes, this can easily be used to anchor the interconnect layer to the substrate.

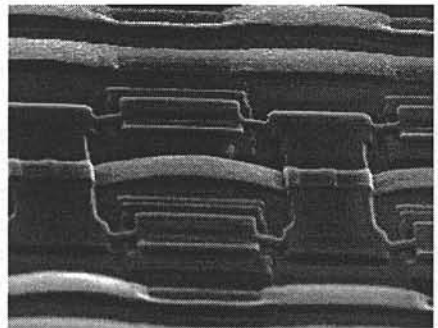


Figure 6. Freestanding interconnect due to underetching of oxide.

- [1] Dudaicevs, H., Y. Manoli, W. Mokwa, M. Schmidt, E. Spiegel, 'A fully integrated surface micromachined pressure sensor with low temperature dependence', *Transducers'95*, 25-29 June, Stockholm, Sweden.
- [2] Linder, C., N.J. de Rooij, 'Investigation on free-standing polysilicon beams in view of their application as transducers', *Sensors and Actuators A*, 21-23 (1990), pp. 1053-1059.
- [3] Tilmans, H.A.C., K. Beart, A. Verbist, R. Puers, 'CMOS foundry-based micromachining', *MME '95*, Denmark, pp. 183-187.
- [4] Jaecklin, V.P., C. Linder, N.F. de Rooij, J.-M. Moret, R. Vuilleumier, 'Line addressable torsional micromirrors for light modulator arrays', *Sensors and Actuators A*, 44 (1994),
- [5] Bühler, J., J. Funk, F.-P. Steiner, P.M. Sarro, H. Baltes, 'Double pass metallization for CMOS Aluminium actuators', *Transducers'95*, 25-29 June, Sweden, vol. 2, pp. 360-363.

Calibration of a Poly-Silicon Piezo-Resistor Array for Package Stress Measurements

A. Bossche and J.R. Mollinger
Electronic Instrumentation Laboratory
Faculty of Electrical Engineering/DIMES
Delft University of Technology
Mekelweg 4, 2628 CD Delft
The Netherlands

ABSTRACT

To measure the stresses exerted on a chip by different package types and package materials a prototype stress test chip has been developed in a standard CMOS process. The stress sensing is performed by four piezo-resistor arrays (one on each chip quarter) that were realized in different silicon layers (n-type active layer, p-type active layer, n-well layer and a polysilicon layer). The 252 resistors in each array have been placed in 6 different orientations. This paper describes a general calibration procedure for a poly-silicon piezo-resistor array for two cases; the case when the crystallites have sufficiently random orientations to assume isotropic behaviour of the poly sheet and the case in which the crystallites show a preference orientation which requires a anisotropic treatment of the poly silicon layer.

1 - INTRODUCTION

To measure the stresses exerted on a chip by different package types and package materials a prototype stress test chip (Figure 1) has been developed in a standard CMOS process [1]. The stress sensing is performed by four piezo-resistor arrays (one on each chip quarter) that were realized in different silicon layers (n-type active layer, p-type active layer, n-well layer and a polysilicon layer). The 252 resistors in each array have been placed in 6 different orientations.

The procedure for calibration of the poly-silicon piezo-resistors depends on the structure and the (planar) orientation of the poly-silicon sheet. In general it can be assumed that the crystallite sizes resulting from different poly-silicon technologies (0.4 .. 2 μ m) are sufficiently small compared to the resistor sizes (approx. 100 x 100 μ m) to neglect the influence of individual crystallite orientation. This means that the poly silicon layer can be assumed uniform for all resistors. However, the crystallites (and so the poly-Si sheet) may still show a preference orientation. Therefore, two different (macro) poly-silicon structures can be distinguished; one having a net orientation of the crystallites (non-isotropic structure), and one having no net orientation (isotropic structure). These cases require different approaches for interpreting the resistance changes for both calibration and stress-

measurements. The following sections describe the calibration procedures for both, isotropic and non-isotropic poly-silicon sheets.

2. CALIBRATION OF ANISOTROPIC POLY-SILICON PIEZORESISTORS

In general piezoresistivity can be described by a fourth-rank tensor equation as:

$$\frac{E_i}{\rho_0} = \delta_{ij} i_j + \pi_{ijkl} T_{kl} i_j + \alpha \delta_{ij} \Delta T i_j$$

For mono-crystalline silicon the crystal symmetry and the mechanical equilibrium conditions require that the electrical and the mechanical indices (in any orthogonal base) are symmetrical as well. This means that $\pi_{ijkl} = \pi_{jikl} = \pi_{ijlk} = \pi_{jilk}$. For this reason usually a simpler notation is used in literature on basis of only two indices running from 1 through 6 according the following scheme: [ij (kl): 11, 22, 33, 23, 13, 12] \rightarrow [a(b): 1..6]. This means that the tensor equation can be rewritten in the new indices as:

$$\frac{E_i}{\rho_0} = \delta_a i_j + \pi_{ab} T_b i_j + \alpha \delta_a \Delta T i_j$$

For monocrystalline silicon (or more general crystals having a diamond like lattice structure) it was proven [2] that piezoresistivity can be described in relation to the crystallographic axes by only three independent coefficient as:

$$[\pi_{ab}] = \begin{bmatrix} \pi_{11} & \pi_{12} & \pi_{12} & 0 & 0 & 0 \\ \pi_{12} & \pi_{11} & \pi_{12} & 0 & 0 & 0 \\ \pi_{12} & \pi_{12} & \pi_{11} & 0 & 0 & 0 \\ 0 & 0 & 0 & \pi_{44} & 0 & 0 \\ 0 & 0 & 0 & 0 & \pi_{44} & 0 \\ 0 & 0 & 0 & 0 & 0 & \pi_{44} \end{bmatrix}$$

For any other orthogonal orientation the π' coefficients can be described in linear combinations of π_{11} , π_{12} , and π_{44} . However, in poly silicon the crystallites show many different orientations even when they show a preference orientation. Although for each individual crystallite the same symmetry rules hold as for mono-crystalline silicon the macro piezoresistivity of the poly cannot be expressed in terms of the principle coefficients. This means that all 36 coefficients should be regarded as independent. However, for planar resistors in the xy-plane (wafer plane) the E_z and i_z contributions can be ignored

leaving only 18 coefficients. Since for each arbitrary oriented individual crystallites (and so for the resistor as a whole) holds that $\pi_{12}=\pi_{21}$, $\pi_{16}=2\pi_{61}$ and $\pi_{26}=2\pi_{62}$ a further reduction to 15 independent equations is possible. This means that the full calibration of an anisotropic poly-silicon layer requires (at least) 15 independent linear equations and so 15 resistors. The relative resistance change of each resistor at an arbitrary angle ψ (see Figure 2) then can be written as:

$$\begin{aligned} \Delta R/R &= \sigma_0 \Delta E/i = (\Delta E_x \cos\psi + \Delta E_y \sin\psi)/i \\ &= \cos\psi [(\pi_{11}\sigma_1 + \pi_{12}\sigma_2 + \pi_{13}\sigma_3 + \pi_{14}\sigma_4 + \pi_{15}\sigma_5 + \pi_{16}\sigma_6)\cos\psi \\ &\quad + (\frac{1}{2}\pi_{16}\sigma_1 + \frac{1}{2}\pi_{26}\sigma_2 + \pi_{63}\sigma_3 + \pi_{64}\sigma_4 + \pi_{65}\sigma_5 + \pi_{66}\sigma_6)\sin\psi] \\ &+ \sin\psi [(\pi_{12}\sigma_1 + \pi_{22}\sigma_2 + \pi_{23}\sigma_3 + \pi_{24}\sigma_4 + \pi_{25}\sigma_5 + \pi_{26}\sigma_6)\sin\psi \\ &\quad + (\frac{1}{2}\pi_{16}\sigma_1 + \frac{1}{2}\pi_{26}\sigma_2 + \pi_{63}\sigma_3 + \pi_{64}\sigma_4 + \pi_{65}\sigma_5 + \pi_{66}\sigma_6)\cos\psi] \end{aligned}$$

or in matrix form: $\Delta R/R = [\sigma\text{vector} \times \text{Trans}\pi\text{poly}] \times [\pi\text{vector}]$ with $\sigma\text{vector} = [\sigma_1 \ \sigma_2 \ \sigma_3 \ \sigma_4 \ \sigma_5 \ \sigma_6]$, $\pi\text{vector} = [\pi_{11} \ \pi_{12} \ \pi_{13} \ \pi_{14} \ \pi_{15} \ \pi_{16} \ \pi_{22} \ \pi_{23} \ \pi_{24} \ \pi_{25} \ \pi_{26} \ \pi_{63} \ \pi_{64} \ \pi_{65} \ \pi_{66}]^T$ and with Trans π poly:

$$\begin{vmatrix} \cos^2\psi & \sin^2\psi & 0 & 0 & 0 & \cos\psi\sin\psi & 0 & 0 & 0 & 0 & 0 & 0 & 0 & 0 & 0 & 0 \\ 0 & \cos^2\psi & 0 & 0 & 0 & 0 & \sin^2\psi & 0 & 0 & 0 & \cos\psi\sin\psi & 0 & 0 & 0 & 0 & 0 \\ 0 & 0 & \cos^2\psi & 0 & 0 & 0 & 0 & \sin^2\psi & 0 & 0 & 0 & 2\cos\psi\sin\psi & 0 & 0 & 0 & 0 \\ 0 & 0 & 0 & \cos^2\psi & 0 & 0 & 0 & 0 & \sin^2\psi & 0 & 0 & 0 & 2\cos\psi\sin\psi & 0 & 0 & 0 \\ 0 & 0 & 0 & 0 & \cos^2\psi & 0 & 0 & 0 & 0 & \sin^2\psi & 0 & 0 & 0 & 2\cos\psi\sin\psi & 0 & 0 \\ 0 & 0 & 0 & 0 & 0 & \cos^2\psi & 0 & 0 & 0 & 0 & \sin^2\psi & 0 & 0 & 0 & 0 & 2\cos\psi\sin\psi \end{vmatrix}$$

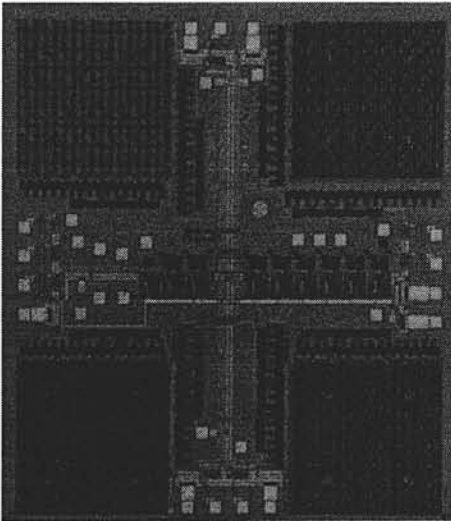


Figure 1: Stress test chip

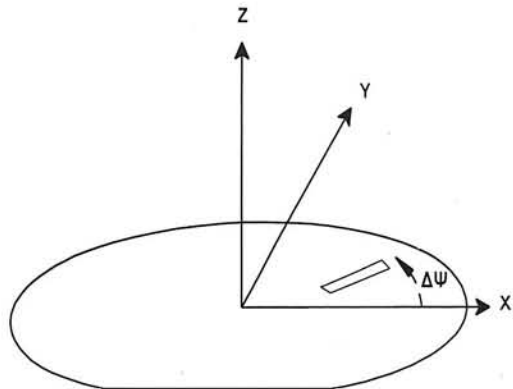


Figure 2: Wafer and arbitrary resistor orientation.

3. CALIBRATION OF ISOTROPIC POLY-SILICON PIEZORESISTORS

For planar resistors in a isotropic poly layer with all coefficients and stresses given with respect to the longitudinal (l), transverse (t) and perpendicular (p) directions of the resistor, the piezoresistance relation can be written as:

$$\Delta R/R = \sigma_0 \Delta E/i = \pi_l \sigma_l + \pi_t \sigma_t + \pi_p \sigma_p + \pi_{lp} \sigma_{lp} + \pi_{lp} \sigma_{lp} + \pi_{lt} \sigma_{lt}$$

independent of the direction (ψ) of the resistor. In order to express the relation with respect to the x, y and z axes of the wafer the stresses $\sigma_1 \dots \sigma_6$ should be expressed in terms of $\sigma_1 \dots \sigma_6$ so that the piezoresistance equation becomes: $\Delta R/R = [\sigma \text{vector} \times \text{Trans}\pi \text{isotrop}] \times [\pi \text{vector}]$ with $\sigma \text{vector} = [\sigma_1 \ \sigma_2 \ \sigma_3 \ \sigma_4 \ \sigma_5 \ \sigma_6]$ and $\pi \text{vector} = [\pi_{11} \ \pi_{12} \ \pi_{13} \ \pi_{14} \ \pi_{15} \ \pi_{16}]^T$ and with $\text{Trans}\pi \text{isotrop}$:

$$\begin{vmatrix} \cos^2\psi & \sin^2\psi & 0 & 0 & 0 & -\cos\psi\sin\psi \\ \sin^2\psi & \cos^2\psi & 0 & 0 & 0 & \cos\psi\sin\psi \\ 0 & 0 & 1 & 0 & 0 & 0 \\ 0 & 0 & 0 & \cos\psi & \sin\psi & 0 \\ 0 & 0 & 0 & -\sin\psi & \cos\psi & 0 \\ 2\cos\psi\sin\psi & -2\cos\psi\sin\psi & 0 & 0 & 0 & \cos^2\psi - \sin^2\psi \end{vmatrix}$$

4 CONCLUSIONS

It has been shown that the piezo-resistive behaviour of polysilicon layers can be described by either 15 (anisotropic poly) or 6 (isotropic poly) independent coefficients. This means that in the calibration procedures at least 15 (respectively 6) independent resistor measurements are required. For stress measurements only 6 resistors are required to resolve the 6 stress components. In that case the relations are best rewritten as: $\Delta R/R = [\pi \text{vector}^T \times \text{Trans}\pi \text{xxxx}^T] \times [\sigma \text{vector}^T]$. This notation yields a set of linear equations ready to be solved.

5. ACKNOWLEDGEMENT

This project is funded by the Dutch Foundation of Applied Research (STW).

6. REFERENCES

[1] Gestel, H.C.J.M. van, Reliability related research on plastic IC-packages: a test chip approach, PhD Dissertation Delft University of Technology, The Netherlands, 1994, ISBN 90-6275-960-2.

[2] Nye, J.F., Physical Properties of Crystals, Clarendon Press, 1985

Advances in Biosensors

David C. Cullen* and Anthony P.F. Turner

Cranfield Biotechnology Centre
Cranfield University
Cranfield, Bedfordshire, U.K.

Tel. +44 (0)1234 754339
Fax. +44 (0)1234 750907
e-mail d.cullen@cranfield.ac.uk

This contribution highlights recent advances in biosensor technology. Examples are drawn from the areas of electrochemical, optical and piezoelectric biosensors and immunosensors together with examples of biomimicry, surface characterisation, manufacturing techniques and the role of molecular biology and molecular engineering in biosensor design.

Introduction

Biosensors combine the selectivity and sensitivity of biology with the processing power of modern microelectronics to offer powerful new analytical tools with major applications in medicine, environmental diagnostics and the food and process industries. Many extensive reviews of the area have been previously published (Turner *et al.*, 1989; Newman & Turner, 1992; Freitag, 1993) and the reader is referred to these for a comprehensive historical perspective. The present article will focus on recent developments in the field of biosensors that offer possible solution of key problems in the design, production and application of biosensors.

Electrochemical

Electrochemical transduction of bio-recognition events have been the dominant approach to biosensor design. In general, redox enzymes are utilised to detect low molecular weight analytes in the micromolar, and greater, concentration range. The detection of electroactive products such as hydrogen peroxide has proved a very practical approach for enzyme electrodes based on oxidoreductases. The detection of glucose using glucose oxidase has received the majority of attention (Turner and Yevdokimov, 1994) and the possibility of rational design of transduction at a molecular level has been boosted by the recent elucidation of the 3D structure of this enzyme (Hecht *et al.*, 1993). The relatively high potential required to oxidise hydrogen peroxide at conventional electrodes, however, leads to problems of

interference due to other electroactive species present in the sample. The most successful commercial solution to this has involved the use of mediators such as ferrocene and its derivatives. Recent attention, however, has focused on the alternative strategy of reducing the potential at which hydrogen peroxide oxidation occurs. Examples include the use of platinised carbon (Cardosi and Birch, 1993) and ruthenised carbon (Cagnini *et al.*, 1995).

The elegance of direct electron transfer between redox enzymes and an electrode has long been sort and is still actively investigated. If sustained and sizeable currents could be achieved this would offer the simplest way to interface catalytic proteins to electronic circuits opening the way for a range of biosensors and other bioelectronic devices. Such an intimate connection would also presumably indicate ways to avoid unwanted redox reactions at the electrode and thus eliminate the prime source of interference in amperometric biosensors. The direct electrochemistry of electron transfer proteins such as cytochrome *c* has been extensively studied in recent years. Few reports have appeared describing electron transfer between electrodes and the larger redox enzymes. Where observed, electrochemistry has been typically poor due to the existence of a thick insulating protein shell around the active centre of the enzyme.

Optical

The direct measurement of refractive index changes associated with biological affinity reactions such as antibody-antigen binding has enabled rapid real-time analysis of binding events without the traditional requirement for labelled reagents. Pharmacia already have a successful instrument on the market based on surface plasmon resonance (Szabo *et al.*, 1995) and other commercial devices based on related principles have followed such as Fison's IAsys resonant mirror. These systems have developed a new niche market in bioscience R&D laboratories but one very different from the originally expected clinical analysis market.

Various optical formats continue to be investigated. Examples include Mach-Zehnder interferometers on planar waveguides (Schipper *et al.*, 1995), integrated optical grating couplers (Clerc & Lukosz, 1993) and surface plasmon resonance at IR wavelengths (Brink *et al.*, 1995). Combinations of techniques have been demonstrated such as a surface plasmon sensor on an optical waveguide with electrochemical control (Lavers *et al.*, 1995).

Although developments in transducers continues, the fundamental problems of direct immunosensors and affinity sensors are not being addresses to the same extent. Specificity, sensitivity and time-response are still major limitations to the commercial success of direct sensors.

Piezoelectric

The successful application of piezoelectric materials in biosensors has been limited due to the lack of supporting theory when devices are immersed in liquids and generally poor sensitivity in their main application as affinity sensors. Various formats of devices such as bulk acoustic wave and surface acoustic wave resonators and more recently Lamb wave and horizontal polarized shear wave resonators are being investigated (Benes *et al.*, 1995).

Molecular Engineering

The modern tools of protein engineering together with an increasing knowledge of protein behaviour at the molecular level is enabling a new "molecular" approach to biosensor design. This entails the modification of naturally occurring molecules to better suit their role in biosensors. Thus antibody fragments (F_v) have been investigated for increased specific surface activity due to their reduced size and hence greater packing density and to reduce non-specific binding through the elimination of redundant components (Spitznagel and Clark, 1993). The ability to insert unique attachment points by site directed mutagenesis has enabled fluorescent reporter groups to be optimally placed adjacent to binding sites suggesting an alternative route to "direct" affinity sensors (Gilardi *et al.*, 1994).

A novel example of protein engineering involved the formation of a pore-forming protein switch sensitive to metal ions. Staphylococcal alpha-hemolysin, a pore-forming exotoxin, assembles to form hexameric pores in lipid bilayers. A glycine-rich peptide loop is involved in activity and when five consecutive amino acids were replaced by histidine residues they provided a switch with which pore activity could be turned off by micromolar concentrations of divalent zinc ions and turned back on with the chelating agent EDTA. This result suggests that genetically-engineered pore-forming proteins could be useful components of future metal ion sensors (Walker *et al.*, 1994).

Elegant illustrations of the use molecular biology in biosensor engineering to form "gene switch" biosensors include the insertion of the gene for firefly luciferase into the TOL plasmid responsible for the degradation of benzene and its derivatives (Ikariyama *et al.*, 1993). This resulted in a luminescent *E. coli*, *i.e.* a whole organism-based optical biosensor, which could be used to monitor environmental pollution caused by benzene and its derivatives. In a similar manner, the firefly luciferase gene has been inserted as a reporter under the control of the mercury-inducible mer promoter from transposon Tn21 in *E. coli* and in a resultant luminescence-based sensor was able to detectable concentrations of mercury in the femtomolar range (Virta *et al.*, 1995).

The use of artificial ligands, artificial enzymes or other analogues of biological behaviour offers a powerful conceptual approach to the design of stable "bio" sensors. Affinity systems can be constructed that incorporate reporter functions; a fluorescent sensor molecule for the chiral discrimination of monosaccharides has been demonstrated (James *et al.*, 1995). Another aspect of biomimicry is represented by work on the "artificial nose" using chemical sensor arrays in conjunction with artificial neural networks (Neaves and Hatfield, 1995). Combinatorial chemistry is beginning to offer new methods for the development of affinity ligands.

Manufacturing

Much of the development work on biosensors feature hand-built devices, which while demonstrating the operational principle, are not realistic for commercial production. Significant efforts are being applied to transform these proof-of-concept systems into devices suitable for mass-production (Alvarez-Icaza and Bilitewski, 1993). The development work carried out on devices such as the MediSense ExacTech glucose biosensor has clearly demonstrated the importance of automated manufacturing techniques. The ExacTech is

constructed using a technique adapted from the electronics industry; namely screen-printing, which is widely used for the fabrication of printed circuit boards. Considerable effort is currently directed to the development of screen-printable inks optimised for biosensor (Cagnini *et al.*, 1995; Koopal *et al.*, 1994; Rohm *et al.*, 1995). Ink-jet printers, which deposit inks in dot matrix form, are familiar to office workers. A variant of this process, the industrial ink-jet, is used, for example, to print sell-by dates on food packaging. This ability to print materials in the form of highly controlled droplets at high speed is clearly desirable for the mass production of analytical devices such as biosensors (Newman *et al.*, 1992). Developments in this area are leading to systems that deposit individual droplets with volumes of less than a nanolitre. Furthermore, ink-jet printing is a non-contact process, which is therefore suitable for printing on delicate or non-planar materials.

Characterisation

The importance of surface characteristics in determining the performance of biosensors is increasingly recognised. Many problems associated with stability, activity and specificity of the biosensor interface can be traced to a limited knowledge of how biomolecules interact with surfaces. Parameters such as surface chemistry, surface heterogeneities, solution conditions, *etc.* all affect the resultant biosensor function.

Various scanning probe microscopies are currently being applied to increase the understanding of biomolecule interactions at solid-liquid interfaces. Atomic force microscopy (Cullen and Lowe, 1994; Huber *et al.*, 1994), scanning tunnelling microscopy (Czajka *et al.*, 1992; You *et al.*, 1994; You *et al.*, 1995) and scanning electrochemical microscopy (Wittstock *et al.*, 1995) have all been applied to such studies. Other novel techniques such as scanning laser photochemical microscopy are being investigated (Hutton *et al.*, 1995).

Increasingly, the transduction techniques of direct immunosensors such as optical evanescent wave systems and acoustic devices are seen as surface characterisation tools by the biosensor community together with traditional tools such as ellipsometry, surface spectroscopies, calorimetry and contact angle measurements.

Conclusion

Both the potential for biosensors and the hurdles to their introduction have been thoroughly documented in the literature. Emerging information about molecular structures and mechanisms and surface science will provide the basis for a rational and systematic engineering of biosensors to overcome current limits to the widespread commercial application.

References

- Alvarez-Icaza, M. and Bilitewski, U. (1993) Mass production of biosensors. *Analytical Chemistry* **65**, 525A-533A.
- Benes, E., Groschl, M., Burger, W. and Schmid, M. (1995) Sensors based on piezoelectric resonators. *Sensors and Actuators A* **48**, 1-21
- Brink, G., Sigl, H. and Sackmann, E. (1995) Near-infrared surface plasmon resonance in silicon-based sensor: New opportunities in sensitive detection of biomolecules from

- aqueous solutions by applying microstep for discriminating specific and non-specific binding. *Sensors and Actuators B* **24-25**, 756-761.
- Cagnini, A., Palchetti, I., Lioni, I., Mascini, M. and Turner, A.P.F. (1995) Disposable ruthenized screen-printed biosensors for pesticides monitoring. *Sensors and Actuators B* **24-25**, 85-89.
- Cardosi, M.F. and Birch, S.N. (1993) Screen printed glucose electrodes based on platinised carbon particules and glucose oxidase. *Analytica Chimica Acta* **276**, 69-74.
- Clerc, D. and Lukosz, W. (1993) Integrated optical output grating coupler as refractometer and (bio-)chemical sensor. *Sensors and Actuators B* **11**, 461-465.
- Cullen, D.C. and Lowe, C.R. (1994) AFM studies of protein adsorption: 1. Time-resolved protein adsorption to highly oriented pyrolytic graphite. *Journal of Colloid & Interface Science* **166**, 102-108.
- Czajka, R., Koopal, C.G.J., Feiters, M.C., Gerritsen, J.W., Nolte, R.J.M. and Van Kempen, H. (1992) Scanning tunnelling microscopy study of polypyrrole films and of glucose oxidase as used in a third-generation biosensor. *Bioelectrochemistry and Bioenergetics* **29**, 47-57.
- Freitag, R. (1993) Applied Biosensors. *Current Opinion in Biotechnology* **4**, 75-79.
- Gilardi, G., Zhou, L.Q., Hibbert, L. and Cass, A.E.G. (1994) Engineering the maltose-binding protein for reagentless fluorescence sensing. *Analytical Chemistry* **66**, 3840-3847.
- Hecht, H.J., Kalisz, H.M., Hendle, J., Schmid, R.D. and Schomburg, D. (1993) Crystal structure of glucose oxidase from *Aspergillus niger* refined at 2.3Å resolution. *Journal of Molecular Biology* **229**, 153-172.
- Huber, W., Richmond, T., Anselmetti, D., Schlatter, D., Dreier, M., Frommer, J. and Guntherodt, H.-J. (1994) Local distribution of biomolecules on biosensing surfaces investigated by scanning force microscopy. *Nanobiology* **3**, 180-200.
- Hutton, R.S., Williams, D.E., Allen, R.M., Bennetto, H.P. and Meininghaus, C. (1995) Scanning laser photoelectrochemical microscopy of immobilized glucose oxidase. *Journal of Electroanalytical Chemistry* **391**, 203-205.
- Ikariyama, Y., Nishiguchi, S., Kobatake, E., Aizawa, M., Tsuda, M. and Nakazawa, T. (1993) Luminescent biomonitoring of benzene derivatives in the environment using recombinant *Escherichia coli*. *Sensors and Actuators B* **13-14**, 169-172.
- James, T.D., Samankumara Sandanayake, K.R.A. and Shinkai, S. (1995) Chiral discrimination of monosaccharides using a fluorescent molecular sensor. *Nature* **374**, 345-347.
- Koopal, C.G.J., Bos, A.A.C.M. and Nolte, R.J.M. (1994) Third-generation glucose biosensor incorporated in a conducting printing ink. *Sensors and Actuators B* **18-19**, 166-170.
- Lavers, C.R., Harris, R.D., Hao, S., Wilkinson, J.S., O'Dwyer, K., Brust, M. and Schiffrin, D.J. (1995) Electrochemically-controlled waveguide-coupled surface plasmon sensing. *Journal of Electroanalytical Chemistry* **387**, 11-22.

- Neaves, P.I. and Hatfield, J.V. (1995) A new-generation of integrated electronic noses. *Sensors and Actuators B* **27**, 223-231
- Newman, J.D. and Turner, A.P.F. (1992) Biosensors: principles and practice. In *Essays in Biochemistry* **27**. Edited by K F Tipton. Portland Press, London. 147-159.
- Newman, J.D., Turner, A.P.F. and Marrazza, G. (1992) Ink-jet printing for the fabrication of amperometric glucose biosensors. *Analytica Chimica Acta* **262**, 13-17.
- Rohm, I., Kunnecke, W. and Bilitewski, U. (1995) UV-polymerizable screen-printed enzyme pastes. *Analytical Chemistry* **67**, 2304-2307.
- Schipper, E.F., Kooyman, R.P.H., Heideman, R.G. and Greve, J. (1995) Feasibility of optical waveguide immunosensors for pesticide detection: physical aspects. *Sensors and Actuators B* **24-25**, 90-93.
- Spitznagel, T.M. and Clark, D.S. (1993) Surface-density and orientation effects on immobilized antibodies and antibody fragments. *Bio-Technology* **11**, 825-829.
- Szabo, A., Stolz, L. and Granzow, R. (1995) Surface-plasmon resonance and its use in biomolecular interaction analysis (BIA). *Current Opinion in Structural Biology* **5**, 699-705
- Turner, A.P.F., Karube, I. and Wilson, G.S. (1989) *Biosensors: Fundamentals and Applications*. Oxford University Press, Oxford.
- Turner, A.P.F. and Yevdokimov, Y.M. (1994) *Advances in Biosensors*, **Vol. 4**, JAI Press, London.
- Virta, M., Lampinen, J. and Karp, M. (1995) A luminescence-based mercury biosensor. *Analytical Chemistry* **67**, 667-669
- Walker, B., Kasianowicz, J., Krishnasastry, M. and Bayley, H. (1994) A pore-forming protein with a metal-actuated switch. *Protein Engineering* **7**, 655-662
- Wittstock, G., Yu, K.J., Halsall, H.B., Ridgway, T.H. and Heineman, W.R. (1995) Imaging of immobilized antibody layers with scanning electrochemical microscopy. *Analytical Chemistry* **67**, 3578-3582.
- You, H.-X., Disley, D.M., Cullen, D.C. and Lowe, C.R. (1994) Physical adsorption of immunoglobulin G on gold studied by scanning tunnelling microscopy. *International Journal of Biological Macromolecules* **16**, 87-91.
- You, H.-X., Disley, D.M., Cullen, D.C. and Lowe, C.R. (1995) A scanning tunnelling microscopic study of covalent immobilisation of immunoglobulin G on gold: Effect of the bias voltage on topography. *Micron* **26**, 121-132.

Self-assembled monolayers of receptor adsorbates on a gold surface.

M.W.J. Beulen; B.-H. Huisman; E.U. Thoden van Velzen; F.C.J.M. van Veggel; D.N. Reinhoudt.

University of Twente, MESA Research Institute, Lab. Dept. of Organic Chemistry, PO Box 217, 7500 AE Enschede, The Netherlands.
tel. + 31 53 4892933
Beulen@ct.utwente.nl

Abstract. Self-assembled monolayers can be used as the chemical interface in sensors. Resorcin[4]arene monolayers show a high selectivity for perchloroethylene as was proven with a Quartz Crystal Microbalance and Surface Plasmon Resonance. Self-assembled monolayers can also be used for the electrochemical detection of electro-inactive species.

The modification of surfaces by means of self-assembly has been investigated extensively. In particular, organosulfur-modified gold surfaces have been studied, because of their high stability and high degree of ordering. Self-assembled monolayers are appealing as a chemical interface in sensors as they are thermodynamically stable, and well-defined on a molecular level. Fast response times are obtained because of the short diffusion lengths. Self-assembled monolayers can be studied with several techniques like electrochemistry, surface plasmon resonance, infrared spectroscopy, ellipsometry, X-ray photoelectron spectroscopy and wettability studies. Furthermore, a flexible design of the chemical interface is possible. Sensitivity and selectivity can be obtained by molecular recognition at the monolayer interface. Here, two examples of self-assembled monolayers as the chemical interface in sensors will be described: a sensor with a high selectivity for perchloroethylene and the concept for an electrochemical sensor for the detection of electro-inactive species.

Previously, we have described highly-ordered self-assembled monolayers of resorcin[4]arene (**1**) and calix[4]arene (**2**) based tetrasulfides (see Figure 1).¹⁻⁴ In this system, the headgroup is readily available for complexation as it is directed to the outer interface.

The interaction between volatile guests and a receptor monolayer of adsorbate **1a** was studied with a Quartz Crystal Microbalance (QCM).⁵ QCM's were coated with self-assembled monolayers of resorcin[4]arene **1a**. The resonance frequency of the crystal strongly depends on the total mass of the crystal. Complexation in the cavity of the receptor leads to a gain of weight of the crystal and results in a decrease in resonance frequency. A QCM that was coated with the resorcin[4]arene monolayer **1a** strongly responded to different perchloroethylene concentrations, whereas the QCM's coated with a reference monolayer of didecylsulfide showed only small responses (see Figure 2). The resorcin[4]arene-coated QCM's were also exposed to different gasses, such as chloroform, carbon tetrachloride, toluene and trichloromethylene. The responses were much smaller for these gasses as compared to perchloroethylene. So, the sequential selectivity for perchloroethylene is high.

Complexation by monolayers of resorcin[4]arene **1a** was also studied by Surface Plasmon Resonance (SPR). SPR is a technique where changes in the refractive index near an

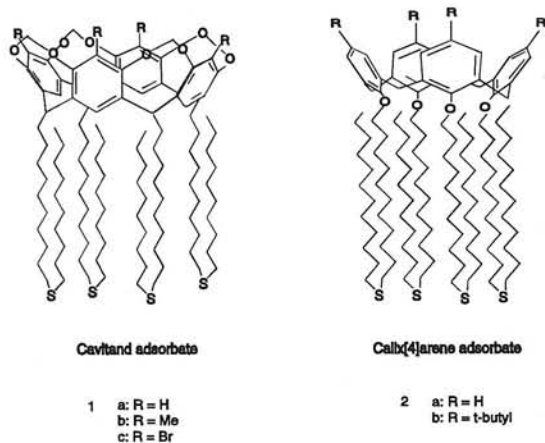


Figure 1. Resorcin[4]arene and calix[4]arene adsorbates.

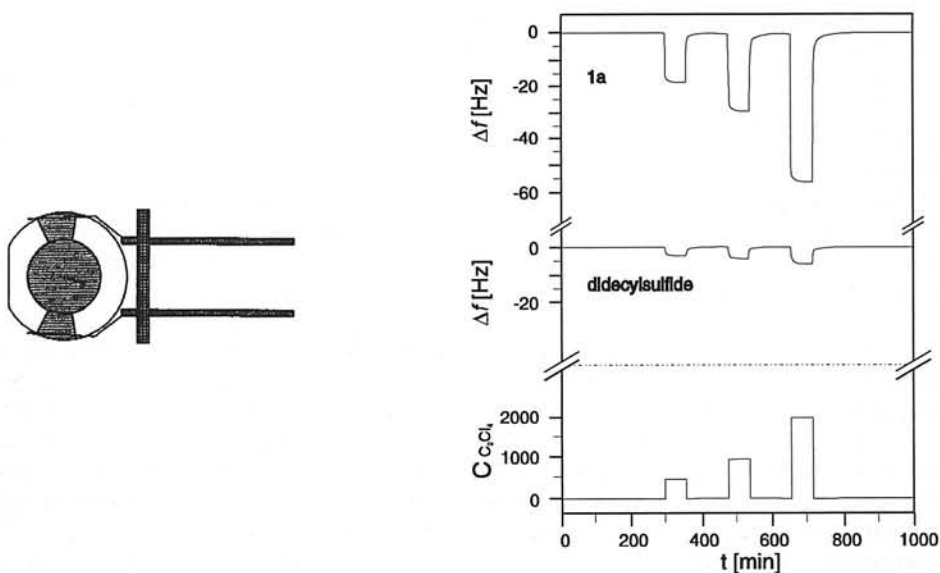


Figure 2. Response-curves for monolayer coated QCM's that are exposed to perchloroethylene.

interface can be readily detected. The change of the plasmon angle during a surface binding experiment can be shown to be proportional to the amount of material bound to the interface. The change in plasmon angle ($\Delta\alpha$) was determined as a function of the concentration of toluene, tetrachloroethylene, tetrachloromethane, chloroform, dichloromethane, and 1,2-dichloroethane. Changes in the concentration of different vapors resulted in a change of plasmon angle, both for the cavity monolayer and to a much lesser extent for a reference

monolayer of octadecanethiol. A typical experimental response curve is shown in figure 3, where different concentrations of perchloroethylene were subsequently applied to the monolayers. Also with SPR a sequential selectivity for perchloroethylene was observed. An advantage of the SPR measurements over the QCM measurements is the high stability of the signal, so that a more precise measurement was possible. With the current equipment a detection limit of less than 300 ppm for tetrachloroethylene was obtained.

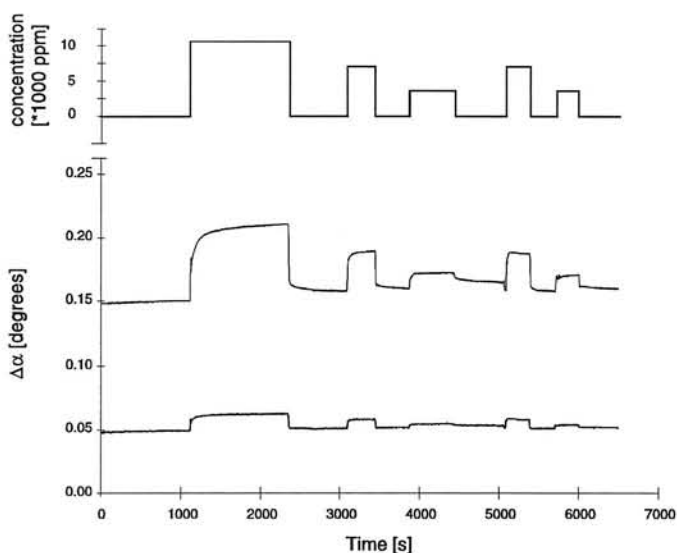


Figure 3. Typical SPR time response curve for perchloroethylene in contact with monolayers of cavitant **1** (top) and $C_{18}SH$ (bottom).

Currently self-assembled monolayers as the chemical interface in an electrochemical sensor for the detection of electro-inactive species are under investigation. The sensor consists of a gold electrode modified by metallo-receptors. The receptor is designed to have changing electrochemical properties (shift in reduction or oxidation potential) when the detectable species are complexed. Receptors that have electrochemical properties which change upon binding of the guest can be used for the electrochemical detection of electro-inactive species. The sensor is schematically depicted in figure 4. Complexation of the detectable species in the cavity changes the electrochemical properties of the metal ion M (the redox-center). Using this principle, an electrochemical sensor can be built for the detection of in principle electro-inactive species like cations, anions or neutral molecules (e.g. pyridines, amino acids, sugar molecules) via a permanently present redox-center (a metal ion). Binding of the guest can occur by hydrogen-bonds, electron pairs of the guest or π - π interactions. Detection can be accomplished by electrochemical techniques like cyclic voltammetry. Receptor adsorbates, as shown in figure 5, were synthesized and can complex cations.

Self-assembled monolayers of the salophene adsorbates were prepared. Reduction of the Ni- and Cu salophene could not be accomplished because desorption of the monolayer occurred first. The reduction potential of these salophenes are on the borderline of the electro-

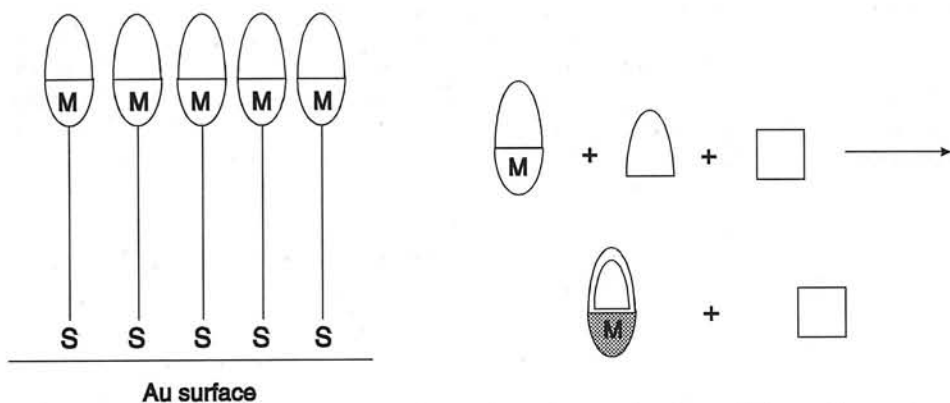


Figure 4. Schematic picture of a monolayer of receptor molecules which can be used as a sensor.

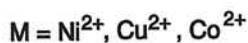
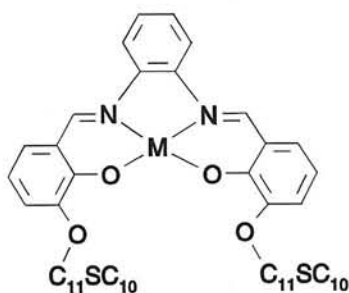


Figure 5. Salophene adsorbates which are used in an electrochemical sensor.

chemical stability of self-assembled monolayers. Therefore, also monolayers of the cobalt-salophenes were prepared, which can also be oxidized at a considerably less negative potential. Studies on these type monolayers are performed now.

- 1 E. U. Thoden van Velzen, J. F. J. Engbersen, D. N. Reinhoudt, *J. Am. Chem. Soc.* **1994**, 116, 3597.
- 2 B.-H. Huisman, E. U. Thoden van Velzen, F. C. J. M. van Veggel, J. F. J. Engbersen, D. N. Reinhoudt, *Tetrahedron Lett.* **1995**, 36, 3273.
- 3 E. U. Thoden van Velzen, J. F. J. Engbersen, P. J. de Lange, J. W. G. Mahy, D. N. Reinhoudt, *J. Am. Chem. Soc.* **1995**, 117, 6853.
- 4 E. U. Thoden van Velzen, J. F. J. Engbersen, D. N. Reinhoudt, *Synthesis* **1995**, 8, 989.
- 5 K.-D. Schierbaum, T. Weiß, E. U. Thoden van Velzen, J. F. J. Engbersen, D. N. Reinhoudt, W. Göpel, *Science* **1994**, 265, 1413.

Sensors for Agricultural Production in the 21st Century

F.W.H. Kampers, J.C. Bakker, G.P.A. Bot, H. Breteler, C. Eerkena and
O.C.H. de Kuijer*

Institute of Agricultural and Environmental Engineering (IMAG-DLO)
PO Box 43, NL-6700 AA Wageningen, The Netherlands

*Sustainable Technological Development
PO Box 6063, NL-2600 JA Delft, The Netherlands

Abstract

A result of three studies of the sub-programme Nutrition of STD was the identification of the need for new sensor and measurement technology to obtain the aim: a twenty fold reduction of environmental strain in the year 2040. In Sustainable Land Use, measurement technology has to be able to determine the composition of waste in order to optimise it as the source of nutrients. In Integrated Conversion the measurement technology described focuses on the reduction of herbicides and pesticides by detecting health problems in an early stage. High-Tech Agro-Production describes a closed agricultural production unit. The measurement technology aims at quality assurance. There naturally is a gap between what is feasible at present and what is necessary in 2040. Indications are given on how to bridge that gap.

Introduction

A Dutch interdepartmental research programme Sustainable Technological Development (STD) studies how a more sustainable future can be achieved in the next 50 years. The aim of the programme is to investigate how long term development of new technologies can enable a twenty fold reduction of environmental strain in a number of important societal necessities. The programme is divided into five sub-programmes: Transportation; Housing; Water; Chemistry; Nutrition. The method used is called backcasting: first a desirable future in 2040 is described, next the necessary technological path and critical technologies are identified to achieve that future.

The sub-programme Nutrition, on which we will focus in this paper, studies how the needs of an increasing number of people can be fulfilled in a more sustainable way [1]. In 2040 food should be: tasty but not too expensive; healthy and functional; recognisable and natural; easy and fast to prepare; varied in supply and consumption; and producible without environmental or socio-economic problems. To obtain this situation various problems have to be solved. Four different directions have been identified in which solutions for these problems can be found: Sustainable Land Use [2]; Integrated Conversion [3]; High-Tech Agro-

Production [4]; and Novel Protein Foods [5]. In all these four directions the development of sensor and measurement technologies that can provide specific and reliable information on food production processes, were a critical success factor.

Of three of the four directions: Sustainable Land Use; Integrated Conversion; and High-Tech Agro-Production we will try to identify what measurement technology can contribute to the desired situation, and investigate in which directions this new technology can be found. We will limit ourselves to the specific measurement technology that is most important for the achievement of the system described in each of the directions. However, the technology associated with the other directions will also contribute to its success.

Sustainable Land Use

In 2040 the country side is characterised by multi-functional use of the available land. Apart from the production of food, a new type of agriculture also recycles waste, allows nature to develop, provides possibilities for recreation and supplies us with fresh water. The products but also the wastes are used within the region of production. To combine the food production function in the new land production system with the other functions in a more sustainable way, five critical technologies have been identified at three different scales: the region, the farm and the plot. These technologies are: recirculation and re-use of organic waste; renewable energy sources and energy management; management information systems at farm level; sensor and information technology to manage the logistics of nutrients and to monitor the vitality of the plants; processing of organic wastes [2]. We will focus on the aspects of nutrient logistics and the re-use of wastes; the measurement technology relevant to plant health will be dealt with in the section on Integrated Conversion.

To use the animal and other wastes in sustainable production, waste must have a texture and nutrient content which corresponds to the needs of the plants and the soil. To optimise the waste accordingly, composting processes must be monitored and controlled, the composition of the different types of waste must be measured and the wastes must be mixed. Since it is undesirable to store the waste until the results of off-line analyses are available, sensors need to be developed that can measure in-line the composition in a complex matrix. The problem with the measurement of the components of wastes is that elements may be present in a variety of different chemical compounds. Phosphorus, for instance, can be present in the inorganic form or in various organic molecules. At present specific chemical treatments of the samples are used to bring the element of interest in a well defined chemical state prior to the analysis. These analyses in future may be implemented in microsystems resulting in a micro laboratory [6]. Another solution may be the use of measurement technology based on nuclear or inner electron shell properties, which are not affected by the chemical state the element is in. At the moment this technology (NMR and x-ray fluorescence spectroscopy) is available in laboratories. It will probably be very difficult to use these systems in farm conditions and to make them cheap enough for large scale application.

The need of plants for nutrients depends on soil type and conditions, weather conditions in time and in place, neighbouring land use, etc. To prevent production loss or pollution of the aquatic system it is very important to administer exactly the required amount of nutrients. With radar and other high-frequency electromagnetic techniques from the vehicle dispensing the fertiliser, it may be possible to determine the amount of water and the concentration of ions in the soil remotely. Chemical sensors, like Ion Selective Field Effect Transis-

tors (ISFETs) may be used to measure the concentration of specific types of ions [7]. Finally, sensors may become available that can derive the need for certain chemicals from the plants itself. Possibly in analogy to chlorophyll fluorescence, other probing techniques based on the absorption or scattering of light in certain wavelength bands can be developed that contain this information.

The amount of water available to the plants is also important. Excess water will drain to the ground water, transporting nutrients out of the root zone. A too small amount of water will inhibit the development of the plants. It will be important to continuously monitor the amount of water available to the plants and to control it. This can be done using artificial drainage systems, which prevent drainage to the ground water and allow the re-use of the water and nutrients dissolved; and through efficient water supply systems, in times of drought. The sensors must measure both the water tension, which determines *when* to take action, and the water content, which determines *what* action should be taken. These measurement systems must be able to function reliably and reproducibly during one growing season. Such sensor systems are currently under development [8]. Large scale cost-effective application will be possible within the next few years.

Integrated Conversion

The primary aim of the study Integrated Conversion was to find ways to convert nutrients, water and energy into food products in the most efficient way and with as little waste as possible. The study has focused on two systems: the *(bio)refinery* in which micro-organisms convert raw materials into a wide range of consumer products; and the *cultivation boom* with which the primary agricultural production can be optimised [3]. Although the (bio)refinery has many aspects of measurement technology, because of the factory set-up of the refinery, we will not go into these aspects here, but will focus on the measurement systems necessary to efficiently operate the cultivation boom.

A cultivation boom is a system that can position tools and measurement systems sufficiently close to the plants in an open-field plot. In the study [3] the cultivation boom continuously moves over open-field agricultural production plots which may contain different types of plants [9]. It may move in circles, getting its energy and other supplies from a central pivot [10] or it may move linearly. Because of the fact that the boom moves over well-defined tracks (rails), combined with an accurate position measurement system, its position is well known and, more importantly, well reproducible.

Apart from the plants being supplied with the nutrients and the water required, it is also necessary to monitor the health of the plants. Sensory systems that can detect plagues in an early stage can greatly facilitate controlling and curing them. Depending on the specific plague and the moment of detection different approaches can be chosen. In all cases it is beneficial to detect the plague as soon as possible. Administration of pesticides, natural bio-cides or biological agents can be done locally and, in some cases, other means of control, like removal of the infected plants, mechanical or biological methods, can be used.

Sensors for early plague detection may rely on changes in the colour or disfigurements of certain parts of the plants, changes in the fluorescence behaviour, changes in the metabolism, the presence of specific chemical substances or anti-bodies, etc. Detection based on the colour of leaves and other visible parts of the plant can be done by comparing the spectral information contained in the reflected light from two consecutive passes. Changes in shape of certain parts

of the plants will be detected by systems based on computer vision. If necessary colour information and/or the combination of images taken in different spectral bands can be taken into consideration. The fluorescence behaviour of the plants can be measured during the night. Certain biological molecules, sensitive to specific diseases, are excited with light with the right spectral composition from a bright source. After the source has been switched off, detectors can measure the intensity as a function of time of the light emitted by these molecules when they return to their original state. This technique is already available in the case of chlorophyll fluorescence at close range [11]. In some cases it may also be possible to detect plagues through certain chemical substances being released in the air. Photo-acoustic measurement systems may be able to detect the very low concentrations involved, but have not outgrown the laboratory stage. Plagues caused by insects can also be detected by monitoring the insect density in the air above the plants and, in some cases, from specific noises. If diseases can not be detected with non-destructive sensors, the tools on the boom may be used to take tissue or soil samples that can be analysed in an autonomous boom-borne laboratory.

The detection of weeds, in first instance, will rely on the fact that plants developing at locations where no seed or plant was planted (position reproducibility) is a weed. Because of the relative short period between passes of the boom, weeds developing at these locations can easily be removed mechanically. Weeds can also be detected because they have a different appearance or because they develop differently (more quickly) than the plants of interest.

High-Tech Agro-Production

The study High-Tech Agro-Production [4] focuses on a closed production system, for instance a greenhouse, in which high quality fresh vegetables can be produced in close proximity to the consumers in agreement with their demands. The primary production process is plant growth, in which mineral nutrients, light, energy, water and CO₂ are converted into fresh vegetables. To achieve the aim (a twenty fold reduction of the environmental strain) it is necessary to drastically reduce the need for non-renewable energy of present production systems. Consequently one of the starting points was to design a so called High-Tech Agro production system (HTA) that does not use non-renewable energy sources and requires minimal inputs of agro-chemicals (nutrients, herbicides and pesticides). The HTA would obtain its energy, necessary to maintain the optimal growth conditions, predominantly from the sun. Waste produced within the region is the source of the nutrients necessary for the plants. For the control of nutrients the technology described in the section Sustainable Land Use can be used.

Because of the fact that the HTA is a closed system which is difficult to invade by organisms causing them, pests and diseases will be rare. Optimisation of the cultivars for resistance and genetic manipulation will result in plants that are much less susceptible or resistant to plagues and diseases. However, in view of the closed character of the system, which requires recirculation of air and water, and since no chemical substances are allowed to control a plague, timely removal of infected plants is essential to avoid loss of all the plants in the HTA. Therefore it is necessary to have a system that continuously checks the plants for possible diseases and insects. These systems should be able to move through the HTA autonomously. They will be equipped with early plague detection systems based on the technology described in the Integrated Conversion section.

The fruit producing plants growing in the HTA will tend to produce too many leaves. To optimise the photosynthetic process of the average plant, a well-defined leaf area index must be maintained. In practice this means that leaves, at places where there is insufficient light to absorb, must be removed. Apart from leaf picking, also other cultivation measures need to be performed in different stages of the development of the plant. All these actions will probably be performed by an autonomous robotic system. Such a system will need different sensors enabling the detection of objects that require handling. These systems will be based on vision systems that are already available.

When the fruits or the other sellable organs have reached the desired development, it is time to harvest. Because harvesting in an HTA will also be done by an autonomous harvesting system, sensors are necessary to determine the position of the product. The moment of harvesting may depend on the demand for a specific quality of the product. Measurement systems must be able to determine the quality of the products non-destructively or with minimal damage before they are harvested. The quality can be derived from the colour and shape of the product, but other parameters like sugar content may be a better parameter. At the moment sugar content of some fruits can be determined with Near InfraRed (NIR) spectroscopy. This technique is already being applied in sorting lines. Finally, when the system handles individual products it can determine a number of parameters of the produce (weight, firmness) that can be used to sort the products more accurately and objectively in different quality categories.

A possible way to go

Monitoring requires measurement principles and sensors that produce an output that correlates via a known relationship with the parameter to be measured. The problem with agricultural products and processes is that the parameters to be measured are not well-defined. For instance measuring the ripeness of a fruit can in some fruits be correlated with colour, in others with firmness or sugar content. Also the biological variability introduces problems. No two agricultural products are the same. The measuring principles must be able to cope with this variability. The products very often also are fragile or easy to bruise.

The production processes investigated here take place in living cells in plants. The plants must be in optimal condition to be able to produce to their full potential. To monitor the health of plants different parameters in, on or close to the plant can be measured; the speaking plant approach [12,13]. Sensors for these parameters preferably should not be harmful to the plant itself. It can be expected that the sensors will not be applied to every individual plant. Measurements on a few representative plants in the growing system will be used to monitor the health of all plants. The best results will be obtained if as many parameters as possible are monitored and their information combined.

Finally the environment in which the systems must be able to perform usually is not high-technology friendly or laboratory-like. Sensors, for instance, that determine the composition of manure will have to be able to resist aggressive substances.

These problems may be solved by combining several technologies, some already developed, others presently emerging. Smart sensors, in which sensing elements are combined with micro-electronic circuitry for signal processing and calibration and sensor fusion, combining the outputs of several sensors to get reproducible estimates for certain parameters will be applied. Contactless principles based on the interaction of electromagnetic radiation (light,

microwaves) with the objects to be measured will solve problems with contamination or fragile objects. Microsystems are based on the micro machining technology developed for micro-electronic purposes and based on the same mass production techniques. They are electro-mechanical systems, that combine very small mechanically moving parts like pumps, motors, mirrors etc. with micro-electronics for the control of parts and the signal processing of sensors [6]. Microsystems can provide solutions to measuring principles that require wet chemistry or recalibration of sensing elements. These systems will also allow complex sensors and systems which are small and cost effective. At the moment micro spectrometers and simple micro laboratories are already available. Chemical and biochemical sensors, already available at present, must be improved to have substantial longer life times and better applicability in complex environments [7].

Sensor and measurement technology can make all the previously mentioned future developments possible. However, although the technology partly already exists, most of the sensors still have to be developed or improved to be applicable as suggested here. This will require substantial research in measurement technology and sensor development.

References

- 1 Documentatiemap behoeftenveldanalyse Voeden, 1994. Heidemij Advies B.V., ATO-DLO, Imd, TNO-Voeding en de vakgroepen Levensmiddelentechnologie en Voeding van de LUW, DTO-werkdocument V0, in Dutch
- 2 Duurzaam Landgebruik, definitiestudie, 1995. AB-DLO, PE-LUW, MiBi-RUL en Heidemij Advies B.V., DTO-werkdocument VD0, *in Dutch*, in preparation
- 3 Geïntegreerde Conversie: duurzame nieuwe voeding, definitiestudie, 1995. TNO-Voeding, TNO-STB, Imd Micon B.V. en IMAG-DLO, DTO-werkdocument VG0, *in Dutch*, in preparation
- 4 High-Tech Agroproductie, definitiestudie, 1995. Heidemij Advies B.V., ATO-DLO, IMAG-DLO en PBG, DTO-werkdocument VH0, *in Dutch*, in preparation
- 5 Novel Protein Foods, definition study, 1993. Arthur D. Little, DTO-werkdocument VN0
- 6 Microsystem technology, exploring opportunities, Gerben Klein Lebbink (Ed.), Netherlands Study Centre for Technology Trends, STT 56, 1994
- 7 Gieling, Th.H. and H.H. van den Vlekkert, Application of ISFETs in Closed-loop Systems for Greenhouses, *Adv. Space Res. Vol. 18 (4/5)*, 135-138, 1996
- 8 Hilhorst, M.A. and C. Dirksen, Dielectric Water Content Sensors: Time Domain versus Frequency Domain, Proc. of symposium held at Northwestern University, Evanston, Bureau of Mines Special Publication SP 19-94, 23-33, 1994
- 9 Eerkens, C., The emergence of new technologies: projections of cultivation methods in the 21st century, Proceedings AgEng Conference, Milan, 1994
- 10 Wilton, B., P. Strange and H.R. Ghasemzadeh, Centre pivot cultivation: power supply and control of a mains electric tractor, *Agricultural Engineer*, 1989
- 11 Snel, J.F.H., O. van Kooten and L.W.A. van Hove, Assessment of stress in plants by analysis of photosynthetic performance, *Tr. Analyt. Chem. Vol. 10 (1)*, 26-30, 1991
- 12 First International Workshop on Sensors in Horticulture (1991), Noordwijkerhout, The Netherlands, Convenor: Th.H.Gieling; K.Schurer (Ed.), *Acta Hort. 304*, 1992
- 13 2. International Symposium on Sensors in Horticulture (1995), Copenhagen, Denmark, Th.H.Gieling, B.Bennedsen, W.T.M.van Meurs (Eds.), *Acta Hort. 421*, (in print)

A SYMMETRICAL TRIAXIAL CAPACITIVE ACCELEROMETER FOR BIOMEDICAL PURPOSES

J.C. Lötters, W. Olthuis, P.H. Veltink, P. Bergveld

MESA Research Institute, University of Twente
P.O. Box 217, 7500 AE Enschede, The Netherlands
Phone: +31-53-4892755; Fax: +31-53-4892287
E-mail: j.c.lotters@el.utwente.nl

ABSTRACT - *Triaxial accelerometers are needed in the biomedical field for the monitoring of mobility. A new highly symmetrical inherently triaxial accelerometer has been designed. Its advantages are a small size, a low off-axis sensitivity and an equal sensitivity in all axes. A number of triaxial accelerometers were realized with dimensions $5 \times 5 \times 5 \text{ mm}^3$. They show an off-axis sensitivity of $< 4\%$ g/g but unfortunately have an unequal sensitivity in the three axes. A clinical measurement of the movement disorders of Parkinson's disease patients indicated that the triaxial accelerometer is suited to measure the kind of tremor which appears in this disease.*

INTRODUCTION

There is a need for very small triaxial accelerometers in the biomedical field. These sensors can for instance enable the ambulant monitoring of movement disorders of patients suffering from Parkinson's disease [1]. The most important specifications for biomedical applications are [2]: amplitude range $\pm 5 \text{ g}$, resolution 1 mg , bandwidth $0\text{-}50 \text{ Hz}$, off-axis sensitivity $< 5\%$ g/g, dimensions $< 2 \times 2 \times 2 \text{ mm}^3$ and power consumption $< 1 \text{ mW}$.

Up to now, triaxial accelerometers presented in the literature [3,4] have a lack of symmetry and therefore show a large off-axis sensitivity up to 21% [3]. The sensor proposed in this paper has a highly symmetrical configuration which ideally should not have any off-axis sensitivity. Its basic structure consists of a centre mass surrounded by six capacitors.

Using the triaxial accelerometer for clinical purposes can help medical doctors to get insight in the progress of diseases concerning movement disorders like Parkinson's disease. A characteristic symptom of this disease is a tremor at a certain frequency and amplitude, for the measurement of which a triaxial accelerometer would be very useful.

In this paper the sensor structure, its characterization and an example of a clinical measurement on Parkinson's disease patients will be described.

THEORY

(a) sensor structure

The basic concept of the total sensor consists of six capacitors with nominal capacitance value C_0 [pF] surrounding one centre cubic mass, as shown in figure 1.

When an acceleration is applied, the mass moves with respect to the fixed electrodes and, consequently, the values of the capacitors change. Each pair of opposite capacitors can differentially sense the acceleration in one direction. The total acceleration vector can be composed of the three separately measured accelerations.

The configuration is highly symmetrical and should thus have very little off-axis sensitivity. The highly symmetrical structure can be obtained with a new spring concept, based upon the flexibility and stability of elastomer structures in between the movable and the fixed electrode [2,5]. The dimensions of these structures determine both the nominal capacitance, the damping and the spring constant.

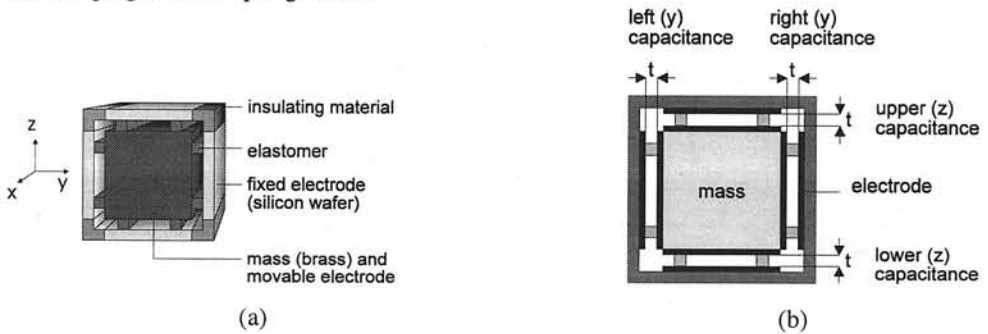


Figure 1. Cross-sectional (a) 3D and (b) 2D view of the basic structure of the triaxial accelerometer

(b) stress-strain relations in a rubberelastic material

When the accelerometer of figure 1 is accelerated in for instance the z-direction, the elastomer structures in the two capacitances who sense this direction will be extended or compressed (CE). The elastomer structures in the four other capacitances will be subjected to a shear stress (S). It can be shown that the resulting spring constant k_{tot} [N/m] in one direction (x,y, or z) is [5]:

$$k_{tot} = 2.k_{CE} + 4.k_S = 10.G.A_R / t \quad (1)$$

with G Shear elastic modulus [N/m²]
 A_R area of the elastomer on which the force due to the acceleration is applied [m²]
 t thickness of the layer on which the force is applied [m]

(c) output voltage due to an applied acceleration

The capacitance variations ΔC are measured with a specially designed differential capacitance to voltage converter (CVC) [6] resulting in an output voltage V_{out} due to an applied acceleration a

$$V_{out} = H.2\Delta C / C_0 = H.2\Delta t / t = H.2.m.a / (k_{tot} . t) \quad (2)$$

with H amplification factor of the CVC
 m seismic mass of the accelerometer [kg]
 a acceleration [m/s²]

RESULTS & DISCUSSION

characterization of the triaxial accelerometer

A number of capacitive triaxial accelerometers has been realized with dimensions $5 \times 5 \times 5 \text{ mm}^3$. Each axis is connected to a corresponding differential capacitance to voltage converter with gain factor $H = 2000$ [6]. The seismic mass is 220 mgrams in all devices, the theoretical spring constants are $k_{tot,A1} = 63.10^3 \text{ [N/m]}$, $k_{tot,A4} = 18.10^3 \text{ [N/m]}$ and $k_{tot,A6} = 10^5 \text{ [N/m]}$ and the initial layer thicknesses were designed to be $t_{A1} = 16 \text{ }\mu\text{m}$, $t_{A4} = 8 \text{ }\mu\text{m}$ and $t_{A6} = 10 \text{ }\mu\text{m}$. The results of the calculations using equation (2) are shown in table I.

Table I: Measurement results of the triaxial accelerometer

	Sensitivity [V/g] Calculated			Sensitivity [V/g] Measured			Off-axis sensitivity [g/g] Measured		
	A1	A4	A6	A1	A4	A6	A1	A4	A6
Device:	A1	A4	A6	A1	A4	A6	A1	A4	A6
x-axis:	8.8	62	8.8	8.5	20	7.3	<2%	<4%	<1%
y-axis:	8.8	62	8.8	1.9	38	3.5	-	-	<1%
z-axis:	8.8	62	8.8	2.6	10	8.8	-	-	<2%

The measurement results show that the highly symmetrical triaxial accelerometer is well-functioning, because all devices are able to detect accelerations in three directions with very little cross-talk between the axes. However, in almost all cases the theory predicts a higher sensitivity than that which is measured. This is due to sometimes severe variations in height of the elastomer structures and pre-stressing of some of the elastomer structures due to preparation variances and assembly, respectively. The first problem has been solved, the second will be solved in due time.

pilot test on patients with Parkinson's disease

Characteristic symptoms of Parkinson's disease are a certain rigidity or a tremor of the hands at a certain frequency and amplitude. A triaxial accelerometer should be able to measure such symptoms, so a pilot test has been carried out on several Parkinson's patients.

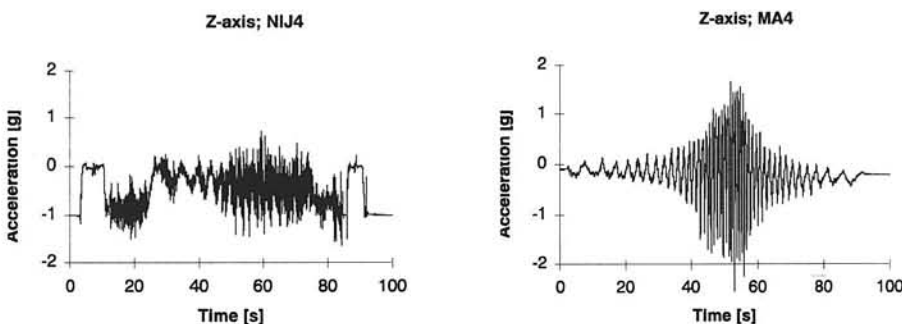


Figure 2. Z-axis acceleration of two different Parkinson's disease patients performing a prescribed movement: the patients' elbow was on a table, they rotated their underarm backward and forward in the horizontal plane, first slowly, then rapidly and finally slowly again; the first curve shows a patient with a visible tremor (with an amplitude density of $22.8 \text{ g}^2/\text{Hz}$ at 4.85 Hz), the second curve shows a patient with a more fluent movement which is the result of using particular drugs

In clinical practice, four stages of the disease are defined, based on the level of disfunctioning [7]. However, individual characteristics, such as those shown in figure 2, are not taken into account.

The measurement has been done with accelerometer A6 connected to the right wrist of the patient. The measurement results indicate that the triaxial accelerometer is sensitive enough to registrate the kind of tremor which appears in Parkinson's disease.

When an accelerometer is used, the doctor should be able to determine the mean frequency and amplitude of the tremor of each patient before and after the use of particular drugs. So, for each patient an individual progress report can be made. A portable system, with which a patient can be monitored for 24 hours during normal daily life, has been developed for this purpose.

CONCLUSIONS

A number of prototypes of the symmetrical triaxial accelerometer with outer dimensions of $5 \times 5 \times 5 \text{ mm}^3$ has been designed and realized. The highly symmetrical structure is advantageous with respect to the reduction of off-axis sensitivity: a maximum of 4% was measured.

The overall sensitivity of the realized sensors varies between 1.9 V/g and 38 V/g. The sensitivity of all axes in one device should have been equal due to the symmetrical structure of the sensor. Unfortunately, variations in sensitivity within one device appeared. These are caused by unequal height of the elastomer layers and the presence of pre-stress in the layers.

A test with Parkinson's disease patients has shown the usability of the miniaturized triaxial accelerometer in the registration of movement disorders. Further research is necessary to develop a method which relates the appearing accelerations to the progress of the disease in individual patients.

ACKNOWLEDGMENT

The authors would like to thank Mr. J.G. Bomer, Mr. A.J. Verloop and Mr. Ed A. Droog for their assistance in technology and electronics and the Dutch Technology Foundation (STW) for its financial support.

REFERENCES

- [1] P.H. Veltink, E.G. Olde Engberink, B.J. van Hilten, R. Dunnewold, C. Jacobi, *Towards a new method for kinematic quantification of bradykinesia in patients with Parkinson's disease using triaxial accelerometry*, on CD ROM proceedings of IEEE EMBS conference, Montreal, September 1995
- [2] J.C. Lötters, W. Olthuis, P.H. Veltink, P. Bergveld, *On the design of a triaxial accelerometer*, Journal of Micromechanical Microengineering, 5 (1995) 128-131
- [3] K. Jono, M. Hashimoto, M. Esashi, *Electrostatic servo system for multi-axis accelerometers*, Proceedings IEEE MEMS, 1994, 251-256
- [4] T. Mineta, S. Kobayashi, Y. Watanabe, S. Kanauchi, I. Nakagawa, E. Sugauma, M. Esashi, *Three-axis capacitive accelerometers with uniform axial sensitivities*, Proceedings Transducers '95, 554-557
- [5] L.R.G. Treloar, *The physics of rubber elasticity*, Clarendon press, Oxford, 1975
- [6] J.C. Lötters, W. Olthuis, P.H. Veltink, P. Bergveld, *A sensitive differential capacitance to voltage converter for sensor applications*, submitted to IEEE Instrumentation and Measurement
- [7] M.M. Hoehn, M.D. Yahr, *Parkinsonism: onset, progression and mortality*, Neurology, Volume 17, Number 5, May 1967

A Waveguide Material for Integrated Optical Sensors: Silicon Oxynitride

H. Albers, L.T.H. Hilderink, J.H. Berends, K. Wörhoff,
N.F. van Hulst and P.V. Lambeck

MESA Research Institute, University of Twente, P.O.Box 217, 7500 AE
Enschede, The Netherlands

E-mail: H.Albers@el.utwente.nl

Abstract: SiO_xN_y is a flexible material for making planar waveguide structures for sensors. This material can be deposited with different technologies; PECVD and LPCVD are described. Layer properties of films produced with these technologies are presented. High optical transparency, tunable refractive index and high uniformity are the main characteristics. The layer properties of PECVD films can be improved by annealing. Besides optical loss from scattering also the absorption due to hydrogen is reduced. The development of the application of SiO_xN_y in devices is shown. Finally the relation between uniformity and device performance is discussed.

Introduction

Silicon oxynitride (SiO_xN_y) is a flexible material for making planar waveguide structures for sensors. The material is transparent in a wide wavelength range from the UV region up to the near infrared. Therefore it can be applied in the field of integrated optical sensors, which operate mostly in the visible region as well in devices for telecommunication, which operate in bands around 850 nm, 1300 nm and 1550 nm. The thickness of SiO_xN_y films can be varied from several tenths of nanometers up to several tenths of micrometers without a significant change in other properties like structure and texture, and refractive index. Very important for integrated optic devices is the uniformity in thickness and optical properties over large areas. An adequate uniformity can already be reached and further improvement is expected. The most conspicuous flexibility is the tunable refractive index from 1.46 - 2.0. This offers the device designer another degree of freedom to optimize his device. The most important applications of this freedom are:

- Optimizing the extension of the optical field outside the waveguiding layer
- Optimizing the field strength on the interface of the waveguiding layer
- Match the refractive index with that of another material in the device
- Optimizing the index contrast between waveguiding and gladding layers
- Optimizing the dimensions of the waveguide

Of course the mentioned properties are strongly interconnected. Another degree of freedom is therefore so important. The first two aspects determine how strong a waveguide senses the "outside world". They are very important for sensors, especially chemical sensors. The last two are important for connecting the integrated optics device with other optical components, semiconductor lasers, detectors and fibers.

Another advantage of the flexible refractive index is that within the same technology layers with different refractive indices can be easily combined in a device without compatibility problems that can be expected if different technologies have to be used.

For the shaping of channel waveguides and other structures a well-developed number of wet and dry etching techniques are available. Accurate dimensions and sharp edges can be obtained.

The application of SiO_xN_y in integrated optic devices started in the mid 80's with the use of Si_3N_4 waveguides^{1, 2}. Shortly afterwards several other groups started with SiO_xN_y waveguides^{3, 4, 5}. In Germany this work was stimulated in the framework of a stimulation program "Mikrosystemtechnik" with a sub-program for integrated optics on silicon⁶. Many of these activities were focused on sensors^{3, 7, 8, 9}.

**Table I. Source gases used
in CVD processes**

Element	PECVD	LPCVD
Si	SiH_4	SiH_2Cl_2
N	N_2, NH_3	NH_3
O	$\text{N}_2\text{O}, \text{O}_2$	$\text{N}_2\text{O}, \text{O}_2$

gaseous precursors that are mostly first absorbed on the substrate surface. An overview of the source gases is given in table I. The reaction mostly takes place only if an energy source is available to overcome an activation barrier.

Different types of energy sources used in CVD processes are shown in Table II. We will give a short introduction to both and then we compare them.

PECVD

In plasma enhanced CVD (PECVD) the process gasses are feed through a plasma. Molecules are ionized, dissociated and activated. The resulting species are more reactive than the process gasses and can perform a reaction to SiO_xN_y . A PECVD reactor is basically a vacuum vessel with two electrodes that are connected to a RF power supply. There are two general used designs (Fig. 1 and 2).

Deposition Technologies

Silicon oxynitride can be deposited with different technologies. Plasma enhanced chemical vapour deposition (PECVD) and low pressure chemical vapour deposition (LPCVD) are the most extensively used technologies. Both technologies have been used for integrated optics devices. The layer growth is based on a chemical reaction between

Table II. CVD processes

Process	Acronym	Energy
Atmospheric CVD	APCVD	thermal
Low pressure CVD	LPCVD	thermal
Plasma enhanced CVD	PECVD	electrical
Photo CVD	Photo-CVD	UV-light
Laser CVD	LCVD	UV-light IR-light

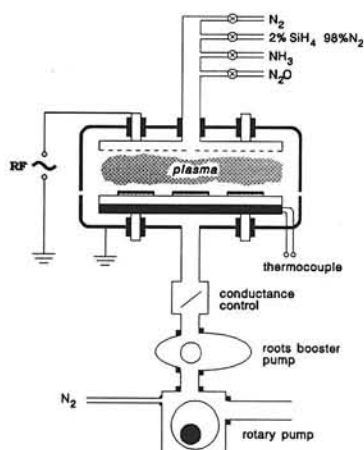


Fig. 1. Parallel plate PECVD reactor

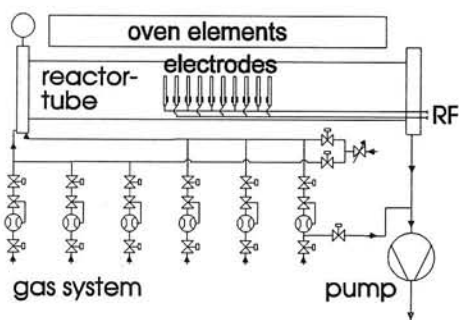


Fig. 2. Hot Wall PECVD reactor.

In both reactors the substrates are heated to 300-380 °C. The parallel plate reactor is operated with a RF frequency of 13.56 MHz or about 200 kHz, while the Hot Wall reactor is only operated in the range 50-200 kHz.

A new type of reactor using a high density plasma source, ICP, ECR or microwave, has been used incidentally. These reactors are developed mainly for reactive ion etching (RIE) but may have also advantages in deposition rate, layer composition and uniformity for deposition.

LPCVD

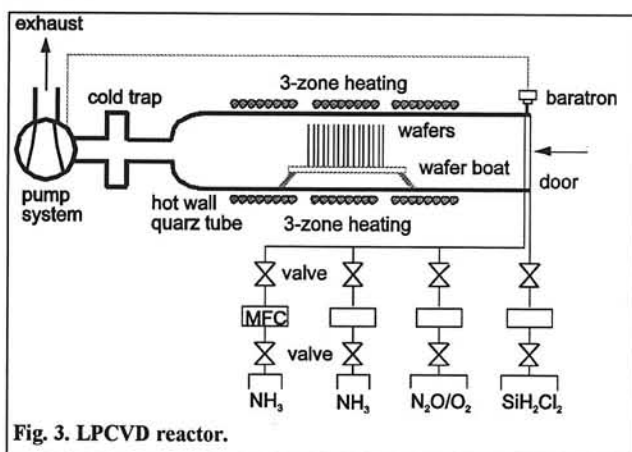


Fig. 3. LPCVD reactor.

In a Low pressure CVD process the energy needed for the reaction is generated by heating the substrate and gas phase to a sufficient high temperature. For SiO_xN_y deposition temperatures between 800 and 980 °C are used. Special tube ovens with a zone of constant temperature have been developed for these processes (Fig 3).

Comparison of PECVD and LPCVD

A parallel plate reactor is typically a single wafer or small batch size reactor, while a PECVD hot wall and a LPCVD reactor can process large batch sizes. There is a large difference in

process temperature between PECVD and LPCVD. The higher temperature in the LPCVD process results in in principle higher quality films, but it appears that these films have also a larger tensile stress, which restricts the layer thickness that can be deposited.

Silicon Oxynitride Layer Properties

PECVD

The main optical property is the refractive index. As stated in the introduction, this index can be changed by changing the process, e.g. the N_2O flow (fig.4). This change is caused by a change in composition. For low N_2O concentrations the change in index is large. The process reproducibility is doubtful in this region. In fact the process is useful for refractive indices lower than 1.75.

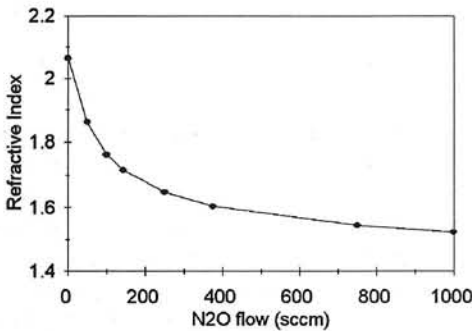


Fig. 4. Refractive index as function of the N_2O flow for a parallel plate reactor.

The growth rate increases over the same range from 20 - 35 nm/min. The optical loss of a fabricated waveguide, as deposited, is about 0.5 - 1 dB/cm at a wavelength of 632.8 nm. This loss is mainly bulk and surface scatter loss. A reduction of the loss to < 0.2 dB/cm is obtained after annealing at temperature between 500 - 700 °C. The uniformity of the PECVD process depends on the reactor type and process conditions. Most important is that the electrodes are very well parallel and the reactor is not too strong contaminated. The best results obtained after well aligning and cleaning

are presented in table III. The uniformity in a parallel plate reactor is better because the flow to the surface is more directly controlled. Further improvements specially for the parallel plate reactor are expected by improving the reactor design, deposition and cleaning procedures and process optimization.

Table III. Uniformity of PECVD process for Parallel Plate and Hot Wall reactor. The values are the difference between the maximum and minimum over a square of 50x50 mm on a 3" wafer.

reactor	refractive index (n)	n - uniformity (Δn)	thickness - uniformity (Δd in %)
Parallel Plate	1.7	0.0005	2
Parallel Plate	1.5	0.0006	1.4
Hot Wall	1.6	0.005	8

LPCVD

Also for this process the refractive index can be varied. Two processes, based on either N_2O or O_2 as an oxygen source, have been used (fig. 5 and 6).

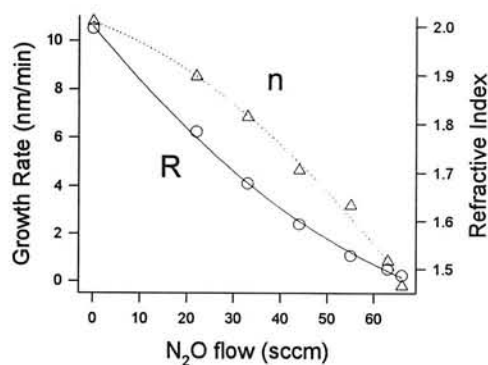


Fig. 5. Refractive index and growth rate as function of the N_2O flow for the LPCVD process.

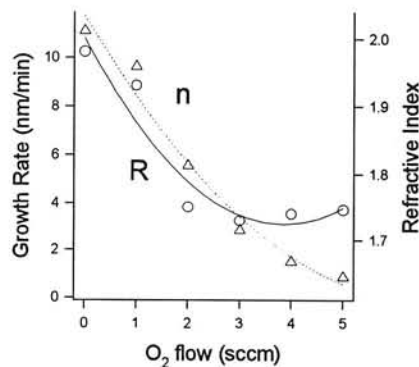


Fig. 6. Refractive index and growth rate as function of the O_2 flow for the LPCVD process.

Unlike the PECVD process the deposition rate strongly decreases for higher N_2O or O_2 flows. Films grown with both processes have very low losses (< 0.2 dB/cm) in the visible region.

In the IC industry mainly the nitride process is used. Good uniformity is reached in this process because the growth rate is determined by the rate of a surface reaction. Therefore non-uniformity due to variation in transport to different parts of the wafer is a second order effect. In oxynitride deposition the process is more complicated and position dependent concentration variations occur. Larger non-uniformity than for nitride is found (Table IV). The strongest increase is found in the refractive index variation, while also the thickness uniformity is worse for layers with a refractive index below 1.85.

Table IV. Uniformity of LPCVD process using oxygen. The values are the difference between the maximum and minimum over a square of 50x50 mm or 20x20 mm on a 3" wafer.

material	refractive index (n)	n - uniformity (Δn)		thickness - uniformity (Δd in %)	
		50x50	20x20	50x50	20x20
Si_3N_4	2.0	< 0.0005	$<< 0.0005$	2	0.2
SiO_xN_y	1.82	0.008	0.003	2	0.2
SiO_xN_y	1.7	0.006	0.003	5	0.5

Comparison between PECVD and LPCVD

PECVD and LPCVD appear to be complementary technologies for integrated optics applications. Films with a refractive index below 1.75 can be deposited with PECVD. Better uniformity can be obtained and the process is more suitable for the required higher layer thickness because of the higher deposition rate and lower stress. Films with a higher refractive index than 1.75, especially the nitride, can better be deposited with LPCVD. The better uniformity together with lower scattering losses are the main advantages. Growth rate is not so important because the required thickness is only a few tenths of a micron. The low surface roughness of these thin films is very important to avoid scatter losses.

Hydrogen induced losses

PECVD and LPCVD film contain hydrogen due to the use of hydrogen compound in the deposition process. Reported concentration range from 20-30 at% in PECVD films to 3 at% in LPCVD films. Absorption losses due to the incorporated hydrogen are more important at wavelengths in the near infrared (1300 - 1600 nm), which find more application in telecommunication. The main absorption peaks are at 1380 nm and 1520 nm, both are overtones from vibration absorption's of the Si-OH and N-H bonds. The first occurs only in PECVD SiO₂ while the second is present in all nitrogen containing material. The amount of hydrogen is determined by infrared spectroscopy that is calibrated with Elastic Recoil Detection (ERD) (fig. 7).¹⁰ The absorption loss in the peak maximum (1520 nm) can be as high as 16 dB/cm. With high temperature

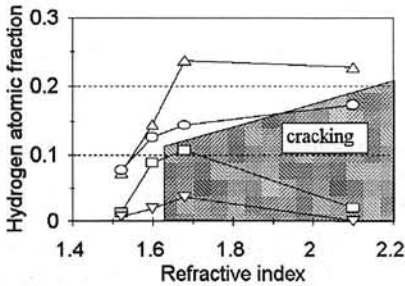


Fig. 7. Hydrogen content of PECVD films as function of the refractive index, as deposited (Δ) and after 700°C (O), 1000°C (\square) and 1150°C (∇) annealing. If the point is in the gray area the film cracked upon annealing.

annealing (1150 °C) the amount of incorporated hydrogen is reduced to 1 - 2 at%. An example of an absorption loss spectrum is given in figure 8. The peak height and width are reduced, so the residual loss at the important telecommunication wavelength of 1550 nm is < 0.2 dB/cm. Unfortunately the film tensile stress increases such that films with a refractive index above 1.6 cracked. The here presented data are for a PECVD process using a 187.5 kHz plasma generator. For the often used frequency of 13.56 MHz the hydrogen is bonded more to silicon, which causes increased stress and cracking.

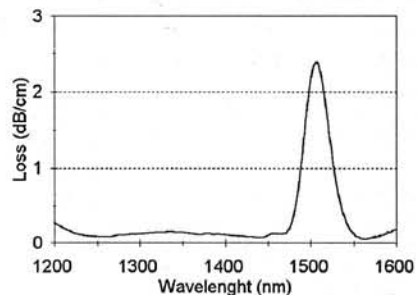


Fig. 8. Loss spectrum of an annealed (1150 °C) waveguide of PECVD SiO_xN_y, with n=1.6. Residual hydrogen: 2 at%.

Applications

Layer uniformity is for integrated optic devices very important because the mode of propagation of light is directly coupled to the optical properties and layer thickness. Most basic functions are based on the phase of the optical signal. Such a situation is rare in other thin film or electronic devices. The demand is uniformity in propagation constant or effective refractive index of the waveguide. In principle a non-uniformity in thickness can be compensated with a non-uniformity in refractive index. In practice this is hard to realize and uniformity of both thickness and refractive index are needed. Not all functions or devices are as sensitive for non-uniformity. We will discuss first several functions with increasing demands and thereafter look at more complex devices build of functions on different positions on a chip.

Absorption sensor

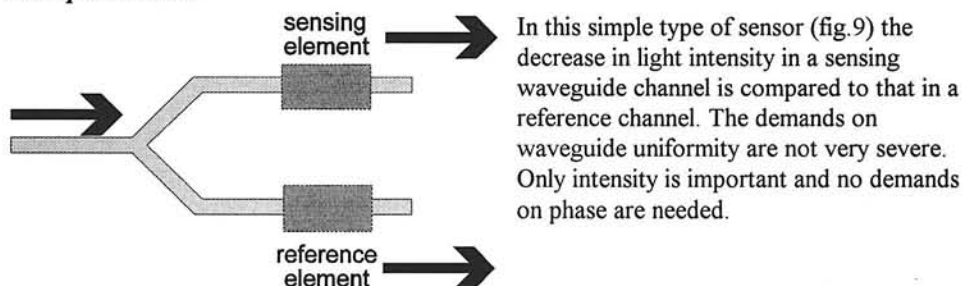


Fig.9. A schematic absorption sensor.

In this simple type of sensor (fig.9) the decrease in light intensity in a sensing waveguide channel is compared to that in a reference channel. The demands on waveguide uniformity are not very severe. Only intensity is important and no demands on phase are needed.

Mach-Zehnder interferometer.

A Mach Zehnder interferometer is an optical structure in which light is splitted in two branches and recombined. The output is maximal if the light arrives in phase at the point of combining.

In figure 10. a general design for an integrated version is shown. The basic idea is that the propagation is changed in one of the branches, e.g. by a sensing element. Both branches are normally not identical and another source of difference e.g. non-uniformity of the effective index off the waveguide is no real problem. In some situations the branches are designed to be identical and the Mach-Zehnder is operated close to the symmetrical situation.

Fig. 10. A schematic Mach Zehnder interferometer.

As an example we will present the effect of non-uniformity for such a device. For the waveguide structure shown in figure 10. and a branch length of 30 mm and separation of 50 μm the effect of the thickness variation on the phase, the signal level and the sensitivity is presented in table V. The output signal of a Mach-Zehnder varies with the phase as:

$$\frac{I_{out}}{I_{in}} = \cos^2 \frac{\Delta\varphi}{2}$$

in which I_{out} and I_{in} are the intensities in the input and output and

$\Delta\varphi$ the phase difference between the branches.

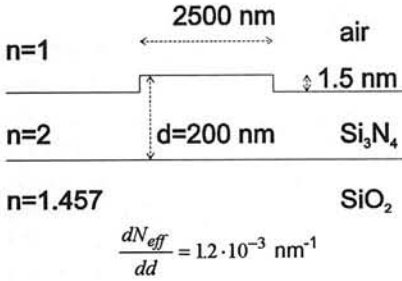


Fig. 11. Cross-section of nitride waveguide used in the Mach-Zehnder interferometer.

The phase difference corresponding with the steepest output change is chosen as working point: $\Delta\phi = \pi/2$. For absolute measurements the change in signal level, $\Delta\left(\frac{I_{out}}{I_{in}}\right)$, is important,

while for relative measurements the change in sensitivity, $\Delta\left(\frac{\partial\left(\frac{I_{out}}{I_{in}}\right)}{\partial\phi}\right)$, is important. From

table V. it is clear that absolute accuracy is hard to reach even with very uniform layers. Relative accuracy as presented here needs clearly a high uniformity. More general the Mach-Zehnder is not so demanding because when $\Delta\phi$ is varied over more than 2π the exact position of the interference fringes is known.

Gratings

Gratings are functions with different applications in sensors:

- coupling free space light beam into a waveguide
- coupling light from a waveguide through free space to a detector
- coupling light between two modes in the same or different waveguides

This function can be used to make a wavelength filter because the coupling condition:

$$\Lambda = \frac{\lambda}{\Delta n_{eff}} \text{ with } \Lambda = \text{grating period, } \lambda = \text{wavelength and}$$

Δn_{eff} = the difference in effective refractive indexes of the modes

If the Δn_{eff} is effected by the sensing layer, the read-out is in terms of a wavelength change. For a small bandwidth filter the length must be as large as possible. One can derive for a non-uniform waveguide the maximum useful length is restricted by the non-uniformity. This results in the following relation for the minimum bandwidth:

$$\Delta\lambda_{FWHM} = \Lambda \sqrt{2\lambda \frac{\partial n_{eff}}{\partial z}}$$

In designing a waveguide structure with two vertical TE modes the sensitivity of Δn_{eff} for

Table V. Effect of non-uniformity on a Mach-Zehnder interferometer.

$\frac{\Delta d}{d}$ (% / cm)	$\Delta\phi$ (rad)	$\Delta\left(\frac{I_{out}}{I_{in}}\right)$ (%)	$\Delta\left(\frac{\partial\left(\frac{I_{out}}{I_{in}}\right)}{\partial\phi}\right)$ (%)
1	$0.2 \cdot 2\pi$	-	4
0.5	$0.1 \cdot 2\pi$	~30	2
0.1	$0.02 \cdot 2\pi$	6	0.4

either thickness variations or refractive index variations can be minimized. In table VI. the minimum bandwidths and optimal lengths for both situations are presented.

Table VI. Grating length and bandwidth limited by non-uniformity.

n SiO _x N _y	Thickness insensitive $\Delta n = 0.001 / \text{cm}$		Refractive index insensitive $\Delta d = 0.2 \% / \text{cm}$	
	L_{max} (mm)	$\Delta\lambda$ (nm)	L_{max} (mm)	$\Delta\lambda$ (nm)
1.6	2.1	1.9	5.1	1.5
1.7	2.1	1.1	3.6	1.3
1.8	2.1	0.8	2.9	1.1
1.9	2.1	0.6	2.5	1.0
2.0	2.1	0.5	2.3	0.9

The bandwidths are acceptable for many applications but this can only be reached for a good uniformity. Even in this case the optimum length is only a few millimeters.

Second Harmonic Generating Device

One way of generating visible light for use in integrated optical waveguide sensors is second harmonic generation (SHG) from cheap diode lasers with a wavelength of about 850 nm. A planar waveguide version of such a device has been realized on the basis of SiO_xN_y waveguides covered with non-linear calix[4]arene. In this device the modes at the fundamental wavelength (ω) and the second harmonic wavelength (2ω) must be phase matched very well. To reach a coherence length of 10 mm a $\Delta n_{\text{eff}} < 2 \times 10^{-5}$ is needed for optimal efficiency. In practice this is a very hard to reach demand. Here every increase in uniformity pays off in much better efficiency. For a device with a refractive index of SiO_xN_y well matched with that of calix an efficiency of 1 % was reached with 500 W input power¹¹.

Complex devices

The above considerations are only for a single function. In practice devices will consist of at least some functions. The separation of the functions will be much more than the separations within a function. Often the performance of the same functions on different positions must be the same. Integrated optical components are large, so a complex device will cover a whole wafer or at least a significant part of it. As an example of such a situation we will consider here two Bragg reflector gratings¹² on different positions. The demand is that the bandwidths (0.2 nm) have sufficient overlap. For this type of grating we can derive:

Table VII. Maximum variations for refractive index (n), thickness (d) and channel width (w) for a Si₃N₄ waveguide resulting in a $\Delta n_{\text{eff}} = 0.0005$.

parameter	parameter value	variation
n	2.0	0.0007
d	120 nm	0.25 nm
w	2.5 μm	0.5 μm

$\Delta\lambda = 2 \cdot \lambda \cdot \Delta n_{\text{eff}}$, so for a maximum change in wavelength of 0.2 nm the uniformity in n_{eff} must be better than 0.0005. In table VII. the maximum variations in parameters for a Si₃N₄ waveguide are presented.

Conclusions

SiO_xN_y is a flexible material for integrated optical applications. The deposition facilities are well developed for the IC production. It was shown that after some improvements in processing the properties are already very good and that further improvements can be expected. From the device examples it can be concluded that the demands range from very tolerant for variations in thickness and refractive index over the wafer to very hard to completely matched. This is a very fruitful situation in which the technology is already well enough developed to fabricate useful devices and on the other hand there is challenge for further improvement.

References

- ¹ S. Valette, J.P. Jadot, P. Gidon, S. Renard, A. Fournier, A.M. Grouillet, H. Denis, P. Philippe, E. Desgranges, "Si-based integrated optics technologies", Sol. State Technol., febr. '89, pp.69-75, 1989.
- ² C.H. Henry, R.F. Kazarinov, H.J. Lee, K.J. Orlowsky, L.E. Katz, "Low loss Si₃N₄-SiO₂ optical waveguides on Si", Appl. Opt. 26(13), pp.2621-2624, 1987.
- ³ H.Kreuwel, "Planar Waveguide Sensors for the Chemical Domain", Thesis, University of Twente, 1988.
- ⁴ W. Gleine, J.Müller, "Integrated optical components on silicon substrates", Proc. EFOC/LAN 88, p.38-42, 1988.
- ⁵ H. Bezzaoui, A. Baus, E. Voges, "Integrated optics on silicon with PECVD-fabricated waveguides", Micro System Technol., Ed. H.Reichl, p.283-288, 1990.
- ⁶ "Integrierte Optik auf Silizium", Abschlussbericht des Verbundprojektes: "Entwicklung eines CMOS-kompatiblen Gesamtprozesses zur Herstellung integriert-optoelektronischer Schaltungen auf Silizium", 1989-1992, VDI/VDE Technologiezentrum Informationstechnik GmbH, 1992.
- ⁷ P. Gidon, S. Valette, P. Schweizer, "Vibration sensor using planar integrated interferometric circuit on oxidised silicon substrate", Proc.SPIE Vol.514, pp.187-190, 1984.
- ⁸ D. Peters, K. Fischer, J. Müller, "Integrated optics based on silicon oxinitride thin films deposited on silicon substrates for sensor applications", Sens. & Actuators A 25-27, p.425-431, 1990.
- ⁹ E. Voges, "Integrierte optik auf Glas und Silizium für Sensoranwendungen", Techn.Messen 58(4), pp.140-145, 1991.
- ¹⁰ H. Albers, L.T.H. Hilderink, E. Szilágyi, F. Paszti, P.V. Lambeck, Th.J.A. Popma, "Reduction of hydrogen induced losses in PECVD-SiO_xN_y optical waveguides in the near infrared, LEOS '95, IEEE Lasers and electro-optics Society Annual Meeting 1995, San Francisco, pp. 88-89.
- ¹¹ K. Wörhoff, O.F.J. Noordman, N.F. van Hulst, H. Albers and P.V. Lambeck, "Phase matched second harmonic generation in silicon[oxy]nitride - calix[4]arene waveguides", CLEO Pacific RIM '95, Technical Digest, p.199, 1995.
- ¹² G.J. Veldhuis, R.G. Heideman and P.V. Lambeck, "Bragg-reflector used as integrated chemo-optical sensor", This conference.

Electro-optical phasemodulation in zincoxide (ZnO)

R.G. Heideman, R. Lammers, P.V. Lambeck

MESA Research Institute, University of Twente
P.O. Box 217, 7500 AE Enschede
e-mail: R.G.Heideman@el.utwente.nl

Abstract. This paper describes the use of electro-optically induced phasemodulation in ZnO for optical sensor applications. A Mach-Zehnder interferometer is fabricated with a voltage \times length product -corresponding to a phase difference π (at a used wavelength of 632.8 nm)- equivalent to ≈ 25 V \times cm for TE-polarized light. The modulation depth is better than -10 dB. Efficient phasemodulation can be achieved from 1 kHz upto 20 kHz.

I. Introduction.

In the field of integrated optical sensors the Mach-Zehnder interferometer (MZI) shows a very high potential [1,2]. The interferometer geometry is especially suited for detecting the analyte induced optical phasechange, while the Mach-Zehnder configuration is intrinsically balanced resulting in a stable sensorsignal. In figure 1a, the basic layout of the MZI is shown.

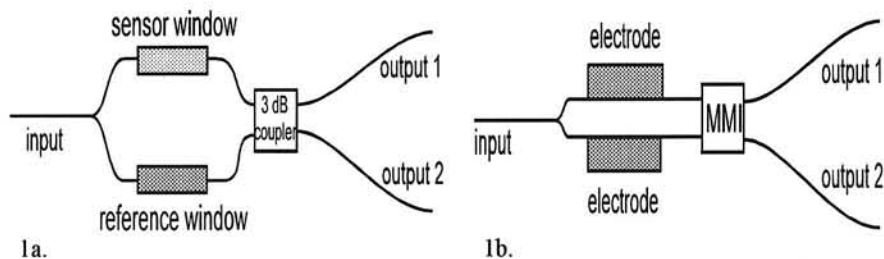


Figure 1. Schematic representation of an integrated Mach-Zehnder interferometer (MZI) for sensor applications (1a) and for the phasemodulation experiments described in this paper (1b). The two outputsignals are mutually out of phase (for explanation see text).

The input optical channel is transformed into the two identical branches of the interferometer through a Y-junction, which equally splits the intensity of the incoupled mode. In the 3 dB-coupler, the branches are recombined, yielding two output signals mutually out of phase:

$$I_{\text{output 1}} = I_0 \sin^2(\Delta\varphi) \quad (1a)$$

$$I_{\text{output 2}} = I_0 \cos^2(\Delta\varphi) \quad (1b)$$

Here $\Delta\varphi$ is the optical phasechange induced by the analyte to be detected. As this phasechange and therefore the sensor response is caused by any external parameter -physical or chemical- causing a variation of the refractive index of (a part of) one of the waveguide branches, the MZI can be applied for a large variety of sensing applications [2-4].

Despite of its strong points, the integrated optical MZI is seldomly applied for commercial sensor applications untill now. This is probably caused by two major drawbacks. Firstly, there is the general problem of connecting the optical chip via fibers to external parts, e.g. the lightsource and the detection unit, in an economical way. Secondly, the MZI sensor signal is not easily linearized (see eq.1), which is essential for exploiting the high sensitivity potentials.

By using ZnO optical waveguides both problems can be overcome. For such IO chips we have developed a simple selfaligning fiber-to-chip coupling scheme, enabling quick and reliable connection of the fiber to the optical chip without losing the high sensor sensitivity. This coupling scheme is essentially based on photolithographically defined V-grooves in the silicon substrate, combined with a sawcut. The sawed ZnO-optical waveguide endface shows small roughness only, so polishing is not needed. Elsewhere we treat this coupling scheme in more detail [5]. Furthermore, ZnO allows for electro-optically induced phase modulation, which can be used for linearizing the sensor signal (for instance by applying an ac-phase modulation of magnitude π in combination with an electronic readout system).

In this paper the modulation principle, the fabrication process and the experimental results obtained with this integrated MZI phase modulator will be described.

II. Electro-optical phase modulation.

The modulation principle is based on the electro-optic effect of ZnO. By applying an electric field over a layer of this material, the optical refractive index is changed. Used as an optical waveguide, the corresponding optical phase of the guided mode is changed. The sign of this phasechange is depending on the direction of the electric field.

The electro-optical phase modulation will be demonstrated using a MZI as shown in figure 1b. As 3 dB-coupler a 2×2 MMI, a multimode interference coupler [6], is used.

Both interferometer branches are covered with an electrode. The optical phase difference between the two interferometer branches determines the light intensities in (each of) the output channels (eq. 1). The voltage \times length product necessary to switch the intensity from output 1 to output 2 is called V_π .

III. Device fabrication process.

3.1. Device design.

Thin layers of sputtered ZnO show a polycrystalline structure with the columnar (c-)axis perpendicular to the substrate, while the columns show a random orientation parallel to the substrate. Only an external electrical field component in the vertical direction will therefore result

in a macroscopic refractive index effect. The polarization of the light used will be TE (showing a much lower electrode induced attenuation compared to TM polarized light). The wavelength used is 632.8 nm.

The cross-section of the layer configuration used is shown in figure 2. The top-electrodes cover the channels completely. These top electrodes are 12 μm apart. The voltage can be applied either between the top-and the bottom electrode or between the two top-electrodes (coplanar electrode configuration). The latter configuration is technologically less complicated, but shows a less-effective electrical field distribution. The length of the devices is 4 cm, while electrode lengths of 1 cm, 1½ or 2 cm are chosen.

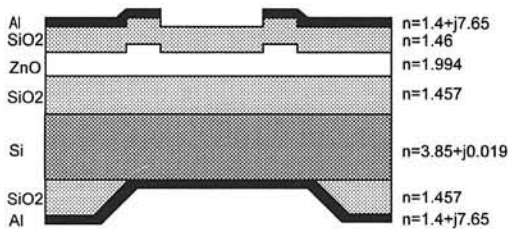


Figure 2. Cross-section of the waveguide configuration used in the experiments. The refractive indices are given for TE-polarized light at $\lambda = 632.8 \text{ nm}$.

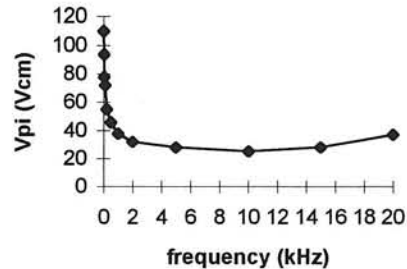


Figure 3. Voltage \times length product V_{π} as a function of frequency.

Attention has been paid to the layer configuration with respect to minimizing the required V_{π} and the waveguide attenuation, while keeping the channel waveguide single-moded. In practice, this means a maximized ZnO-thickness and a minimized buffer SiO₂-layer thickness. The thickness of the upper SiO₂-layer is a trade-off between a low electrode induced attenuation and a low required V_{π} . An electrode induced attenuation value of 0.5 dB/cm is regarded as acceptable by the authors: the channel attenuation without electrodes is $\approx 2 \text{ dB/cm}$.

3.2. Device fabrication.

The ZnO layer with thickness of 440 nm is sputtered (R.F. planar magnetron sputtering [7]) on top of a thermally oxidized Si-wafer (10 minutes at 1150 °C, resulting in a SiO₂-layer thickness of 520 nm thick). The ridge height of the 4 μm wide channels is 5 nm, and is fabricated through ion beam etching (IBE). The 2 \times 2 MMI-coupler has a width of 45 μm and a length of 4800 μm .

On top of the ZnO-layer a thin (PECVD, Plasma Enhanced Chemical Vapour Deposition) SiO₂ layer (0.35 μm) is grown. The electrodes are made of a sputtered layer of aluminium, with thickness of 200 nm. The bottom electrode is sputtered directly onto the silicon substrate, through selective removal of the thermally oxidized SiO₂ layer in this region.

IV. Experimental results.

The phasemodulation experiments were done at an applied frequency of 2 kHz. The voltage is applied between the top electrode and the bottom electrode. The maximum intensities measured in both output channels differ less than 5%. The modulation depth, being defined as $10 \times \log(I_{\min}/I_{\max})$ dB, is measured, in combination with V_{π} . In table 1 the experimental results are summarized.

Table 1. Typical results of the electro-optical phasemodulator at 2 kHz.

V_{π} (volts×cm)	modulation depth (dB)
25 ± 4	≤ -10

In figure 3 the V_{π} -voltage is shown as a function of the frequency. The increases at 10 kHz and 1 kHz are due to the RC-time related to the electrodes and the electronic conduction of ZnO, respectively. Using the coplanar electrode configuration increases the electrode related RC-time to 20 kHz, but does not require a larger V_{π} -value. From this figure it follows that the electro-optical phasemodulation is only applicable from (approximately) 1 kHz.

V. Discussion and conclusion.

For linearizing a MZI-sensor the electro-optic phasemodulation in ZnO was investigated for TE-polarised light; outside the frequency interval 1-20 kHz the voltage×length product V_{π} -i.e. the voltage required for obtaining a π -phasechange over 1 cm propagation- is equal to ≈ 25 V×cm. The modulation depth is better than -10 dB. The upper frequency boundary of 20 kHz can be easily increased as it is caused by the RC-time related to the electrodes. Furthermore, 20 kHz is fast enough for most sensing applications.

It can be concluded that the electro-optic effect of ZnO can be successfully applied for obtaining a phasemodulation required for the linearization of a MZI-sensor. The combination with the simple fiber-to-chip connection scheme, which can be applied to the same layer configuration, offers the prospect of a very attractive integrated optical Mach-Zehnder interferometer sensor family.

References.

- [1] P.V. Lambeck, Sensors and Actuators B, 8 (1992) p.103-116.
- [2] R.G. Heideman et al., Sensors and Actuators B, 10 (1993) p.209-217.
- [3] R. Dangel and W. Lukosz, Proceedings ECIO '95 (1995) p.371-374.
- [4] J. van Gent, PhD. thesis, University of Twente 1990.
- [5] R.G. Heideman et al., in progress.
- [6] L.B. Soldano et al., Journal of Lightwave Technology, vol. 13(4) (1995) p.615-27.
- [7] R.G. Heideman et al., Optical Materials, vol. 4 (1995) p. 741-755.

High-voltage probe

A. Fransen, G.W. Lubking, M.J. Vellekoop

Delft University of Technology
Electrical Engineering Department, Electronic Instrumentation Laboratory
PO Box 5031, 2600 GA DELFT, Netherlands
tel.: +15 2786285, email: alwin@ei.et.tudelft.nl
DIMES
PO Box 5053, 2600 GB DELFT, Netherlands

Abstract

Several techniques for measurements of voltages up to 20 kV are compared and surface acoustic wave (SAW) based voltage sensors offer the best features to obtain a small and accurate device for use in high-voltage supplies or measuring instruments. The sensing principle of SAW voltage sensors is based on changes in time delay of an SAW delay line, caused by the applied voltage. The calculated sensitivity of a sensor in 128° rotated Y-X LiNbO₃ amounts to $(\Delta f/f)/E \approx 59 \times 10^{-12}$ m/V. Measurements reveal a higher sensitivity of 105×10^{-12} m/V which yields a resolution of better than 0.2 V. The design of a complete instrument is also described.

Introduction

The determination of high voltages in the range of 1 kV to 20 kV with a high accuracy and stability (10^{-5} to 10^{-6}) usually requires costly and bulky resistive or capacitive voltage dividers. These voltage dividers determine a large part of the price and size of the equipment in which they are used, for instance in a high voltage source or in a high voltage measuring instrument. In this paper, we are focusing on a voltage sensor that must provide a reduction in price and size, and that must be able to be used in the feedback system of a high-voltage supply, or in a stand alone high-voltage measuring instrument.

Several techniques are available for the measurement of voltages up to 20 kV, the principal ones being: the electrostatic voltmeter, the sphere gap and the resistive or capacitive divider in combination with a multimeter or oscilloscope [1]. Less common techniques use electro-optic and acoustic voltmeters. Which voltage measurement technique is useful for the sensor depends on several criteria: cost, size, accuracy, resolution, stability and the type of output signal. In the following part, the available techniques are discussed.

The electrostatic voltmeter and the sphere gap are typically used as laboratory equipment for reference measurements. They are rather large, not very accurate, and not able to produce an electric output. They are therefore not suited for use in a power supply or in a measurement system.

Resistive and capacitive dividers are frequently used as voltage dividers in power supplies and measurement systems. They are simple to implement and can be very accurate. However, if an accuracy of 10^{-5} is demanded, the dividers become large (e.g. wire wound resistors) or expensive (e.g. thin metal foil resistors cost thousands of guilders).

Electro-optic voltage measurements are based on the change of the optical transmission characteristics (the refractive index) of an electro-optic material when it is subjected to the electric field generated by the voltage. The refractive index of the material is measured by an optical system, which electrically isolates and physically separates the measuring system from the system being measured. This isolation and separation is the major advantage of electro-optic measuring. Electro-optic voltage sensors can be fabricated as bulk and as integrated-optic devices. The bulk optic devices, such as Pockel's and Kerr cells, can be used for very high voltages (up to several hundreds of kV's) and can reach an adequate accuracy [2]. However, they use a large electro-optic crystal and need several optical components, like lenses and polarizers which are bulky and expensive. Integrated optic devices, monolithically integrated on a electro-optic crystal (usually LiNbO_3), offer a size reduction and do not need optical components. However, integrated optical devices have linear dynamic ranges of no more than tens of volts, so a voltage divider [3] or a special electrode structure [4] (on a 40 cm long crystal for 20 kV) is still necessary. An extended description of electro-optic voltage measurements can be found in [2,5].

In surface acoustic wave (SAW) based voltage sensors, acoustic waves propagating in a piezoelectric material are modulated by an electric field which is caused by the high voltage. SAW voltage sensors have several attractive features: (1) They are small. (2) They show a linear and sensitive response to the modulating voltage. (3) They have a high input resistance and a low capacitance, and are therefore suited for the direct measurement of a high voltage without the use of a prescaler. (4) They have a frequency signal output, so the signal can directly and accurately be measured using a digital measurement system with no need for an A/D convertor. (5) They are produced using existing IC-technologies. Hence, the production of the sensors is cost-effective and reproducible.

Comparing all these voltage measurement techniques it appears that SAW based voltage sensors are the best choice. In this paper we will describe the theory, the design and measurements of a SAW based voltage sensor: The High Voltage Probe.

Acoustic Voltage Sensors

The sensing principle of acoustic voltage sensors is based on the detection of changes in the time delay of a SAW delay line caused by an electric field. If a voltage is applied to two high-voltage electrodes on the delay line, see Figure 1, the resulting electric field causes a strain in the piezoelectric material and a shift in velocity of the acoustic wave. Both effects cause a shift in the time delay.

The delay line is used in an oscillator loop as the frequency-determining element, and the shift in the time delay will therefore result in a shift in the oscillating frequency, according to:

$$(1) \quad \frac{\Delta f}{f} = - \frac{\Delta \tau}{\tau} = - \left(\frac{\Delta l}{l} - \frac{\Delta v}{v} \right) = \gamma E$$

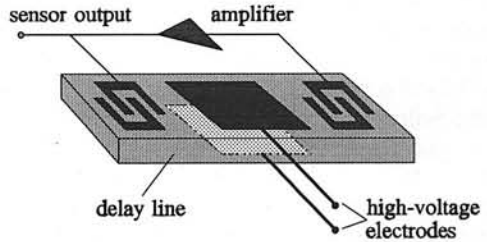


Figure 1. SAW voltage sensor

$\Delta f/f$ is the fractional change in oscillating frequency, $\Delta\tau/\tau$ is the fractional change in the time delay $\tau = l/v$, l is the length of the delay line and v the SAW velocity. E is the electric field. The strain in the direction of propagation S ($= \Delta l/l$) can be calculated from the piezoelectric equations [6]. For the 128° rotated Y-cut, X propagating (128° YX) LiNbO_3 , used in the voltage probe, an electric field normal to the wave propagation direction and no external stress, the strain in the material in the propagation direction, S_1 , is given by:

$$(2) \quad S_i = d_{mi} E_m \quad ; \quad S_1 = d_{21} E_2 + d_{31} E_3 = (d_{21} \alpha_2 + d_{31} \alpha_3) E$$

where d_{mi} is the piezoelectric tensor, $d_{21} = -21 \times 10^{-12}$ C/N, $d_{31} = -1 \times 10^{-12}$ C/N [7], $\alpha_2 = \cos(128^\circ)$ and $\alpha_3 = \sin(128^\circ)$. S/E then equals 12×10^{-12} m/V.

The sensitivity of the SAW velocity ($\Delta v/v$) in LiNbO_3 to the electric field was calculated by Gafka [8]. He presented a derivation of the constitutive equations for electroelastic media upon mechanical or electrical bias. Combining these constitutive equations with the equation of motion ($T = \rho d^2 U/dt^2$, $D=0$), it was found that the sensitivity of the SAW velocity on an external electric field is a linear tensor function of the form:

$$(3) \quad \frac{\Delta v}{v} = G_i E_i^{bias}$$

where G_i is the first order sensitivity tensor with three components. This tensor was calculated for all different planes and directions of SAW propagation in LiNbO_3 . For the 128° YX with E normal to the surface, $(\Delta v/v)/E$ equals -47×10^{-12} m/V. A SAW oscillator fabricated on 128° YX LiNbO_3 therefore shows a γ of -59×10^{-12} m/V, and because the LiNbO_3 has a thickness of 0.5 mm, the voltage sensitivity of the oscillator results in: $(\Delta f/f)/U = 0.12 \times 10^{-6} \text{ V}^{-1}$ (U is the applied voltage, max 10 kV, see following chapter). This value is fairly close to the experimental value found by Joshi [6] of $0.18 \times 10^{-6} \text{ V}^{-1}$.

Instrument Design

The design of a measurement instrument can be divided into two parts: packaging design and sensor design. The package of the sensor has to offer safe input and output terminals and protection against electric breakdown and against external disturbing influences, like humidity, temperature and EM pickup. The type of in- and output of the instrument depends on its final use. If the voltage sensor is to be used in the feedback loop of a power supply, the sensor only needs electrical input and output terminals, so no extra measures have to be taken. If the sensor is to be used in a stand alone instrument, it also needs a display, control buttons and, for instance, a RS-232 connection for computer control. The easiest way to implement all these features is the use of a microcontroller, which will read and control the sensor and will process its information.

Experiments [6] showed that LiNbO_3 can withstand electric fields greater than 20 MV/m without breakdown, so the sensor (thickness 0.5 mm) can withstand voltages up to 10 kV. 20 kV can be reached with a substrate of 1 mm. However, the voltage sensitivity will then be decreased by a factor 2.

Breakdown along the surface of the substrate can occur at much lower field strengths. A (very) safe limit to prevent surface breakdown is 500 V/mm. This means that the package of the sensor must provide a distance between the electrodes of minimal 40 mm.

To protect the sensor from external influences it is placed in a hermetically closed (metallized) container, which, in case of a stand alone instrument, also contains the microcontroller. The temperature sensitivity of the sensor can be greatly reduced by using a dual sensor configuration [6]. In such a configuration, one sensor measures the applied voltage and the other will function as a reference.

The basic layout of the sensor is given in Figure 1. The bias is applied to the bottom electrode while the top electrode is grounded, this to prevent breakdown between the electrode and the IDTs. The typical dimensions of the sensor, the IDTs and the high voltage electrodes are given in Table 1. The sensors are fabricated on a $10 \times 10 \text{ mm}^2$ 128° YX LiNbO_3 crystal at the DIMES IC factory, using a slightly adapted IC process.

Table 1. Typical dimensions of SAW voltage probe delay lines

path length [mm]	5.8-7.3
HV electrode length [mm]	1.4-6.3
number of fingerpairs	15-36
finger period [μm]	32-96
aperture [mm]	1

Measurements

Preliminary voltage measurements were performed using 0.5 mm thick SAW delay lines with 22 fingerpair IDTs having a periodicity of $48 \mu\text{m}$ and a path length (centre-to-centre distance of the IDTs) of approximately 7 mm. These dimensions result in an oscillation frequency of 80.4 MHz and an insertion loss of about 8 dB. A preliminary result can be given: the voltage sensitivity is $0.21 \times 10^{-6} \text{ V}^{-1}$ ($\gamma = 105 \times 10^{-12} \text{ m/V}$) and the short term stability is smaller than 1 Hz; this yields an obtainable resolution of better than 0.1 V.

Conclusions

From comparison of different voltage measurement techniques, it appears that acoustic wave based voltage sensors are a very good choice for accurate high-voltage (HV) measurements (up to 20 kV) in HV sources and HV measuring instruments. Preliminary measurements with sensors fabricated on 0.5 mm thick 128° Y-X LiNbO_3 show a voltage sensitivity of $0.21 \times 10^{-6} \text{ V}^{-1}$ for measurements up to 10 kV. This yields a resolution of better than 0.1 V. With a 1 mm thick substrate 20 kV measurements are possible. They will have a sensitivity of $0.1 \times 10^{-6} \text{ V}^{-1}$, yielding a resolution better than 0.2 V.

Acknowledgements

We would like to thank W. van der Vlist and Dr P.M. Sarro for their help in the fabrication of the devices.

References

- [1] Kreuger, F.H., 'Industrial high voltage', Vol. II, Delft University Press, Delft, 1992, p.59.
- [2] Massey, G.A., 'Electromagnetic field components; their measurement using linear electro-optic and magneto-optic effects', *Applied Optics* 14 (11), Nov 1975, p. 2712.
- [3] Jaeger, N.A.F., 'High-voltage sensor employing an integrated optics Mach-Zehnder interferometer in conjunction with a capacitive divider', *J. of Lightw. Tech.* 7 (2), feb. 1989, p. 229.
- [4] Lee, S.-S., 'Integrated optical High-voltage sensor using a Z-cut LiNbO_3 cutoff modulator', *IEEE Photonics Tech. Lett.* 5 (9), sept. 1993, p. 996.
- [5] Donaldson, A., 'Candidate materials and technologies for integrated optics: fast and efficient electro-optic modulation', *J. Phys. D.: Appl. Phys.* 24, 1991, p. 785.
- [6] Joshi, S.G., 'Surface acoustic wave device for measuring high voltages', *Rev. Sci. Instrum.* 54 (8), August 1983, p. 1012.
- [7] Inaba, R., 'An electrostatic voltage sensor using SAW', 1982 Ultrasonics Symposium, p.312.
- [8] Gafka, D., 'Sensitivity of SAW velocity in lithium niobate to electric field or biasing stress', *J. Appl. Phys.* 73 (11), 1 june 1993, p. 7145.

Luminescence quenching for chemo-optical sensing

G.L.J. Hesselink, P.V. Lambeck, Th.J.A. Popma, H.J. v.d. Bovenkamp, J.F.J. Engbersen.

MESA, Institute for Micro-electronics, Materials Engineering, Sensor and Actuators, University of Twente, P.O. Box 217, 7500 AE Enschede, The Netherlands

Abstract

A new sensor principle for chemo-optical sensing is proposed and analysed, based on luminescence quenching in a layered structure¹. A theoretical framework is used to predict the luminescence quenching.

Introduction

In the search for reliable chemo-optical sensors, much work has been done on the development of both the chemo-optical transduction layer and the optical read-out system. The chemo-optical transduction layer converts a change in chemical concentration of a specific compound into a change of an optical property of the layer. That optical property can be a refractive index, an absorption coefficient or the intensity of a luminescent emission. The optical read-out circuit subsequently converts the change of this property into a change of an output light intensity.

Here we will focus onto a specific novel optical read-out principle based on luminescence quenching. Although this luminescence quenching (LUQUEN) sensor uses luminescence, the probing is based on a change in absorption, which will be explained hereafter.

The goal of this paper is to show the possibilities and prospects of this principle. Some comparison is made to other optical sensing principles. In our research we used as an example an ammonia sensing two layer system, the luminescent layer being a polymer layer with Rhodamine incorporated and the quenching layer consisting of the pH-indicator BCP.

Sensing based on luminescence quenching

An excited luminescent molecule can return to the ground state by emission of light, but also by transferring its excitation energy (also called exciton) radiationless to another molecule. The physical origin of this exciton transfer is often an electric dipole-dipole interaction between the excited molecule (donor) and the other molecule (acceptor). It can be calculated² that the probability P of this transfer (or transfer rate) is strongly dependent on the distance R between both centres, involved in the transfer:

$$P = \frac{1}{\tau_0} \left(\frac{R_0}{R} \right)^6 \quad (1)$$

where τ_0 is the luminescent decay time of the luminescent centre, if no transfer occurred. R_0 is the critical distance, i.e. the distance for which probability for transfer is equal to the probability for decay. This parameter is mainly dependent on the overlap of the emission spectrum of the donor and the absorption spectrum of the acceptor and it can be experimental determined¹.

The energy transfer mechanism can be utilised for chemical sensing by applying a receptor which is only acting as an efficient acceptor in complexated state. This means that the emission spectrum of the luminescent centre has to show a large overlap with the absorption

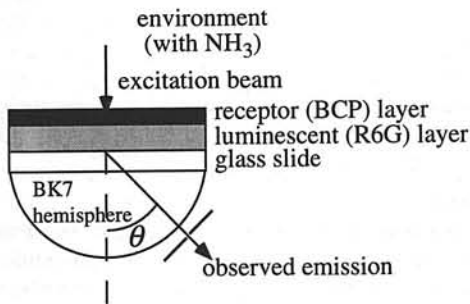
spectrum of the complexated receptor molecules but a small overlap with the absorption spectrum of the uncomplexated ones. Besides the excited receptors have to return to the ground state radiationless.

The LUQUEN sensor system consists two adjacent layers (see fig.1), one containing the luminescent centres, the other the receptor molecules. The receptor layer is adjacent to the environment so that complexation with the species to be measured is possible, after which the receptor becomes an exciton acceptor. Then energy transfer from luminescent centre to the receptor causes quenching of the luminescence, and the luminescent intensity decreases. Thus the measured intensity is a measure of the concentration of the species to be measured, the measurand.

The quenching can be enhanced by a second phenomenon; exciton migration along the luminescent centres itself. The closer the excitons are to the boundary between both layers, the larger their chance on being transferred to the acceptors and thus the smaller their lifetime, and the lower their concentration. Due to this concentration gradient the excitons show the tendency to diffuse to the boundary where their chance on being quenched is larger. In this way the region, where exciton behaviour is sensitive to the presence of quenchers in the top layer, is drastically enlarged. The quenching centres can be seen as antennas picking up the energy released by the luminescent centres.

The main factors influencing the quenching are the energy transfer rates between the luminescent centres and between these centres and the acceptors. The important parameters therefore are the critical distances for energy transfer, the real distances between the luminescent centres (for exciton migration), the concentrations and the distances between the luminescent centres and the acceptors. The latter means, that for the quenching induced intensity decrease of the complete system also the thicknesses of the layers are relevant.

Measurements



QUEN sensor.

parameter	value
R_0 for Rh6G→BCP	4.9 nm
R_0 for Rh6G→Rh6G	5.5 nm
thickness Rh6G layer	0.9 μm (for fig. 3)
thickness BCP layer	15 nm (for fig. 3)
Rh6G concentration	9 10^{-3} M
BCP concentration	3.2 M (for fig. 3)

figure 1. Model layer system for the LU-*QUEN sensor*

In our model system (see fig. 1 and table 1) we use as a luminescent centre the well known laser dye Rhodamine 6G (Rh6G) embedded in a poly-urethane polymer layer. As a receptor we use the pH indicator BCP, which forms a complex with NH₃. The BCP is evaporated onto the Rh6G-polymer layer. In the complexated state only, the absorption spectrum of the BCP molecules overlaps the Rh6G emission spectrum very well, thus forming an acceptor for the Rh6G excitation energy. The Rh6G is excited with an Ar⁺ laser at a wavelength of 488 nm. The emission is filtered and detected by a photo-multiplier system.

The emission measured is highly dependent on the angle of observation, which is caused by the angle dependence of both the reflection at the interfaces and the interference effects. We measured this angle dependence and also calculated it with a theory³ based on the Fresnel coefficients. The agreement between measurement is shown in fig. 2 for a bare 1.8 μm thick Rh6G-polymer layer. From this it can be shown that the best angle of observation for

quenching experiments would be 0° .

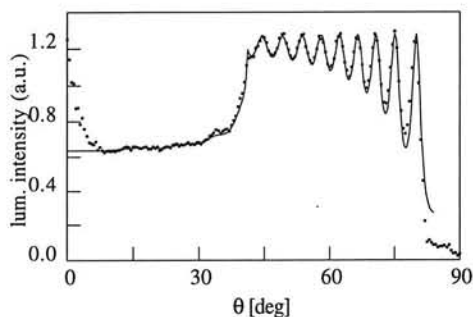


figure 2 Measured (dots) and calculated (solid line) angle dependence of the luminescent intensity of the Rh6G-polymer layer.

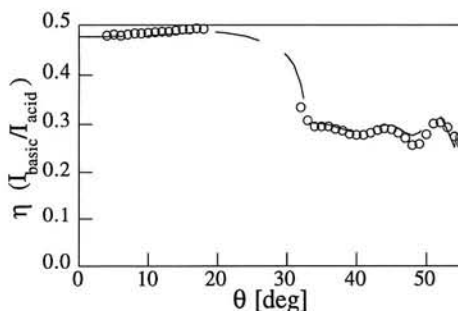


figure 3 Measured and calculated ratio for the luminescent intensity in basic and acid environment.

Effects of the quenching of the luminescence in basic environment (with NH_3) as a function of the emission angle are presented as the ratio of the intensities in complexated and uncomplexated state, the so called luminescent quantum yield η . In this way the effects of interference are neglectable (but not the effects of reflection). It can be concluded that complexation with NH_3 causes a quenching of more than 50%. At higher emission angle there is an additional effect due to the change of the reflection coefficient at the Rh6G-BCP layers interface.

Calculations

Above it is shown qualitatively that the LUQUEN principle is feasible for application in chemo-optical sensors. For detailed quantitative analysis however, calculation of the performance as a function of relevant parameters has to be preferred. A thorough theory is developed¹ for the layer set-up as shown in fig. 1. We will not go into detail of these theory, but rather show some results of a model system, to demonstrate the possibilities of the LUMQUEN sensor. To give large quenching the distances between donor and acceptors should be small, therefore the layer with the luminescent centres should be thin. For our calculations we have chosen a thickness of 25 nm for both layers, the 10^{-2} M Rh6G containing layer and the BCP layer. In fig. 4 the luminescent quantum yield of this system is shown as a function of the fraction of BCP molecules acting as acceptors. The figure shows that already a small fraction can cause quenching, and that this quenching is enlarged by increasing the Rhodamine concentration, due to the exciton migration along the Rhodamine molecules. A further increase of the quenching can be achieved by using a thinner Rh6G layer and a larger concentration. For a Rh6G monolayer supporting a BCP layer of 25 nm thickness, we calculated the quantum yield dependence as given in fig. 5, only taking into account the Rh6G-BCP exciton transfer. The fraction of BCP molecules in basic state can be converted to the equivalent amount of ammonia in the environment by using an appropriate equilibrium equation⁴.

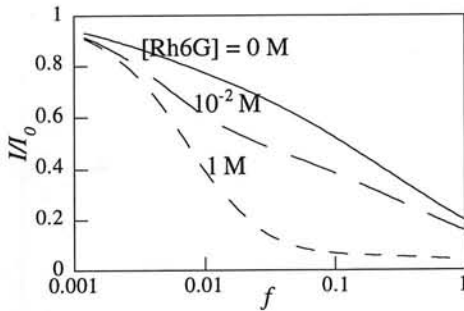


figure 4. Luminescent intensity as a function of the fraction of BCP in basic state, for different Rhodamine concentrations.

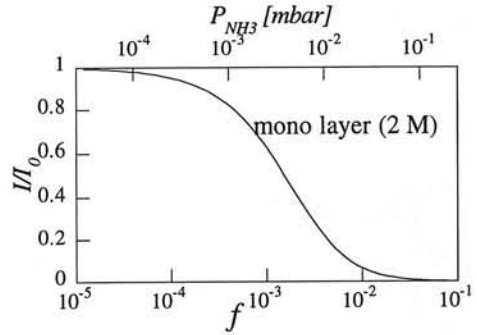


figure 5. Luminescent intensity as a function of the fraction of BCP in basic state for a monolayer of Rhodamine. The upper x-axis shows the equivalent partial pressure of ammonia,

We see in fig. 5 that a partial ammonia pressure of 10^{-3} mbar (1 ppm) already gives a reasonable quenching. Compared to the NH_3 MAC value of $2.5 \cdot 10^{-2}$ mbar (25 ppm), this means that the sensor would already be usable in practical situations. Further calculations, using a simplified model, however showed that by taking into account the exciton migration along the Rhodamine molecules, now being parallel to the boundary plane only, the sensitivity can be even enlarged by a factor 100.

Discussion, prospects

It is shown that the performance of a LUQUEN sensor can be calculated and it appeared that the largest sensitivity can be obtained, using a monolayer of the luminescent material. Calculations show that in general the evanescent field integrated optical absorption sensors show larger sensitivity reading out the chemical induced absorption changes of the BCP layer. Note the words in general! The thinner the luminescent layer, the better the LUQUEN performance, and calculations show that the sensitivity of the mono-layer type exceeds that of the evanescent field sensor. Of course the thinner the luminescent layer, the smaller the intensities. However, even at mono-layer thickness, the intensities are larger than those obtained from the well known luminescence-labelled competitive antigen-antibody sensors⁵. We expect the LUQUEN sensor to be most useful for systems, where in addition to the luminescent layer also the receptor layer has to be monomolecular, e.g. in immunosensors.

References:

- 1 G.L.J. Hesselink, "Luminescence quenching for chemo-optical sensing," Ph.D. thesis, University of Twente, Enschede, The Netherlands, november 1995.
- 2 T. Förster, *Disc. Farad. Soc.*, vol. 27, 7, 1959.
- 3 W. Lukosz and R.E. Kunz, *J. Opt. Soc. Am.*, vol. 67, 1607-1614, 1977.
- 4 J. van Gent, "Surface Plasmon Resonance - based Chemo-Optical Sensors," Ph.D. thesis, University of Twente, The Netherlands, October 1990.
- 5 S. Mansouri and J.S. Schultz, *Bio/Tech. okt.* 84, 885, 1984.

INDEX

A

- Albers, H. 93, 221
 Antonisse, M. 79

B

- Bakker, J. 211
 Bakker, M. de 39
 Balijon, M. 155
 Bartek, M. 189
 Berckmans, D. 87
 Berends, J. 59, 221
 Berg, A. van den 143
 Berg, M. van den 173
 Bergveld, P. . 17, 55, 63, 143, 163, 217
 Beulen, M. 207
 Boogaard, A. van den 103
 Bossche, A. 197
 Bot, G. 211
 Bouwstra, S. 177
 Bovenkamp, H. v.d. 239
 Breteler, H. 211
 Brixy, H. 167
 Brugman, A. 71
 Bruijn, M. 173
 Buis, G. 159
 Burnus, M. 99

C

- Chattle, M. 167
 Chu, Z. 121
 Cullen, D. 201

D

- Demeijer, E. 139
 Dhupia, G. 167
 Dominguez, C. 71
 Drieënhuizen, B. van 193
 Dubbeldam, J. 167

E

- Edler, F. 167
 Eerkens, C. 211
 Egberink, R. 83
 Elders, J. 131
 Elwenspoek, M. . . 21, 35, 93, 99, 143
 Engbersen, J. 79, 83, 239
 Eijk, C. van 103
 Eijkel, J. 63

F

- Fluitman, J. 21, 35
 Fransen, A. 235
 French, P. . . 109, 113, 159, 189, 193

G

- Gardeniers, 21, 35, 93
 Gennissen, P. 189
 Goes, F. van der, 125, 147
 Gomez, J. 173
 Goosen, J. 193
 Gorte-Kroupnova, N. 135
 Graaf, G. de 45
 Greve, J. 71
 Groot, M. de 155
 Groot, M. de 167
 Gui, C. 93

H

- Harteveld, J. 67
 Heideman, R. 59, 231
 Heidenblut, T. 99
 Hendrikse, J. 55
 Hesselink, G. 239
 Hilderink, L. 221
 Hollander, R. 103
 Houkes, Z. 135
 Huisman, B. 207

Huizenga, J.	103
Hulst, N. van	221
Huijsing, J.	155
Huybrechts, G.	87
Hijzen, E.	103

K

Kampen, E. van	155
Kampers, F.	211
Kaptein, W.	75
Kerkvliet, H.	139, 147
Khadouri, S.	125
Kiewiet, F.	173
Kindt, W.	51
Kooyman, R.	71
Korf, J.	75
Korte, P. de	99, 173
Kovalchuk, A.	1
Kruise, J.	63
Kuhl, M.	113
Kuijer, O. de	211

L

Lambeck, P.	59, 93, 221, 231, 239
Lammers, R.	231
Lechuga, L.	71
Li, X.	151
Lieshout, H. van	173
Logothetis, E.	1
Lötters, J.	217
Lubking, G.	235
Lugtenberg, R.	79, 83
Luiten, O.	173

M

Meijer, G.	125, 139, 147, 151
Meijerink, M.	163
Michalke, W.	99
Middelhoek, S.	117
Mollinger, J.	197

N

Nanver, L.	103
Neagu, C.	21, 35
Ni, J.	87
Nieuwenhuizen, M.	67
Nihtianov, S.	139
Nivelle, M. de	99

O

Olthuis, W.	17, 55, 163, 217
O'Halloran, G.	113

P

Pedersen, M.	163
Pierdominici, F.	55
Poenar, D.	109
Popma, Th.	239

R

Regtien, P.	135
Reinhoudt, D.	79, 83, 207
Riedijk, F.	155
Roggen, J.	87
Rudolf, F.	25
Ruiters, M.	75

S

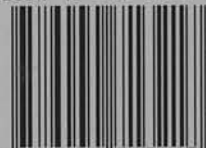
Sánchez, S.	99
Sarro, P.	103, 189
Schipper, E.	71
Schoonen, A.	13
Schwierzi, B.	99
Shahrjerdy, N.	51
Slabbekoorn, J.	103
Smith, A.	35
Smith, T.	25
Snijders, N.	173
Soltis, R.	1
Spiering, V.	131, 143
Steenvoorden, G.	39
Steinbeiss, E.	99

- T**
- Thoden van Velzen, E. 207
 Trimp, P. 113, 159
 Turner, A. 201
- V**
- Valk, H. 103
 Vdovin, G. 117
 Veggel, F. van 207
 Veldhuis, G. 59
 Vellekoop, M. 235
 Veltink, P. 217
 Venema, K. 75
 Verbeek, P. 39
 Visser, J. 1
 Vlekkert, H. van der 25
- Volanschi, A. 17
 Vranken, E. 87
 Vries, R. de 99
- W**
- Wang, G. 147
 Wientjes, K. 13
 Wils, E. 67
 Wolffenbittel, R. 45, 109, 193
 Wörhoff, K. 221
- Z**
- Zanini, M. 1
 Zeijl, H. van 51
 Zwaagstra, J. 75





ISBN 90-407-1321-9



9 789040 713217